UNIVERSITY OF SOUTHAMPTON

CONTINUOUS COOLING TRANSFORMATION KINETICS AND MICROSTRUCTURE OF MILD AND LOW-ALLOY STEEL WELD METALS

by

Peter Lindley Harrison, B.Sc(ENG), ARSM, MIM

A thesis presented to the University of Southampton
for the degree of Doctor of Philosophy.

Department of Mechanical Engineering,
University of Southampton,
Hampshire.

UNIVERSITY OF SOUTHAMPTON

ABSTRACT

FACULTY OF ENGINEERING AND APPLIED SCIENCE
MECHANICAL ENGINEERING

Doctor of Philosophy

CONTINUOUS COOLING TRANSFORMATION KINETICS AND MICROSTRUCTURE OF MILD AND LOW-ALLOY STEEL WELD METALS

by Peter Lindley Harrison

Twelve continuous cooling transformation (CCT)diagrams, applicable to reheated (coarse grained region) mild and low-alloy steel weld metals, were produced using techniques of high speed dilatometry, thermal analysis, and quantitative metallography.

A detailed study of these CCT diagrams revealed the practical significance of variations in weld cooling rate, alloy content, prior austenite grain size, and oxygen-rich inclusion content, on weld metal $\gamma \rightarrow \alpha$ phase transformation behaviour.

Carbon, manganese and nickel were all shown to have a similar influence on CCT kinetics. This generally involved depression of the CCT curves to lower temperatures and longer times and encouraged the development of fine grained intragranular acicular ferrite at the expense of grain boundary nucleated morphologies. The rôle of niobium was shown to be complex and highly dependent on overall hardenability. Molybdenum was shown to have a very strong influence on separation of the bainite and ferrite noses of the CCT diagram. Oxygen-rich inclusion content and austenite grain size were found to be inter-related in reheated weld metals due to grain boundary pinning. The CCT kinetics of the phase transformation were also seen to be influenced by an inclusion related nucleation effect.

All these factors have been discussed in detail and a new theoretical model has been presented which explains weld metal microstructural development in terms of competitive nucleation and supercooling from Ae_3. A practical model based on CCT data has also been presented to predict optimum toughness transformation regimes in C-Mn and C-Mn-Ni weld metals.

ACKNOWLEDGEMENTS

The author wishes to thank Dr. R.A.Farrar for his valuable suggestions and many stimulating discussions during the course of this work. Thanks are also due to Professor S.P. Hutton for providing suitable research facilities in the Department of Mechanical Engineering and the Science and Engineering Research Council (SERC) for financial support through contracts GR/A/24482 and GR/B/02750.

I am also greatly indebted to the following for their help with the production of suitable weld materials.

Dr. A. Price, Dr. D.A.Wolstenholm, Mr. P. Blandford and Mr. J.Eariss	C.E.G.B., Marchwood Engineering Laboratories
Dr. T. Boniszewski and Dr. D.S. Taylor	E.S.A.B. Ltd, Gillingham.
Dr. R.E. Dolby, Dr. D.J. Abson and Dr. M.N. Watson	The Welding Institute Cambridge.
Mr. J. Prior	Babcock Power Ltd., Renfrew.

Technical assistance provided by the following members of staff at Southampton University is also very highly appreciated.

Mr. M.A. Batey, Mr. A.C. Riddell, Mr. R.J. Hammond and Mr. E. Heath.

Finally, thanks are due to Mrs. D. Harris for typing this thesis, and last but not least the warmest thanks to my wife, who not only provided great encouragement during the preparation of this thesis, but was also quite willing to discuss many of the scientific aspects of the work as an equal.

CONTENTS

CONTENTS (cont...) Page

CONTENTS (cont...) Page

CONTENTS (cont...)

CHAPTER 1: INTRODUCTION

1.1 General Background

The great technological stimulus of World War II promoted rapid development of electric arc welding as a major fabrication process, but unfortunately this rapid development was not without its setbacks. Following numerous catastrophic failures in this early post-war period, caused by brittle fracture of welded joints, it became increasingly important to incorporate recommendations of toughness minima into new design specifications for welded structures. For example, in the early 1950's a Charpy energy of 20J at -15°C (15 ft.lb at +5°F) was recommended for thick sections in large storage tanks and offshore platforms [1]. Since then metallurgical development has continually improved the quality of structural steels and by the late 1970's a toughness minima of 51J at -20°C (38 ft.lb at -4°F) was recommended for seam welds in Arctic gas pipelines [2]. Ideally, some steel manufacturers would now like to see guaranteed weld metal toughness values of 68J at -46°C (50 ft.lb at -50°F) as this can now be guaranteed in the parent material[3].

Clearly the problem of guaranteeing the above mechanical properties in weld metals is always more difficult for the welding consumable designer, than for the steel manufacturer. In steelmaking, accurate control of chemistry and deoxidation can be maintained, because sufficient time is available for chemical reactions to approach their equilibrium states. In arc welding, on the other hand, the entire process occurs in a matter of seconds. This results in an essentially non-equilibrium situation, in which a fine dispersion of non-metallic deoxidation products become trapped within the solidifying steel matrix. In addition the steel manufacturer has the additional advantage of further improving properties by controlled rolling schedules or heat treatment. The welding consumable manufacturer, on the other hand, may be required to produce optimum properties simply through natural cooling directly from the molten state.

Bearing in mind the above problems it would not be unreasonable to imagine that weld metal mechanical properties would rarely match those of the parent plate. However, it is now well established that certain combinations of welding fluxes and alloying elements can be used to produce a very fine grained microstructure in the final weld metal. This fine grained microstructure, termed acicular ferrite, simultaneously improves both strength and toughness, and in ideal conditions can match the best structural steel plates in terms of mechanical properties. For example Charpy values in excess of 100J at $-50^{o}C$ (72 ft.lb at $-58^{o}F$) have been reported for acicular ferrite microstructures produced with a Mo-Ti-B/OP121TT flux-wire combination [4]. In addition, recent studies on fatigue behaviour have shown that weld metals with the acicular ferrite microstructure are in fact superior to the parent plate, in terms of resistance to fatigue crack propagation[5].

Unfortunately reliable production of weld metals with an acicular ferrite microstructure is not easy. Moreover, although the best properties require the acicular ferrite microstructure, this alone does not guarantee optimum toughness. Recent research has shown that the following factors are also highly significant in determining the structure toughness relationships.

(1) Embrittlement by high proportions of blocky martensite-austenite (M-A) constituents.
(2) Precipitation or strain ageing effects.
(3) Excessive solid solution strengthening.
(4) Grain boundary embrittlement.

From above it is clear that production of the best weld metal toughness is not a simple proposition. Nevertheless, our understanding of weld metal structure versus toughness relationships indicates that the acicular ferrite route should provide the best prospect for future improvements, as long as the above considerations are taken into account. There is therefore a great incentive to develop a good understanding of weld metal microstructural development.

1.2 Factors Influencing Weld Metal Microstructural Development

Weld metal microstructural development is complex, but in simple terms it may be considered to be influenced by the following four variables.

(1) Cooling rate.
(2) Chemical analysis.
(3) Austenite grain size.
(4) Deoxidation products.

Clearly all four variables are inter-related in the welding process and it is therefore not uncommon for a small change in one variable to result in changes in the other three.

Although there is this strong inter-dependency between variables it is possible to define the major factors influencing each variable. For example, cooling rate is controlled primarily by a combination of heat input and the thermal mass of the work piece. These factors are in turn influenced by welding current and voltage, travel speed, plate thickness and geometry and the preheat or interpass temperature.

Chemical analysis of the weld metal is controlled primarily by the chemistry of the welding consumable and dilution from the parent plate. In addition the welding flux also clearly plays an important rôle in determining the final balance of residual deoxidants in the chemical analysis.

Austenite grain size is probably influenced by cooling rate and chemistry through the $\delta \rightarrow \gamma$ transformation regime, although it has also been recently suggested that deoxidation products play an importance rôle through austenite grain pinning.

Finally, the deoxidation products themselves are clearly influenced by flux type and the chemical analysis of the welding consumables. However, welding process variables such as heat input, arc length and travel speed also have a clear influence on deoxidation due to their influence on atmospheric oxygen uptake and the time available for the deoxidation reactions to occur.

1.3 Objectives of the Present Investigation

In view of the complicated nature of mild and low alloy steel weld metal $\gamma \rightarrow \alpha$ transformation behaviour, the emphasis of the present work has been on the construction of suitable transformation diagrams to describe weld metal microstructural development. Clearly the use of equilibrium phase diagrams is inappropriate for welding, because microstructural development, through the $\gamma \rightarrow \alpha$ phase transformation, occurs under non-equilibrium conditions. A more appropriate diagram is therefore one which describes the kinetic influences of alloying, nucleation sites and cooling rate, on $\gamma \rightarrow \alpha$ transformation temperature and microstructure, during continuous cooling. Such diagrams are known as continuous cooling transformation (CCT) diagrams and their application to weld metals would clearly constitute a significant advance in our understanding of these materials.

The objectives of the present investigation have therefore been as follows:

(1) To develop CCT diagrams applicable to weld metals.

(2) To use CCT diagrams to understand the influence of cooling rate on weld metal microstructural development.

(3) To use CCT diagrams to understand the relationships between the various phases and morphologies found in weld metals.

(4) To use CCT diagrams to understand the influence of alloying on weld metal microstructural development. In particular the elements manganese, nickel, niobium, carbon and to a lesser extent molybdenum have been investigated.

(5) To briefly study the influence of prior austenite grain size on weld metal transformation behaviour.

(6) To study the influence of inclusions on transformation behaviour by using a remelting technique to alter inclusion distributions.

To enable the above objectives to be carried out satisfactorily, it was necessary to review the following areas of the literature.

(1) $\gamma \rightarrow \alpha$ transformation products.

(2) $\gamma \rightarrow \alpha$ transformation diagrams.

(3) Influence of alloying elements and prior austenite grain size on $\gamma \rightarrow \alpha$ transformation behaviour.

(4) Influence of inclusions on $\gamma \rightarrow \alpha$ transformation behaviour.

Clearly the above topics constitute a large proportion of the entire ferrous metallurgical literature and therefore a totally exhaustive literature survey is beyond the scope of the current work. However, it is believed that the data generated in the current work constitutes a significant advance in our understanding of weld metal transformation behaviour.

It is also hoped that the models proposed in the present investigations provide stimulation for discussion and further studies, so that a complete understanding of weld metal transformation behaviour will be forthcoming in the near future.

CHAPTER 2: LITERATURE REVIEW

2.1 Introduction

To put the results of the current investigation into perspective with previous transformation studies, four areas of literature have been reviewed.

Firstly, as the carbon content of some weld metals can be as low as 0.03 wt %C, it is useful to review transformation products occurring in carbon free iron alloys, as well as those occurring in low carbon low alloy steels. The first section therefore deals with the $\gamma \rightarrow \alpha$ transformation products of pure iron, carbon free iron alloys, low carbon low alloy steels, and low carbon weld metals.

Secondly, it is of interest to review the ways in which transformation data may be presented, and to review the major sources of transformation diagrams. The second section therefore reviews the dilatometric technique used in the construction of Isothermal transformation (IT) and CCT diagrams, and reviews the major sources of CCT diagrams, with particular reference to those applicable to welding.

Thirdly, it is important to understand why transformation behaviour varies from one CCT diagram to another. This requires a knowledge of the influence of alloying elements and austenite grain size on the thermodynamics and kinetics of phase equilibrium. The third section therefore reviews the influence of alloying elements on equilibrium transformations, and on hardenability,and considers how alloying elements, and austenite grain size, can alter the shape of the CCT diagrams.

Finally, having reviewed the major factors influencing the $\gamma \rightarrow \alpha$ transformation behaviour of low carbon low alloy steels, it would seem to be a relatively simple matter to apply this knowledge to the understanding of weld metals. Unfortunately, this is not always so, and one further factor must be considered before a full understanding of weld metal transformation behaviour can be obtained. This final factor concerns the presence of a fine distribution of "frozen in" deoxidation products, which is now widely regarded as being fundamental to the transformation behaviour of weld metals. The fourth section therefore deals with the influence of inclusions and considers such factors as grain boundary pinning, thermal contraction strain effects, and the direct nucleation of ferrite, in an attempt to elucidate weld metal transformation behaviour.

2.2 Review of $\gamma \rightarrow \alpha$ Transformation Products

2.2.1 Introduction

The main purpose of the following section is to help in the identification and classification of the various weld metal transformation products. To achieve this the transformation products occurring in similar materials such as pure iron, carbon free iron alloys, and low carbon low alloy steels and weld metals are reviewed.

2.2.2 Allotropy of pure Iron

Before discussing the microstructures of iron and steel it is useful to briefly describe the allotropic nature of iron.

If pure iron is cooled slowly from the molten state it will undergo three phase transformations before reaching room temperature. All three phase transformations are reversible and occur at precisely the same temperatures, during heating, provided the iron remains pure and the heating rates are slow.

The transformation behaviour of pure iron may be summarised by the following:

$$\text{liq} \overset{1539^{\circ}\text{C}}{\rightleftharpoons} \delta(\text{BCC}) \overset{1400^{\circ}\text{C}}{\rightleftharpoons} \gamma(\text{FCC}) \overset{910^{\circ}\text{C}}{\rightleftharpoons} \alpha(\text{BCC}) \qquad (2.1)$$

2.2.3 Transformation products of pure Iron

Examination of the microstructure of pure iron, produced by slow cooling, will reveal large equiaxed grains of α (termed ferrite) which result from the $\gamma \rightarrow \alpha$ transformation at 910°C.

If the cooling rate of pure iron is rapid, the equilibrium transformation temperatures will no longer hold and the phase transformations may proceed via alternative routes, resulting in development of metastable transformation products. In pure iron very fast cooling rates are required to produce such products.

The effect of rapid cooling rate on the $\gamma \rightarrow \alpha$ transformation behaviour of pure iron has been studied by several researchers [6-9]. Bibby and Parr [6] identified three separate transformation products;

equiaxed ferrite, massive ferrite* and martensite, during fast cooling experiments in iron containing 0.001-0.005%C. More recently Wilson et al [7] [8] have identified four distinct transformation plateaux in iron containing 0.011%C. These four microstructures were described as:-

(1) EQUI-AXED FERRITE - consisting of equi-axed or polygonal grains.

(2) MASSIVE FERRITE - consisting of small grains of ragged outline.

(3) BAINITIC FERRITE - an acicular structure which is thought to occur by movement of ledges giving rise to surface tilts on a pre-polished surface.

(4) MASSIVE or LATH MARTENSITE - consisting of parallel laths with a high dislocation density.

The above results indicate that γ iron can decompose to several different transformation products at different cooling rates. A similar situation may also be expected in high purity iron alloys.

2.2.4 Transformation products of high purity Iron alloys

Over the years several investigations have been carried out into the decomposition of austenite in iron alloys with very low or nominal carbon contents [10-14]. Table 2.1 summarises the findings of three such investigations into the Fe-Mn, Fe-Cr, Fe-Cu-Ni and Fe-Au-Ni systems. In each study the main experimental techniques used were dilatometry, and optical and electron optical metallography.

From Table 2.1 it can be seen again that there are generally four distinct morphological varieties of transformation products. These four transformation products will be discussed in more detail in the following sections.

2.2.4(a) Equiaxed ferrite or polygonal ferrite

This transformation product forms at the highest $\gamma \rightarrow \alpha$ transformation temperatures and consists of large equiaxed or

---

*Massive Ferrite - In the case of absolutely pure iron there is clearly no change in overall chemical composition between γ and α. Therefore any civilian type transformation to ferrite occurring by short range diffusion can be termed massive ferrite. For this reason the Widmanstätten ferrite and equiaxed ferrite reactions in pure iron may be referred to as massive ferrite.

TRANSFORMATION PRODUCT	Fe-Mn SYSTEM (Bolton and Petty [10])	Fe-Cr SYSTEM (Bee and Honeycombe [11])	Fe-Cu-Ni and Fe-Au-Ni SYSTEMS (Ricks et al [12][13])
(1) EQUIAXED FERRITE POLYGONAL FERRITE	Described as a massive or equiaxed structure with no evidence of substructure, or austenite grain boundaries. Thin foils revealed large areas of more-or-less dislocation free ferrite separated by high-angle boundaries.	Described as polygonal/ equiaxed grains (Grain boundary allotriomorphs)	Described as equiaxed grains with a low dislocation density. A generally equiaxed structure with many planar sections was also noted and termed FACETED EQUIAXED FERRITE.
(2) WIDMANSTÄTTEN FERRITE	-	Described as irregular grains (Primary and secondary sideplates)	Described as acicular ferrite grains with a generally low dislocation density.
(3) BAINITIC FERRITE UPPER BAINITE	Described as "ragged feathery ferrite". Thin foils revealed irregularly shaped subcells, produced at slow cooling rates, with high dislocation density and separated by low angle grain boundaries. At faster cooling rates the subcells were more lath like.	Described as irregular grains with many planar boundary segments. Consists of broad, heavily dislocated laths.	Described as very irregular grains, consisting of broad heavily dislocated laths.
(4) LATH MARTENSITE	Described as consisting of parallel bundles of highly dislocated laths.	Described as classical lath martensite, consisting of fine heavily dislocated laths.	Described as fine, heavily dislocated, low angle related laths. (∿0.5μm in width).

TABLE 2.1: $\gamma \rightarrow \alpha$ transformation products in high purity Iron alloys.

polygonal ferrite grains separated by smoothly curved grain boundaries. The preferred nucleation sites are prior austenite grain boundaries or triple points. Movement of the curved, high energy, incoherent α/γ interfaces during transformation is probably controlled by solute diffusion in the case of the high purity alloys and by short range diffusion of iron in pure iron.

At slightly lower transformation temperatures the morphology of equiaxed ferrite may change slightly, resulting in the formation of some planar boundaries. These α/γ interfaces are thought to be of the planar, low energy, partially coherent type, and probably migrate by the lateral movement of steps or ledges along the α/γ interface.

The characteristic appearance of equiaxed ferrite, when viewed in the TEM, is of relatively clean subgrains containing few free dislocations [11][12]. These subgrains are usually separated by low angle boundaries, which may form as a result of dislocation climb at the high transformation temperatutes [15].

2.2.4(b) Widmanstätten ferrite

As the $\gamma \rightarrow \alpha$ transformation temperature is gradually lowered, the morphology of the ferrite transformation products change from equiaxed to a well defined acicular lath or plate morphology. It will be seen later that there are many different varieties of Widmanstätten ferrite, but all are believed to transform by the same basic transformation mechanism. This mechanism involves the migration of steps or ledges along the partially coherent planar α/γ interfaces enabling the Widmanstätten plates to thicken. The preferred nucleation sites for Widmanstätten ferrite are austenite grain boundaries or grain boundary allotriomorphs. Occasionally intragranular plates may occur, which appear to have nucleated in the vicinity of second phase particles or inclusions. Widmanstätten ferrite invariably adopts a crystallographic orientation relationship within the prior austenite grain. This relationship is known as the Kurdjumov-Sachs relationship, viz. $\{111\}_\gamma \; // \; \{110\}_\alpha$, $<110>_\gamma \; // \; <111>_\alpha$.

As the major growth mechanism of Widmanstätten ferrite is through the lateral migration of ledges along the semi-coherent α/γ interface, any interference with this mechanism will control the growth rate of Widmanstätten ferrite. In the case of high purity Fe-Cu-Ni and Fe-Au-Ni alloys, interphase precipitation of Cu and Au occurs at the ledges during transformation [12][13]. The growth rate of ferrite is therefore likely to be controlled by either the diffusivity of the solute, or the nucleation rate of the precipitating phase on the interphase boundary.

The characteristic features of Widmanstätten ferrite when examined in the TEM are as follows. The number of free dislocations is noticeably greater than in equiaxed ferrite. A substructure consisting of parallel subgrain plates, separated by straight low angle subgrain boundaries, is sometimes observed [11][12] and occasionally the coarse growth steps or ledges may be observed on planar ferrite/retained austenite interfaces.

2.2.4(c) Bainitic ferrite

At lower transformation temperatures Widmanstätten ferrites no longer form and the $\gamma \rightarrow \alpha$ reaction proceeds with the formation of an alternative transformation product; - bainitic ferrite.

Although this transformation product often bears great similarities to Widmanstätten ferrite, careful TEM studies [11] have been able to make the distinction between the two products because of the much higher dislocation density of bainitic ferrite.

A further, important distinction between Widmanstätten and bainitic ferrite has recently been demonstrated by Ricks et al [12][13]. Using techniques of high speed dilatometry and electron microscopy Ricks was able to produce TTT diagrams for high purity Fe-Cu-Ni and Fe-Au-Ni alloys which clearly show different "C-curve" kinetics for Widmanstätten and bainitic ferrite. This difference in kinetic behaviour is attributed to whether or not interphase precipitation of Cu (or Au) occurs on the advancing α/γ interface. It can be concluded from these observations that rejection of solute and subsequent precipitation at the advancing interface occurs in Widmanstätten ferrite. In bainitic ferrite, however, the ferrite forms with an initial supersaturation of the solute.

The mechanism of transformation of bainitic ferrite is not yet clearly understood although it has been suggested that it may be either a shear [10] or a ledge mechanism [12].

The microstructural features of bainitic ferrite are generally quite similar to Widmanstätten ferrite when viewed at the optical level. However, its more blocky or irregular shape has sometimes been commented on [11][12]. Observations of bainitic ferrite in the TEM show the ferrite to consist of broad heavily dislocated laths separated by low angle boundaries [11][12].

2.2.4(d) Lath martensite

If the $\gamma \rightarrow \alpha$ transformation temperature can be depressed sufficiently, either by alloying or rapid cooling, the subsequent transformation will proceed via a martensitic mechanism.

In pure iron or carbon free iron alloys the martensite morphology usually encountered is described as Lath martensite or Massive martensite. It is normal for these martensites to obey the Kurdjumov-Sachs orientation relationship with the prior austenite grains.

The characteristic appearance of lath martensite is of large colonies of fine (often $\sim$0.5µm width) martensite laths of very high dislocation density, which are separated by low angle boundaries.

2.2.4(e) Summary

The work reviewed in the previous paragraphs shows that there are probably at least four different types of $\gamma \rightarrow \alpha$ transformation products to be considered even in carbon free iron alloys; viz Equiaxed Ferrite, Widmanstätten Ferrite, Bainitic Ferrite and Lath Martensite. A generalised schematic CCT diagram, similar to that proposed by Wilson [2] is shown in Figure 2.1, illustrating the major transformation products expected to form in high purity iron alloys.

2.2.5 Transformation products in low carbon low alloy steels

According to the iron-carbon equilibrium phase diagram, slow cooling a low carbon (hypo-eutectoid) steel, from the austenitic state will produce two transformation products; pro-eutectoid ferrite and pearlite.

The temperatures at which these transformation products start to form under equilibrium cooling conditions are designated Ar_3 and Ar_1 respectively. The former temperature is carbon dependent (e.g. $\sim$845°C for a 0.1 wt%C alloy), but the latter temperature of 723°C,

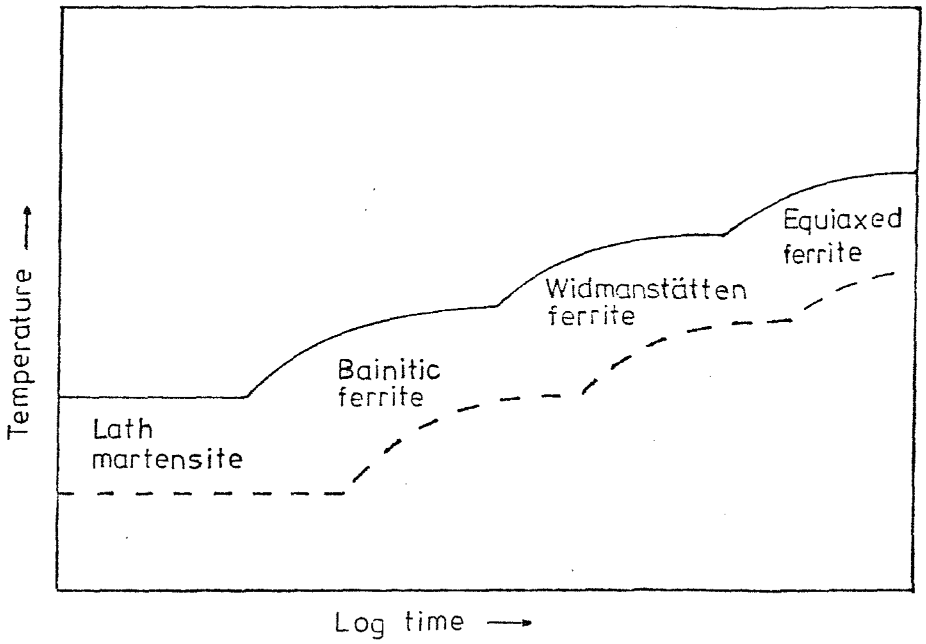

Figure 2.I Schematic CCT diagram for high purity iron alloys.

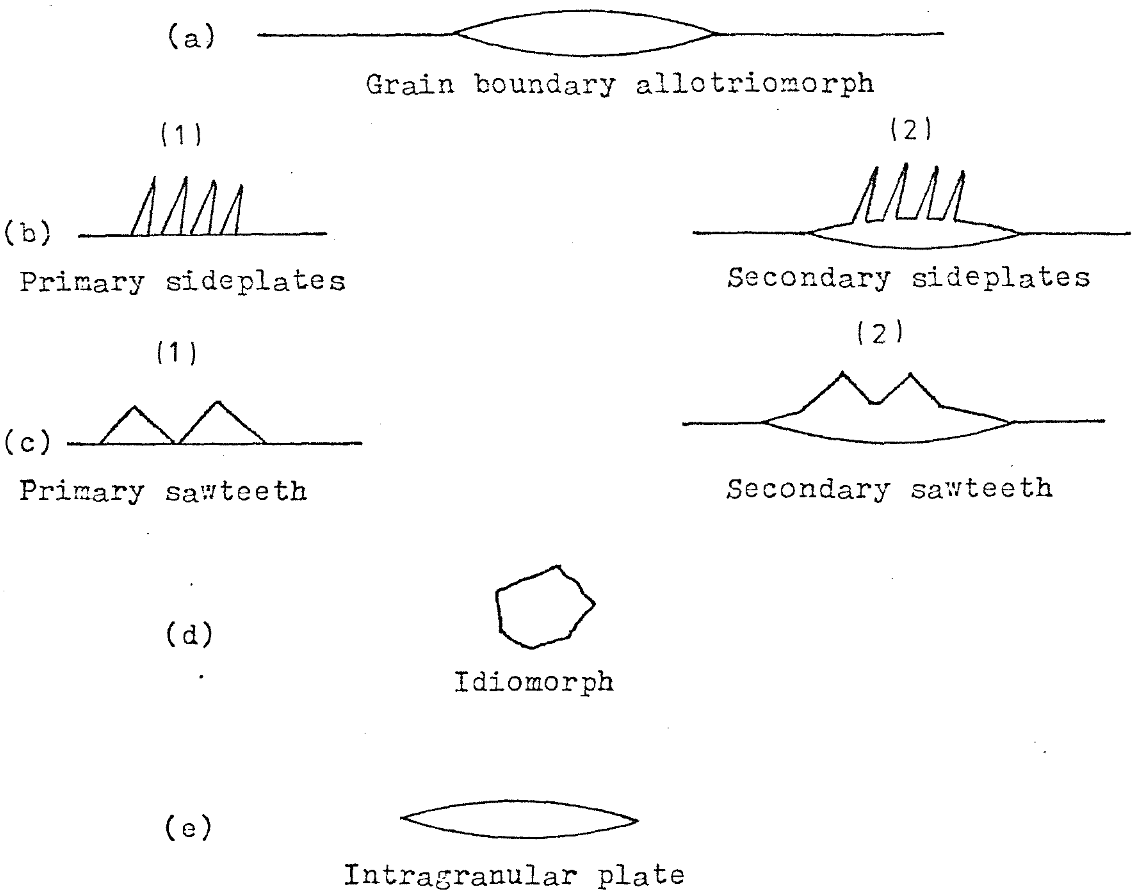

Figure 2.2 The Dubé morphological classification system.

known as the eutectoid temperature, is constant regardless of carbon content. Strictly speaking only ferrite which forms above 723°C is pro-eutectoid ferrite (according to the equilibrium diagram). In practice the term pro-eutectoid is used to describe any ferrite which forms prior to the eutectoid reaction.

In actual practice the $\gamma \rightarrow \alpha$ transformation behaviour of steels very rarely obeys the equilibrium diagram and a range of transformation products may be produced, depending on alloy composition and cooling rate. These various types of transformation products can usually be classified under one of the following categories:-

(1) Pro-eutectoid Ferrite Reaction
(2) Pearlite Reaction
(3) Bainite Reaction
(4) Martensite Reaction

2.2.5(a) Pro-eutectoid ferrite reaction

Pro-eutectoid ferrite may be defined as any type of ferrite that rejects carbon during growth and forms prior to the eutectoid reaction. This definition includes all the various Widmanstätten ferrite morphologies in addition to the high temperature ferrites which grow by the migration of curved high energy, incoherent interfaces.

The various morphological varieties of proeutectoid ferrite are generally classified according to the Dubé classification system [16] as illustrated in Figure 2.2.

Grain Boundary Allotriomorphs (Figure 2.2.(a))

Grain boundary allotriomorphs of ferrite are the highest temperature transformation product of the proeutectoid ferrite reaction and as such are the first to form during slow cooling.

Nucleation of allotriomorphs occurs at austenite grain boundaries and, in the initial stages of growth, the grains are lenticular [15] or pancake [17] shaped. Growth along the austenite grain boundary is rapid and impingement with other allotriomorphs soon occurs. This often results in the formation of a continuous network of grain boundary ferrite, from which it is difficult to resolve the original inter-allotriomorph grain boundaries [17]. The allotriomorphs therefore appear as single elongated grains, in the optical microscope, but are often made up of a series of smaller impingeing grains.

The development of ferrite allotriomorphs is by a nucleation and diffusional growth process and is controlled by the rate of volume diffusion of carbon in austenite [17].

There is now increasing evidence that the allotriomorph α/γ interface is faceted even during the initial stages of growth [18] [19]. The extent of this faceting tends to increase with decreasing transformation temperature and this reflects on the morphology of the allotriomorph. As temperature decreases the allotriomorphs have been observed to follow a morphological progression from smooth to ragged, to blocky, and eventually to the development of sawteeth and sideplates.

Although many allotriomorphs have a non-crystallographic appearance, a crystallographic relationship between the allotriomorph and the austenite grain in which it nucleated, is believed to exist [20][21]. Clearly an allotriomorph which grows into an adjacent austenite grain is unlikely to bear any crystallographic relationship with the austenite in this adjacent grain.

Widmanstätten Sideplates (Figure 2.2(b))

Widmanstätten sideplates of ferrite are often described as plates or needle shaped crystals, developing from the vicinity of austenite grain boundaries. In a single plane of polish these sideplates often appear as laths or needles, but careful sectioning studies have established that they are in fact plates [17]. Sideplates are usually considered to taper towards their tips and are therefore most accurately described as thin wedges. The length-width ratio (aspect ratio) varies considerably with transformation temperature resulting in colonies of short-thick plates at high temperatures and long-thin plates at lower transformation temperatures. The tips of all sideplates are rounded; the radius of curvature decreasing with decreasing transformation temperature.

Nucleation of sideplates usually occurs at either a pre-existing ferrite allotriomorph or at an austenite grain boundary. In the former the resultant sideplate is referred to as a Widmanstätten secondary sideplate (Figure 2.2(b)(2)). In the latter, which is considered to be a much rarer event [22], a Widmanstätten primary sideplate will result (Figure 2.2(b)(1)).

It would seem that the major factors favouring sideplate development are large austenite grain size, intermediate reaction temperatures, and low carbon contents. It has been noted that the pearlite reaction inhibits sideplate development at higher carbon contents [17], but at lower carbon contents, sideplates often grow to impingement if conditions are favourable. This observation suggests that the magnitude of the carbon diffusion profile, close to the transformation interface, is important in sideplate development. The theory of the diffusional growth of Widmanstätten sideplates is complex, incorporating lengthening and thickening mechanisms. Lengthening of sideplates occurs much more rapidly than thickening. Data obtained by Aaronson [17] for the lengthening of plates, in a Fe-0.3 wt%C alloy transformed isothermally at 700°C, gave a sideplate lengthening rate of $\sim 1.3 \times 10^{-3}$ cm/sec. Similarly Townsend and Kirkaldy [23] measured isothermal sideplate lengthening rates in the range ~ 4 to 18×10^{-4} cm/sec for a range of carbon compositions and transformation temperatures in high purity Fe-C alloys.

The mechanism of lengthening of sideplates must be considered in relation to the characteristics of the interphase boundaries at the plate tips. These boundaries, which are highly curved are incoherent (or disordered), are appreciably mobile at elevated temperatures due to the ease of atomic transfer across the interface. The lengthening rate of sideplates is therefore believed to be controlled by the rate of volume diffusion of carbon in austenite [17].

The rate of thickening of sideplates on the other hand has been shown to be in poor agreement with that predicted by volume diffusion of carbon in austenite[24].

The mechanism of sideplate thickening is believed to be controlled by the lateral movement of ledges along the partially coherent α/γ interphase boundary [25] and this probably explains the growth irregularities often measured experimentally [26].

In addition to the morphologies described as primary and secondary sideplates, a third morphological type of sideplate is often encountered, termed the degenerate sideplate [17].

Degenerate sideplates tend to form at intermediate temperatures within the sideplate transformation range and are generally much less symmetrical and much more complex than classical sideplates. The three main classifications of degenerate sideplates are illustrated in Figure 2.3.

Type A structures consist of sideplates in which the growth is more or less parallel to the original habit, but extensive irregularities develop on the broad faces of the sideplates.

Type B structures are often referred to as "offset" sideplates

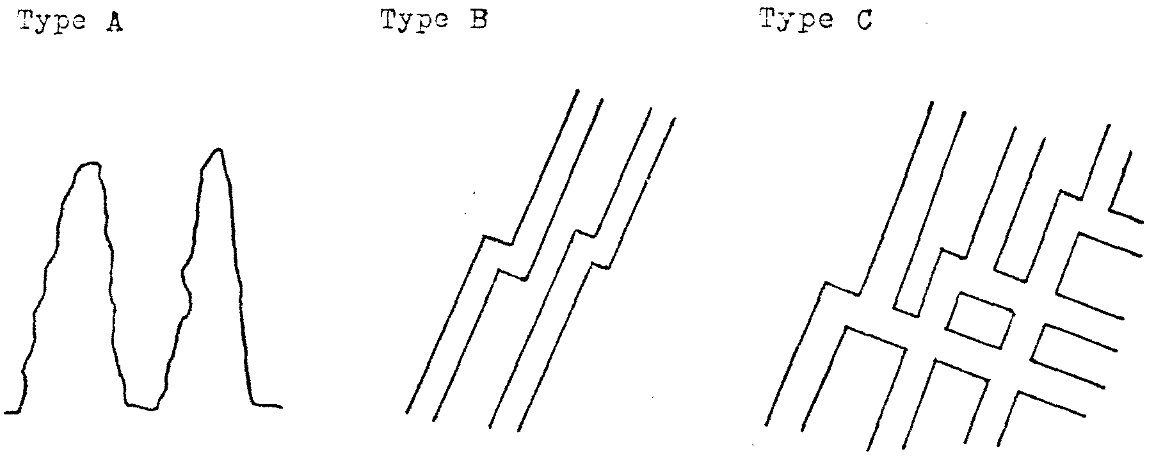

Figure 2.3 The three major categories of degenerate sideplates

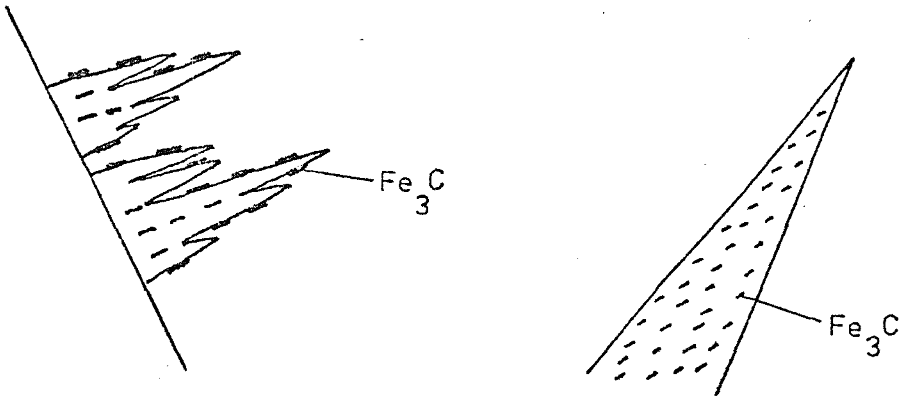

Upper bainite   Lower bainite

Figure 2.4(a) Morphology of classical upper and lower bainite.

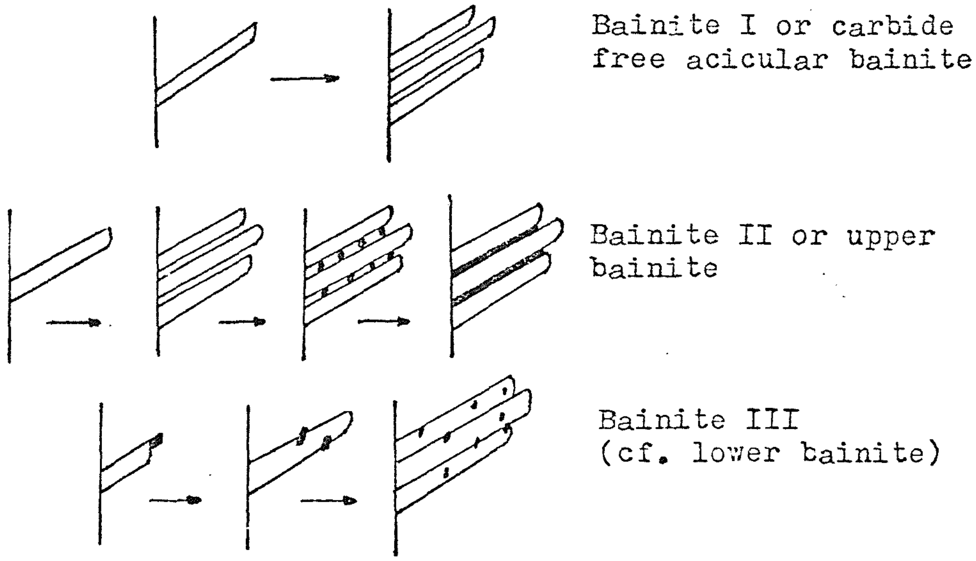

Figure 2.4(b) Bainite classification according to Ohmori (39)

in which new development occurs parallel to the original habit plane but with varying amounts of offset.

Type C structures occur when new sideplates develop within an existing sideplate colony, on an alternative habit plane. Of the three types of degeneracy, type C is believed to proceed even at the lowest transformation temperatures, where the proeutectoid ferrite reaction tends to merge into the bainite reaction.

The primary mechanism responsible for degeneracy of sideplates is thought to be sympathetic nucleation. In types B and C degeneracy this nucleation often occurs on the broad faces or steps of the sideplates. These steps are themselves dependent on the combined effects of temperature and orientation, which influence the production of ledges and superledges. Transformation strains are also believed to be important, particularly in the degeneracy of type A structures. In this case it has been suggested that these strains affect the dislocation structure of broad faces and produce local polygonization of the surrounding austenite, which increases plate thickening in localised areas [17].

It should be noted that if conditions are favourable the continued development of degenerate sideplate structures soon results in the formation of continuous networks, which bear little resemblance to classical sideplate structures. As in the case of ferrite allotriomorphs, the α/α grain boundaries are difficult to detect optically, giving the impression that the network is one continuous entity, rather than a series of sympathetically nucleated degenerate sideplates.

Widmanstätten Sawteeth (Figure 2.2(c))

Widmanstätten sawteeth are usually described as triangular ferrite crystals growing from the vicinity of austenite grain boundaries. As in the case of Widmanstätten sideplates there are two distinct morphologies of sawteeth depending on the point of nucleation. Primary sawteeth nucleate and grow from austenite grain boundaries whereas the secondary sawteeth nucleate and grow from grain boundary allotriomorphs. As with sideplates the primary variety is much less common than the secondary variety. In most respects the Widmanstätten sawteeth morphologies may be considered intermediate between the allotriomorphic and sideplate morphologies. At low transformation temperatures sawteeth have been observed to be transitory and are quickly converted into sideplates.

Intragranular Plates (Figure 2.2(e))

The morphology of intragranular Widmanstätten plates has been described as "lenslike" by Carpenter and Robertson [27] and as "double-ended isosceles triangles" by Aaronson [17].

The most favourable conditions for the development of this morphology seems to be very large austenite grain size, low carbon content and a relatively low transformation temperature. For example, Robertson observed the formation of a lattice work of intragranular plates at temperatures below about 600°C in a 0.1 wt%C, 0.39 wt%Mn steel of large austenite grain size.

As in the case of sideplates, a certain amount of degeneracy may also occur in intragranular plates. Again the maximum degeneracy is usually associated with intermediate temperatures in the transformation temperature range. In the case of intragranular plates, types A and C degeneracy are most common.

Initial nucleation of intragranular plates must occur at some suitable nucleation site and isolated plates have sometimes been seen to be associated with non-metallic inclusions. Subsequent sympathetic nucleation of degenerate plates often occurs, which is probably aided by localised transformation strains.

Intragranular Idiomorphs (Figure 2.2(d))

Intragranular idiomorphs of ferrite may be described as roughly equiaxed ferrite crystals which nucleate and grow in intragranular regions. The simple regular morphology of idiomorphs can sometimes be almost cubic at high temperatures, but becomes less regular and more plate like at lower temperatures.

The conditions favouring development of idiomorphs are large austenite grain size, low carbon content and a transformation temperature in the upper part of the Widmanstätten transformation region.

One of the most surprising characteristics of intragranular idiomorphs reported by Carpenter and Robertson [27] and Hanemann and Schrader [28] is that they are first formed close to grain boundary ferrite regions rather than at austenite grain interiors in continuously cooled specimens. Obviously an appreciable rate of nucleation is developed at relatively small undercooling for this morphology to develop. Non-metallic inclusions have previously been suggested as possible intragranular nucleation sites for ferrite [17]. In this case however, initial nucleation is limited to the intragranular region close to grain boundary nucleated ferrite grains, thus suggesting some alternative mechanism of intragranular nucleation may be operating.

In an attempt to explain this, Aaronson [17] suggested that dislocation structures developed during austenitising, combined with transformation strains accompanying ferrite growth at the austenite grain boundaries, could presumably also act as suitable sites for intragranular ferrite nucleation. Further augmentation of this dislocation structure by strains caused by the different coefficients of thermal expansion of ferrite and austenite was also proposed by Aaronson.

2.2.5(b) Pearlite reaction

The morphology of a pearlite colony may be described as consisting of two interwoven crystals [29] of parallel ferrite and cementite lamellae.

Generally speaking the interlameller spacing, which ranges from $\sim 1\ \mu m$ to $\sim 0.1\ \mu m$ [30], is considered to be inversely proportional to the degree of undercooling from the eutectoid temperature, during transformation [31][32]. At very low transformation temperatures however, the lamellar appearance of pearlite is often lost and is replaced by irregular morphologies known as "degenerate" pearlite, "divorced" pearlite or "semipearlite" [33].

The development of lamellar pearlite is by a diffusional nucleation and growth process, involving mutual cooperation of the two phases. Nucleation occurs with the formation of either a ferrite or a cementite nucleus at some suitable nucleation site, such as an austenite grain boundary [29][31]. In the case of low carbon steels, nucleation is more likely to occur on the proeutectoid ferrite/austenite boundaries due to site saturation of austenite boundaries. In such steels it is thought that nucleation occurs on high energy incoherent γ/α interfaces so as to allow the pearlite colony to grow with an incoherent interface as proposed by Smith [34]. Further development of additional lamellae may occur either by sideways nucleation [31] or by branching of lamellae during growth [35]. In a recent investigation by Dippenaar and Honeycombe [36] both the above mechanisms were shown to occur.

2.2.5(c) Bainite reaction

A general definition of the bainite reaction is one that occurs between the low temperature martensitic reaction, and high temperature ferrite and pearlite reactions. As such, bainite is believed to share some of the transformation characteristics of both "military" and "civilian" type transformations. Subsequent to the pioneering studies of Davenport and Bain [37] two distinct morphologies were encountered, termed Upper and Lower bainite. More recent studies by other investigators [38][39] have frequently noted alternative structures forming in the bainite transformation regime. In the case of continuously cooled low carbon low alloy steels for instance, Habraken and Economopoulos [38] identified two further bainitic structures termed carbide-free acicular and massive or granular bainite. Similarly, a study of the bainite reaction in low carbon HSLA steels by Ohmori, Ohtani and Kunitake [39] identified three distinct morphologies which were termed bainite I, bainite II and bainite III.

Upper Bainite

The morphology of upper bainite is often described as parallel needles or laths of bainitic ferrite separated by fine platelike precipitates of cementite, as shown schematically in Figure 2.4(a) [40][41][42]. In the optical microscope a characteristic feature of upper bainite is the appearance of many crystallographically oriented colonies or sheaves [41] (consisting of parallel laths) separated by planar high angle boundaries. In the electron microscope a substructure of small laths about 0.5 μm wide and separated by low angle boundaries is often observed [43][44]. The dislocation density of the bainitic laths increases with decreasing transformation temperature and is always greater than in Widmanstätten ferrite [43].

The mechanism of growth of upper bainite is still the subject of much debate. The two principal theories concern the development of bainitic ferrite by either a displacive or a reconstructive mechanism. In the former the repeated sympathetic nucleation of small martensitic sub-units (∿0.5 μm x 10 μm long)[44] is believed to occur, i.e. a time dependent shear mechanism [44][45]. In the latter it has been claimed that sub-units are in fact "ledges" which propagate along the broad faces of bainitic plates in a similar manner to the Widmanstätten growth mechanism [47]. In either case an important characteristic of the bainite reaction is that the bainitic ferrite forms with an initial supersaturation of carbon [45][47][48]. Immediately subsequent to transformation this carbon may tend to diffuse out and precipitate as carbides. In the case of upper bainite, diffusion of carbon during transformation enriches the surrounding austenite and carbides precipitate from this enriched austenite at the α/γ phase boundaries.

Other important features of upper bainite are its crystallographic relationship with austenite (Kurdjumov-Sachs relationship), its tendency to form surface relief affects, and its independent 'C' curve kinetic behaviour.

Lower Bainite

The optical appearance of lower bainite is of many individual acicular laths. Some of these laths seem to have been nucleated at grain boundaries and others intragranularly. Detailed sectioning studies have shown that these acicular grains are in fact individual plates with a lenticular habit [41]. Electron microscopy often reveals an internal substructure very similar to that found in upper bainite (i.e ∿0.5 μm wide subgrains separated by low angle boundaries). The dislocation density of the bainitic ferrite is intermediate between upper bainite and martensite of similar chemical composition.

The major distinguishing feature of lower bainite is the intragranular arrays of carbide precipitates. These precipitates have an orientation relationship with the bainitic ferrite plate axis of 60° (Figure 2.4(a)).

As in the case of upper bainite, the growth mechanism of lower bainite, by either a "martensitic sub-unit" or a "broad face ledge mechanism" is still the subject of much debate. However, the key to this debate may lie in the mechanism of carbide precipitation. Those favouring the ledge mechanism suggest that the carbides precipitate as interphase precipitates during transformation [41]. On the other hand, Bhadeshia [49] has recently studied the carbide precipitation in lower bainite and concluded that lower bainitic cementite nucleates and grows within the supersaturated ferrite. Such precipitation is not consistent with the concept of interphase precipitation.

As in the case of upper bainite, lower bainite adopts a crystallographic relationship with the austenite, forms surface relief and has independent 'C' curve kinetic behaviour. However, all these features do differ slightly from upper bainite and thus make lower bainite a distinct transformation product on its own right.

Acicular Bainite (Low C steels)

An acicular, carbide free, morphology of bainite has been observed by several investigators in continuously cooled low carbon low alloy steels [38][39][41]. This morphology consists of side by side ferrite plates, often growing from austenite grain boundaries, separated by bands of aligned particles of retained austenite. This structure has been termed carbide-free acicular bainite by Habraken and Economopoulos [38] and bainite I by Ohmori et al [39]. According to Ohmori the morphology forms in the upper region of the bainite field. This suggests that it may be a form of upper bainite in which the carbon enriched austenite remains stable during and after transformation.

Granular Bainite (Low C steels)

Granular bainite is another morphology of bainite that is quite commonly encountered in low carbon low alloy steels. This morphology is often described as a massive or granular structure containing small islands of carbon enriched austenite. In some cases the small austenite islands occasionally transform to ferrite-carbide aggregates or martensite-austenite (MA).

The mechanism of formation of granular bainite proposed by Habraken and Economopoulos [38] involves segregation of carbon above the Bs temperature, followed by a massive transformation to ferrite. Townsend [50] on the other hand has recently studied the formation of granular bainite in a Cr-Mo-V steel and suggested that it is a degenerate form of upper bainite. According to Townsend, upper bainite laths form in the initial stages of transformation, during continuous cooling. Subsequently the carbon supersaturation adjacent to the laths produces perturbations, which encourage development of degenerate laths. Eventually, these laths impinge producing bridging points and trapping regions of untransformed austenite. The final appearance is that of a massive or granular structure containing isolated islands of entrapped retained austenite.

Bainite I, II and III

In addition to the bainitic transformation products discussed, the classification system presented by Ohmori et al [39], for low carbon HSLA steels, has now gained acceptance with several investigators.

Figures 2.4(b) shows the schematic representation of bainitic transformation products including the terminology used by Ohmori It can be seen that bainite I, II and III are analagous to carbide free acicular bainite, upper bainite and lower bainite respectively. In the case of lower bainite however, the morphology described by Ohmori differs from a true lower bainite, the ferrite morphology being of typical upper bainitic ferrite laths. All three morphologies, bainites I, II and III, can therefore be considered as upper bainites with differing carbide morphologies.

2.2.5(d) Martensite reaction

If the transformation temperature of steel is reduced sufficiently, by either alloying or quenching, the transformation will proceed via a shear mechanism to martensite. Kelly and Nutting [51] noted two distinct martensite morphologies in steels. In high carbon steels the morphology was platelike, consisting of internally twinned grains. In low carbon steels the morphology was lath-like with no evidence of twinning. In low carbon low alloy steels the predominant morphology is lath martensite. However, twinned martensite may occur if the preceding transformation has caused sufficient carbon enrichment of the surrounding austenite.

Lath Martensite

Lath martensite occurs in steels with a carbon content of less than about 0.5 Wt%C. The morphology consists of packets of very long (typically tens of μm) and thin (∿0.5 μm) parallel laths. The individual laths have a very high dislocation density [52] consisting of tangled arrays of dislocations, and are usually separated by low angle boundaries. The lath packets are usually separated by high angle boundaries.

Detailed examination of the crystallography of lath martensite has shown it to obey the Kurdjumov-Sachs relationship and have a $\{111\}_\gamma$ habit plane [53].

Twinned Martensite

At carbon contents above about 0.5 wt%C the morphology of martensite begins to change from lath to plate shaped and evidence of micro-twinning becomes apparent. The martensite plates become lenticular and tend to form in isolation rather than in packets. This results in the rather complex overall shape which is often termed acicular martensite.

At carbon contents below about 1.4 wt%C the Kurdjumov-Sachs relationship is obeyed and the habit plane is $\{225\}_\gamma$. Above this carbon content the habit plane becomes $\{259\}_\gamma$ and the K-S relationship is replaced by the Nishiyama relationship [41] viz:

$\{111\}_{\gamma} // \{110\}_{\alpha}, \; <112>_{\gamma} // <011>_{\alpha},$

2.2.5(e) Summary

The previous few sections have described many of the transformation products associated with low carbon low alloy steels, and have highlighted some of the uncertainties that still exist regarding the bainite transformation.

In an attempt to rationalise low carbon steel transformations, a schematic CCT diagram is presented in Figure 2.5. This diagram is based on a combination of the schematic CCT diagrams of Wilson [7] and Ohmori [39] with the addition of some of the data reviewed in the previous sections. It must be appreciated that such a diagram is unlikely to exist in practice as the bainite, Widmanstätten ferrite, and equiaxed ferrite noses are all likely to overlap. In practice the reactions which dominate the CCT diagram will be a function of the constitution and transformation temperature of the material concerned.

2.2.6 Transformation products in low carbon low alloy steel weld metals

At first sight it would seem likely that the transformation products of low carbon low alloy weld metals would be very similar to those of the parent material, particularly in situations where chemistry and thermal cycles are very similar. For example, in a multipass weld the coarse grained HAZ and coarse grained reheated weld metal regions will have experienced very similar thermal cycles, and assuming their chemistries are matched, they would be expected to transform in a very similar manner. In practice this expected similarity of transformation behaviour very rarely occurs, and an alternative series of transformation products, which in some cases appear to be unique to weld metals, are developed. These transformation products have been classified by welding metallurgists into the following categories, in order of decreasing transformation temperature.

(1) Proeutectoid or Grain Boundary Ferrite
(2) Sideplate Structures (formerly termed Upper Bainite)

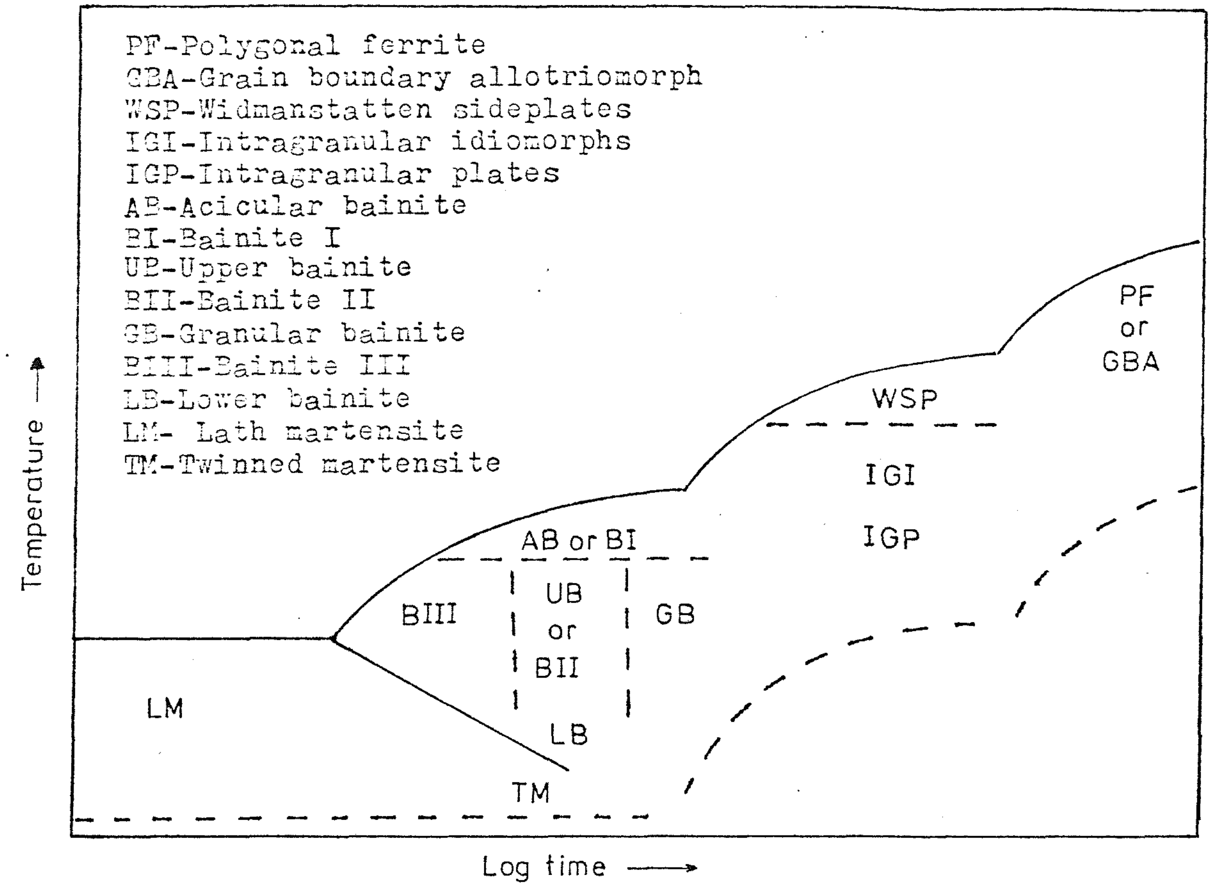

Figure 2.5 Schematic CCT diagram for low carbon low alloy steels.

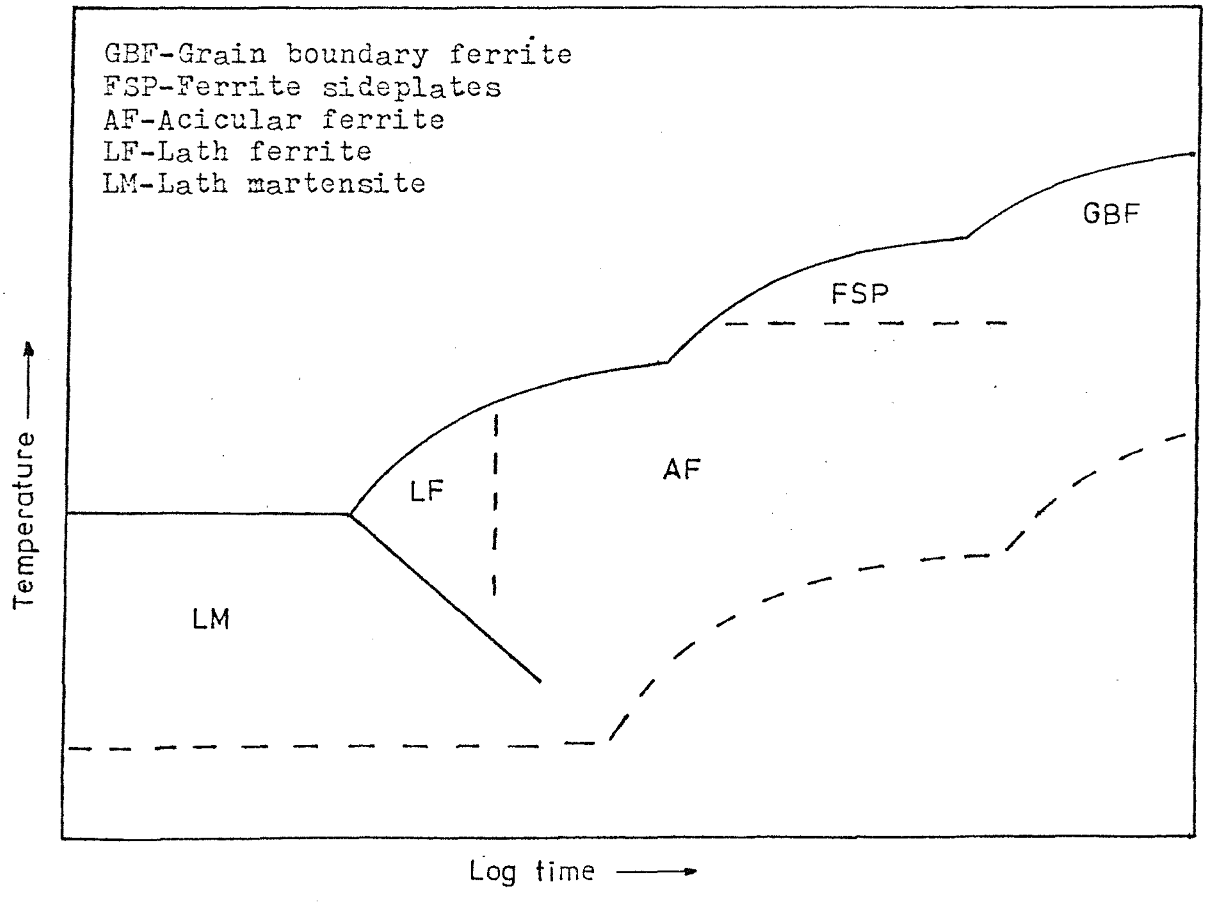

Figure 2.6 Schematic CCT diagram for low carbon weld metals.

(3) Acicular Ferrite (termed uniform fine grained ferrite in some Japanese literature)

(4) Low temperature Lath Structures or Lath Ferrite

2.2.6(a) Grain boundary ferrite

In as deposited low carbon weld metals, grain boundary ferrite is usually the first transformation product to form [54][55]. This structure rapidly envelopes the entire network of prior austenite grain boundaries if conditions of cooling rate and chemical analysis are favourable.

Optical examinations show that the α/γ interfaces can have a range of shapes [56] and may even show signs of incipient sideplate development. Electron microscopy [57] shows these ferrite grains to have a low dislocation density and are often surrounded by grain boundary cementite films. Microprobe analysis carried out by Watson* [57] indicated that manganese partitioning occurs at the α/γ interface making the phase truly proeutectoid in nature.

All the above evidence points to the fact that the grain boundary ferrite in weld metals is identical to the morphology referred to as grain boundary allotriomorphs in the proeutectoid reaction as discussed in section 2.2.5(a).

2.2.6(b) Ferrite sideplates

After grain boundary ferrite, the next weld metal $\gamma \rightarrow \alpha$ transformation product to form during continuous cooling has been shown to be ferrite sideplates [55]. In the majority of cases sideplates develop from grain boundary allotriomorphs and have been seen to extend right across columnar austenite grains in certain weld metals.

Sideplates consist of parallel laths or plates of ferrite oriented on preferred growth directions in the austenite grains. These plates may be separated by carbides, retained austenite, or martensite-austenite, depending on the composition and thermal history of the specimen. Electron optical investigations of weld metal sideplates have noted its comparatively low dislocation density

---

* Unfortunately, segregation at the prior delta ferrite boundaries complicated Watson's analyses.

which is a reflection on its high transformation temperature.

In a recent investigation, the lengthening rate of weld metal sideplates during continuous cooling was estimated at approximately 12-24 x 10^{-4} cm/sec [56]. This is in reasonable agreement with the measurements of Townsend and Kirkaldy [23] and Aaronson [17] quoted in section 2.2.5(a). In view of the similarities in terms of morphology, transformation temperature and growth rate, it seems likely that the grain boundary related sideplate structures in weld metals are probably identical to the Widmanstätten secondary sideplates as discussed in section 2.2.5(a).

2.2.6(c) Acicular ferrite

At slightly lower transformation temperatures [54][55] a fully intragranular, fine grained, transformation product termed acicular ferrite may be developed. This morphology is often described as a series of fine interlocking ferrite laths with a typical length to width ratio of about 4:1* [58]. Several investigators have also observed regions of retained austenite or twinned martensite associated with acicular ferrite laths. TEM investigations of thin foils have shown acicular ferrite grains to have a high dislocation density [57] [59] and to be separated by high angle grain boundaries.

The mechanism of development of acicular ferrite is still the subject of much debate. Nucleation is widely accepted as occurring at intragranular sites, but there is still uncertainty as to whether these sites are deoxidation products [60][61], second phase particles such as nitrides [62][63], or the austenite sub-boundaries [56]. To date nucleation at deoxidation productions has received most attention, but a major drawback to this mechanism appears to be in the ratio of deoxidation products to acicular ferrite grains [64] and the apparent rarity of observing a believable nucleation event. To overcome this shortcoming Barritte et al [61] recently suggested that acicular ferrite development occurs with the nucleation of a few acicular ferrite grains at deoxidation products, followed by considerable sympathetic nucleation and growth of additional infilling

---

* The exact grain size and aspect ratio of acicular ferrite varies with both transformation temperature and chemistry and so limits of grain size and aspect ratio may sometimes be stipulated.

grains. However, this mechanism is, as yet, by no means certain.

Similarly, the growth behaviour of acicular ferrite is still debatable. During continuous cooling acicular ferrite growth usually continues until grain impingement occurs, leaving isolated regions of carbon enriched austenite. These regions then either transform to twinned martensite or remain untransformed. The presence of twinned martensite (carbon content > 0.5 wt%Carbon) is clear evidence that a considerable degree of carbon rejection has occurred during the acicular ferrite transformation. This observation has led several investigators to suggest that acicular ferrite is a truly proeutectoid phase which is probably best described as an intragranularly nucleated Widmanstätten plate morphology as discussed in section 2.2.5(a).

On the other hand it should be remembered that all the various upper bainite morphologies reviewed in section 2.2.5(c) grow with a certain amount of carbon enrichment of the surrounding austenite. Therefore it cannot be ruled out that acicular ferrite may be a form of intragranularly nucleated carbide free acicular bainite or intragranular granular bainite.

Evidence that acicular ferrite is a bainitic transformation product comes from work carried out on by Bosansky et al on niobium bearing weld metals [65]. In these materials it was shown that Nb(C,N) precipitation occurs on dislocations within the acicular ferrite grains at stress relieving temperatures (550^{o}C-640^{o}C). Thus there is evidence that acicular ferrite forms with a degree of supersaturation typical of a bainitic transformation product. Another bainitic feature of acicular ferrite is its high dislocation density, which is considered by many to be incompatible with a product of the proeutectoid reaction.

2.2.6(d) Lath ferrite

When hardenability is sufficiently high a low temperature lath structure is sometimes observed in weld metals.

The morphology of this structure has been described by Choi and Hill [55] as consisting of fine ferrite laths growing side-by-side with intervening carbide precipitates or martensite-austenite islands. The laths are separated by low angle boundaries ($<13^{o}$) and have an extremely high dislocation density. According to Choi and Hill the lath structure is probably a form of bainite and transforms below about 500^{o}C.

2.2.6(e) Summary

The major transformation products of low carbon steel weld metals are summarised on the schematic CCT diagram in Figure 2.6. Again the comments made in section 2.2.4(e) will apply, in that the three noses are quite likely to overlap in a real weld metal. It should be noticed that the position of the acicular ferrite field will be almost identical whether it is an intragranular Widmanstätten ferrite or an intragranular bainite (c.f. Figure 2.5).

2.3 Review of $\gamma \rightarrow \alpha$ Transformation Diagrams

2.3.1 Introduction

In the last 50 years many hundreds of transformation diagrams have been produced to describe the kinetics of the $\gamma - \alpha$ transformation in steels. Initially most detailed investigations studied the transformations under isothermal conditions producing the Time, Temperature Transformation (TTT) or Isothermal Transformation (IT) diagram. More recently, much research effort has gone into producing the more useful Continuous Cooling Transformation (CCT) diagrams. Unlike TTT diagrams CCT diagrams can be directly applied to everyday heat treatment cycles or welding thermal cycles if the relevant variables such as cooling rate, composition and austenitising conditions are known.

In the following section a detailed account of the isothermal and continuous cooling dilatometric techniques, normally used to produce IT and CCT diagrams will be given. Sources of transformation diagrams will also be reviewed including, in particular, CCT diagrams applicable to welding processes.

2.3.2 Isothermal dilatometry

Isothermal dilatometry is the most commonly used method for producing IT or TTT diagrams in steels. The thermal cycle required is a suitable austenitisation treatment, followed by a rapid quench to the desired transformation temperature. Transformation is then allowed to proceed isothermally at this temperature, until the dilatometric record indicates the end of transformation. The specimen is then rapidly quenched to room temperature and examined metallographically.

A schematic dilatation versus time record produced by isothermal dilatometry is shown in Figure 2.7. Position (a) represents the specimen length during the high temperature austenitisation period, position (b) being the new specimen length after the rapid quench to transformation temperature. From (c) to (d) the specimen is undergoing transformation and is expanding due to the f.c.c. - b.c.c. volume change. Position (e) is the new length when transformation ceases, and (f) is the final length of the specimen after quenching to room temperature. The final quench to room temperature is important because the transformation may not have gone to completion and any remaining austenite will therefore be easily identified as martensite in the subsequent metallographic examination.

If the transformed specimen consists of more than one transformation product, separate curves may appear on the trace, indicating the start of transformation of each product. However, in many cases a single curve is produced even though more than one product is formed.

In such cases, a simple graphical construction can be made to obtain the time taken for any given percentage transformation. This construction is shown in Figure 2.7. If length (d) is known to represent 100% transformation, (checked metallographically) then the difference in length ΔL between (d) and (c) must be due to 100% transformation. Assuming the specific volumes of the various microstructural constituents are equal, the value ΔL can then be divided linearly to give any desired percentage transformation. The time taken for this percentage transformation is then obtained by drawing the vertical line, from the point of intersection of the percentage line with the transformation curve, to the time axis, as illustrated in Figure 2.7.

Assuming the order of transformation of the various microconstituents is known, the construction allows prediction of transformation start times for any of the microconstituents, provided accurate quantitative metallographic data is available from the transformed specimen. As a check on the accuracy of the method specimens may be transformed for just less and just more than the calculated start time of the microconstituent in question, and then examined metallographically.

The method of construction is strictly only valid for transformation to a single transformation product, e.g. 100% pearlite or bainite. In practice, the differences in specific volume of

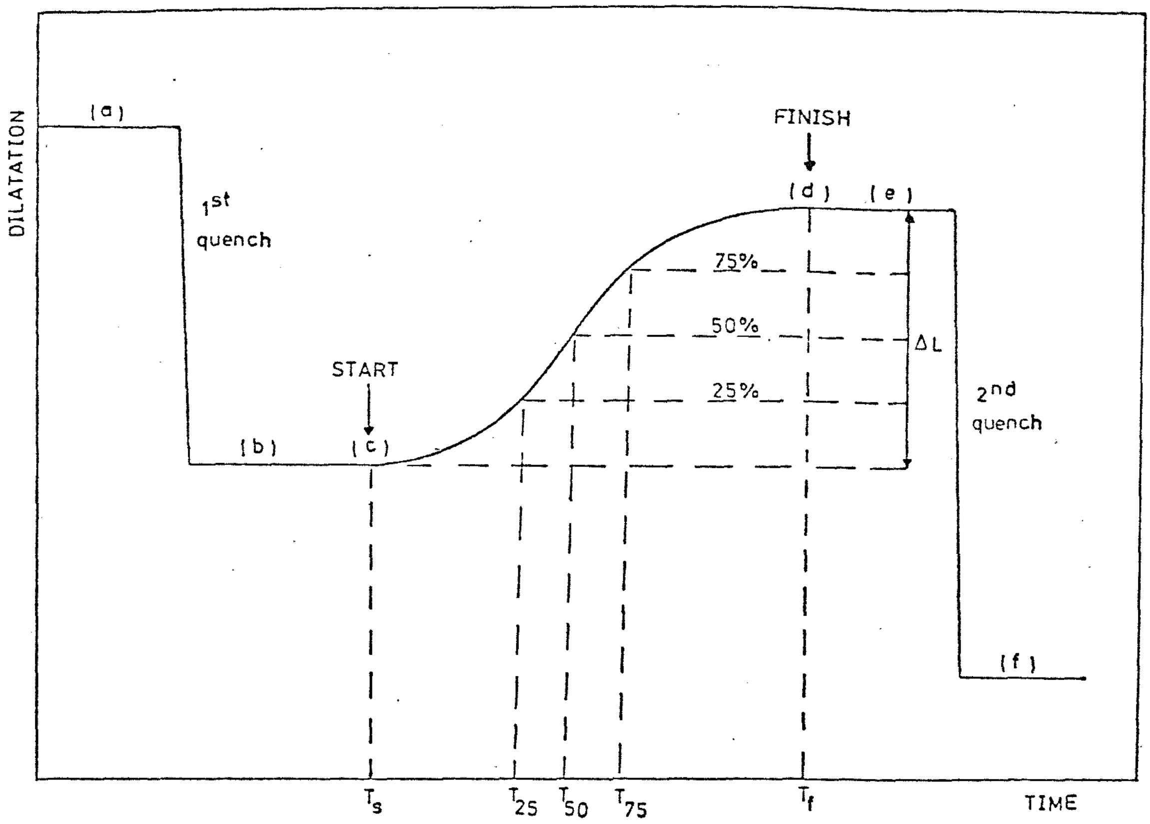

Figure 2.7 Schematic dilatation versus time trace for isothermal transformation.

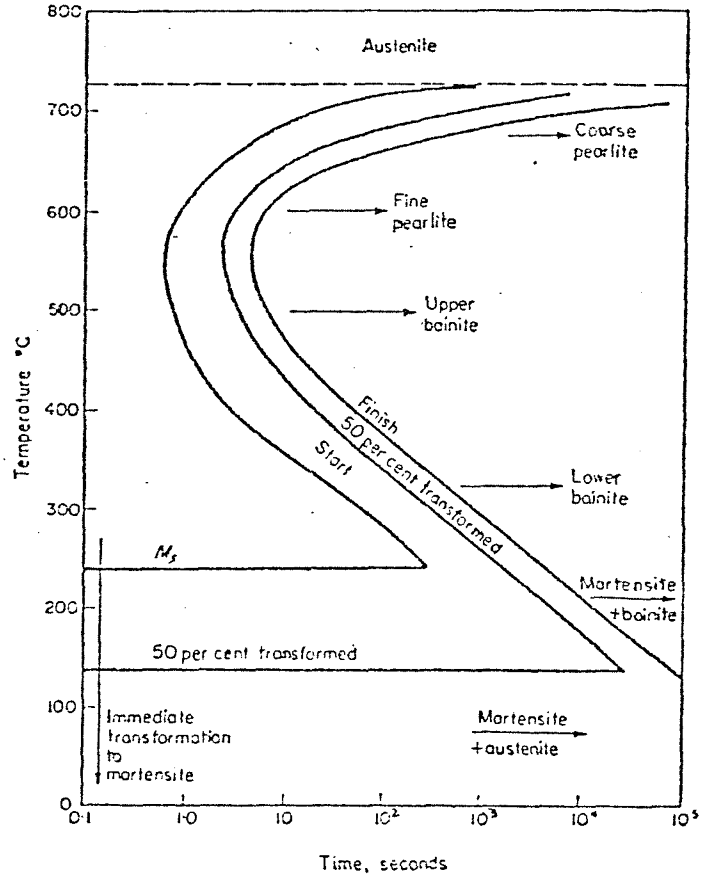

Figure 2.8 TTT diagram for a eutectoid steel (66).

various microstructural constituents are small and the construction is generally accepted as being sufficiently accurate for all mixtures of transformation products.

Finally, construction of the TTT diagram is achieved by plotting the various transformation start and finish points, on a graph of temperature versus log time, as illustrated in Figure 2.8.

2.3.3 Continuous cooling dilatometry

Continuous cooling dilatometry is the most widely used method of producing CCT diagrams. The thermal cycle necessary to produce CCT diagrams is a suitable austenitisation period, followed by continuous cooling to room temperature at various pre-determined cooling rates.

Typical dilatation versus temperature curves are shown schematically in Figure 2.9 for a steel specimen cooled at four different cooling rates. Specimen (a), which has been cooled at the fastest cooling rate has transformed completely to martensite and the dilatation trace shows a continuous smooth curve. The start and finish temperatures, Ms and Mf, are obtained by locating the temperature at which the trace starts and finishes deviating from linearity.

The next three traces (b)-(d) are representative of specimens cooled at progressively slower cooling rates. It can be seen from these traces that the temperature of the transformation progressively increases with decreasing cooling rates. The traces also show a more complex curve during the transformation due to the presence of mixtures of martensite, bainite, ferrite and pearlite, in the transformed microstructures.

A simple schematic CCT diagram produced from the schematic data of Figure 2.9 is shown in Figure 2.10; the original cooling curves for specimens (a)-(d) being plotted first as temperature versus log time.

Unfortunately, the construction of real CCT diagrams is often more complicated than the model just considered. As in the case of isothermal dilatometry, specimens transforming to a number of microconstituents do not always show independent curves. In such cases it is again necessary to use a construction to find the transformation temperature for any given percentage transformation, as shown in Figure 2.11. With such information, it is then possible to use quantitative metallography, and again assuming the order of transformation, calculate microconstituent start temperatures. As

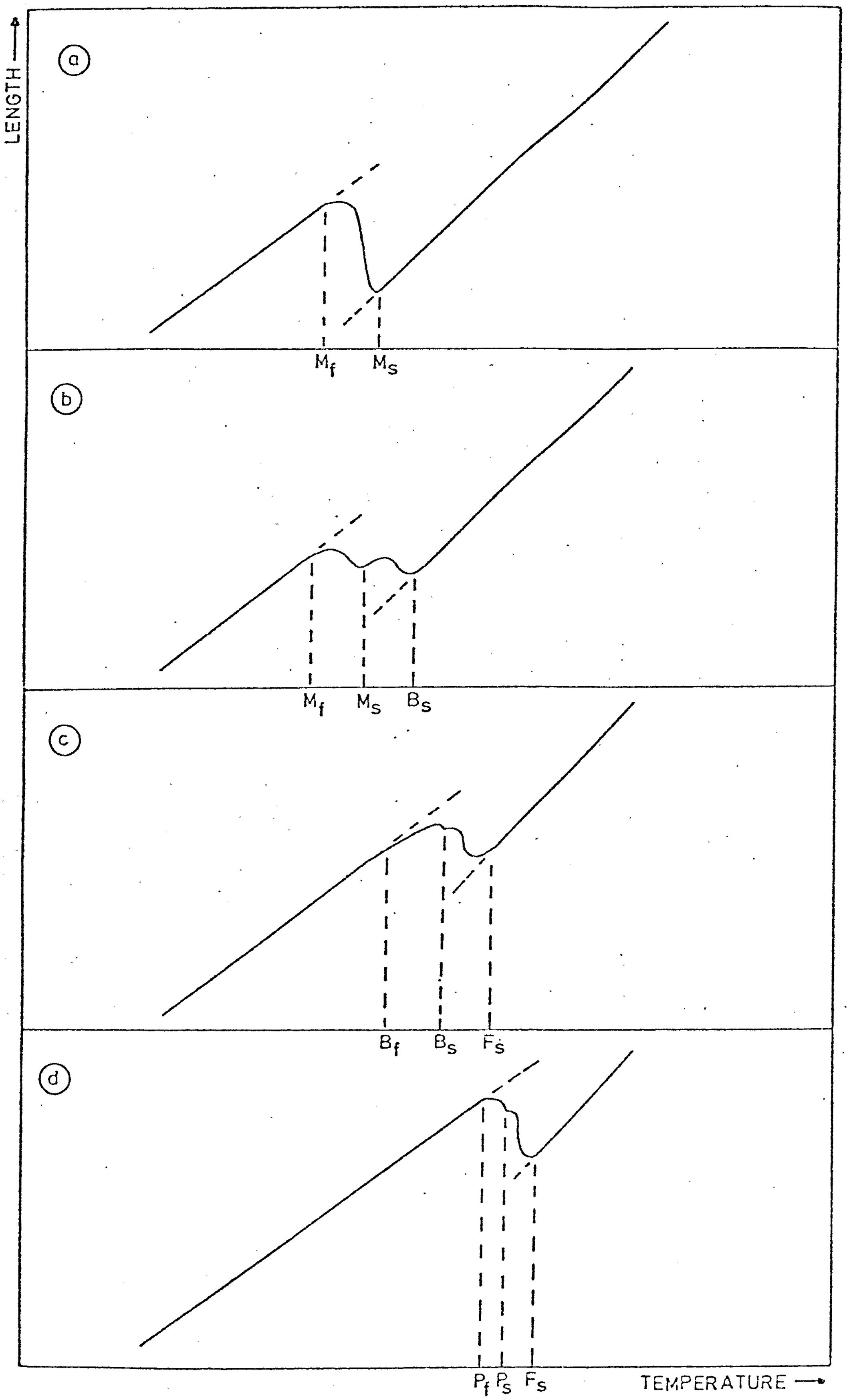

Fig. 2·9 Schematic length versus temperature plots for 4 different cooling rates: ⓐ>ⓑ>ⓒ>ⓓ

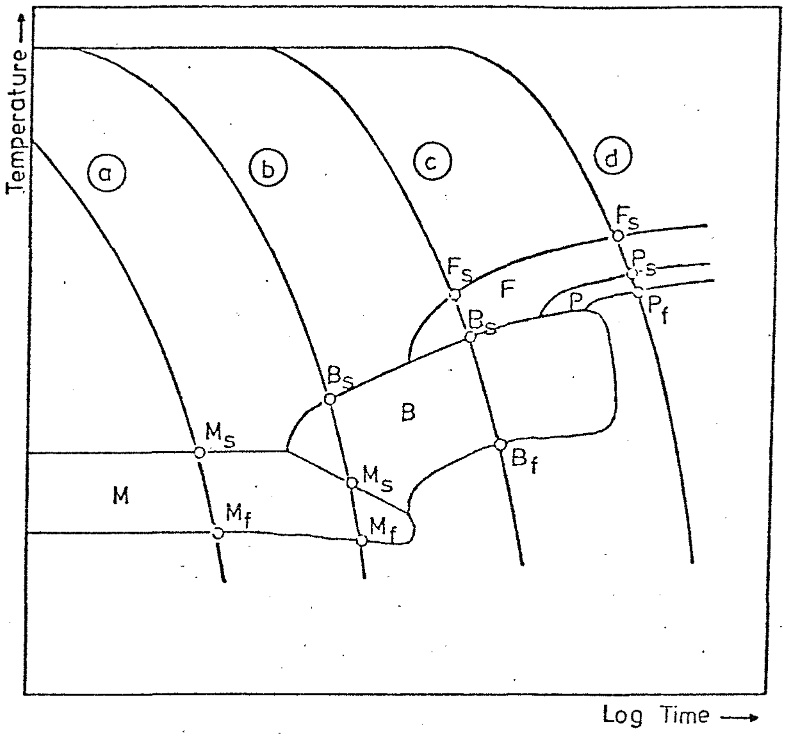

Fig.2·10 Schematic CCT diagram produced from the data in fig.2·9

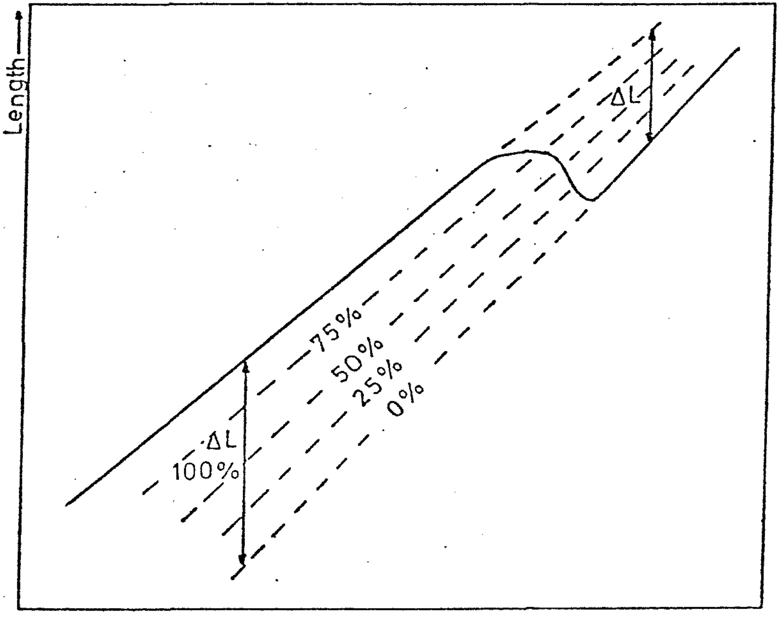

Fig. 2·11 Construction to determine the transformation temperature for any percentage transformation.

a check, various specimens may then be cooled at the same cooling rate, to temperatures just above and just below the calculated value. These specimens are then "quenched out" to freeze the transformation at these particular points in time and examined for the microconstituent in question.

2.3.4 Presentation of CCT diagrams

As yet there are no standards governing the presentation of CCT diagrams, although A.S.T.M. do give some recommendations on dilatometric analysis [67]. Therefore, the amount and method of presentation of additional data is very much at the discretion of the author.

Most diagrams published in the literature use Ac_3 as the start time for the cooling curves; the Ac_3 temperature being determined dilatometrically. Details of austenitising treatment is very important as variation in prior austenite grain size dramatically influences the shape and position of the CCT diagram. Unfortunately, not all CCT diagrams give sufficient details of austenitisation, or prior austenite grain size.

Most diagrams show hardness results from the dilatometer specimens. Most diagrams also give details of the percentage transformation. These details are sometimes derived from quantitative metallography or else obtained directly from the dilation curve via the construction previously described.

Finally, by no means all CCT diagrams give adequate microstructural information. In a few cases detailed micrographs are given, but in many cases morphological variations are not given. This is a serious shortcoming, particularly in cases where morphology plays an important role in influencing mechanical properties. If known microstructure versus mechanical properties relationships are to be used to the full, future CCT diagrams must give more adequate microstructural information.

2.3.5 Sources of transformation diagrams

A considerable number of transformation diagrams have been produced over the years, in various countries. Unfortunately, these diagrams are widely scattered throughout the literature, making an exhaustive review of all diagrams virtually impossible. Table 2.2

Country	Author	Comments
BRITAIN	Atkins [68]	BSC Atlas - refers to 172 steels mostly austenitised between 800°-900°C.
	Stevens & Mayer [69]	
	Mond Nickel Co. [70]	Handbook - CCT diagrams of company products
	Samuel Fox Co. [71]	Catalogue - CCT diagrams of company products
	Kenneford et al [72]	TTT diagrams applicable to Al bearing steels
	Baker [73]	CCT diagrams applicable to welded low-alloy steels
	Alberry [74]	CCT diagram applicable to a welded Cr-Mo-V steel
	Harrison et al [75]	CCT diagrams applicable to C-Mn-(Nb) weld metals
	Barrite & Edmonds[76]	CCT diagrams applicable to C-Mn weld metals
U.S.A.	US Steel [77,78]	Atlas of several hundred IT diagrams
	ASM [79]	Atlas of IT and CCT diagrams
	Climax Molybdenum [80,81]	2 Volumes of CCT diagrams
	Gray [82]	CCT diagrams applicable to Nb bearing HSLA steel
	Pope & Grozier [83]	CCT diagram for V bearing HSLA steel
	Smith & Siebert [84]	CCT diagrams for thermomechanically worked MO-B steels
FRANCE	Delbart et al [85]	IRSID Atlas - CCT diagrams for most French grades of steel
	Serin et al [86]	Nb and Nb-B bearing steels
GERMANY	Wever et al [87]	Max-Planck Institute
	Rose et al [88]	Max-Planck Institute - shows effect of carbon
	Lauprech et al [89]	CCT diagrams for Mn-Nb-Mo steels
	Peetz [90]	CCT diagrams applicable to welding
BENELUX	Economopoulos et al [91]	CNRM-CCT diagrams for commercial steels
USSR	Popov & Popova [92]	Atlas of CCT and IT diagrams
	Shorshorov et al [93]	CCT diagrams for HSLA steels
CZECHO-SLOVAKIA	Kraus [94]	CCT diagrams - produced by magnetic methods
JAPAN	Inagaki [95]	CCT diagrams applicable to welding
	Nakajima [96]	CCT diagrams for Cr-Mo grades austenitised at 850°C
	Kunitake [97]	CCT diagrams for low C low alloy steels austenitised at 840°C and 1350°C
AUSTRALIA	Brownrigg & Boelen[98]	CCT diagrams applicable to welded C-Mn-(Nb) steels
NORWAY	Christensen & Simonsen [99]	CCT diagrams applicable to C-Mn and low-alloy steel weld metals

TABLE 2.2: Sources of CCT and IT Data.

shows most of the major sources of compilations of CCT diagrams at present known to the author and a few individual CCT diagrams thought to be of interest to the present work.

It can be seen that a large amount of transformation data is presently available in the literature. However, little of this data is applicable to low carbon steels and even less is directly applicable to welding.

2.3.6 CCT Diagrams applicable to welding

Table 2.3 shows most of the CCT diagrams which, by virtue of their high temperature austenitisation treatment, may be considered as being directly applicable to welding processes. It can be seen that most of these diagrams are applicable to HAZ structures rather than weld metal,(e.g. Figure 2.12).

In view of the lack of CCT data applicable to weld metal, a few schematic CCT diagrams have been produced to describe the transformation behaviour of weld metals. These diagrams attempt to show the relative positions of the commonly encountered weld metal microstructural constituents: proeutectoid ferrite, ferrite side-plates, acicular ferrite and bainite. More recently a number of real weld metal CCT diagrams have been produced which now provide a more definitive means of describing weld metal transformations, and suggest how variations in alloying and cooling rate may influence these reactions [75][76][90][99].

2.4 Influence of Alloying and Prior Grain Size on $\gamma \rightarrow \alpha$ Transformations

2.4.1 Introduction

The following section deals with the influence of alloying elements and prior γ grain size on $\gamma \rightarrow \alpha$ transformation behaviour. In view of the nature of the present study, particular emphasis will be given to the elements involved in the experimental work, i.e. C, Mn, Ni, Nb and Mo.

When considering the effect of alloying elements on the $\gamma \rightarrow \alpha$ transformation behaviour of steels, both the thernodynamic and kinetic influences must be taken into account.

The thermodynamics are best understood by examining the individual

Origin		Austenitising Temperature	Comments
Baker	[73]	1325° (without holding)	Applicable to HAZ
Alberry	[74]	1000°C (without holding)	Applicable to HAZ (fine grained region)
Constant (IRSID)	[100]	1100-1300°C (without holding)	Applicable to HAZ
Creusot Loire		1200-1400°C (1 sec - 6 min)	Applicable to HAZ
Inagaki (Japan)	[95]	1350°C (without holding)	Applicable to HAZ
Kunitake (Japan)	[97]	1350°C (without holding)	Applicable to HAZ
Ohmori (Japan)	[39]	1200°C (5 min)	Applicable to HAZ
Shorshorov (USSR)	[93]	1350°C (without holding)	Applicable to HAZ
Brownrigg	[98]	1200°C+	Applicable to HAZ
Glover	[101]	Schematic CCT diagram	Applicable to weld metal
Abson	[58]	Schematic CCT diagram	Applicable to weld metal
Harrison	[75]	1250-1400°C (1sec-5min)	Applicable to weld metal
Barritte	[76]	1310°C (10 min)	Applicable to weld metal
Christensen	[99]	1000-1350°C (without holding)	Applicable to weld metal
Peetz	[90]	950-melting temp. (2-5sec)	Applicable to weld metal
Dorling	[102]	Melting temperature	Obtained from real welds

TABLE 2.3: CCT Diagrams Applicable to welding situations.

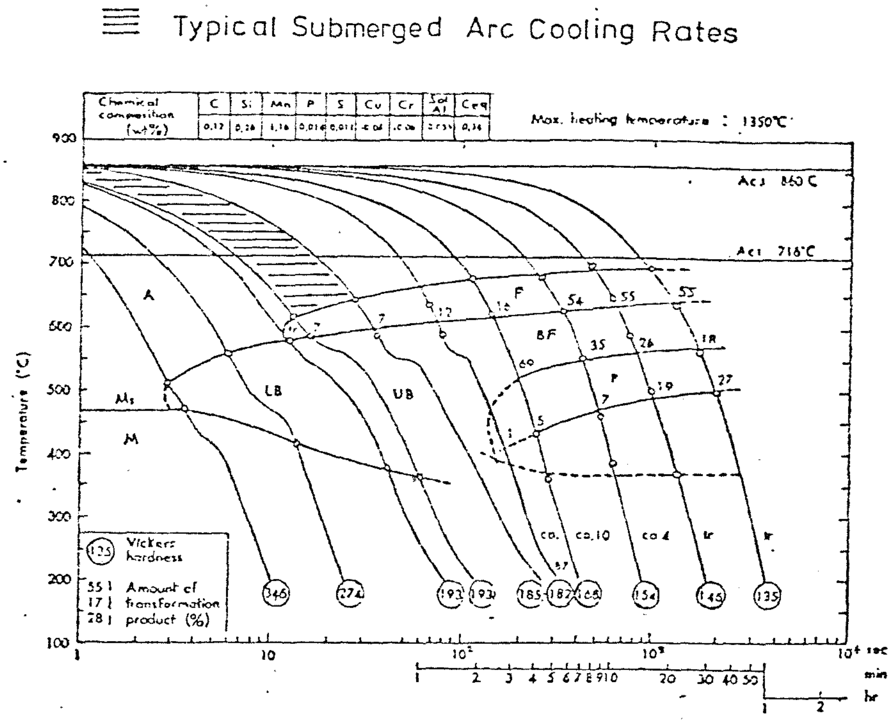

Figure 2.12 CCT diagram applicable to a weld HAZ after Kunitake (97).

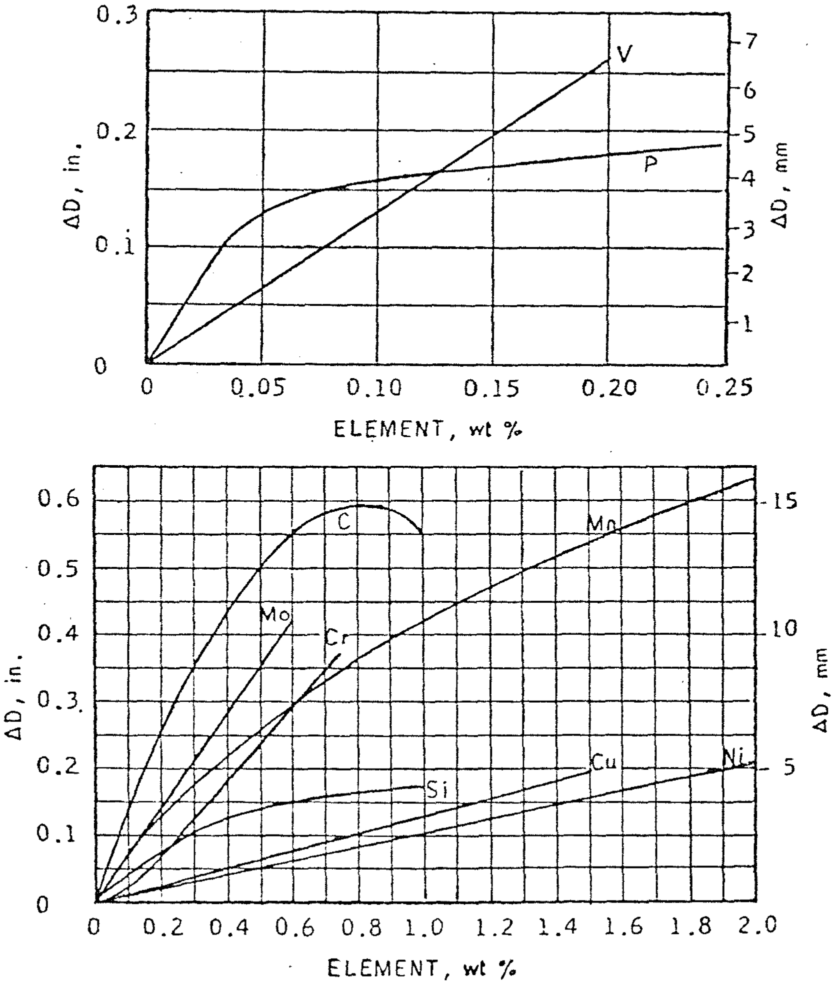

Figure 2.13 Effect of alloying elements on hardenability after Grange (107).

Fe-x binary equilibrium phase diagrams. This type of analysis enables us to rank the elements into groups with similar influences, such as α-stabilising or γ-stabilising elements.

In practice few metallurgical processes are carried out under equilibrium conditions. Consequently, it is important to examine the influence of alloying elements on the kinetics of transformation. This leads to the concept of hardenability and the measurement of transformation behaviour during continuous cooling. Several distinct definitions of hardenability exist (e.g. 100% Martensite, 50% Martensite, 100% bainite, etc.). In general terms hardenability may be considered as a measure of an alloys ability to harden, due to the suppression of the equilibrium transformation products, under specific cooling conditions.

2.4.2 Equilibrium transformation of low alloy steels

A review of iron binary equilibrium systems shows that there are four main categories of Fe-x binary diagrams [103][104]. In general, the elements which tend to open or expand the austenite phase field are called γ stabilisers whereas those which close or contract the austenite phase field are called α stabilisers.

The more important elements involved in low alloy steels can thus be categorised as follows:-

Austensite Stabilisers

MANGANESE	open γ field
NICKEL	
CARBON	expand γ field
NITROGEN	
COPPER	

Ferrite Stabilisers

SILICON	Close γ field
CHROMIUM	
MOLYBDENUM	
VANADIUM	
ALUMINIUM	
TITANIUM	
BOROM	Contract γ field
NIOBIUM	
ZIRCONIUM	

Austenite and ferrite stabilisation is usually explained in terms of the atomic size factor and electronic structure of the solute atoms. For example elements whose size or electronic structure favour the f.c.c. structure open or expand the f.c.c. (γ) phase field whereas elements which favour the b.c.c. structure close or contract it.

According to the thermodynamic analyses of Zener [105] and Andrews [103] the open or closed γ fields can be explained in terms of the enthalpy change associated with solute dissolution in α and γ. If the heat absorbed per unit of solute dissolving in γ is greater than that absorbed per unit of solute dissolving in α, a closed loop will be formed. The converse situation results in an open γ phase field.

Consider now the transformations occuring at faster cooling rates. Hardenability, at a given cooling rate is almost invariably increased by alloying additions, be they γ or α stabilisers. It is easy to see that γ stabilisers, in reducing A_3 (expanding the γ field) reduce the driving force for transformation and thus increase hardenability. The converse argument, that α stabilisers increase the driving force and should therefore reduce hardenability is not borne out in practice. According to Kircaldy [106] this is because at any degree of undercooling, ferrite stabilisers have a much stronger tendency to segregate between different regions of the reaction products than do austenite stabilisers, thus providing a diffusion inhibition against the transformation.

We can see therefore that division of elements into α and γ stabilisers is of interest at slow cooling rates but has less significance at high cooling rates where martensite formation is the major consideration. In order to understand the relative effects of alloying elements on hardenability it may be useful to refer to some of the empirically derived hardenability data relating to low alloy steels.

2.4.3 Hardenability of low carbon low alloy steels

Grange [107] used a "Hot-brine" hardenability test in a systematic study of the effect of carbon and the common alloying elements on steels of low hardenability. The criterion of 90% martensite was used rather than the more common 50% used for medium and higher hardenability steels. The results of this work are shown in Figure 2.13. These results are based on a prior austenite grain size of A.S.T.M.4, a correction being necessary for other grain sizes.

It can be seen that the weight for weight order of effectiveness of the elements on 90% Martensite hardenability at low concentrations is as follows:

P, C, V, Mo, Mn, Si, Cr, Cu and Ni.

The effectiveness of phosphorus and silicon tail off with increasing concentration, but the other elements increase hardenability more or less uniformly throughout the low alloy range. Grange also studied the effects of S, Ti and Zr on hardenability.

In the range of composition tested, sulphur had an apparent negative effect on hardenability. This is thought to be due to the element's strong interaction with manganese: the MnS inclusions thus formed reducing hardenability by removing Mn from solution in austenite.

The results for titanium were complex, hardenability varying from positive to negative with different austenitising temperature and alloy concentration. Titanium is known to have a very high affinity for C and N and it is possible that negative hardenability is due to the removal of C or N from solution in austenite. Whether titanium has a positive or negative effect on hardenability is probably dependent on the interstitial content of the steel and the previous heat treatment.

Zirconium showed a definite negative hardenability effect. Like titanium, zirconium has a high affinity for C and N and the reason for negative hardenability may be the removal of these elements from solution in austenite.

Eldis [108] recently investigated the effects of microalloying elements, Nb, V and Ti on the hardenability of HSLA steels. The experimental approach was to use Jominy end-quench bars, austenitised at 925°C and 1200°C, with a base composition of 0.1C, 1.47Mn, 0.11Si, 0.008N. The criterion for assessing hardenability was the position of the point of inflection on the hardness versus distance curves. The results of the investigation for specimens austenitised at 1200°C are shown in Figure 2.14 and are corrected for A.S.T.M.2 grain size.

It can be seen that, at low concentrations, the weight for weight effectiveness of the elements is as follows:

N, Nb, C, V, Mo, Mn, Si and Ti.

It is interesting to note that the strong carbide-nitride formers Nb, V, and Ti first increase hardenability and then decrease

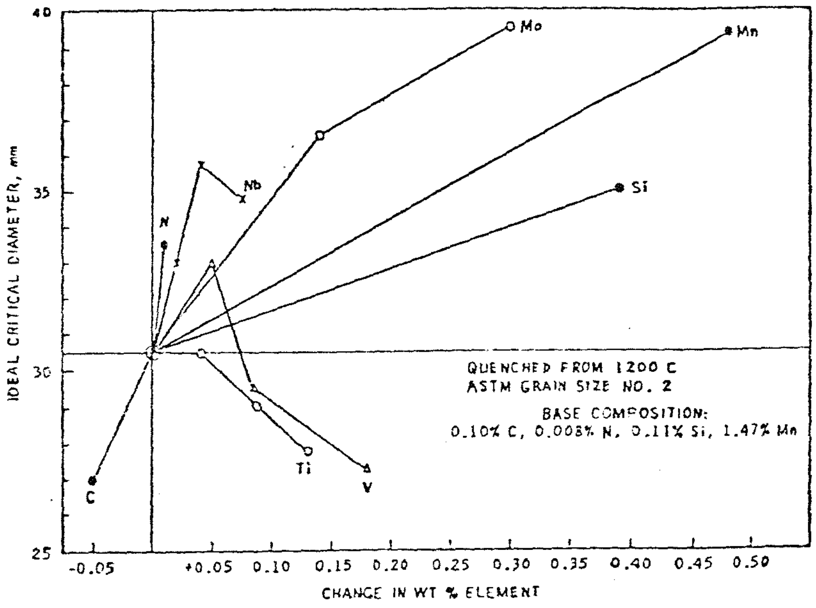

Figure 2.14 Effect of alloying on hardenability after Eldis(108).

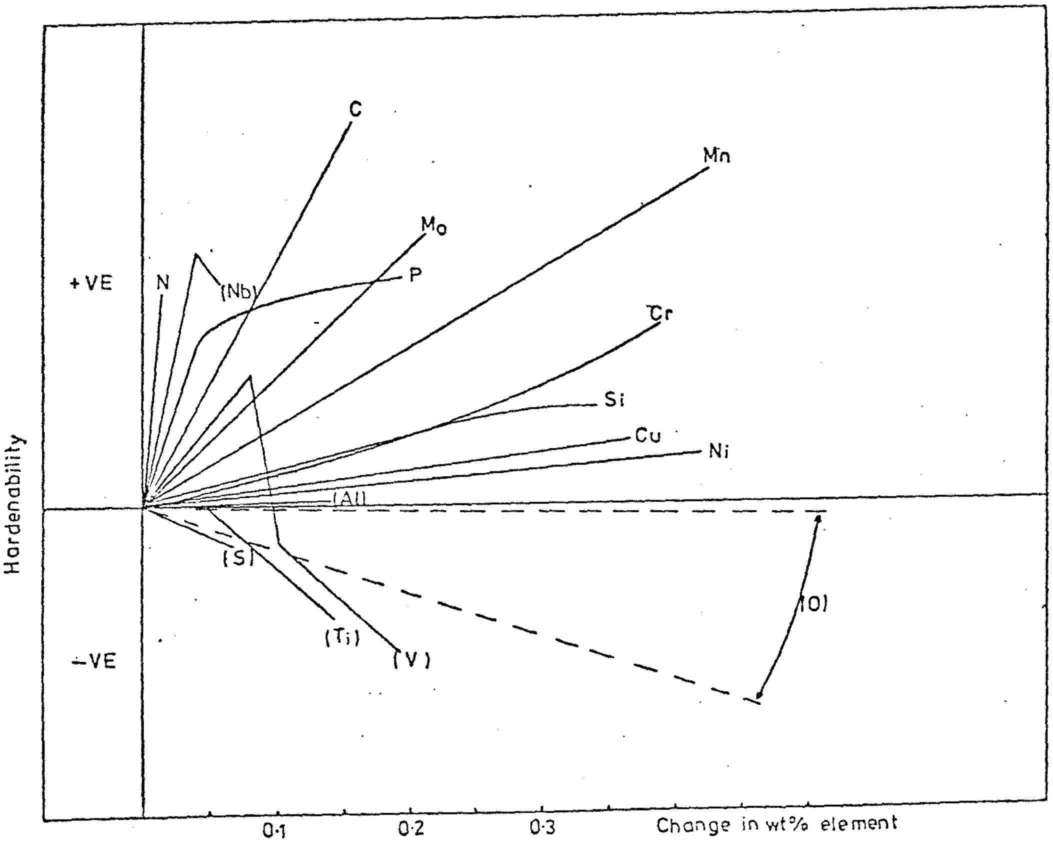

Figure 2.15 Schematic presentation of the effect of alloying elements on hardenability of coarse grained low carbon low alloy steels.

it, probably due to removal of C and N from solution in austenite.

Unfortunately, the differences in experimental technique make direct comparison between the work of Grange and Eldis difficult. However, for the purpose of this work, a comparison of the weight for weight effectiveness of the various alloying elements on hardenability is sufficient. Table 2.4 shows the results of Grange and Eldis and one possible overall order of effectiveness on hardenability proposed by the author.

The effect of aluminium was not determined in either of the above investigations, but according to Kenneford et al [72] its effect is small.

Oxygen is unlikely to exert much positive effect on hardenability as it is virtually insoluble in austenite. However, an apparent negative effect, similar to sulphur and the strong carbide-formers, could be envisaged due to removal of certain alloying elements from solution in austenite during doxidation reactions. This could be important in weld metals where oxygen contents are usually high.

In Figure 2.15 the proposed relative effectiveness of most alloying elements on the hardenability of coarse grained low carbon low alloy steel is presented schematically. Elements in parentheses are known to show a complex effect due to removal of other elements from solution. Oxygen is shown over a range of negative hardenability which is intended to be a reflection of the numerous different deoxidation practices that occur either in steelmaking or welding.

2.4.4 Effect of alloying elements on the shape of CCT diagrams

In the previous section the effect of alloying elements on hardenability was assessed for coarse grained low carbon low alloy steels. The two criteria used being the formation of 90% martensite and the point of inflection of Jominy test specimens, hardness versus distance, plots. In both these experiments the effect of alloying elements was being measured on the hardenability of mixed martensite and bainite microstructure. Consideration of a typical CCT diagram, as illustrated in Figure 2.16 shows that these criteria are only two of many other possible criteria. For example, to consider the effect of alloying on the production of a totally ferrite-pearlite microstructure one would need to consider V_3: the critical cooling velocity for 100% ferrite-pearlite transformation. Several investigators have used regression analysis on a selection of CCT

TEST	HOT-BRINE	JOMINY	CCT DIAGRAMS				FROM LITERATURE
AUTHOR	GRANGE	ELDIS	MAYNIER		KUNITAKE	ELDIS	HARRISON
Criterion	90% Martensite	Inflection pt.	$V_1^{(90)}$	$V_1^{(50)}$	C_{50}	log bainite time	Estimated
+ve		N					N
↑		Nb					Nb
	P						P
	C	C	C	C	C		C
	V	V					V
order of effectiveness of alloying elements on hardenability					(Cu)		
	Mo	Mo	Mo	Mo	Mo	Mo	Mo
					(Cr)		
	Mn	Mn	Mn	Mn	Mn	Mn	Mn
						(C)	
	Si	Si					Si
↓	Cr		Cr			Cr	Cr
	Cu						Cu
-ve	Ni		Ni	Ni		Ni	Ni
				(Cr)		(Si)	
							Al
		Ti					Ti
	Zr						Zr
							O
	S						S

Table 2.4 Effect of Alloying Elements on CCVs for Mixed Martensite-Bainite Microstructures

diagrams to determine the effect of alloying elements on various microstructures.

Maynier, Dollet and Bastien [109] used a total of over 300 CCT diagrams to produce 8 statistical equations relating log CCV (critical cooling velocity) at 700°C to chemical composition for 8 microstructural types. The microstructures chosen and the results of the regression analysis are shown in Table 2.5. Figure 2.16 also relates to this work. In each equation an austenitisation parameter, Pa, is included to take account of the prior austenite grain size.

$$Pa = [\frac{1}{T} - \frac{nR}{\Delta H} \log \frac{t}{to}]^{-1} \qquad (2.2)$$

where

T = Temperature
t = time at temperature
to = unit of time
R = gas constant 8.31441 (KJ/Kg molK)
n = 2.3026
ΔH = activation energy 460.55 KJ/mol.

All equations apply to plain carbon low alloy steels. The major sources of data being the CCT diagrams of I.R.S.I.D., Max-Planck Institute, C.N.R.M., Sekiguchi and S.F.A.C.

Similar regression equations have been produced by Eldis [110] using the 300 or more CCT diagrams produced by Cias [80,81]. These equations are shown in Table 2.5. Unfortunately no grain size factor is given with these equations.

Kunitake and Ohtani [111] have also produced a set of regression equations based on CCT diagrams from the Max-Planck Institute. The effect of austenite grain size was disregarded as the diagrams used were all produced from similar grain sizes, (ASTM 7-9). Critical cooling rates are expressed in terms of cooling times from AC_3 to 500°C. The five cooling times, C_B, C_{50}, C_F, C_P, C_E correspond to cooling curves, V_1, $V_1(50)$, V_2, CCV to avoid pearlite (not shown) and V_3 respectively in Figure 2.16. These equations are also shown in Table 2.5.

By comparing the values of the coefficients in each regression equation, an order of effectiveness of each element on hardenability can be obtained.

Table 2.4 compares the previously discussed results by Grange

MAYNIER, DOLLET AND BASTIEN (109)

V_1 - CCV giving 100% martensite

$\log V_1 = 9.81 - (4.62C + 1.05Mn + 0.54Ni + 0.50Cr + 0.66Mo + 0.00183Pa)$

$V_1(90)$ - CCV giving 90% martensite, 10% bainite

$\log V_1(90) = 8.76 - (4.04C + 0.96Mn + 0.49Ni + 0.58Cr + 0.97Mo + 0.001Pa)$

$V_1(50)$ - CCV giving 50% martensite, 50% bainite

$\log V_1(50) = 8.50 - (4.12C + 0.86Mn + 0.57Ni + 0.41Cr + 0.94Mo + 0.0012Pa)$

V_2 - CCV giving 100% bainite

$\log V_2 = 10.17 - (3.80C + 1.07Mn + 0.70Ni + 0.57Cr + 1.58Mo + 0.0032Pa)$

$V_2(90)$ - CCV giving 90% bainite, 10% ferrite-pearlite

$\log V_2(90) = 10.55 - (3.65C + 1.08Mn + 0.77Ni + 0.61Cr + 1.60Mo + 0.0032Pa)$

$V_2(50)$ - CCV giving 50% bainite, 50% ferrite-pearlite

$\log V_2(50) = 8.74 - (2.23C + 0.86Mn + 0.56Ni + 0.59Cr + 1.60Mo + 0.0032Pa)$

$V_3(90)$ - CCV giving 90% ferrite-pearlite, 10% bainite

$\log V_3(90) = 7.51 - (1.38C + 0.35Mn + 0.93Ni + 0.11Cr + 2.31Mo + 0.0033Pa)$

V_3 - CCV giving 100% ferrite-pearlite

$\log V_3 = 6.36 - (0.43C + 0.49Mn + 0.78Ni + 0.27Cr + 0.38Mo + 2\sqrt{Mo} + 0.0019Pa)$

ELDIS (110)

Position of bainite nose

$\log \text{bainite time (sec)} = 1.094C + 0.321Si + 1.407Mn + 1.772Mo + 1.050Cr + 0.632Ni - 1.849$

Position of ferrite-pearlite nose

$\log \text{pearlite time(sec)} = 1.259C + 1.231Mn + 2.339Mo + 0.445Cr + 0.484Ni - 0.711$

KUNITAKE AND OHTANI (111)

$\log C_B = 3.274C + 0.046Si + 0.626Mn + 0.026Ni + 0.706Cr + 0.675Cu + 0.520Mo - 1.818$

$\log C_{50} = 2.738C + 0.458Mn + 0.583Cr + 0.704Cu + 0.648Mo - 0.565$

$\log C_F = 3.288C - 0.168Si + 1.068Mn + 0.300Ni + 1.266Cr + 0.626Cu + 2.087Mo - 1.931$

$\log C_P = 0.597C - 0.100Si + 1.395Mn + 0.395Ni + 1.295Cr + 0.398Cu + 3.730Mo - 0.869$

$\log C_E = -0.538C + 0.018Si + 1.294Mn + 0.609Ni + 0.847Cr + 0.693Cu + 4.936Mo + 0.322$

Table 2.5 Regression Equations for CCT Diagrams

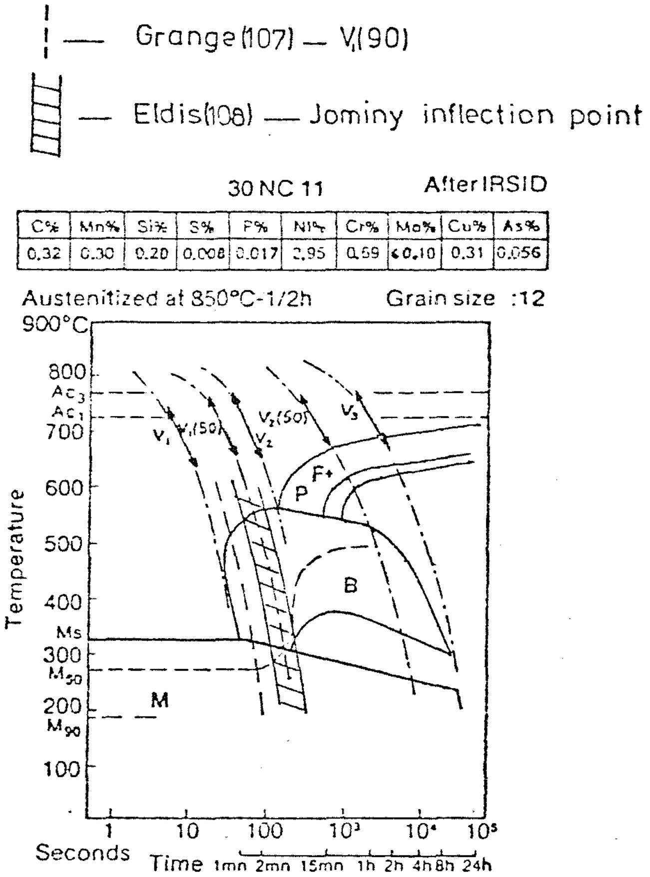

C%	Mn%	Si%	S%	P%	Ni%	Cr%	Mo%	Cu%	As%
0.32	0.30	0.20	0.008	0.017	2.95	0.59	<0.10	0.31	0.056

I. R. S. I. D. CCT diagram of 30 NC11 steel.

Figure 2.16 CCT diagram illustrating several CCV's.

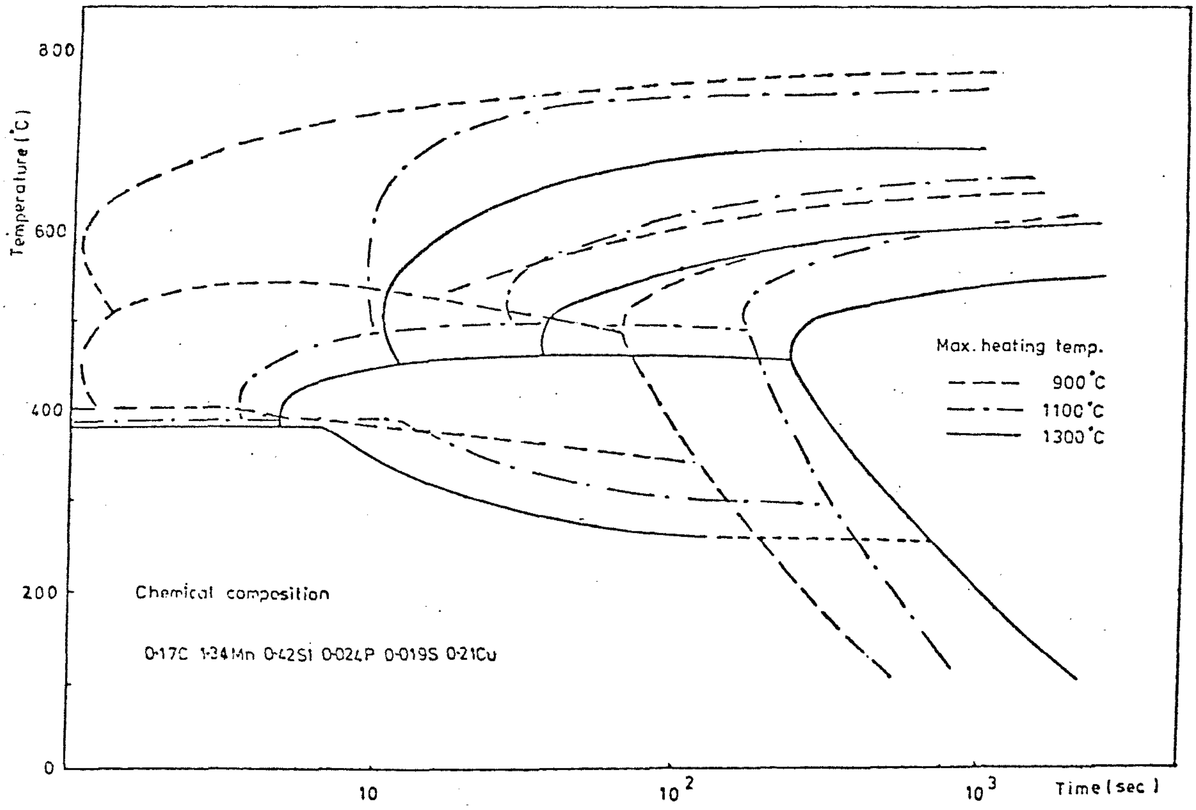

Figure 2.17 Effect of austenitising temperature on CCT diagrams.

[107] and Eldis [108] with the CCT regression analysis of Maynier [109], Eldis [110] and Kunitake [111].

It can be seen that the results of Maynier are in good agreement with the results of Grange and Eldis except for the position of Cr in the 50% martensite equation.

Kunitake and Ohtani [111] are also in good agreement with the previous work for the relative effects of C, Mo and Mn but again the effectiveness of Cr gives an anomalous result. According to Kirkaldy [106] Cr is equivocal with respect to γ or α stabilisation and can be seen to have a non-uniform effect on hardenability. The relative position of Cu reported by Kunitake is very high (between C and Mo). This result is contradictory to the result of Grange who found Cu to exhibit a mild effect on hardenability.

The results of Eldis [110] give the same relative effectiveness of Mo, Mn, Cr and Ni as Grange and Maynier, but give anomalous results for C and Si. This may be due to the fact that these results come from a preliminary trial using a very large data base covering a wide range of carbon and alloy contents. Also no details of prior austenite grain size were given.

A similar comparison of various regression equations can be made for transformations in the mixed bainite/ferrite-pearlite region of the CCT diagram as shown in Table 2.6. The overall order of effectiveness of alloys is similar to those previously presented but again Cr can be seen to be variable in its effect.

If transformations to totally ferrite-pearlite microstructures are considered, at even slower cooling rates, it can be seen that Mo becomes the most effective element in the relevant CCV equations. This observation is consistent with molybdenum's known ability to suppress ferrite-pearlite microstructures.

In the three investigations just reviewed, no information on the effect of microalloying elements was presented. An investigation by Ohmori et al [39] produced two CCT diagrams for HSLA steels of almost identical chemical composition; one with 0.02% vanadium and the other without vanadium. The effect of vanadium on the CCT diagram was to increase slightly the bainite reaction temperatures, making the bainite field flat over a wide range of cooling rates. The vanadium also dramatically moved the ferrite nose to shorter times.

Two CCT diagrams presented by Ronn [112] show the effect of niobium on the shape of the CCT diagram, the apparent effect of adding 0.036 Nb to a 0.11C 1.0Mn steel being to move the ferrite nose to

TEST	CCT DIAGRAMS						FROM LITERATURE
AUTHOR	MAYNIER			KUNITAKE		ELDIS	HARRISON
CRITERION	V_2	$V_2^{(50)}$	$V_2^{(90)}$	C_F	C_P	log pearlite time	Est'd
+ve	C	C	C	C			C
↑	Mo	Mo	Mo	Mo	Mo	Mo	Mo
				$\textcircled{Cr}$		$\textcircled{C}$	
	Mn	Mn	Mn	Mn	Mn	Mn	Mn
		$\textcircled{Cr}$			$\textcircled{Cr}$		$\textcircled{Cr}$
					$\textcircled{C}$		
				Cu	Cu		Cu
	Ni	Ni	Ni	Ni	Ni	Ni	Ni
↓	$\textcircled{Cr}$		$\textcircled{Cr}$			$\textcircled{Cr}$	$\textcircled{Cr}$
-ve				Si	Si		Si

Table 2.6 : Effect of Alloying Elements on CCVs for Mixed Bainite-Ferrite-Pearlite Microstructures

longer times and to suppress dramatically the pearlite reaction. CCT diagrams recently produced in France by Serin et al [86] also show Nb to increase hardenability by moving the whole diagram to longer times and lower transformation temperatures.

2.4.5 Austenite grain size

Several investigators [95][97][100] have demonstrated the effect of varying prior austenite grain size on the shape and position of the CCT diagram. Figure 2.17 shows the work of Inagaki and Sekiguchi [95] in which an HSLA steel, Wel-ten 55 (0.17C, 1.34Mn, 0.42Si, 0.21Cu) was used to produce CCT diagrams after different austenitisation treatments. The three thermal cycles used were rapid heating to 900°C, 1100°C and 1300°C respectively, followed by continuous cooling. The increasing prior austenite grain size can be seen to decrease transformation temperatures and delay transformation to longer times (figure 2.17). This powerful effect of prior γ grain size on transformation behaviour is the major factor restricting the application of most CCT diagrams to welding processes.

The depression of transformation temperature and delay in transformation times can be explained in terms of reduced nucleation due to fewer grain boundaries, and increased diffusional distances required for growth, in the larger grain size. Figure 2.17 also shows a slight depression of the Ms temperature due to larger grain size, but a similar investigation by Constant [100] contradicts this finding.

Another tendency of increasing grain size seems to be an increase in the proportion and variety of the intermediate transformation products formed, some of which are not normally encountered in transformation studies from smaller grain sizes, where transformations tend to be dominated by grain boundary nucleated products. In such cases it may be necessary to divide the intermediate region of larger γ grained CCT diagrams into various morphological regions. This has already been done in the previously described investigations by Kunitake [97] and Ohmori [39].

2.4.6 Effect of alloying elements on weld metal microstructure

Without doubt the most important element in terms of weldability is carbon. Carbon levels must be kept low to prevent martensite formation and associated cracking problems at typical weld cooling rates. This fact is borne out by the values of the coefficient for carbon in the relevant CCV equations. At the C levels commonly encountered, 0.05 - 0.15C, in present day weld metals the major effect of carbon is in the amount of carbides formed. This observation has been made by Dorschu and Stout [113] and Den Ouden et al [114]; the latter authors also comment on the refining nature of C on the microstructure.

The effect of manganese on weld metal microstructure has been systematically investigated by Evans [115]. Evans found that increasing manganese, in the range 0.6 - 1.8% Mn, progressively increased the amount of acicular ferrite and reduced the amount of proeutectoid ferrite and ferrite sideplates in MMA weld metal. There was also a continuous refinement of the acicular ferrite with increasing manganese content. Similar refinement was also experienced by Dorschu [113], who also observed increasing amounts of carbide and at higher Mn levels, (∿1.6 Mn) the formation of upper bainite.

Tuliani [116] also carried out an investigation into the effect of Mn in submerged-arc weld metals. Progressive increases in Mn content from 0.4 - 1.4 Mn changed the microstructure from coarse polygonal ferrite and pearlite, through a fully "bainitic" structure (probably ferrite sideplates), to an acicular ferrite structure with little proeutectoid ferrite.

Variations in silicon from 0.35 - 0.80 Si have been reported as having no effect on weld metal microstructure by Dorschu [113]. Unfortunately, these results are probably subject to considerable error as the Si analysis was calculated from Si additions during welding and not on chemical analysis of the weld metal.

Tuliani and Farrar [117] observed a microstructural change from sideplates to acicular ferrite as Si content increased from 0.2 - 0.4 Si in SA weld metal, although there were accompanying variations in other alloying elements.

Molybdenum has a strong effect on weld metal microstructure. Almqvist et al [118], Yoshino and Stout [119] and Garland and Kirkwood [120] have all shown that up to about 0.5 Mo decreases proeutectoid ferrite and increases acicular ferrite contents of weld metals.

Nickel added in relatively large quantities (up to 2.8%) to weld metals has been shown [113] to mildly refine ferrite grain size.

The effects of niobium on weld metal microstructure has been the subject of many investigations.

Garland and Kirkwood [121] have shown that small additions of Nb tend to suppress grain boundary ferrite in favour of acicular ferrite. This has also been observed by Yoshino and Stout [119]. On the other hand, Sawhill [122] and Jesseman [124] both observed a tendency to form upper bainite as Nb levels were increased. Levine and Hill [54] observed the tendency of Nb to increase acicular ferrite at the expense of grain boundary ferrite for low Nb additions (up to ∿0.02 Nb) but observed a lath morphology similar to sideplates at higher Nb levels.

The obvious confusion surrounding the effect of Nb has been comprehensively reviewed by Watson [57]. Using a model based on schematic CCT diagrams, Watson was able to rationalise some of these observations and showed that some of the confusion was due to the difficulty of interpretation between upper bainite and sideplate structures. Then using the CCT diagrams presented in the present work, he was able to show that the effect of Nb was dependent on the overall hardenability of the weld metal, as determined by other alloying elements. At normal overall hardenability levels acicular ferrite was slightly increased at the expense of proeutectoid ferrite, whereas at lower overall hardenability levels sideplate structures were promoted by Nb. Recently Dolby [124] has also reviewed the influence of Nb on ferrite weld metal microstructure and reached very similar conclusions to those of Watson.

Abson and Evans [125] recently investigated the influence of Nb on the microstructure and properties of C-Mn MMA weld metal. In this investigation Nb was seen to reduce the proportions of grain boundary ferrite and acicular ferrite and increase the proportions of the constituent termed ferrite with aligned MAC [126].

The effect of oxygen on weld metal microstructure has been studied by several investigators recently [60][62] [127-130]. There seems to be general agreement that weld metal microstructure can vary dramatically, at certain chemical compositions, due to variations in oxygen content. Ferrite sideplate structures tend to be favoured at the highest oxygen levels and acicular ferrite at intermediate oxygen contents. Ito and Nakanishi [62] have suggested that very low oxygen contents <200 ppm cause bainitic microstructures to form in weld metals.

Several theories have been postulated in an attempt to explain the "oxygen effect" in weld metals. Due to the virtual insolubility of oxygen in iron, these theories usually revolve around the possible effects of oxide inclusions on weld metal transformations.

2.4.7 Summary

The influences of alloying elements and austenite grain size have been discussed in relation to equilibrium transformations, hardenability and CCT diagrams. From this data, the influences of the major alloying elements on weld metal transformation behaviour may be summarised as follows:

Carbon

Carbon is a strong γ stabiliser and very small additions of carbon cause a large depression of transformation temperatures, particularly at the high-cooling rates. Carbon also has a powerful effect on movement of the pearlite and bainite noses to longer times on the CCT diagram but has little tendency to separate them.

The effect of increasing carbon content on weld metal microstructure has been reported as increasing the volume fraction of carbides. This is to be expected if the weld cooling curves passes through the pearlite field of the CCT diagram. However, if the conditions are such that the cooling curve just touches the pearlite nose, it could be envisaged that increasing carbon would move the pearlite nose to the right and thus reduce carbide volume fraction.

A certain amount of refinement of weld metal grain size has also been reported in the literature, with increased carbon content. This is most probably due to carbon's strong effect on suppressing the γ-α transformation temperature.

Manganese

Manganese is also a strong γ stabiliser causing a general depression of transformation temperature in all regions of the CCT diagram. Like carbon, manganese moves the bainite and pearlite nose to longer times but does not have much effect on separation of the noses.

In weld metals, increasing manganese has been shown to promote acicular ferrite at the expense of proeutectoid ferrite and ferrite sideplates. Increasing manganese also appears to refine the acicular ferrite. Both these observations are consistent with manganese's role of decreasing transformation temperature and thus limiting the temperature range in which proeutectoid ferrite can form.

Carbon and Manganese

The combined effects of carbon and manganese are usually taken as the base line for hardenability of C/Mn or HSLA steels. This base line hardenability defines approximately the shape, position and transformation temperatures of the relevant CCT diagram. Subsequent additions of other alloying elements or microalloying elements may alter the base line slightly or alter the relative positions of phase fields. This is particularly noticeable with the often strong tendency of certain elements to move the ferrite nose relative to the rest of the diagram.

Silicon

Silicon is a ferrite stabiliser and has a quite strong tendency to raise transformation temperatures at slow cooling rates. At fast cooling rates the Andrews formula shows no tendency of Si towards depressing the transformation temperature, although previous Ms formulae [131-134] suggest that Si did slightly lower the Ms.

The effect of silicon on movement of the bainite and pearlite nose is weak and there is little tendency to separate the two noses [135].

Silicon has been reported in the literature as having no significant effect on weld metal microstructure by Dorchu [113]. However, Tuliani and Farrar [117] observed a tendency of Si to promote acicular ferrite in favour of sideplates as weld metal Si content increased from 0.2% to 0.4%.

Molybdenum

Molybdenum is also a ferrite stabilising element but exerts very little effect on transformation temperatures. At fast cooling rates the Ms temperature is slightly depressed by Mo, but at very slow cooling rates there is some evidence that transformation temperatures are very slightly raised. Molybdenum has a strong influence on bainite hardenability and an even stronger effect on moving the ferrite nose to longer times.

In weld metals additions of Mo have been shown to decrease proeutectoid ferrite and increase acicular ferrite. This is in agreement with the strong tendency of Mo to delay the ferrite reaction.

Nickel

Nickel is an austenite stabiliser but has only a mild effect on transformation temperatures. These temperatures are lowered slightly at all cooling rates. Nickel exerts little effect on the

CCT diagram although there is some evidence that it may slightly retard the ferrite-pearlite reaction relative to the bainite reaction.

Observations of weld metal microstructure suggest that nickel has a slight refining effect on grain size. This is probably due to the slightly reduced γ-α transformation temperature.

Niobium

Niobium is a ferrite stabiliser and may be expected to increase transformation temperatures at very slow cooling rates. Niobium has been shown to have a very strong effect on hardenability and is also known to move the ferrite nose of the CCT diagram to longer times.

Additions of niobium to weld metals have been shown to promote acicular ferrite at the expense of proeutectoid ferrite. Other studies have shown niobium additions to promote ferrite sideplate structures. Both these observations are consistent with niobium's apparent ability to delay the ferrite reaction.

Oxygen

Oxygen is rarely considered as having any effect on hardenability in wrought steels. Consideration of the Fe-O binary phase diagram shows that oxygen is virtually insoluble in solid iron. However, oxygen may show an apparent negative effect on hardenability through its removal of other alloying elements from the matrix into non-metallic inclusions, as suggested by Farrar and Watson [130]. This has been shown to be the case for sulphur which exerts negative hardenability through the removal of Mn into MnS inclusions.

Observations of weld metal microstructure have shown that high oxygen levels tend to promote ferrite sideplate structures, whereas lower oxygen levels promote acicular ferrite. This is consistent with a strong negative effect on hardenability of oxygen.

2.5 Influence of Inclusions on Weld Metal $\gamma\rightarrow\alpha$ Transformations

2.5.1 Introduction

In the previous section it was noted that oxygen rich inclusions (i.e. deoxidation products) seem to have a very pronounced effect on the transformation behaviour of low carbon steel weld metals. Ito and Nakanishi [62] suggested that acicular ferrite was the dominant microstructural feature at oxygen contents above about 200 ppm.

Below this level, the lath-like structures were often observed.

Abson et al [60] confirmed this view by reducing the oxygen content of a submerged arc weld metal from about 200 ppm to about 120 ppm, using a laser remelting technique, and observed a microstructural change from acicular ferrite to regions of thin parallel ferrite laths, which they termed bainite. In contrast to these low oxygen level studies, Cochrane and Kirkwood [129] demonstrated that high oxygen levels can also affect weld metal transformation behaviour, by promoting sideplate structures.

In an attempt to explain some of these anomalies various authors have considered several possibilities. These include direct nucleation on inclusions or other second phase particles [60] [63], interactions between inclusions and γ grain boundaries [129] and more recently, the possibility of inclusion strain effects has also been postulated [56][76]. The remaining sections of this review will therefore consider the role of inclusions in restricting γ grain growth, thermal contraction strain effects, and ferrite nucleation.

2.5.2 Austenite grain growth

In annealed, high purity, single phase metals the shape adopted by individual grains is usually a compromise between the laws of surface tension and the requirements for total space filling. Theoretically, the ideal grain shape which can satisfy both of these requirements is known as Kelvin's "tetrakaidecahedron of minimum area" and consists of eight hexagonal faces and six square ones [136]. If a regular array of grains of this shape is produced it will be stable and unable to grow due to equilibrium between all surface tensions acting at grain boundaries and grain junctions.

In most random polycrystalline aggregates, however, it is more common to observe a range of grain sizes and grain shapes which are far from the equilirbium state. When such materials are heated, thermal activation allows the out of balance surface tension forces to act, and so produce grain boundary migration, which eventually results in grain growth.

The mechanism of grain growth is illustrated schematically in Figure 2.18 for two dimensional equilibria. Figures 2.18(a) shows the equilibrium situation at a triple point specified by the following equation:

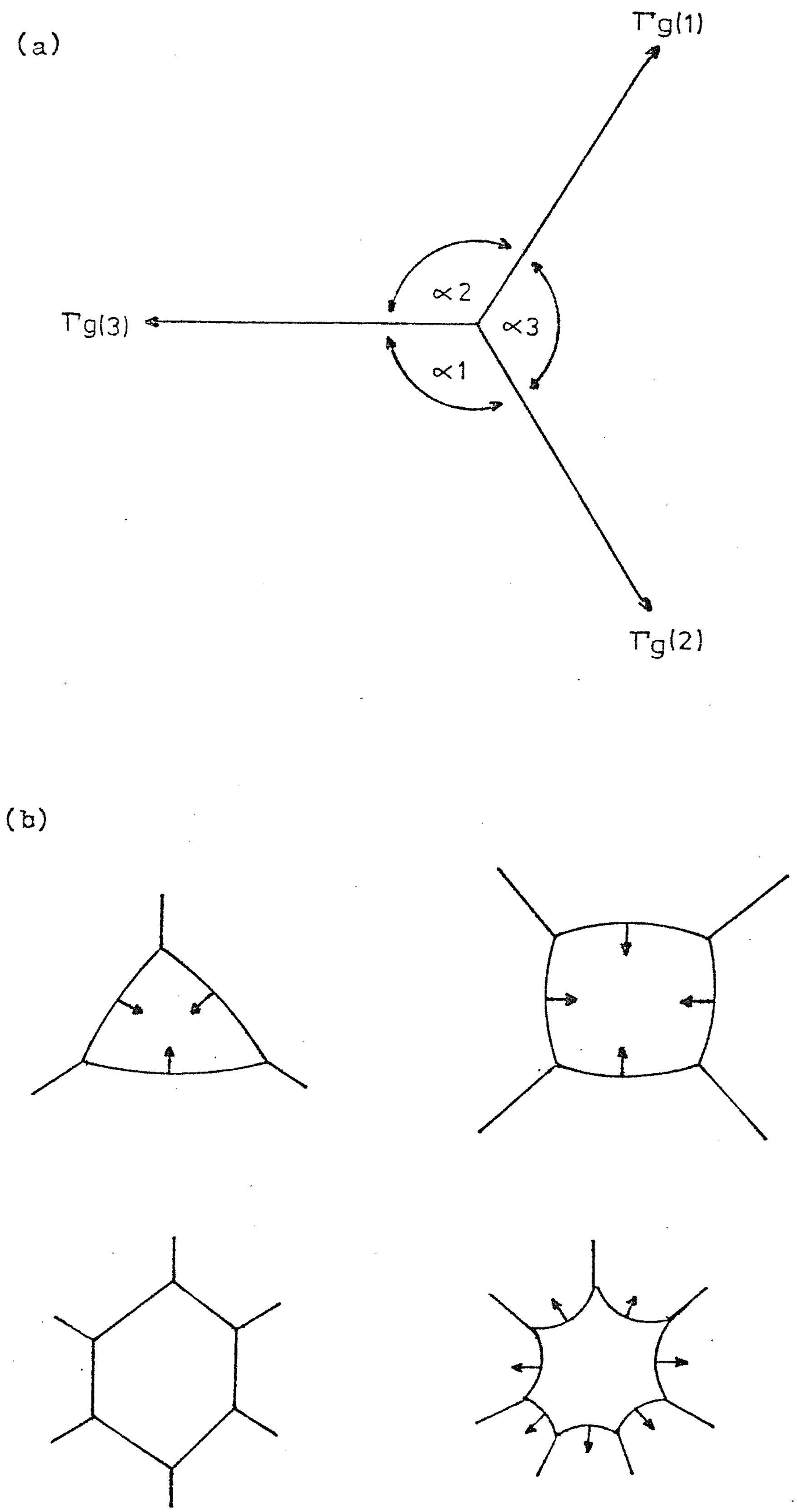

Figure 2.18(a) Equilibrium balance of grain boundary tensions at an intersection.

(b) Mechanism of grain boundary migration.

$$\frac{\Gamma g(1)}{\mathrm{Sin}\alpha_1} = \frac{\Gamma g(2)}{\mathrm{Sin}\alpha_2} = \frac{\Gamma g(3)}{\mathrm{Sin}\alpha_3} \qquad (2.3)$$

** $\Gamma g(1),(2)$ and (3) are the interfacial energies of the grain boundaries.

α_1, α_2 and α_3 are the appropriate dihedral angles.

In practice the interfacial energies, or tensions are usually very similar for a single phase metal and so the grain boundaries will tend to adopt an angle of $\sim 120^{\circ}$ to each other. Figures 2.18(b) shows the result of applying the triple point equilibrium situation to a variety of grain junctions in a polycrystalline material. It can be seen that grains with six sides can adopt the equilibrium condition with straight grain boundaries, but any other configuarion requires the grain boundaries to be curved. A simple resolution of forces shows that a curved grain boundary (radius of curvature R) is acted on by a force, Γ/R, towards its centre of curvature. The result of this is that, with sufficient thermal activation, all the curved grain boundaries in Figures 2.18(b) will tend to migrate towards their centre of curvature. This results in grain growth of the larger grains (>6 sides) and a corresponding shrinkage of the smaller grains, which eventually disappear. According to the thermodynamics of grain growth, the lowest internal energy will only be reached when all the grain boundaries are eliminated from the specimen, i.e. if the specimen becomes a single crystal. However, since the driving force for grain growth is merely the grain boundary interfacial energy, it can be seen that the driving force gradually decreases as grain growth proceeds. This eventually leads to an "ultimate grain size", which is normally a function of annealing temperature and specimen composition.

Several investigators [137-140] have studied the kinetics of grain growth and found that for any given temperature, the average grain diameter (D) depends on the time (t) according to the equation

$$D = k\,t^{n} \qquad (2.4)$$

where K and n are constants.

** To avoid confusion, Γ has been used throughout to represent interfacial energy, instead of the more usual γ.

2.5.2(a) Grain boundary pinning

If a dispersion of second phase particles are introduced into a single phase matrix, interactions will occur between the particles (or inclusions) and grain boundaries, resulting in reduced grain boundary mobility. According to Zener [141] the maximum force exerted by a single particle or a grain boundary is $\pi \; r \Gamma$, where r is the particle radius, and Γ is the grain boundary tension. From statistical analyses it can be shown that the number of particles intersecting unit area of a random plane is $3f/2\pi r^2$, where f is the volume fraction of particles. The maximum retarding force acting on unit area of a migrating grain boundary is therefore:

$$\frac{3f\,\Gamma}{2r} \tag{2.5}$$

From the previous section the driving force for grain growth ($\Gamma/\bar{R}$) can be approximated to:

$$\frac{2\Gamma}{\bar{D}} \tag{2.6}$$

where $\bar{D}$ is the mean grain diameter.

The situation where grain boundaries are effectively pinned is therefore obtained by equating the opposing forces, as shown in Figure 2.19.

$$\frac{3f\,\Gamma}{2r} = \frac{2\Gamma}{\bar{D}} \tag{2.7}$$

Thus the maximum grain size or limiting grain size deduced by Zener is:

$$\bar{D}_{max} = \frac{4r}{3f} \tag{2.8}$$

The main criticisms of the Zener model are, the use of the maximum restraining force for each particle, the failure to account for a volume fraction effect, and the failure to account for interactions with other attached grain boundaries. The net results is that the model tends to predict a much larger limiting grain size than is found experimentally.

In an attempt to overcome some of the shortcomings of the Zener

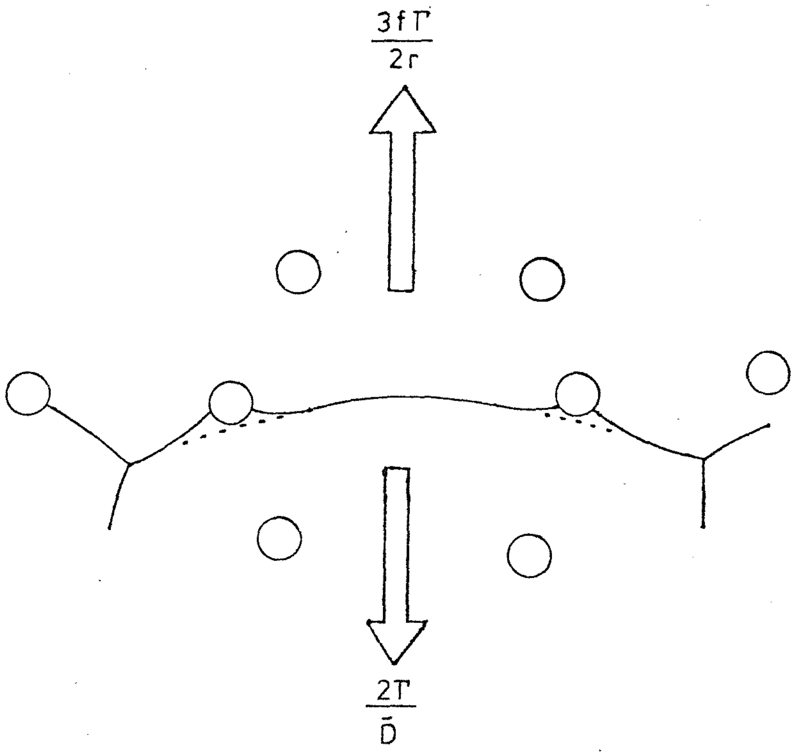

Figure 2.19 Zener model for grain boundary pinning.

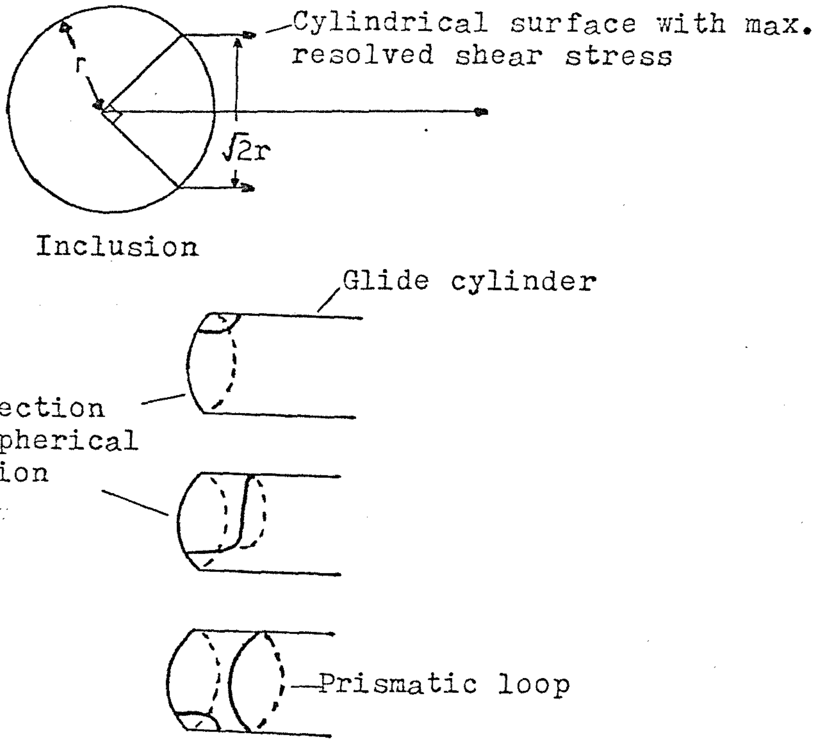

Figure 2.20 Mechanism of formation of prismatic dislocation loops around an inclusion.

model, Hellman and Hillert [142] reconsidered the theory of grain boundary pinning. The Hellman-Hillert theory incorporates a correction factor to take into account the relative positions of particles and grain boundaries. In addition the value for the driving force for normal grain growth is revised from that originally proposed by Zener.

The Hellman-Hillert model predicts a limiting grain radius given by:

$$R_o = \frac{4\ r}{9\ f\ \beta} \qquad (2.9)$$

The limiting grain diameter is thus

$$\bar{D}_{max} = \frac{8\ r}{9\ f\ \beta} \qquad (2.10)$$

where β (a correction factor) = $0.125\ \ell n\ \ \varphi/r$

φ = "unrestricted" grain size

The pinning theories have recently been tested for austenite grain boundary pinning in weld metals by Ferrante and Farrar [143]. In this investigation weld metals with widely differing deoxidation product volume fractions and size distributions were selected. Detailed quantitative electron metallography was carried out to characterise the inclusion distributions before subjecting the specimens to a re-austenitisation cycle of 5 minutes at 1250°C. A reasonable correlation between theoretically and experimentally determined austenite grain size was found for several weld metals. However, the correlation broke down when applied to weld metals with a large mean inclusion size and volume fraction (1200 ppm O). This may be due to some irregularity of the inclusion distribution at high oxygen contents, which would automatically lead to abnormal grain growth. In such an event the grain growth behaviour may be better understood in terms of Gladmans theory of unpinning [144].

2.5.3 Thermal contraction strain effects

During cooling after solidification a metal matrix containing a distribution of stable intermetallic or non-metallic particles will be subject to internal stresses, due to the differential thermal contraction effect. If the coefficients of thermal expansion of the matrix and inclusions are sufficiently different, and the temperature drop sufficiently large, the inclusions will act as nucleation sites for dislocations. A classic example of this mechanism is the work of Jones and Mitchell [145], who used spherical glass inclusions in a silver chloride crystal to generate prismatic dislocation loops during cooling, as shown in Figure 2.20. Another example of the differential thermal contraction effect is that given by Arrowsmith [146] which relates to NbC precipitates in an austenitic steel matrix.

Arrowsmith considered the spherical inclusions to be made up of elementary diametral cylinders of length L_o, which are considered stress free at the upper temperature. At some lower temperature the new length will be that resulting from both the thermal contraction and the elastic compressive stress, σ, built up on the ends of the element by the steel matrix.

i.e. $$L_T = L_o\,(1 - \alpha T) - \frac{\sigma}{E_1}\,L_o \qquad (2.11)$$

where E_1 is Youngs modulus of NbC

α is the expansion coefficient of NbC

At the same temperature the length of the steel "hole" L_T' is that resulting from thermal contraction and the elastic tensile stress, σ, built up on the ends by the carbide element.

i.e. $$L_T' = L_o\,(1 - \beta T) + \frac{\sigma}{E_2}\,L_o \qquad (2.12)$$

where E_2 is Youngs modulus for steel

β is the expansion coefficient of steel

For cohesion $L_T = L_T'$ and therefore the stress at the matrix-inclusion interface

$$\sigma = \frac{\beta - \alpha}{1/E_2 + 1/E_1} \cdot T \qquad (2.13)$$

It is interesting to note that the stress built up at the matrix-inclusion interface is independent of the inclusion radius. However, the criterion for yielding requires that the nucleating dislocation can be bent into a semicircle, radius r, given by:

$$\sigma = E\,\frac{b}{r} \qquad (2.14)$$

where E is Youngs Modulus

b is the Burgers vector

r is equal to $1/\sqrt{2}$ of the radius of the inclusion

It follows that the larger inclusions will act as more efficient nucleation sites for dislocation generation. In Arrowsmith's study it was shown that during cooling from 1300°C, large NbC particles of ∿2.5 μm diameter start to generate dislocations at about 1250°C, whereas small particles of ∿0.2 μm diameter general dislocation loops below about 740°C.

2.5.3(a) Dislocation generation in weld metals

Following the previous section it seems interesting to speculate on the possibility of dislocation generation in weld metals during continuous cooling. However, to carry out an accurate analysis of this type requires a detailed knowledge of the constitution, thermophysical and mechanical properties of the deoxidation products. A limited amount of information is available on the constitution of weld metal deoxidation products [56][61], obtained by Electron Probe Microanalysis (EPMA) and Energy Dispersive X-ray Analysis (EDAX) techniques. The general concensus is that acidic fluxes tend to deposit glassy manganese-silicate type deoxidation products whereas basix fluxes produce alumina rich inclusion types.

In view of the lack of detailed thermophysical data for weld metal deoxidation products a simplified calculation has been carried out based on pure alumina inclusions in a low carbon steel matrix.

From the previous section the stress developed at the matrix-inclusion interfaces during cooling is given by equation (2.13):-

$$\sigma = \frac{\beta - \alpha}{1/E_2 + 1/E_1} \cdot T$$

The values of expansion coefficients and Youngs moduli have been taken for 1100°C as this represents the approximate mean temperature between solidification and the start of the $\gamma \rightarrow \alpha$ transformation.

β = coefficient of expansion for steel at 1100°C
(9.6×10^{-6} °C)

α = coefficient of expansion for alumina at 1100°C
(6.1×10^{-6} °C)

E_2 = Youngs modulus for steel at 1100°C
(∿80 GPa)

E_1 = Youngs modulus for alumina at 1100°C
(∿380 GPa)

substituting in equation (2.13) gives

$$\sigma = 0.2313 \; T \;\; \text{MPa}$$

where T is the temperature drop. Assuming that the $\gamma \rightarrow \alpha$ transformation starts at about 700°C the maximum value of T will be about 800.

$$\therefore \; \sigma = 185 \; \text{MPa}$$

From section 2.5.3 the stress required to bend a dislocation is given by equation (2.14):-

$$\sigma = E \frac{b}{r}$$

where E is Youngs modulus
b is the Burgers vector
r is the radius of the dislocation glide cylinder = $1/\sqrt{2}$ radius of the inclusion

Therefore the minimum inclusion diameter that will nucleate dislocations during cooling, prior to the $\gamma \rightarrow \alpha$ transformation is $\sim$0.3 µm.

In practical terms this means that about 90% of the inclusions in a typical basic flux weld metal could be potential dislocation nucleation sites, if the properties of the alumina rich inclusions are similar to those of pure alumina. This represents a potential increase in dislocation density of about 10^7 per cm^2 (based on typical values for mean inclusion radius and numbers of inclusions per cm^3). Bearing in mind that a typical annealed metal has a dislocation density in the range 10^6 - 10^8 per cm^2, and a heavily deformed metal 10^{10} - 10^{12} per cm^2 [147], it would seem that the potential for dislocation multiplication is indeed significant.

Now if one reconsiders the same calculation for a glassy manganese-silicate type inclusion, it can be seen that there are two major factors limiting the stress build up at the matrix-inclusion interface. The values quoted for the expansion coefficient of $MnO:SiO_2$ do not vary greatly from those for Al_2O_3 and can therefore be considered of minor importance. Examination of the $MnO:SiO_2$ equilibrium phase diagram however, Figure 2.21 [148], shows a eutectic reaction at about 1250°C suggesting that the inclusions remain partially molten long after the steel has solidified. This has the effect of concentrating the thermal contraction stresses within the easily deformable inclusions during the initial stages of cooling. Upon further cooling below about 1250°C there is the

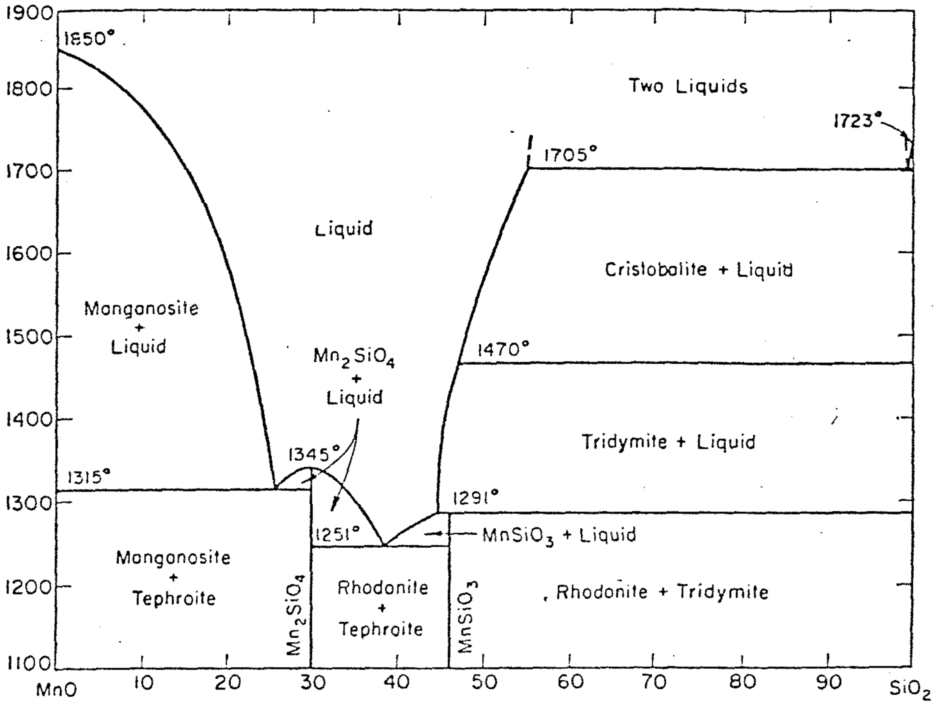

Figure 2.21 MnO-SiO_2 phase diagram (148)

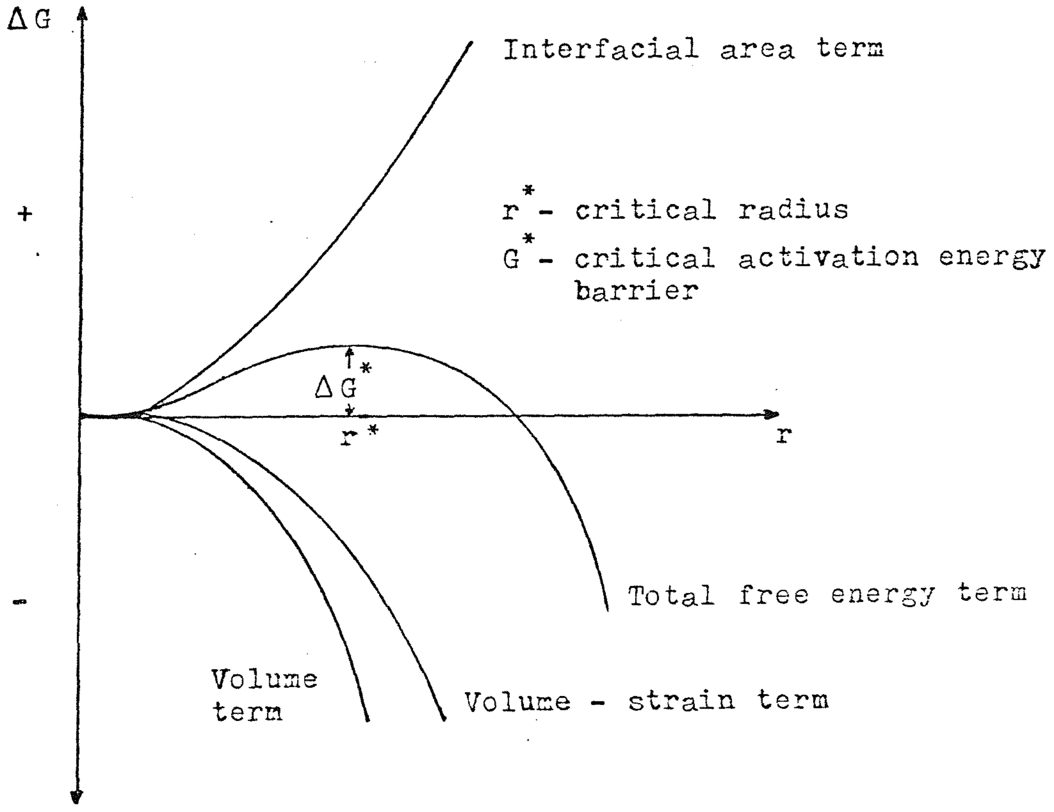

Figure 2.22 The variation of ΔG with r for homogeneous nucleation.

possibility of some matrix-inclusion stress build up, but this will be strongly dependent on the elevated temperature modulus of elasticity of the glassy inclusion which is likely to be very low during the initial stages of cooling.

2.5.4 Ferrite nucleation

In the classical theory of solid state homogeneous nucleation, the free energy associated with the nucleation process will be determined by the relationship between the volume, interfacial and strain energy terms in the following equation.

$$\Delta G = -V \Delta G_v + A\Gamma + V \Delta G_s \qquad (2.15)$$

where $V \Delta G_v$ is the volume free energy term

$A\Gamma$ is the interfacial free energy term

$V \Delta G_s$ is the misfit strain energy term

If the variation of Γ with interface orientation is neglected, and the nucleus is assumed spherical with radius r, the above equation becomes

$$\Delta G = -4/3\ \pi r^3 (\Delta G_v - \Delta G_s) + 4\ \pi r^2 \Gamma \qquad (2.16)$$

This expression is illustrated graphically for differing values of r in Figure 2.22. From this figure it can be seen that both the interfacial energy and the misfit strain energy terms increase the activation energy barrier for nucleation. Any nucleation site that provides a reduction in either of these terms will therefore be a favourable site for heterogeneous nucleation.

In weld metals the most commonly apparent nucleation sites for the $\gamma \rightarrow \alpha$ transformation are the γ grain boundaries.

Possible intragranular nucleation sites are likely to be γ subboundaries or twin boundaries, nonmetallic inclusions and dislocations, but at present the exact ranking of such sites is not clear.

2.5.4(a) Nucleation on grain boundaries

If the misfit strain energy term in equation (2.15) is ignored, the optimum shape for an incoherent grain boundary nucleus is that shown in Figure 2.23. From Figure 2.23 it can be seen that $\cos\theta = \Gamma_{\gamma\gamma}/2\Gamma_{\gamma\alpha}$, and for steel with high energy incoherent boundaries $\Gamma_{\gamma\gamma} \approx \Gamma_{\gamma\alpha}$ and therefore $\theta = 60^{\circ}$.

Again neglecting the strain energy term the free energy of the nucleus will be given by

$$\Delta G = -V\Delta G_V + A_{\gamma\alpha}\,\Gamma_{\gamma\alpha} - A_{\gamma\gamma}\,\Gamma_{\gamma\gamma} \qquad (2.17)$$

where $A_{\gamma\gamma}\Gamma_{\gamma\gamma}$ is the grain boundary energy destroyed during nucleation.

From above it can be shown that the normalised activation energy barrier for an unfaceted nucleus at a grain boundary

$$\frac{\Delta G^{*}_{het}}{\Delta G^{*}_{hom}} = S(\theta) \qquad (2.18)$$

where $S(\theta) = \frac{1}{2}\,(2 + \cos\theta)\,(1 - \cos\theta)^2$ (2.19)

For ferrite nucleation at an austenite grain boundary therefore

$$\frac{\Delta G^{*}_{het}}{\Delta G^{*}_{hom}} \approx 0.31$$

It should be appreciated that the activation energy barrier for nucleation may be reduced still further if faceted nuclei consisting of regions of partially or fully coherent interfaces are considered. Examples of such nuclei are the pillbox and pillbox-cum-spherical cap models discussed by Aaronson [19].

2.5.4(b) Nucleation on inclusions

Ricks and Howell [149] recently carried out a theoretical appraisal of nucleation on inclusions by assuming that the matrix /inclusion interface acts as an inert substrate. In this analysis a simple approach was adopted whereby the ferrite nucleus is considered to be an unfaceted spherical segment as shown in Figure 2.24. From this figure it can be seen that the volume of the nucleus is given by

$$v = 4/3\,\pi R^3 - 1/3\,\pi R^3\,(f\phi) + I^3(f\theta) \qquad (2.20)$$

where R is the nucleus radius

I is the inclusion radius

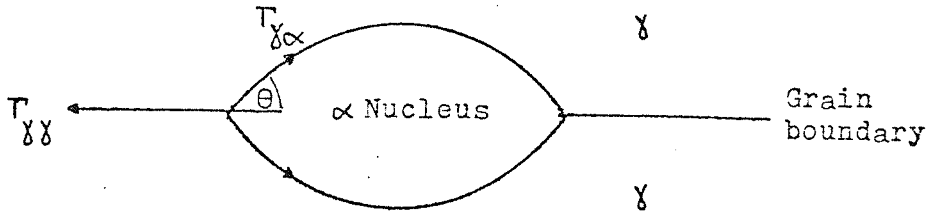

Figure 2.23 Critical nucleus for grain boundary nucleation.

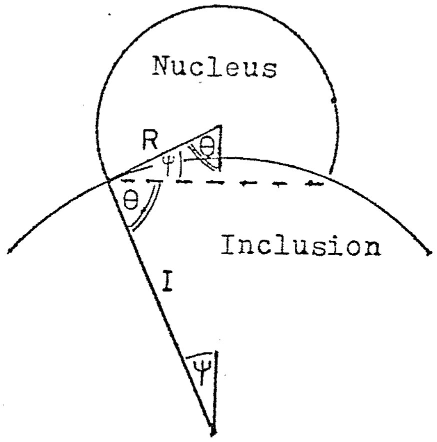

Figure 2.24 Model used to analyse inclusion nucleation after Ricks(149).

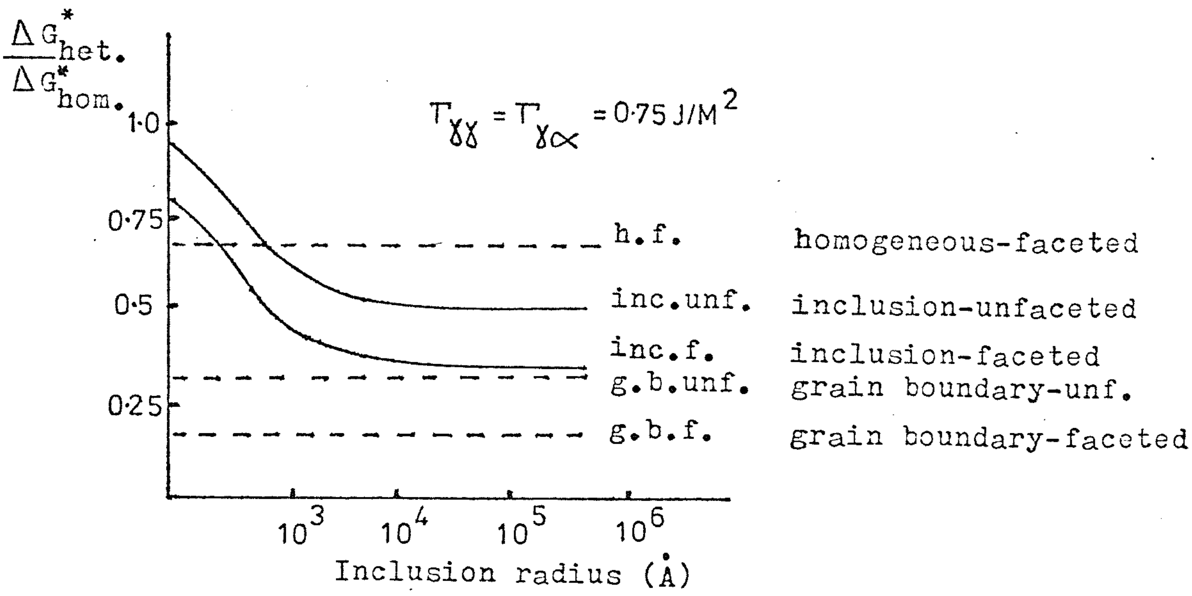

Figure 2.25 Normalised activation energy barriers for nucleation on inclusions and grain boundaries.

ψ and θ are as shown in Figure 2.24

$$f(\psi,\theta) = 2-3\cos(\psi,\theta) + \cos^3(\psi,\theta) \quad (2.21)$$

The increase in surface area of the nucleus is given by

$$A = 4\pi R^2 - 2\pi R^2 (1 - \cos(\psi)) \quad (2.22)$$

The total free energy change, ΔG_T, associated with nucleation may be written

$$\Delta G_T = V\Delta G_V + A\Gamma_{\gamma/\alpha} \quad (2.23)$$

where ΔG_V is the volume free energy change

$\Gamma_{\gamma/\alpha}$ is the interfacial energy of an incoherent γ/α phase boundary

By differentiating equation (2.23) with respect to R and equating to zero, the values for the critical activation energy barrier for nucleation may be obtained. These values are shown in Figure 2.25, in normalised form, as a function of inclusion radius.

The most interesting feature of this analysis is that the activation energy barrier for nucleation decreases with increasing inclusion size. Thus, very small inclusions would be much less effective as nucleation sites than large ones. It can also be seen from Figure 2.25 that grain boundary nucleation will always be much more favourable than inclusion nucleation.

2.5.4(c) Nucleation on dislocations

For some time it has been recognised that dislocations provide favourable nucleation sites for a variety of precipitation reactions. Several fairly recent studies have also highlighted the role of dislocations in the nucleation of polymorphic transformations such as $\gamma \rightarrow \alpha$ and δ-γ reactions in steels [150][151].

Cahn [152] considered a theoretical treatment of nucleation on dislocations and showed that the strain energy released by the dislocation during nucleation provided a significant contribution to the nucleation process. In this analysis the nucleus was assumed to be a cylinder lying along the core of the dislocation and bounded by an incoherent interface. The free energy associated with the formation of unit length of nucleus is given by

$$\Delta G = -A \ln r + 2\pi r\Gamma - \pi r^2 \Delta G_V \quad (2.24)$$

where A is the energy released by the dislocation

r is the radius of the cylindrical nucleus

Γ is the interfacial energy

ΔG_v is the volume free energy change.

The results of Cahn's analysis are shown in Figure 2.26 in which the normalised activation energy barrier for nucleation is plotted as a function of parameter α where

$$\alpha = \frac{G\, b^2 \Delta G_v}{2\pi^2\, \Gamma^2} \quad \text{for a screw dislocation} \qquad (2.25)$$

or

$$\alpha = \frac{G\, b^2 \Delta G_v}{2\pi^2 \Gamma^2 (1-v)} \quad \text{for an edge dislocation} \qquad (2.26)$$

G is the elastic shear modulus

b is the Burgers vector

v is Poisson's ratio

Substituting the values of G as 60 GPa, b as 2.5×10^{-10}m, v as 0.28, and Γ as 0.75 J/m^2 into equation (2.26) and assuming $\Delta G_v \approx 840$ J.mol^{-1} [170] for ferrite nucleation at about 600°C gives a value of $\alpha = 0.036$ or

$$\frac{\Delta G_{dns}}{\Delta G_{hom}} = 0.88$$

Ferrite nucleation on an individual dislocation is therefore favourable in comparison to homogeneous nucleation, but much less favourable than either the inclusion or grain boundary nucleation processes.

2.5.4(d) Nucleation on dislocation sub-boundaries

From the previous sections it is not difficult to appreciate that the suitability of sub-boundaries as nucleation sites will be intermediate with respect to high angle grain boundaries and individual dislocations. As a low angle dislocation sub-boundary consists simply of an array of dislocations, it should be possible to analyse nucleation either in terms of an extension of Cahn's analysis, or by considering the boundary as a normal grain boundary with a low interfacial energy.

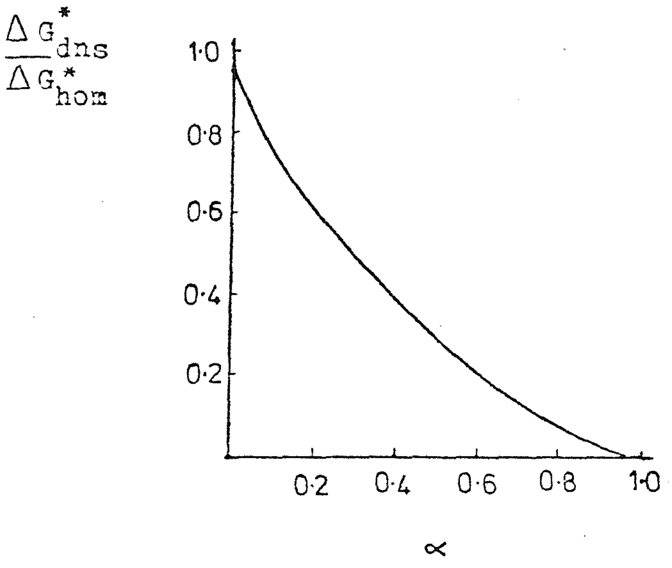

Figure 2.26 Normalised activation energy barrier for nucleation on dislocations as a function of parameter α after Cahn (152).

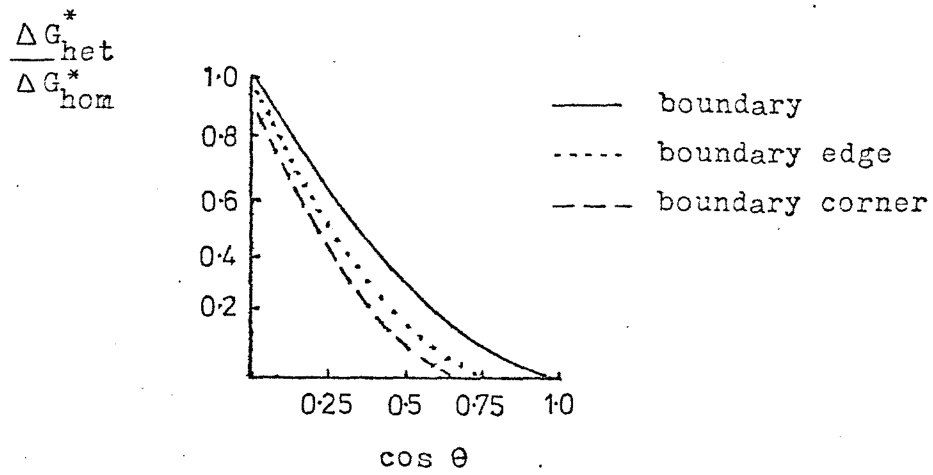

Figure 2.27 Normalised activation energy barriers for nucleation at boundaries, boundary edges and corners as a function of cos θ.

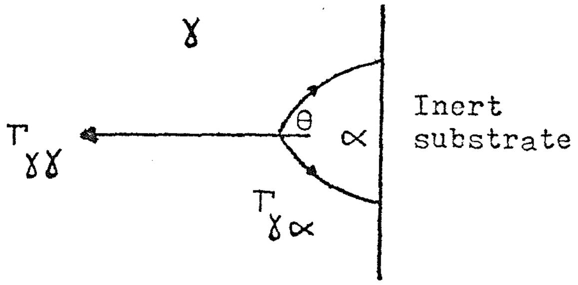

Figure 2.28 Critical nucleus for nucleation on a boundary in contact with an inert substrate.

For simplicity let us consider the sub-boundary to be a low angle tilt boundary consisting of an array of parallel edge dislocations in which the dislocation spacing is given by

$$D = \frac{b}{\sin\theta} \approx \frac{b}{\theta} \qquad \text{for small angles} \qquad (2.27)$$

From Cahn's analysis it can be shown that the length of the critical cylindrical nucleus will be similar to the radius of the critical homogeneous nucleus at low values of parameter α. Therefore

$$\ell \approx r^{*} = \frac{2\Gamma}{\Delta G_V} \qquad (2.28)$$

For the nucleation conditions under consideration ΔG_V is $\sim$840 J.mol^{-1} and Γ is 0.75 J/m^2 giving a critical nucleus length of about 125 Å. Having established a critical nucleus length and knowing the dislocation spacing of the sub-boundary, it is possible to consider the nucleation event in terms of the simultaneous release of strain energy from several dislocation cores. This analysis has been carried out for low angle dislocation sub-boundaries with misorientations, θ, of 2°, 5° and 10° respectively and the results are shown in Table 2.7.

The simpler alternative analysis may be carried out by substituting the relevant sub-boundary energy terms into the appropriate equations in section 2.5.4(a). Theoretical values of sub-boundary energy have been taken from McLean [153], based on the θ_M value of 28°, after the experimental results of Dunn [154] for silicon iron. The results of this alternative analysis are also shown in Table 2.7.

It can be seen that both treatments yield very similar results giving noramlised activation energy barrier values of 0.82, 0.66 and 0.48 for 2°, 5° and 10° misoriented sub-boundaries respectively. These results show that sub-boundaries can provide quite favourable sites for ferrite nucleation. However, even more favourable sites would be at the intersections of such boundaries as shown in Figure 2.27.

2.5.4(e) Nucleation on grain boundaries or sub-boundaries in contact with an inert substrate

In the previous sections we have seen that grain boundaries and

Sub-boundary mis-orientation θ	Dislocation Spacing D	Length of Critical Nucleus ℓ	No. of dislocations per nucleus	Cahn's parameter α	$\frac{\Delta G^{*}\text{sub}}{\Delta G^{*}\text{hom}}$
2^o	$71.6A^o$	$125A^o$	1.75	0.064	0.82
5^o	$28.7A^o$	$125A^o$	4.36	0.161	0.68
10^o	$14.4A^o$	$125A^o$	8.68	0.321	0.49
Sub-boundary misorientation θ	$\theta/\theta M$	E/EM	Interfacial energy[J/m^2 ($\times 10^3$)]	$\cos\theta$	$\frac{\Delta G^{*}\text{sub}}{\Delta G^{*}\text{hom}}$
2^o	0.071	0.21	157.5	0.105	0.84
5^o	0.179	0.46	345	0.23	0.66
10^o	0.357	0.72	540	0.36	0.48

TABLE 2.7: Calculation of activation energy barriers to nucleation for various sub-boundaries.

sub-boundaries, and inclusions all provide favourable sites for heterogeneous nucleation. In the former cases nucleation is aided by the elimination of an existing area of grain boundary or sub-boundary. In the latter case the interfacial energy of the nucleus is reduced due to the presence of the inert substrate. In the case of nucleation at a boundary in contact with an inert substrate, both these factors will operate making this an extremely favourable heterogeneous nucleation site. Figure 2.28 shows the critical nucleus for this situation, which can be seen to be similar to that in Figure 2.23.

The free energy of the nucleus may be expressed as follows:

$$\Delta G = -V\Delta G_V + A_{\gamma\alpha}\,\Gamma_{\gamma\alpha} - A_{\gamma\gamma}\,\Gamma_{\gamma\gamma} \qquad (2.29)$$

Using the following expressions for a spherical cap

volume $= \pi r^3(2 + 2\cos\theta)\,(1 - \cos\theta)^2/3$

surface area of curved surface $= 2\pi r^2(1 - \cos\theta)$

surface area of planar surface $= \pi r^2 \sin^2\theta$

and from section 2.5.4(a) $\cos\theta = \Gamma_{\gamma\gamma}/2\Gamma_{\gamma\alpha}$

it can be shown that

$$\Delta G = (-4/3\pi r^3\Delta G_V + 4\pi r^2\Gamma)[(2 + \cos\theta)(1-\cos\theta)^2/4] \qquad (2.30)$$

i.e. $$\frac{\Delta G^*_{het}}{\Delta G^*_{hom}} = (2 + \cos\theta)(1-\cos\theta)^2/4 \qquad (2.31)$$

Substituting the relevant values for a high angled grain boundary, and 10°, 5° and 2° sub-boundaries, gives normalised activation energy barriers of ∿0.16, 0.24, 0.33 and 0.42 respectively. Thus it can be seen that nucleation sites consisting of both a boundary and inert substrate component, provide a considerable advantage over normal boundary, or inert substrate nucleation.

In weld metals the inclusions provide the inert substrates, and it can be seen from section 2.5.4(b) that large inclusions (>10 μm dia) equate to the infinite substrate used in the present model. As the inclusion diameter decreases the nucleation activation energy barrier is expected to increase, in a similar manner to that of a spherical nucleus shown in section 2.5.4(b). The implications of this model can now be considered.

In a weld metal containing a large volume fraction of large inclusions it may be expected that inclusions in the austenite grain boundaries will provide a significant nucleation advantage over normal grain boundary nucleation. Thus the temperature at which the $\gamma \rightarrow \alpha$ transformation initiates may be expected to be higher than for normal grain boundary nucleation. In weld metals containing fewer or smaller inclusions, this enhanced nucleation effect will be less significant and the transformation temperature will be lower.

Enhanced nucleation may also be significant for intragranular sites. If inclusions are "hard" and produce large matrix-inclusion strains, as discussed in section 2.5.3, the inclusions may be associated with sub-boundaries, which will provide a nucleation advantage over other intragranular sites. Thus the temperature at which the intragranular $\gamma \rightarrow \alpha$ transformation initiates may also be expected to be higher than for normal intragranular nucleation.

2.5.5 Summary

In the previous sections it has been shown that inclusions can influence weld metals in several ways.

Firstly, it would seem that the austenite grain growh behaviour is influenced as predicted by the pinning theories, provided the inclusion size is not excessively large. Pinning may therefore be expected to be significant in reheated weld metals, particularly when large heat inputs are used. Whether pinning is significant during cooling is uncertain, as the austenite grain structure develops by a nucleation and growth process, during the decomposition of delta ferrite. The large austenite grain structure thus formed is presumably stable, and it is doubtful whether significant grain growth occurs during cooling.

Secondly, there is a high probability that certain inclusion types can significantly increase the dislocation density of austenite, by a differential thermal contraction mechanism. This increased dislocation density may be important in influencing the subsequent $\gamma \rightarrow \alpha$ transformation. For example it has been postulated previously that a dislocation substructure may assist the nucleation of acicular ferrite [56].

Finally, most types of nucleation sites have been reviewed, being of fundamental importance to weld metal transformation behaviour. The results of this analysis are shown in Figure 2.29, which compares the normalised activation energy barriers for heterogeneous nucleation sites, assuming unfaceted nuclei. From this figure it can be seen that inclusions associated with austenite grain boundaries provide one of the most potent nucleation sites. These sites are substantially more favourable than grain boundaries on their own. Similarly, intragranular inclusions associated with sub-boundaries also provide favourable nucleation sites which are more favourable than either sub-boundaries or inclusions on their own.

It may therefore be postulated that inclusion distributions influence ferrite nucleation in the following ways:-

(1) Large volume fractions of large inclusions make grain boundary nucleation more energetically favourable.

(2) Highly straining inclusions make intragranular nucleation more energetically favourable.

Both these factors are due to the combined effects of reduced interfacial area and favourable strain energy terms during nucleation.

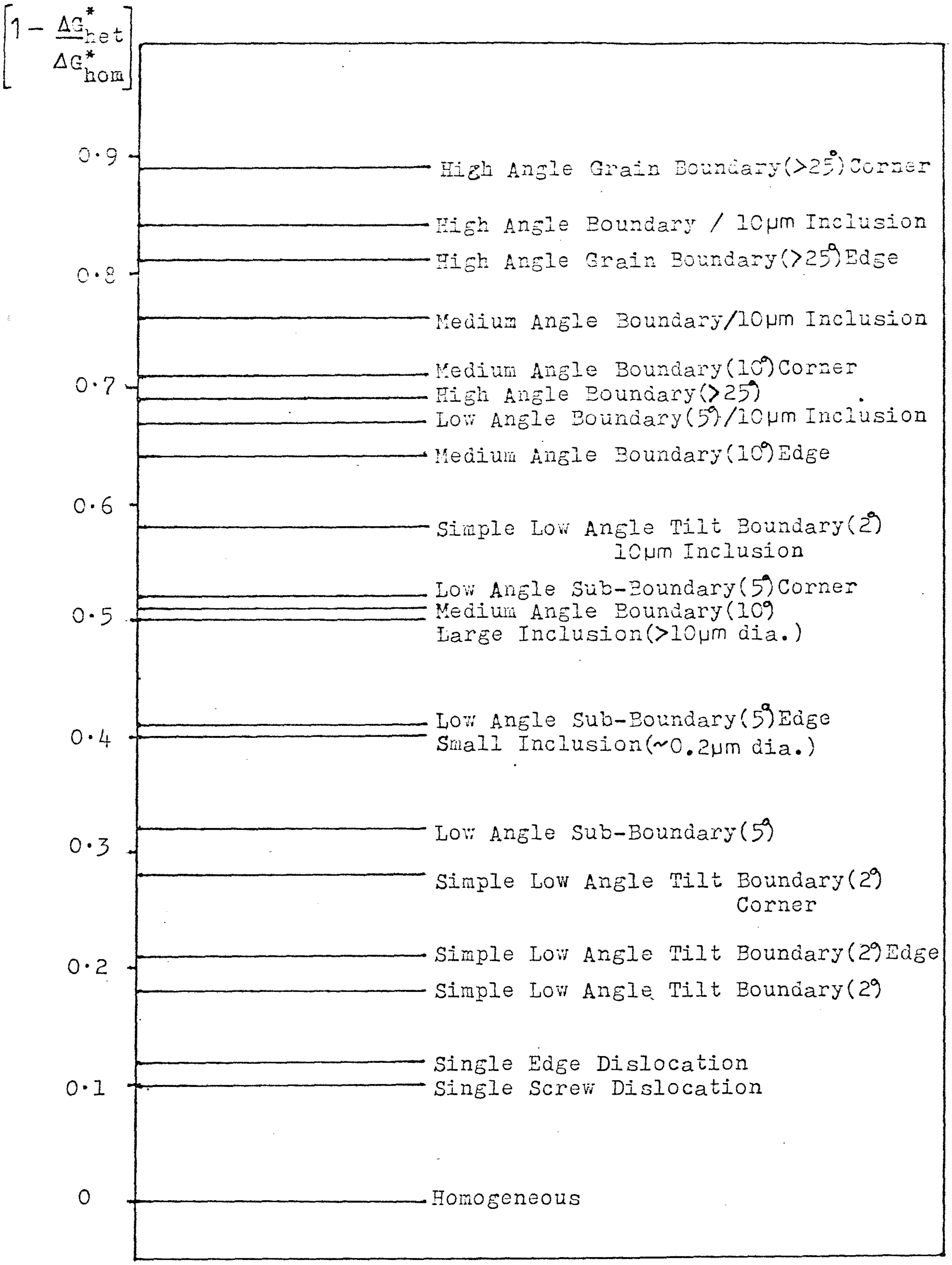

Figure 2.29 Normalised activation energy barriers for nucleation at various heterogeneous sites.

CHAPTER 3: EXPERIMENTAL TECHNIQUES

3.1 Introduction

The importance of being able to produce CCT diagrams that accurately describe the transformation behaviour and microstructure of weld metals has been previously discussed. To achieve this it was decided to use a combination of dilatometric, thermal analysis and quantitative metallographic techniques.

The main objectives of the experimental work are summarised as follows:-

(1) To produce CCT diagrams applicable to weld metals which would elucidate the relative positions, in temperature and time, of the typical weld metal microstructural constituents - acicular ferrite, proeutectoid ferrite, ferrite sideplates and bainite.

(2) To relate the new weld metal CCT diagrams to existing CCT diagrams for weld HAZ structures.

(3) To relate changes in chemical composition (in particular Mn, Ni, Nb, C and Mo) to the final weld microstructure by comparing several CCT diagrams of different chemical composition.

(4) To examine the influence of prior austenite grain size on weld metal $\gamma \rightarrow \alpha$ transformation behaviour.

(5) To examine the influence of oxygen-rich inclusion content on weld metal $\gamma \rightarrow \alpha$ transformation behaviour.

3.2 Selection of Materials

Two considerations affected the selection of suitable weld metal materials for examination. The first and most important consideration was to ensure isolation of only one variable at a time, be it alloy content, austenite grain size or inclusion content. The second consideration was to keep as close as possible to practical every day welding situations, so that any resulting CCT data would be of direct practical importance.

The alloying elements of principal interest were Mn, Ni and Nb and three series of welds were produced to examine these elements.

3.2.1 Manganese

Current practice for depositing C-Mn weld metals, with good notch toughness, is to use a basic flux and produce weld metal of approximate chemical composition:-

0.05 - 0.1 wt%C   0.2 - 0.7 wt%Si   1.0 - 1.7 wt%Mn

To study the influence of manganese it was therefore decided to investigate a series of MMA weld metals, based on the AWS 7016 classification, (BS639:type E51 56B 24(H)) with manganese content ranging from ∿0.5 - 2.0 wt%Mn.

The actual welding consumables used to produce the undiluted all weld metal specimens were as follows:

Electrode designation (ESAB electrodes)	Wt % Mn (aim)	Flux type
Experimental electrode (OK HYTRODE 7016 with reduced manganese content)	0.5	$CaCO_3/CaF_2$ basic flux low hydrogen (without iron powder)
OK HYTRODE 7016	1.0	$CaCO_3/CaF_2$ basic flux low hydrogen (without iron powder)
OK HYTRODE 7016/1	1.5	$CaCO_3/CaF_2$ basic flux low hydrogen (without iron powder)
OK HYTRODE 7016/2	1.7	$CaCO_3/CaF_2$ basic flux low hydrogen (without iron powder)
OK HYTRODE 7016/3	1.8+	$CaCO_3/CaF_2$ basic flux low hydrogen (without iron powder)

3.2.2 Nickel

When good low temperature fracture toughness properties are required in welded high yield strength low alloy steels, it is often common practice to utilise nickel bearing weld metals.

To study the influence of nickel a series of MMA weld metals, based on the AWS 8018 type elctrodes, was chosen with nickel contents ranging from trace to 3.5 wt%Ni.

The actual welding consumables used were as follows:-

Electrode designation (ESAB electrodes)	Wt % Ni (aim)	Flux type
Experimental electrode (OK 8018-C1 without Ni i.e. "7018" type)	-	$CaCO_3/CaF_2$ basic flux low hydrogen with ∿10% iron powder
Experimental electrode (OK 8018-C1 with reduced Ni content)	1.0	$CaCO_3/CaF_2$ basic flux low hydrogen with ∿10% iron powder
OK 8018-C1	2.5	$CaCO_3/CaF_2$ basic flux low hydrogen with ∿10% iron powder
OK 8018-C2	3.5	$CaCO_3/CaF_2$ basic flux low hydrogen with ∿10% iron powder

3.2.3 Niobium

Niobium is not normally added deliberately to low-alloy steel weld metals, but in some circumstances it may be introduced through dilution from the parent plate. Typically this may happen when Nb bearing HSLA steel components are welded with a high heat input process, such as submerged arc welding.

To investigate the influence of niobium a series of submerged arc welds were deposited on Nb bearing and Nb free base plates using two flux systems.

The details of welding consumables used are given below.

Plate	Wire	Wt % Nb (deposit)	Flux
Nb free	SD3 (oerlikon)	-	OP41TT (oerlikon)
0.06% Nb	SD3	0.03%	OP41TT
Nb Free	SD3	-	Experimental (503)
0.06% Nb	SD3	0.02%	Experimental

In addition to the C-Mn, C-Mn-Ni and C-Mn-Nb series of weld metals one further composition was investigated. This was a C-Mn-Ni-Mo weld metal typical of that used for welding types A508 or A533 steels, for the nuclear power industry. The submerged arc weld was produced with Babcock 10B wire and Union Carbide 709.5 flux.

To investigate the influence of oxygen-rich inclusion content, two of the submerged arc weld metals from the C-Mn-Nb series were remelted under an inert atmosphere. This had the effect of reducing the weld metal oxygen content without significantly changing the chemical analysis of any of the other elements.

3.3 Welding Procedures

3.3.1 Manual metal arc welds

The C-Mn and C-Mn-Ni series of weld metals were all produced under the following identical welding conditions.

(1) Weld geometry - A Single 60° V groove preparation was chosen as shown in Figure 3.1. The 22.2 mm (7/8 in.) thick x 450 mm (∿18 in.) x 130 mm (∿5 in.) mild steel plates were buttered with two layers of weld metal to prevent dilution from the plate. Backing bars of dimensions 9.5 mm (3/8 in.) thick x 500 mm (∿20 in.) x 50 mm (∿2 in.) were used with a root gap of 12-15 mm*, to allow easy access of the 4 mm welding electrodes.

(2) Welding current - 140 A
(3) Welding voltage - 26 v (Electrode +ve)
(4) Welding speed - 6" per min.
(5) Heat input - 1.4 KJ/mm
(6) Interpass temperature - <200°C
(7) No. of passes - 14

3.3.2 Submerged arc welds

All the two pass submerged arc welds used in the investigations of the C-Mn-Nb system were deposited under identical welding conditions. The practical conditions described in detail by Watson [57] are summarised below:

---

* Weld M2 had a 5 mm root gap.

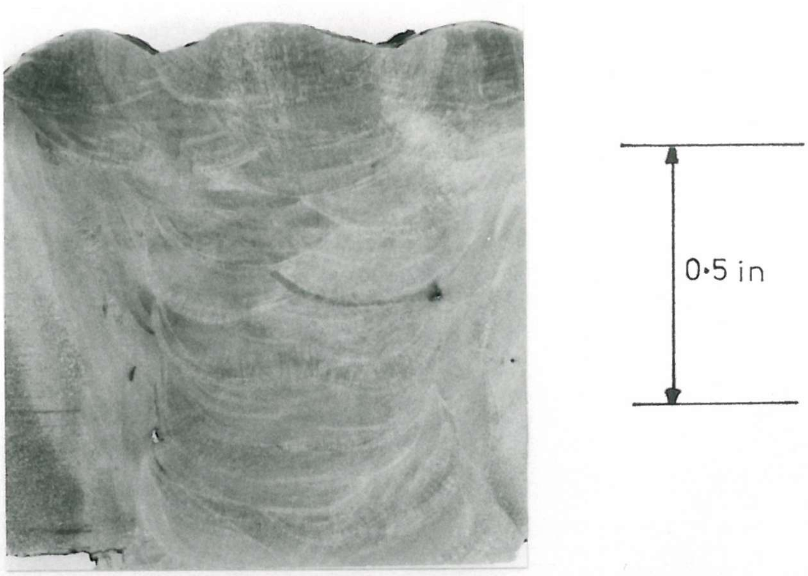

Figure 3·1 Multipass MMA weld

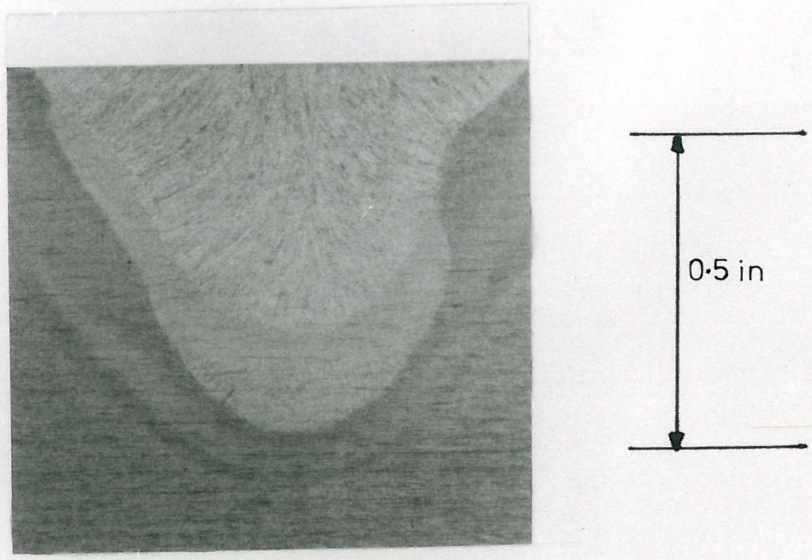

Figure 3·2 Two pass SA weld

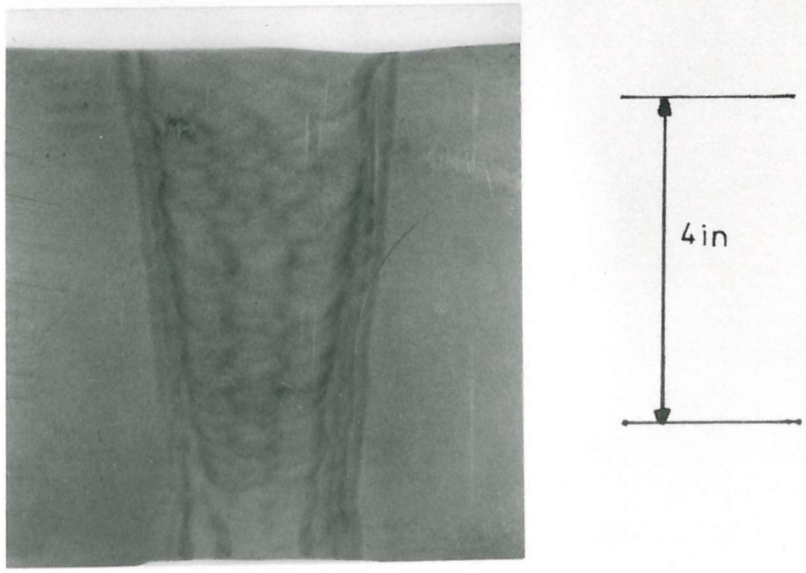

Figure 3·3 Multipass SA weld

(1) Weld geometry - 12.7 mm (½ in.) 60°"V" Grooves were machined in the 25.4 mm (1 in.) thick base plates to take the weld deposits, as shown in Figure 3.2

(2) Flux - Two flux types were used: OP4ITT and 503, each flux being dried for 16 hrs. at 150°C before use.

(3) Wire - SD3

(4) Welding current and voltage - 550A, 28V.

(5) Travel speed - 254 mm min^{-1} (10 in. min^{-1})

(6) Heat input - 3.6 KJ/mm.

(7) Preheat - Not used

(8) Interpass temperature - < 100°C.

The C-Mn-Ni-Mo weld deposit is illustrated in Figure 3.3 and was produced under the following conditions.

(1) Weld geometry - Single V groove preparation, with backing bar, in 6½" thick plate. The plate was initially buttered with two layers of weld metal using Babcock H1 MMA electrodes.

(2) Flux - Union Carbide type 709-5 dried for 2 hrs. at 150°C.

(3) Wire - Babcock type 10B (3.2 mm dia.)

(4) Welding current - 400-600A
and voltage - 32-36V (DC +ve)

(5) Travel speed - 200 - 300 mm/min.

(6) Heat input - ∿4KJ/mm

(7) Preheat - 150°C

(8) Interpass temperature - < 250°C.

(9) No. of passes - 101

3.4 Weld Cooling Rate Acquisition

Cooling rate data was obtained for the C-Mn-Nb series of welds during the welding procedure by manually inserting specially selected thermocouples into the weld pool during the second pass. The thermocouples used were Pt6%Rh, Pt30%Rh with recrystallised alumina twin-bore insulators. The cooling rate data obtained is summarised as follows; (cooling rates between 800°C and 500°C having been considered to make comparison with other work possible), A0-(6.3°C/sec), E0-(3.2°C/sec), A5-(9.1°C/sec), and E5-(14.0°C/sec).

3.5 Weld Metal Remelting

In order to isolate the effect of inclusion content on weld metal transformation behaviour it was decided to remelt certain samples of weld metal in an inert atmosphere. It was hoped that this remelting technique would allow some of the "frozen in" deoxidation products to be removed from the molten metal without significantly altering its overall chemistry.

The two weld metals selected for remelting were taken from the C-Mn-Nb series of welds and were considered to be fairly typical of medium and high oxygen weld metal deposits.

Remelting was carried out in a non-consumable tungsten arc furnace keeping the charge molten for approximately 30 sec.

3.6 Weld Metal Chemical Analysis and Identification

All the weld metals used in the investigation were analysed using standard spectrographic techniques. In addition, vacuum fusion analyses were carried out for the gaseous elements, oxygen and nitrogen.

Identification of the various welds was as follows:-

Identification No.	Weld Metal Details
C-Mn Series	
M1	OK HYTRODE 7016 with reduced Mn
M2	OK HYTRODE 7016
M3	OK HYTRODE 7016/1
M4	OK HYTRODE 7016/2
M5	OK HYTRODE 7016/3
C-Mn-Ni Series	
N1	OK 8018-C1 without Ni
N2	OK 8018-C1 with reduced Ni
N3	OK 8018-C1
N4	OK 8018-C2
N4A	OK8018-C2 (Mn trimmed)
C-Mn-Nb series	
AO	Plate A welded with OP4ITT flux
EO	Plate E welded with OP4ITT flux
A5	Plate A welded with 503 flux
E5	Plate E welded with 503 flux

Plate A and E were Nb free and Nb bearing respectively.

C-Mn-Ni-Mo NMo	Babcock 10B/Union Carbide 709.5
Remelted weld metals EO(r) E5(r)	 As EO above As E5 above

3.7 Electron Probe Microanalysis (EPMA)

Quantitative electron probe microanalysis was carried out to determine the approximate chemical composition of typical weld metal inclusions in the two Nb bearing weld metals (EO and E5).

In each case a suitable large inclusion (>5μm diameter)was chosen, and identified with a microhardness indentation.

Eight elements were selected for analysis as follows:

Aℓ, Fe, Ti, Mn, Nb, Si, Ca and S.

Oxygen was assumed to account for the balance of the analyses.

The raw data was corrected for absorption, atomic number and fluorescence effects using a computer programme developed by Gillham [155] and based mainly on the data of Salter [156].

3.8 Specimen Preparation

All three types of specimens used in the experimental work were machined from the weld metal. In the case of the multipass welds, specimens were taken from the weld centre line, well away from the root region. In the case of the two pass submerged arc welds the specimens were taken from the columnar region of the second pass (top run) of the weld deposit.

3.8.1 Theta dilatometer specimens

The specimen geometry used with the Theta high speed dilatometer was a hollow cylinder ∿5 mm outside diameter x 3 mm inside diameter x 7 mm long. To enable faster cooling rates to be achieved the wall thickness was reduced to ∿0.5 mm. Typically, cooling rates of up to ∿500^{o}C/sec could be produced by helium quenching the latter type of specimens.

A typical Theta dilatometer specimen is illustrated in Figure 3.4.

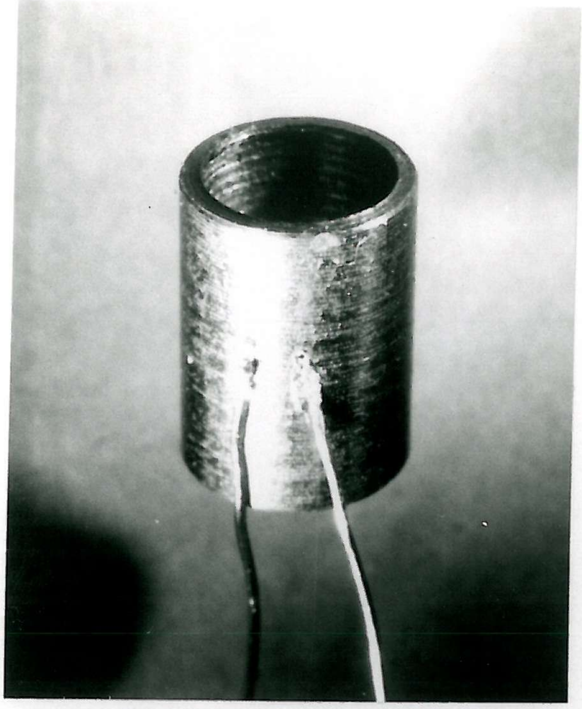

Figure 3·4 Theta dilatometer specimen and thermocouple arrangement.

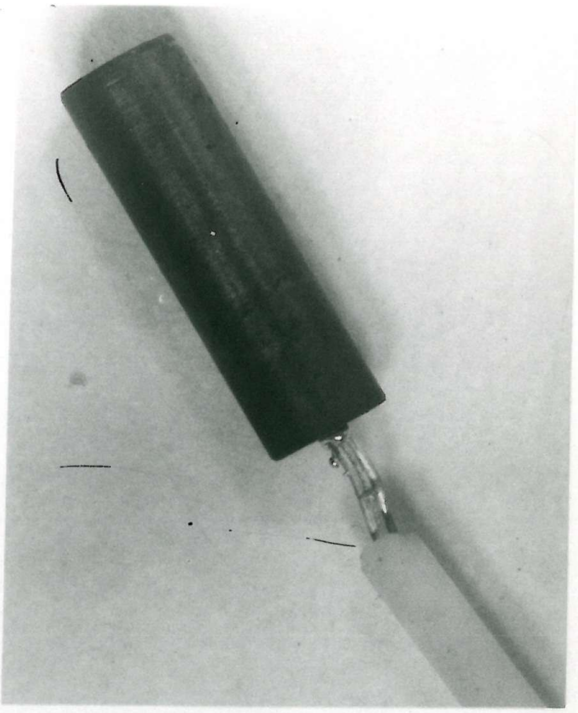

Figure 3·5 Linseis dilatometer specimen and thermocouple arrangement.

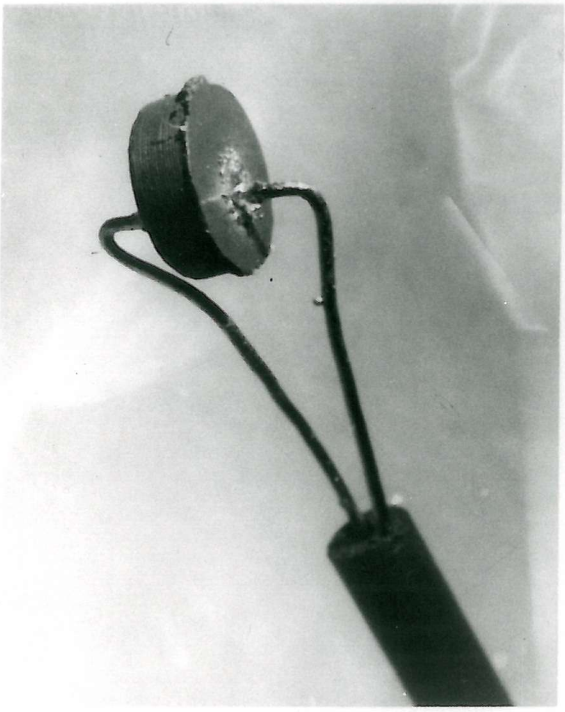

Figure 3·6 Thermal analysis specimen and thermocouple arrangement.

Figure 3·7 Linseis dilatometer specimen holder tube and internal piston.

3.8.2 Linseis dilatometer specimens

The recommended specimen geometry for the Linseis dilatometer used in the investigation was a solid cylinder 3 mm diameter x 10 mm long. These dimensions allowed a reasonable compromise to be achieved between maximum cooling rate and a reasonable dilatation of the specimen during the phase transformation.

Accordingly solid cylindrical dilatometer specimens 3 mm x 10 mm were produced as illustrated in Figure 3.5. In practice these specimens allowed cooling rates up to 80°C/sec to be achieved with a typical dilatation during the $\gamma \rightarrow \alpha$ transformation of 35-40 µm.

3.8.3 Thermal analysis and "quenching out" specimens

For extremely fast cooling rates, thermal analysis specimens of the type described by Habraken and Economopoulos [38][157] were produced, Figure 3.6.

These specimens were thin discs 3 mm diameter and from ½-1 mm thick, depending on the required cooling rate. In practice, cooling rates of up to 1200°C/sec were achieved with these specimens.

3.9 Thermal Etching

In some circumstances determination of prior austenite grain size can be very difficult once the $\gamma \rightarrow \alpha$ transformation products have formed. A good example of this is the polygonal ferrite/coarse Widmanstätten ferrite type structure which often occurs in weld metals of low carbon and alloy content (Figure 4.57 (c)).

A satisfactory solution to this problem is to pre-polish a flat surface on the specimen and allow the austenite grain boundaries to "groove" by diffusional processes during the austenitisation period at high temperature.

This technique was employed extensively in the experimental work using temperatures ranging from 1050°C - 1450°C and either high vacuum ($<1\times10^{-4}$ torr), or high purity argon atmospheres.

3.10 Austenite Grain Coarsening

A combination of the thermal etching and nital etching techniques were used to examine the austenite grain coarsening behaviour of a typical C-Mn MMA weld metal.

The material chosen for this exercise was the Hytrode 7016-1 weld metal (M3) of composition 0.06 Wt%C, 0.36 Wt%Si, 1.57 Wt%Mn with an oxygen content of 295 ppm.

Several thermal cycles were employed in this investigation. In all cases linear heating and cooling rates ($\sim 22^{\circ}$C/sec) to and from the holding temperature were employed.

The various hold times and temperatures were as follows:

10 sec. at 1250, 1300, 1350, 1400 and 1440°C

100 sec. at 1050, 1150 and 1250°C

In addition to the γ grain size measurements a second set of specimens, of the same material, were subjected to identical thermal cycles to determine their $\gamma \rightarrow \alpha$ transformation temperatures by dilatometry.

3.11 Dilatometry

The use of the dilatometric technique to monitor the $\gamma \rightarrow \alpha$ phase transformation in steels has been reviewed in the previous chapter and a detailed discussion of the errors and limitations of the method is contained in the Appendix.

The experimental details of the two dilatometers used in the present investigation are given below.

3.11.1 Linseis dilatometer (classical type)

A standard commercially available Linseis dilatometer was used, with slight modification to allow for the wider range of cooling rates necessary in this investigation. The 3 mm diameter specimen size allowed reasonably high cooling rates to be achieved.

The dilatometer consists of a quartz glass specimen holder tube, inside diameter >3 mm, and a quartz glass piston tube, <3 mm diameter, which is free to slide inside the specimen holder tube. The arrangement is illustrated in Figure 3.7. As the temperature changes, the length change in the specimen is transmitted via the piston to a transducer. After amplification, the electrical signal is fed to one channel of an x-y chart recorder, the other channel being the output of the specimen thermocouple. A typical dilatation versus specimen thermocouple e.m.f. curve produced by this method is shown in Figure 3.8. It can be seen that the temperature range of the phase transf-

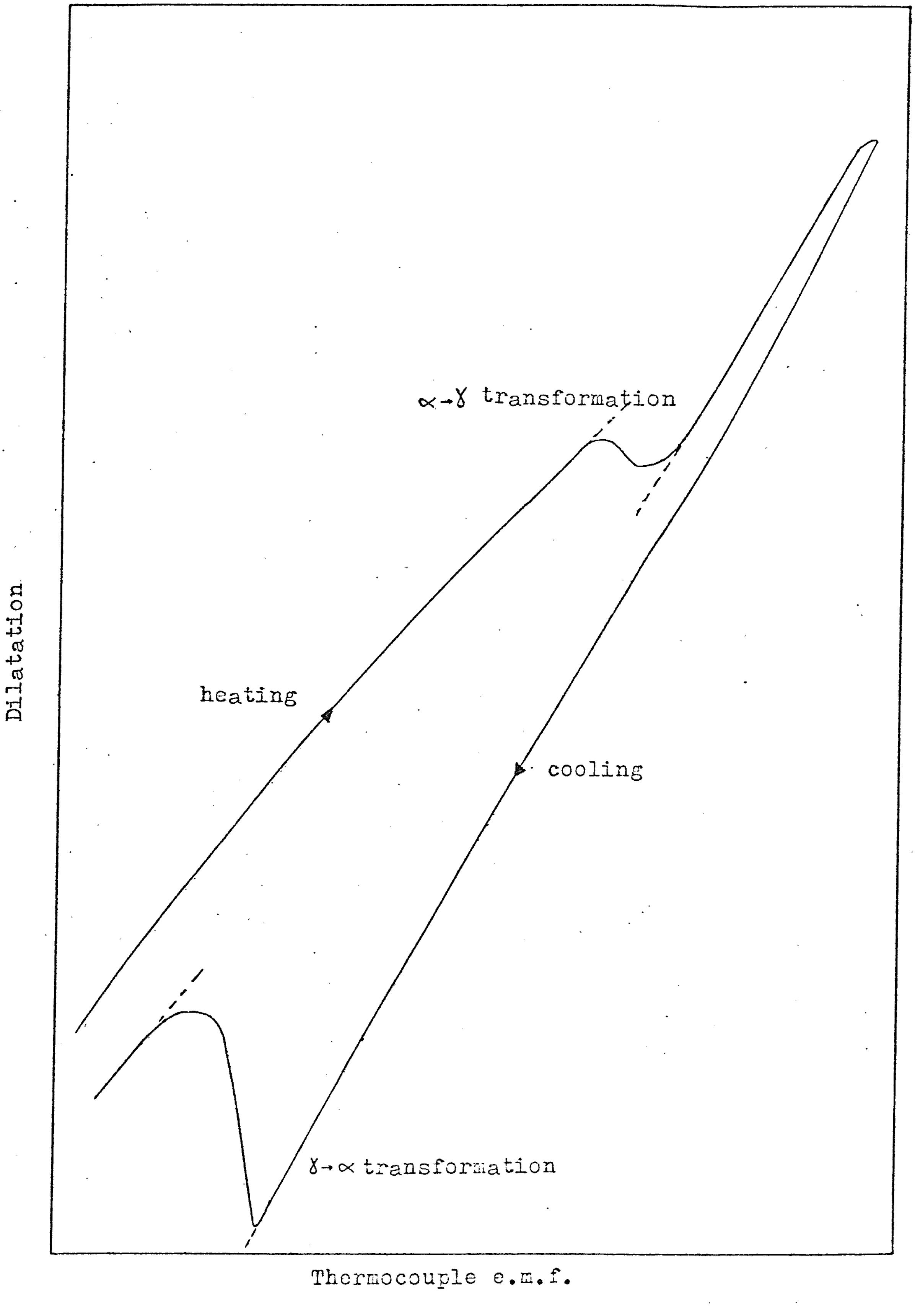

Figure 3.8 Typical dilatation versus thermocouple e.m.f. plot for steel specimen.

ormation can be obtained directly from this plot. The methods of interpretation of dilatometric data were discussed in Chapter 2.

Temperature measurement of the specimen is achieved by using platinum/platinum 10% rhodium thermocouples capacitance discharge welded to one end of the specimen (Figure 3.5). This ensures, as far as possible, that it is the temperature of the specimen and not the thermocouple and surroundings that is recorded when high cooling rates are used. The output from the thermocouple in addition to being fed to one channel of the x-y recorder is also fed to an x-t recorder to give a record of the cooling data necessary for the construction of the CCT diagram.

To prevent contamination of the specimen at high temperature, the specimen holder tube is vacuum purged and filled with high purity helium. The pressure is such as to prevent a positive pressure being built up when the specimen is brought up to temperature.

Temperature control is achieved through the temperature controller, which is programmable to heat and cool the furnace at linear rates between 0.1°C/min and 50°C/min. The furnace is of a low heat capacity to ensure that the temperature gradients between specimen and heating element remain small.

Cooling rates above $\sim 1^{\circ}$C/sec are obtained by air quenching the quartz glass specimen holder. This is done either by withdrawal from the furnace for the fastest cooling rates or from within the furnace for intermediate cooling rates. The full range of cooling rates obtainable varies from 0.0015°C/sec to about 80°C/sec.

Figures 3.9 and 3.10 illustrate the dilatometer with its temperature control equipment, chart recorders and gas quenching attachment.

3.11.2 Theta dilatometer

In addition to the standard Linseis dilatometer, much of the experimental dilatometric data was generated on a high speed Theta dilatometer, (Figure 3.11) which offered several important advantages in terms of capabilities and productivity.

The Theta dilatometer utilises hollow cylindrical specimens which can be cooled very rapidly by passing a suitable quenching gas through the centre of the specimens.

Hollow quartz or alumina tubes are used to hold the specimen in position inside the small radio frequency (R.F.) induction furnace,

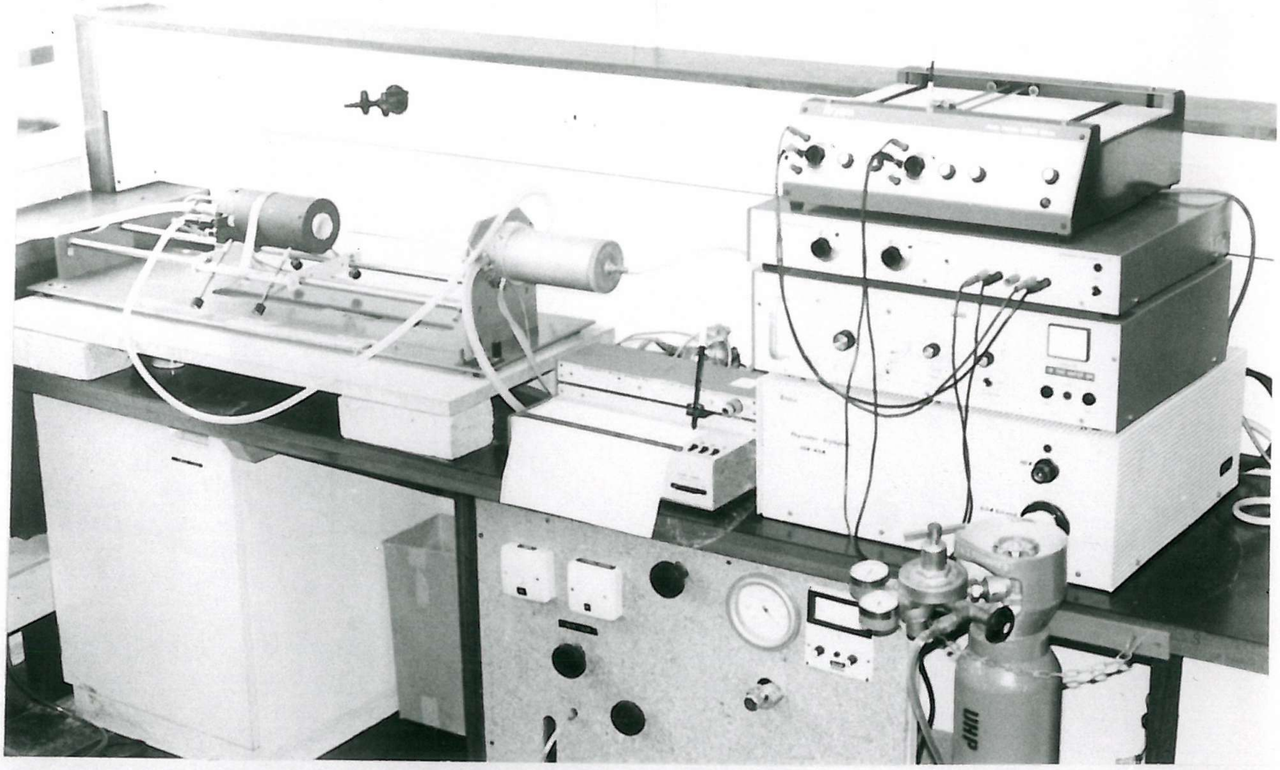

Figure 3·9 Arrangement of dilatometer, temperature controller, chart recorders and atmosphere control system. (Linseis system).

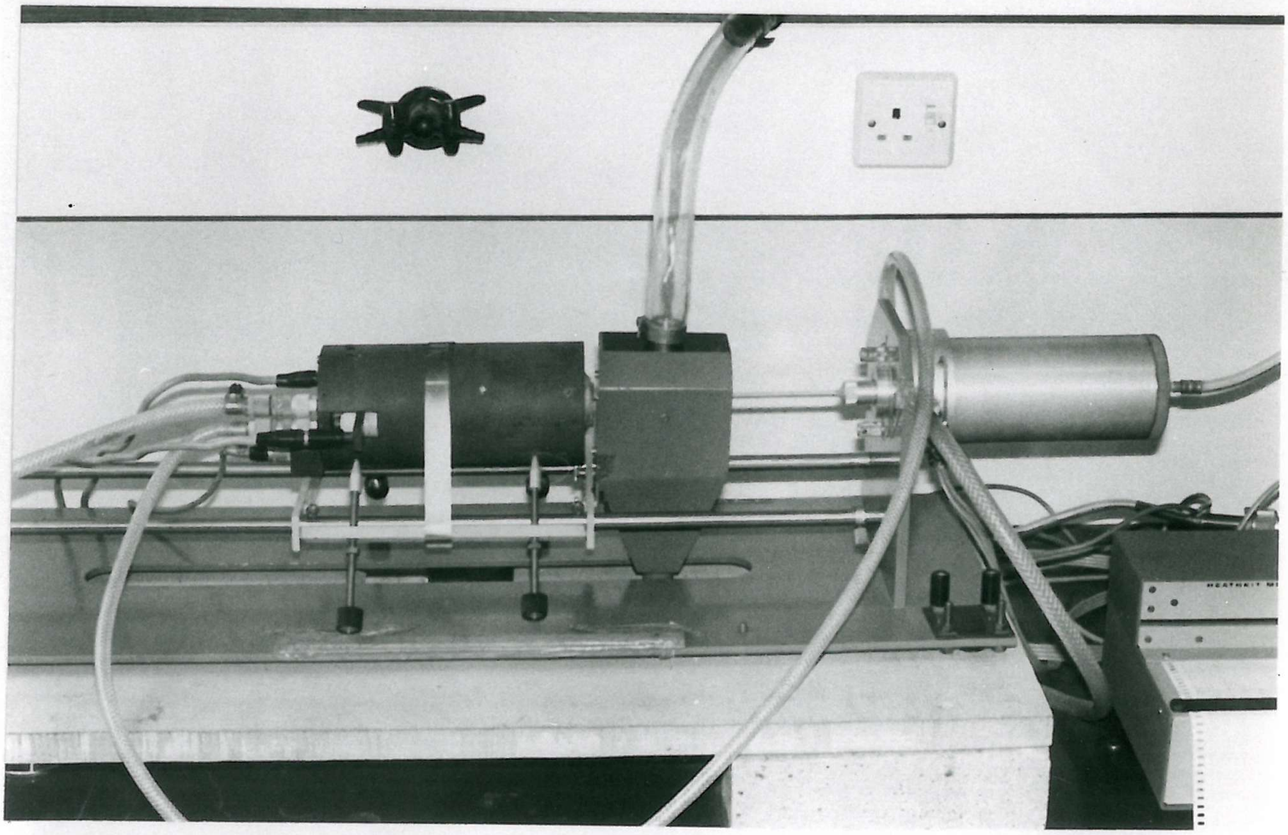

Figure 3·10 Linseis dilatometer gas quenching arrangement.

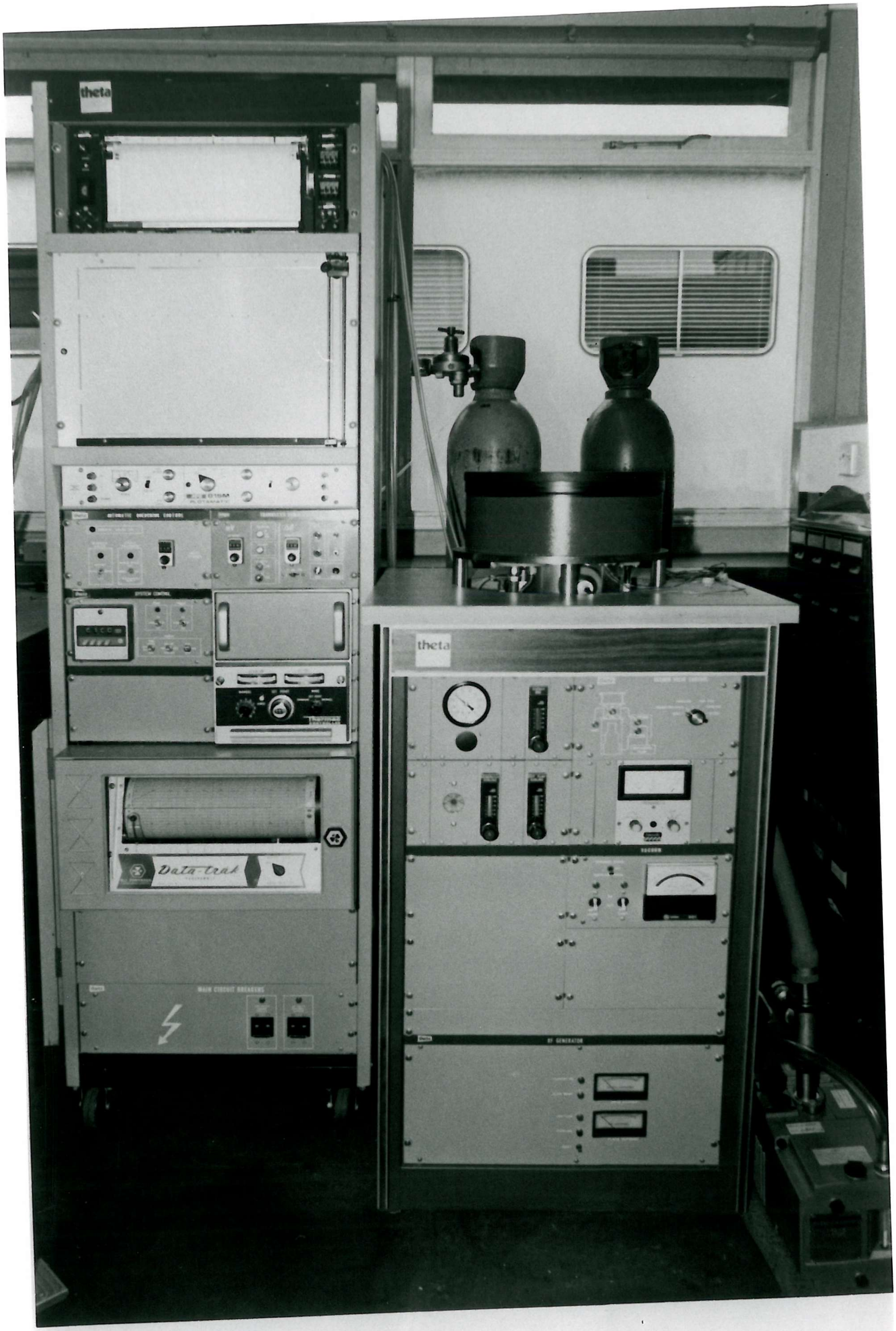

Figure 3·11 Theta dilatometer

and the complete assembly is housed inside a vacuum chamber. The main advantages of this system are the very rapid heating and cooling cycles obtained and the freedom from frictional problems often associated with the classical dilatometer design.

A diagram of the Theta measuring system is shown in Figure 3.12.

Temperature control of the dilatometer specimen is achieved by a feedback system in which the temperature signal from the specimen is compared with the temperature signal dictated by the temperature programmer (i.e. the command signal).

Platinum/Platinum 10% rhodium thermocouples are used in the experimental work and their output is fed directly to the chart recorders and temperature controller.

Temperature programming of the Theta dilatometer is achieved through the Data-Trak programmer. This programmer is of electro-mechanical design and relies on an electrostatic curve following system for its operation. Programme charts are prepared by scribing the required thermal cycle onto the metalised programme surface. This has the effect of dividing the surface of the chart into two electrically isolated conductive planes, which are then sensed by the curve following probe. Programme charts are mounted on the outer surface of the programme drum which can be rotated at various speeds.

For cooling rates faster than the natural cooling rate of the specimen, the automatic quench control may be used in conjunction with the R.F. furnace to produce accelerated controlled cooling.

For very fast cooling rates the furnace is switched off and quench gas passed through the specimens. The exact cooling rate in such cases depends on the specimen wall thickness, the conductivity of the cooling gas and the pressure and flow rate of the cooling gas. Such information is arrived at by trial and error.

Atmosphere control in the theta dilatometer is aided by the presence of a diffusion pump which allows a high vacuum to be achieved. The majority of tests in the present investigation were carried out under an atmosphere of high purity argon or helium, backfilled after initial diffusion pump vaccum purging.

Data collection is achieved by feeding the amplified length change and thermocouple signals to a two pen 10 speed x-t chart recorder. In addition an x-y chart recorder may be used to simultaneously record the cross-plot of dilation versus thermocouple output.

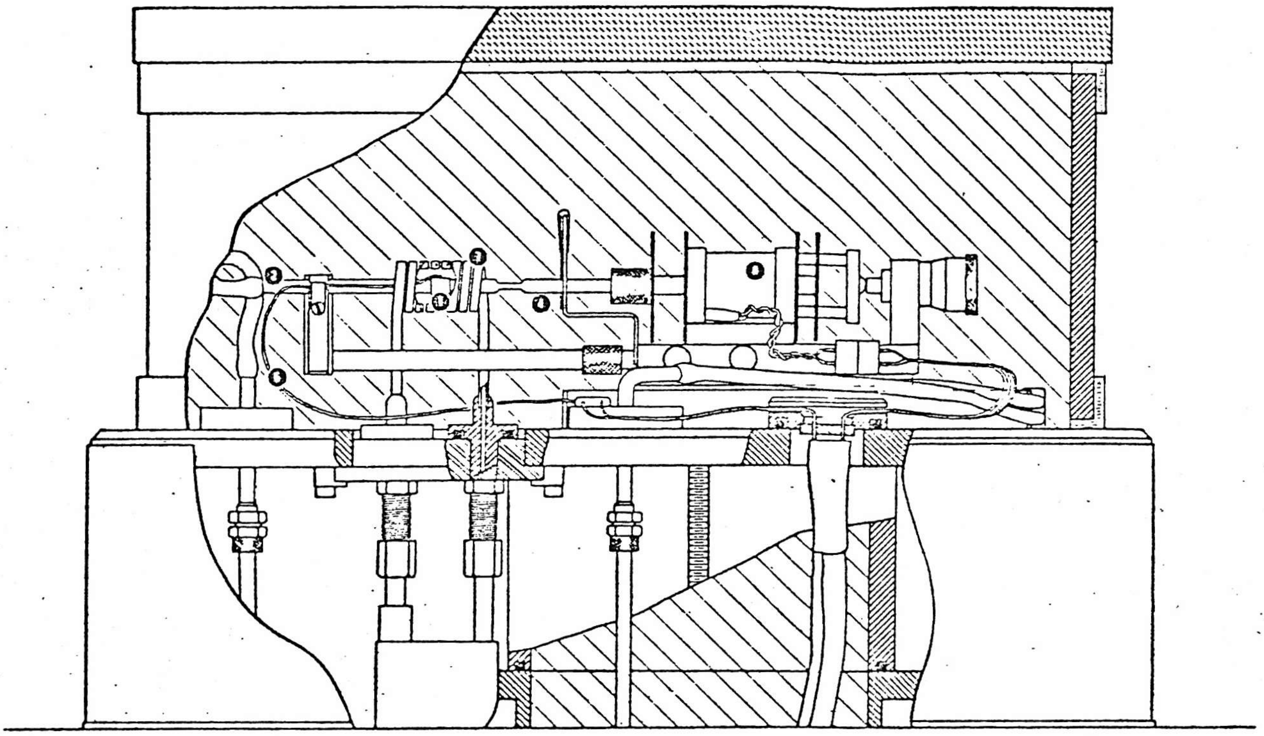

The specimen (1) rests between the tips of the fixed rod (2) and sensing rod (4) in the center of the RF furnace(7). The phase change signal is transfered through the frictionless mounted rod(4) into the transducer (8). The thermocouple (6) senses the temperature. Quenching gas passes through the hollow specimen and escapes through openings.

Figure 3.12 Theta dilatometer specimen holder and measuring head.

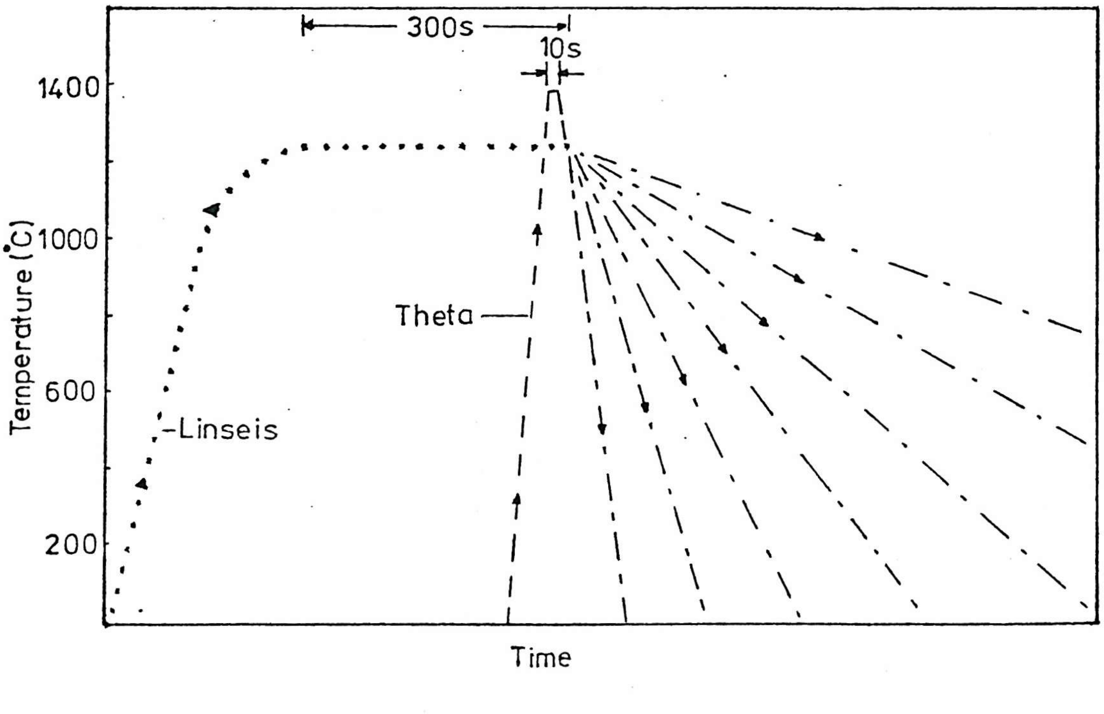

Figure 3.13 Austenitisation cycles used to produce CCT diagrams.

3.12 Thermal Analysis Equipment

Due to the low hardenability of some of the weld metals an additional piece of equipment was developed to produce very fast cooling rates.

This was necessary in order to define the CCV for the martensite transformation in the weld metals, and to allow slowly transforming structures to be quenched out.

The equipment developed consists of a quartz glass tube that can be filled with helium and sealed during the high temperature austenitisation period. For rapid cooling (up to $\sim 1200^{\circ}C/sec$) quenching gas is forced through the tube coming into direct contact with the specimen. High purity nitrogen is used rather than helium for reasons of economy.

The specimen shape in these experiments is a 3 mm diameter thin disc, typically 0.5 - 1 mm thick. The thermocouple is welded to the two faces of the disc, Figure 3.6, and its output recorded on an x-t chart recorder with a sufficiently fast response time.

3.13 Quenching Out

At some of the faster cooling rates the dilatometric data was unable to give details of the carbide reaction. In order to investigate this reaction, certain thin disc specimens were cooled at pre-determined rates, in the thermal analysis apparatus, and then "quenched* out"from several different temperatures. Due to the extreme inefficiency of this technique, in terms of the number of specimens required to define the reaction, quenching out was limited to weld metal EO and cooling rates of $15^{\circ}C/sec$ and $0.4^{\circ}C/sec$. The quenching out temperatures chosen were as follows:

Cooling rate:	$0.4^{\circ}C/sec$	$650^{\circ}C$ $600^{\circ}C$ and $550^{\circ}C$
Cooling rate:	$15^{\circ}C/sec$	$550^{\circ}C$ $500^{\circ}C$ and $400^{\circ}C$

3.14 Austenitisation Considerations

Simulation of weld metal transformation behaviour in reheated specimens requires the following considerations to be satisfied.

(1) Production of a prior austenite grain structure similar to the original weld metal austenite grain structure.

---

* Cooling rate > $500^{\circ}C/Sec$

(2) Solution of all alloying elements in austenite (in particular the strong carbide-nitride forming elements Nb,V,Ti and Al).

(3) Accurate simulation of weld metal cooling cycle.

The third factor can be achieved by suitable programming or development of experimental equipment. The other two factors presuppose a knowledge of the grain coarsening behaviour of weld metal and a knowledge of the solubility relationships of certain strong carbide-nitride forming elements.

3.14.1 Solubility relationships

Certain microalloying elements are known to have a strong effect on the $\gamma \rightarrow \alpha$ transformation in weld metals and therefore these elements must, if possible, be redissolved in the austenite during austenitisation treatment.

In the weld metals under consideration, titanium and vanadium were only present in small amounts. Niobium however, was present in some weld metals in significant quantities.

Calculation of the solubility of Nb in γ at different temperatures can be achieved using the solubility product for Nb (C,N) by Irvine, Pickering and Gladman [158].

$$\log_{10}[\mathrm{Nb}][\mathrm{C} + \frac{12}{14}\mathrm{N}] = \frac{-6770}{T} + 2.26 \qquad (3.1)$$

where T is the absolute temperature.

In the present investigation the calculation for the highest Nb bearing weld metal shows that all Nb should be in solution in austenite above about 1150°C.

3.14.2 Austenite grain size

As previously discussed in Chapter 2, austenite grain size is of fundamental importance to the transformation characteristics of steels. Unfortunately the columnar austenite structure of the weld metal cannot be reproduced in dilatometer specimens. An equiaxed structure of equivalent grain size must therefore be considered as being the best alternative.

If maximum diffusional distances are taken to be the most important factor, then the equivalent equiaxed grain size has a diameter equal to the width of the columnar grain. This approach is bound to lead to the production of a greater proportion of the grain boundary nucleated phases, but the method should ensure that conditions at grain interiors are correctly simulated.

Alternatively, if the ratio of grain boundary area to grain volume is kept constant, the correct proportions of phases should be produced, but there may be a risk of producing different conditions at the centre of the larger equiaxed grains which may affect the subsequent transformation characteristics of the weld metal.

Unfortunately there is very little data in the literature relating to grain coarsening of weld metals and therefore calculation of suitable thermal cycles to produce a given γ grain size can be hazardous.

To obtain a suitable austenite grain size the initial approach was that of trial and error. However, it soon became apparent that even very high temperature austenitisation failed to produce the rapid grain coarsening behaviour common to many wrought steels.

The actual austenitisation treatment finally chosen to produce CCT diagrams was dictated by the practical limitations of the Linseis dilatometer furnace and quartz measuring system.

Treatments of 5 minutes at 1250°C for the Linseis dilatometer and 10 seconds at 1400°C for the Theta were found to produce equivalent grain sizes of ∿ASTM 5 to 6 in most of the weld metals examined.

The equivalence of these two thermal cycles in terms of diffusional processes can be demonstrated by applying equation (2.2) by Maynier [109], which applies to rectangular thermal cycles.

$$P_A = \left[\frac{1}{T} - \frac{\eta R}{\Delta H} \log \frac{t}{t_o} \right]^{-1}$$

where P_A = austenitising parameter (°K/hr)
T = temperature (°K)
t = time at temperature
t_o = unit of time
R = gas constant 8.31441 (KJ/Kg molK)
η = 2.3026
ΔH = activation energy 460.55 KJ/mol.

The result of such analysis shows that 11.5 sec at 1400°C is equivalent to 5 min at 1250°C. A small correction for the heating and cooling time between 1250°C and 1400°C makes the cycle of 10 sec at 1400°C almost exactly equivalent to 5 min at 1250°.

3.14.3 Experimental austenitisation thermal cycles

Details of the austenitisation thermal cycles chosen to produce the CCT diagrams are shown in Figure 3.13.

All Linseis dilatometer specimens and all thermal analysis specimens were rapidly heated to 1250°C (heating time ∿1 min) and held for 5 min, prior to continuous cooling. For practical reasons the Linseis dilatometer specimens each received 3 austenitisation treatments.

All Theta dilatometer specimens used for CCT diagram determinations were heated linearly to 1400°C and held for 10 sec. Specimens were then rapidly cooled to 1250°C before initiating their programmed continuous cooling cycles.

In addition to the two standard austenitisation cycles, one of the weld metals was subjected to several different austenitisation treatments to investigate its grain coarsening and subsequent $\gamma \rightarrow \alpha$ transformation behaviour.

3.15 Optical Metallography

All specimens were mounted in bakelite, mechanically polished to a 1 μm diamond finish, and then etched for optical examination.

The original weld metals were examined on the transverse section with particular emphasis being put on the examination of the top run (i.e. the un-refined weld metal).

Dilatometer specimens and thermal analysis specimens were examined in regions close to the thermocouple connections, so that microstructure and cooling rate correlations could be made with confidence. This meant that all the solid cylinders and thin discs were examined transversely whereas all the hollow cylinders were examined longitudinally. In reality the sectioning direction should not matter in re-austenitised specimens as the prior γ grain shape is fully equiaxed or polygonal. However, segregation effects from initial solidification should always be borne in mind.

Etching was carried out using 2% nital; the etching time varied from 10 sec to 30 sec depending on microstructure. The technique used was to etch for 10 sec followed by etching for 5 sec intervals until the microstructure was fully etched. It proved important to etch for the correct time as some of the microstructures could prove misleading if examined in the under-etched condition.

Optical examination of the etched specimens was then carried out at 150-2000 x magnification using a Neophot II microscope. All the quantitative and photmicrographic work was also performed on this instrument.

3.15.1 Qualitative examination

An initial qualitative examination of the etched specimens was carried out to determine the types of transformation product present, e.g. Ferrite/Pearlite, Widmanstätten ferrite, etc.

Qualitative examinations of the thermally etched specimens were also carried out to determine the extent of the thermal grooving and to observe surface relief effects produced by the lower temperature $\gamma \rightarrow \alpha$ transformation products.

3.15.2 Quantitative examination

Quantitative metallographic techniques were used to assess the relative proportions of the various microstructural constituents in each specimen and to measure the prior austenite grain size.

Point counting with a 1 cm mesh 6x6 grid placed directly onto the microscope projection screen, at a magnification of x500, was used to quantify the microstructural features. To ensure a representative area of specimen was examined, the grid was traversed systematically across the specimen 28 times. This resulted in 1008 points being counted per specimen over a wide area of the specimens surface.

Point counting errors have been assessed and are discussed in detail in the appendix section.

Measurement of prior austenite grain size was achieved by using a quick and accurate variation of the linear intercept method described by Hilliard [159]. This method involves placing a circle of known circumference onto the microscope projection screen (e.g. 20 cm) and measuring the number of γ grain boundary intercepts on this line. The procedure is repeated several times depending on the degree of accuracy required.

The mean linear intercept $\overline{L}$ is then given by the equation

$$\overline{L} = \frac{\text{Circumference of circle x No. of areas counted}}{\text{Total No. of intercepts x Magnification}}$$

In the present work a minimum of 200 intercepts were counted for each mean grain size determination.

Prior γ grain boundaries were identified by thermal etching or by adjusting the thermal cycle to delineate them with fine bands of ferrite, if their chemistry permitted.

By assuming the average austenite grain shape can be described as a regular tetrakaidecahedron it is also possible to calculate the mean grain diamter $\overline{D}$ [140][153], and the equivalent ASTM No. as follows [160]:

$$\overline{D} = 1.776\ \overline{L} \tag{3.2}$$

$$\text{Equivalent ASTM No.} = -10 + 6.64 \log \overline{L} \tag{3.3}$$

3.16 Hardness Testing

Hardness tests were carried out on the solid cylinders and thin discs using a Vickers hardness testing machine with a 20 Kg load.

Tests conducted on the hollow cylinders were carried out on a Matsuzawa microhardness testing machine with a 1 Kg load to avoid deformation of the thin specimen wall.

Microhardness indents were also used as identification markers during microprobe analyses and thermal etching experiments.

CHAPTER 4: RESULTS

4.1 Chemical Analyses

The results of the chemical analyses of the 17 weld metals studied in the investigation are given in Table 4.1.

4.1.1 Carbon-Manganese series

The chemical analysis predicted by the electrode manufacture for the C-Mn (Hytrode) series of weld metals was as follows:-

0.06-0.07 wt%C, 0.3-0.4 wt%Si and 0.5-1.8+ wt%Mn.

It can be seen from Table 4.1 that the target composition for carbon has been achieved quite satisfactorily. The target for silicon content however was slightly exceeded in two cases and the target for manganese was exceeded in all five weld metal deposits. An independent check analysis confirmed these findings, although the absolute values for Mn and Si differed slightly in the two analyses.

The reason for the slightly higher manganese and silicon recoveries is believed to be due to the welding conditions used. From steelmaking experience, manganese is known to be one of the more volatile alloying additions. Similarly in arc welding it has been suggested that manganese recovery in the weld metal is linked to the arc temperature due to vaporisation effects. In the present study the C-Mn weld metals were deposited at a quite modest heat input of ∿1.4 KJ/mm (DC +ve) rather than the more productive high heat input AC welding technique often specified for filling passes. It is therefore assumed that the present welding conditions resulted in a slightly cooler arc, and correspondingly higher alloy recovery than was at first anticipated.

Another interesting point arising from the chemical analysis is the systematic variation in oxygen content (Figure 4.1). Although the variation in oxygen content is not particularly large, there is,nevertheless, a clear decrease in oxygen content of about 100 ppm as the manganese level increases from 0.5 wt% to 1.5 wt%. The fact that this occurs independently of silicon (compare M1 and M4) demonstrates the importance of manganese as a deoxidant in its own right.

WELD METAL CHEMICAL ANALYSES Wt%

Weld Ident.	Consumables	C	Si	Mn	P	S	Cr	Mo	Ni	Al	As	B	Cu	Nb	Sb	Sn	Ti	V	N_{ppm}	O_{ppm}
M1	Experimental	0.06	0.41	0.56	0.023	0.008	<0.01	<0.01	0.05				0.04			<0.01		<0.01	71	411
M2	OK 7016	0.07	0.52	1.35	0.022	0.005	<0.01	<0.01	0.05				0.03			<0.01		<0.01	94	352
M3	OK 7016-1	0.06	0.33	1.57	0.020	0.004	<0.01	<0.01	0.05				0.05			<0.01		<0.01	91	295
M4	OK 7016-2	0.06	0.40	1.85	0.020	0.005	<0.01	<0.01	0.05				0.04			<0.01		<0.01	67	304
M5	OK 7016-3	0.07	0.33	2.12	0.023	0.008	<0.01	<0.01	0.06				0.04			<0.01		<0.01	81	317
N1	Experimental	0.05	0.33	0.98	0.017	0.011	<0.01	0.06	0.06				0.03			<0.01		<0.01	45	446
N2	Experimental	0.04	0.41	1.20	0.024	0.014	0.01	0.07	1.10				0.05			<0.01		<0.01	120	430
N3	OK 8018-C1	0.05	0.38	1.18	0.022	0.010	<0.01	0.08	2.52				0.06			<0.01		<0.01	178	482
N4	OK 8018-C2	0.04	0.27	0.91	0.025	0.014	<0.01	0.07	3.30				0.06			<0.01		<0.01	42	487
N4A	OK 8018-C2	0.04	0.38	1.29	0.030	0.017	<0.01	0.08	3.58				0.08			<0.01		<0.01	141	432
A0	OP41TT/SD3	0.09	0.31	1.32	0.017	0.009	0.04	<0.01	0.05	0.014	<0.01	<0.001	0.11	<0.01	<0.01	<0.01	<0.01	<0.01	95	233
E0	OP41TT/SD3	0.1	0.31	1.37	0.028	0.020	0.06	0.02	0.08	0.013	<0.01	<0.001	0.15	0.03	0.01	0.02	<0.01	<0.01	99	336
A5	503/SD3	0.09	0.18	1.05	0.017	0.013	0.05	0.01	0.10	<0.005	<0.01	<0.001	0.11	<0.01	<0.01	<0.01	<0.01	<0.01	100	511
E5	503/SD3	0.08	0.16	0.97	0.024	0.021	0.07	0.02	0.15	<0.005	0.01	<0.001	0.19	0.02	0.01	0.02	<0.01	0.01	95	685
E0	OP41TT/SD3	0.13	0.29	1.38	0.025	0.017	0.07	0.02	0.08	0.019		<0.0005	0.21	0.035		0.01	0.005	<0.01	91	305
E0(r)	Remelt	0.12	0.28	1.33	0.025	0.018	0.06	0.01	0.08	0.020		<0.0005	0.20	0.031		0.02	0.004	<0.01	84	58
E5	503/SD3	0.10	0.10	0.80	0.019	0.021	0.06	0.02	0.15	0.006		<0.0005	0.19	0.008		0.02	0.006	<0.01	89	654
E5(r)	Remelt	0.10	0.11	0.85	0.021	0.024	0.06	0.02	0.15	0.007		<0.0005	0.19	0.011		0.02	0.008	<0.01	94	278
NMo	709/10B	0.05	0.19	1.72	0.010	0.009	0.06	0.31	1.87			<0.0005	0.03	<0.005			0.005			

TABLE 4.1: Chemical Analyses and Identification of Weld Metals.

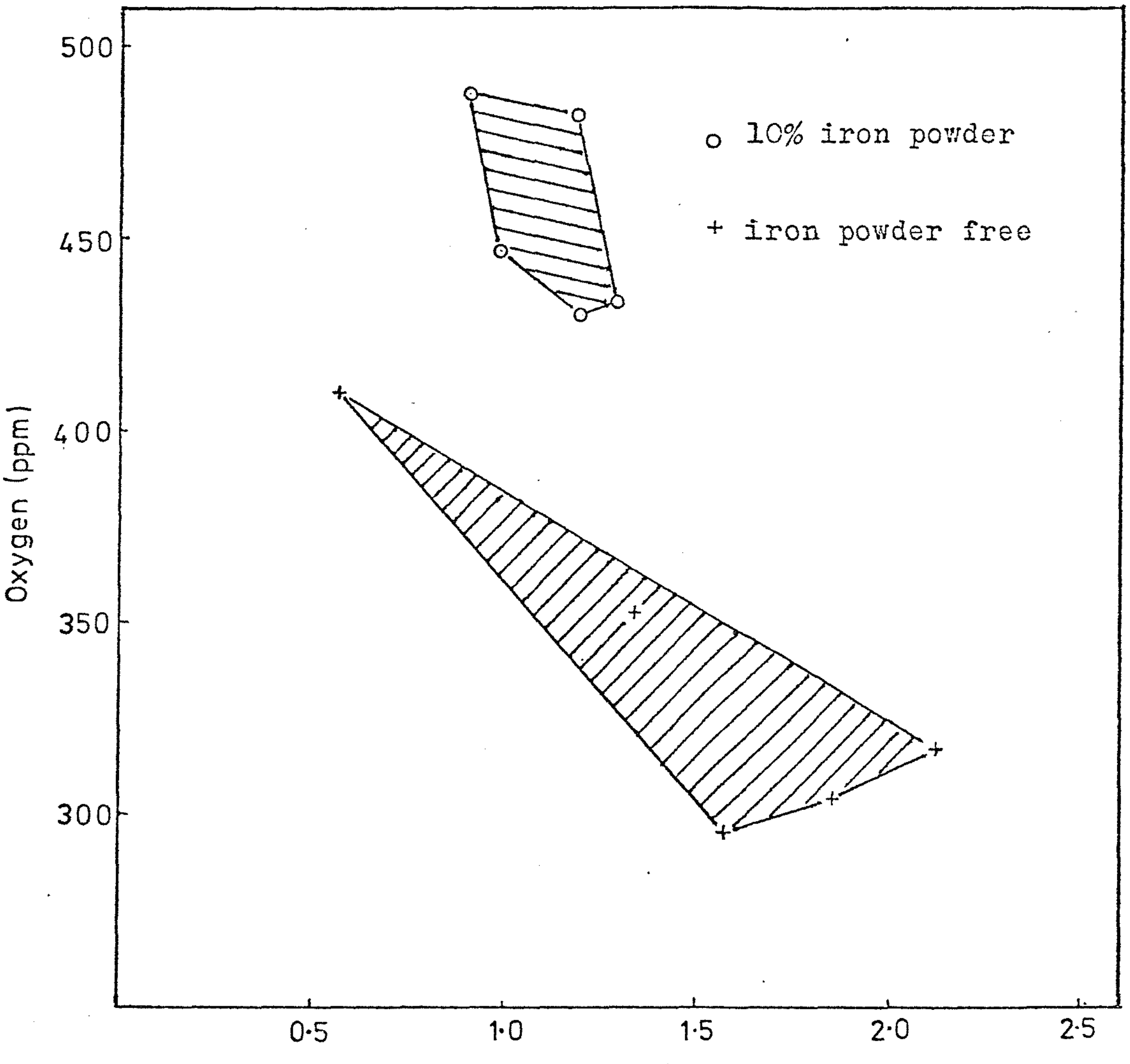

Figure 4.1 Weld metal oxygen versus manganese contents for MMA weld metals.

However, one must also bear in mind that increasing the ferromanganese content on the electrode coating simultaneously reduces the $CaCO_3$ content and therefore may also alter the initial oxidising power of the flux.

Although the analyses of the carbon-manganese series differed slightly from that initially predicted, the experimental welds provided a good systematic series for manganese.

Experimental work was carried out on these weld metals as follows:-

M1 - CCT diagram determination (0.56 wt%Mn)
M2 - CCT diagram determination (1.35 wt%Mn)
M3 - γ grain growth measurements (1.57 wt%Mn)
M4 - Future studies (isothermal & quenching out)(1.85 wt%Mn)
M5 - CCT diagram determination (2.12 wt%Mn)

4.1.2 Carbon-Manganese-Nickel series

The chemical analyses predicted by the electrode manufacturer for the nickel bearing weld metals were as follows:

0.03-0.04 wt%C, ∿0.3 wt%Si, ∿0.8 wt%Mn, and 0-3.5 wt%Ni

Again the results in Table 4.1 indicate a higher than expected recovery of manganese in the weld metal. The reason for the discrepancy is again believed to be due to the relatively "cool arc" welding conditions used.

In addition to the high manganese recoveries, the nickel contents were also very slightly higher than originally anticipated.

All the electrodes used in the nickel series contained about 10% iron powder in the electrode coating and this is reflected in the weld metal oxygen contents. Oxygen contents ranged from ∿430 ppm to 490 ppm whereas the oxygen content of the equivalent iron powder free electrode is estimated to be ∿350 to 375 ppm at the same manganese level(Figure 4.1).

Experimental work was carried out on the nickel bearing weld metals as follows:-

N1 - CCT diagram determination (0.06 wt%Ni)
N2 - CCT diagram determination (1.1 wt%Ni)
N3 - CCT diagram determination (2.52 wt%Ni)
N4 - Future studies (isothermal & quenching out)(3.30 wt%Ni)
N4A- CCT diagram determination (3.58 wt%Ni)

4.1.3 Carbon-Manganese-Niobium series

The chemical analyses of the submerged arc weld metals produced with the Oerlikon OP41TT/SD3 flux-wire combination given in Table 4.1 are more or less as expected. In the case of the niobium bearing base plate, niobium was introduced into the weld metal through dilution giving a weld metal niobium content of 0.03 wt%. Oxygen contents of these weld metals were typically between 250 ppm and 350 ppm which is normal for this flux/wire combination.

The weld metals produced with the experimental carbonate (type 503)/SD3 flux-wire combination were somewhat leaner in manganese and silicon than originally expected. This is believed to be due to the more vigorous oxidation reactions occurring in the arc and weld pool, caused by the experimental flux, which were not correctly balanced by the wire composition used. This belief is supported by the fact that an experimental 503/high silicon (∿1 wt%) wire combination has been shown to produce a weld metal of more conventional composition [59].

Again, niobium was introduced into the weld metal through dilution from the Nb bearing plate. However, only 0.02 wt%Nb was detected in the chemical analysis, suggesting that niobium had also been oxidised during welding [57][59]. This is confirmed in Table 4.2. Oxygen contents of these weld metals were high, being typically between about 500 ppm and 700 ppm (c.f. Figure 4.1).

Experimental work was carried out on the C-Mn-(Nb) series of weld metals as follows:

A0 - CCT diagram determination (Nb free)
E0 - CCT diagram determination (0.03 wt%Nb)
A5 - CCT diagram determination (Nb free)
E5 - CCT diagram determination (0.02 wt% Nb)

4.1.4 Weld metal remelts

In carrying out the remelting experiment it was hoped that the oxygen content could be varied independently of all other elements.

The results of the chemical analyses given in Table 4.1 show that this has in fact been achieved quite satisfactorily. In the case of weld metal E0, the oxygen content has been reduced from 305 ppm to 58 ppm. Similarly, in weld metal E5, the oxygen content

ELEMENT	WELD METAL EO	WELD METAL E5
Al	18.85	2.84
Fe	1.90	31.64
Ti	1.47	1.06
Mn	22.91	20.94
Nb	0.12	0.23
Si	10.88	13.06
Ca	0.43	0.15
S	0.34	0.80
O	43.08	29.29

Table 4.2 Inclusion Chemistry Determined by EPMA (values given in weight per cent)

has been reduced from 654 ppm to 278 ppm.

Due to the limited quantity of remelted weld metal material it was not possible to determine complete CCT diagrams for those materials. However, the $\gamma \rightarrow \alpha$ transformation behaviour was studied in the typical welding cooling rate range.

4.1.5 Carbon-manganese-nickel-molybdenum weld metal

The chemical analysis of the higher alloy Mn-Ni-Mo weld metal is given in Table 4.1, and is quite typical for this type of weld metal.

Experimental work was carried out on this material to determine its CCT characteristics, and to elucidate the effect of molybdenum in weld metals.

4.2 Electron Probe Microanalysis(EPMA)

The results of the quantitative EPMA of weld metal inclusions, corrected for absorption, atomic number and fluorescence, are shown in Table 4.2.

From these results it is suggested that the inclusion type produced by the OP41TT flux is an aluminium manganese silicate type as follows:

$$Al_2O_3 : Mn(Fe)O : SiO_2 .$$

The inclusion also contains measurable amounts of Ti, Nb, Ca and S.

The inclusion type produced by the 503 carbonate flux is thought to be an iron rich manganese silicate type as follows:

$$2(Mn,Fe)O : SiO_2 .$$

This inclusion also contains ∿3wt.% Aℓ and measurable amounts of Ti, Nb, Ca and S.

The above weld metal inclusion analysis confirms the view that incomplete deoxidation has occurred in the 503 weld metal. Due to insufficient quantities of deoxidising elements, in particular Si, a large amount of iron oxide (19% Fe) has remained associated with the inclusions.

Another interesting feature of the inclusions produced by the carbonate flux system is their Nb and S contents. The quantities of both elements can be seen to be about double that found in the inclusions produced by the OP41TT flux system.

4.3 Thermal Etching

To demonstrate the validity of the thermal etching technique a specimen of weld metal was polished and etched in the normal way and marked with microhardness indents. This specimen was then lightly repolished before being subjected to the thermal etching conditions in the dilatometer (10 sec at 1400°C). Following a further examination of the specimen, progressive repolishing and etching was carried out until the microhardness indents were almost completely removed and the typical bulk microstructure was again visible. The complete sequence of operations is shown in Figure 4.2.

Figures 4.2(a) shows the acicular ferrite microstructure of the original submerged arc weld metal, with the prior austenite grain boundaries clearly delineated with grains of polygonal ferrite.

In Figure 4.2(b) the new thermally etched austenite grain structure is clearly visible,along with the surface relief effects caused by the $\gamma \rightarrow \alpha$ transformation products. It should also be noted that the new γ structure bears no relation to the original γ structure although the treatment at 1400°C has produced grains of reasonably similar size.

In Figure 4.2(c) the thermally etched structure of Figure 4.2(b) has been polished back and etched in nital to reveal the underlying ferrite grain structure. It should be noted that this structure is not representative of the bulk structure of the material, probably because of some local decarburisation occurring in the surface layers. However similar structures do sometimes occur in the bulk of lower hardenability weld metals.

By comparing Figures 4.2(b) and 4.2(c) it is possible to relate some of the surface relief features to their corresponding microstructural features. For example there are a few small areas (e.g. marked A) in which there is no surface relief. These regions seems to correspond to isolated polygonal ferrite grains found at prior austenite grain boundaries or triple points. At the regions marked B, fairly coarse 'V' shaped surface relief features are evident. These

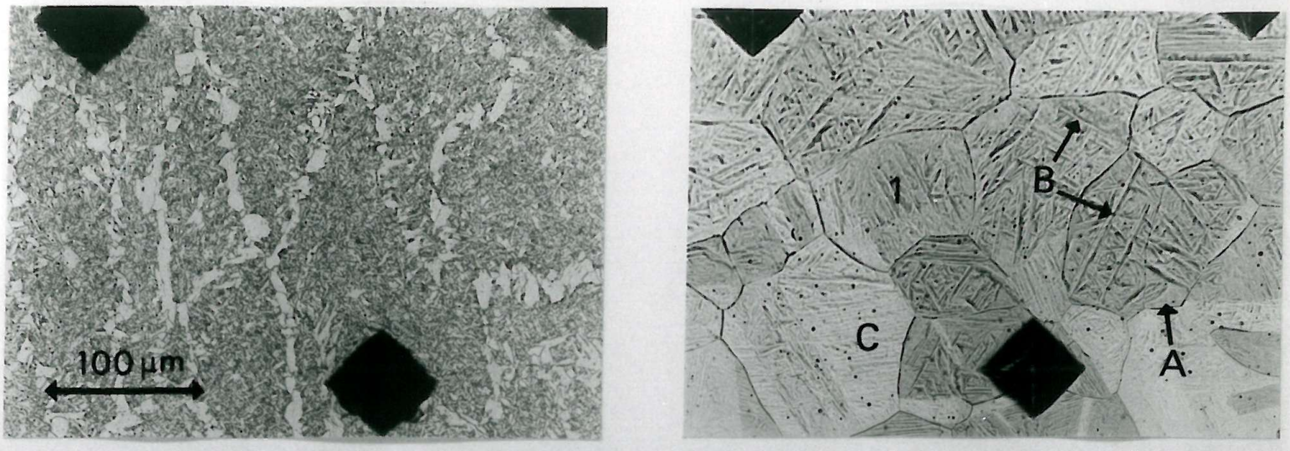

(a) As welded

(b) Thermal etch (10Sec.1400°C)

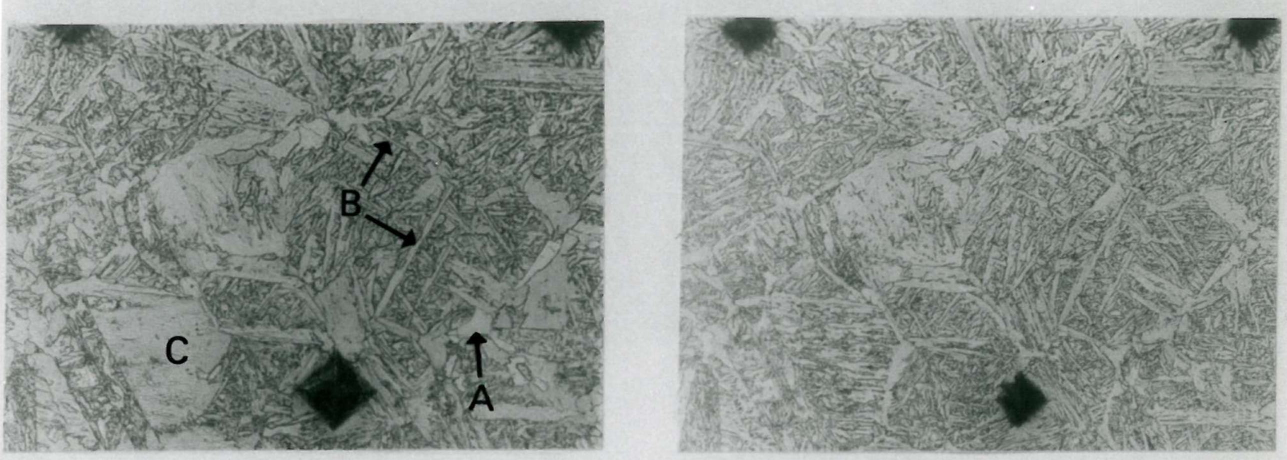

(c) Repolised and etched

(d) Repolised and etched

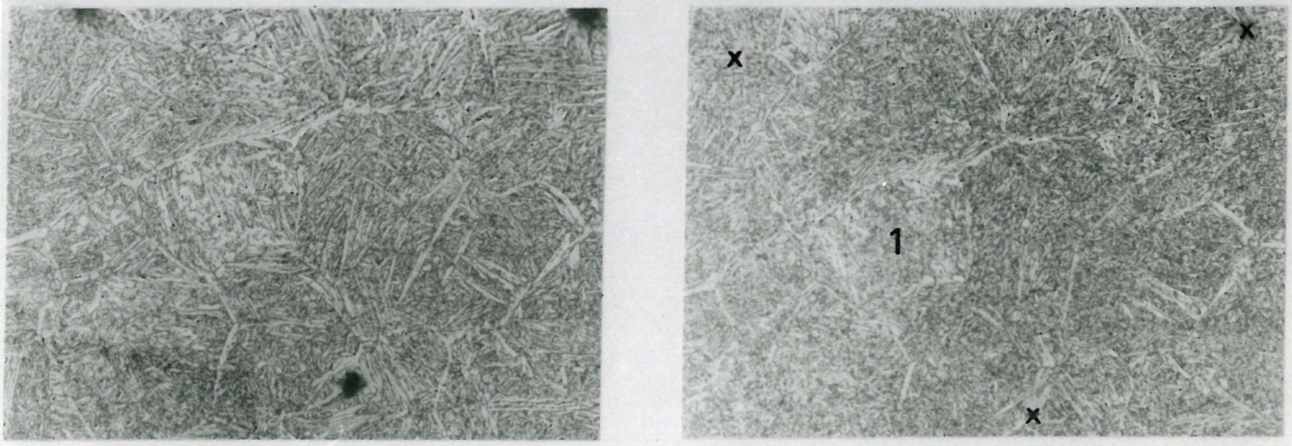

(e) Repolised and etched

(f) Repolised and etched

Figure 4·2 Correlation between thermal and nital etched microstructures features seem to correspond to coarse intragranular acicular ferrite laths or plates which occur at a variety of orientations within the austenite grains. A third surface relief feature is the much finer parallel striations shown in region C, which seem to be related to large almost featureless areas of ferrite.

The final three figures 4.2(d),(e) and (f) illustrate the effect of polishing back from the surface regions. In Figure 4.2(f) the root of each microhardness indent marker is still just visible. This means that a $\sim$12 μm of material have been polished away from the original surface. The microstructure of Figure 4.2(f) consists of fine acicular ferrite with thin bands of grain boundary ferrite and is more refined than the original weld due to its faster cooling rate. This microstructure is considered to be representative of the bulk microstructure which means that the non representative surface decarburised region of this and other dilatometer specimens is about 12 μm.

The point of major importance from this thermal etching exercise is the relationship between the thermal "grooves" of the prior γ grain boundaries shown in Figure 4.2(b) and the prior γ grain boundaries delineated by fine bands of ferrite in the bulk (Figure 4.2(f)). For example the grain marked No. 1 has a very distinctive shape and is clearly visible in both the thermally etched and nital etched conditions (Figures 4.2(b) and (f)). This finding gives confidence to the use of the thermal etching technique for measuring γ grain sizes representative of the bulk material.

4.4 Austenite Grain Coarsening

The results of the austenite grain coarsening studies carried out on the 1.57 wt%Mn carbon-manganese weld metal are given in Table 4.3, and selected micrographs are presented in Figures 4.3 to 4.8.

The micrographs clearly show agreement between the thermally etched prior austenite grain structures and the ferrite delineated austenite grain structures of the polished and etched dilatometer specimens. This gives further confidence in the thermal etching technique in estimating bulk γ grain size as discussed in section 4.3. In speciman M3A there is some evidence of surface transformation from $\gamma \rightarrow \delta$ at 1440°C.

However, no bulk $\gamma \rightarrow \delta$ transformation was observed dilatometrically and the good correspondence between the thermally etched

Specimen Identification	Thermal Cycle Time (secs)	Temp (^{o}C)	γ-grain size ASTM No.
M3A	10	1440	4.30
M3H	10	1400	4.77
M3B	10	1350	5.91
M3C	10	1250	6.31
M3I	100	1300	5.85
M3D	100	1250	5.98
M3F	100	1150	6.65
M3F	100	1050	8.76

TABLE 4.3: Influence of thermal cycle on austenite grain size for weld metal M3.

Specimen Identification	Thermal Cycle		γ-grain size ASTM No.
	Time (secs)	Temp (^{o}C)	
M1	10	1400	5.8
M2	10	1400	5.8
M5	10	1400	5.7
N1	10	1400	5.4
N2	10	1400	5.5
N3	10	1400	5.0
N4A	10	1400	4.8
A0	300	1250	5.2
E0	300	1250	5.3
A5	300	1250	5.1
E5	300	1250	6.4
NM0	10	1400	4.7
E0(r)	300	1250	4.2
E5(r)	300	1250	4.0

TABLE 4.4: Austenite grain sizes developed during CCT diagram austenitisation thermal cycles.

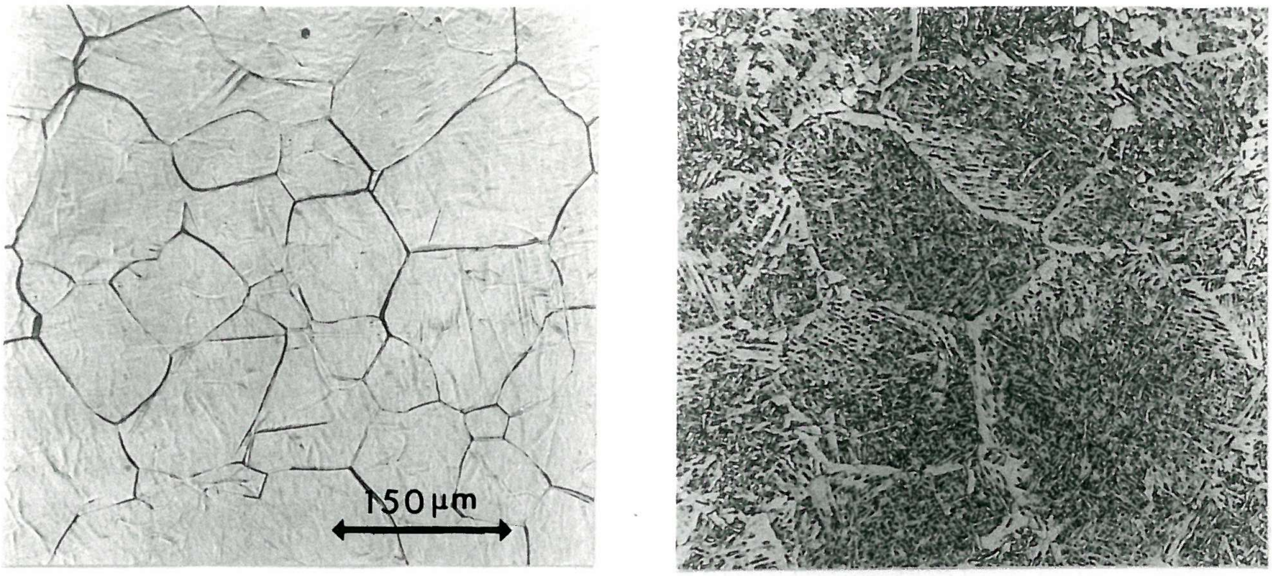

Thermal etch

Nital etch

Figure 4·3 M3A (10Sec. 1440°C)

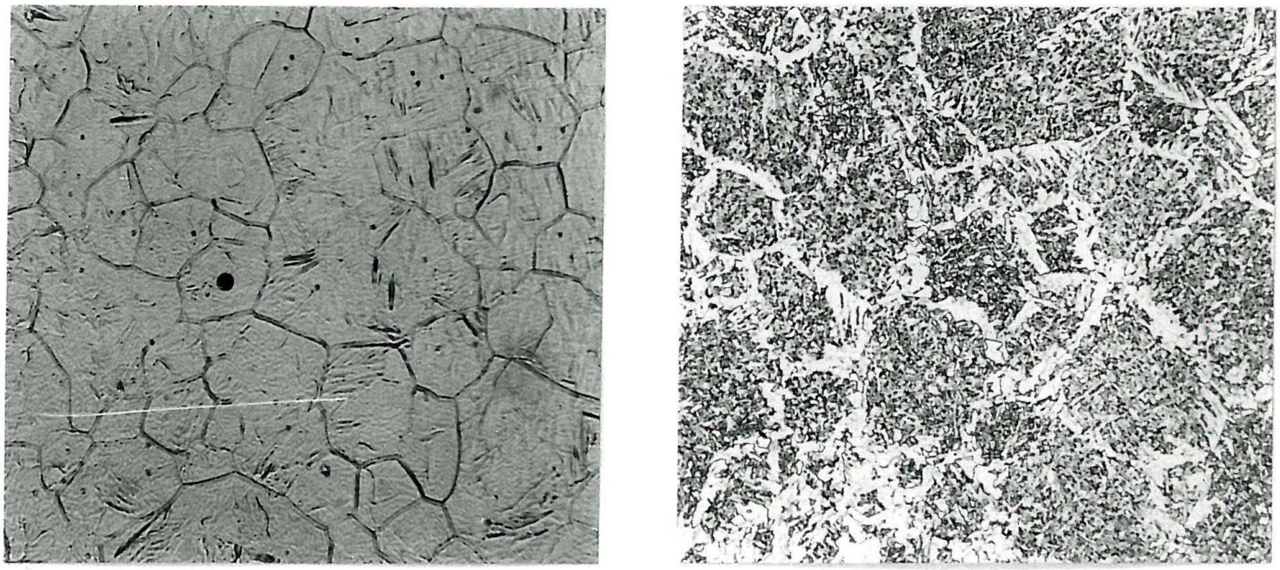

Thermal etch

Nital etch

Figure 4·4 M3B (10Sec. 1350°C)

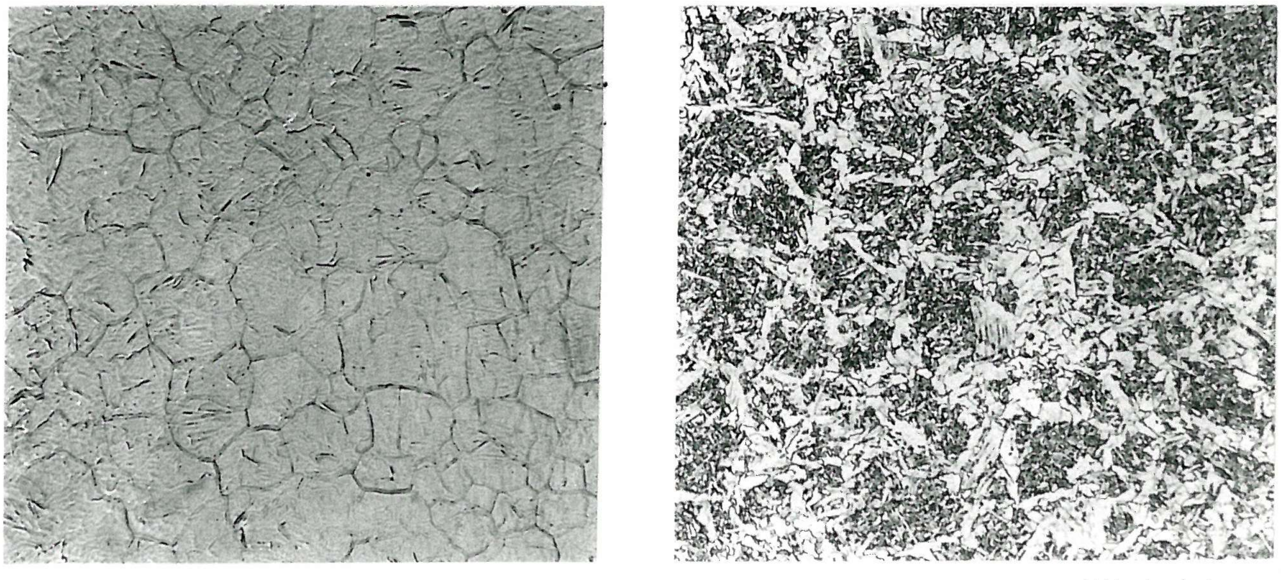

Thermal etch

Nital etch

Figure 4·5 M3C (10Sec. 1250°C)

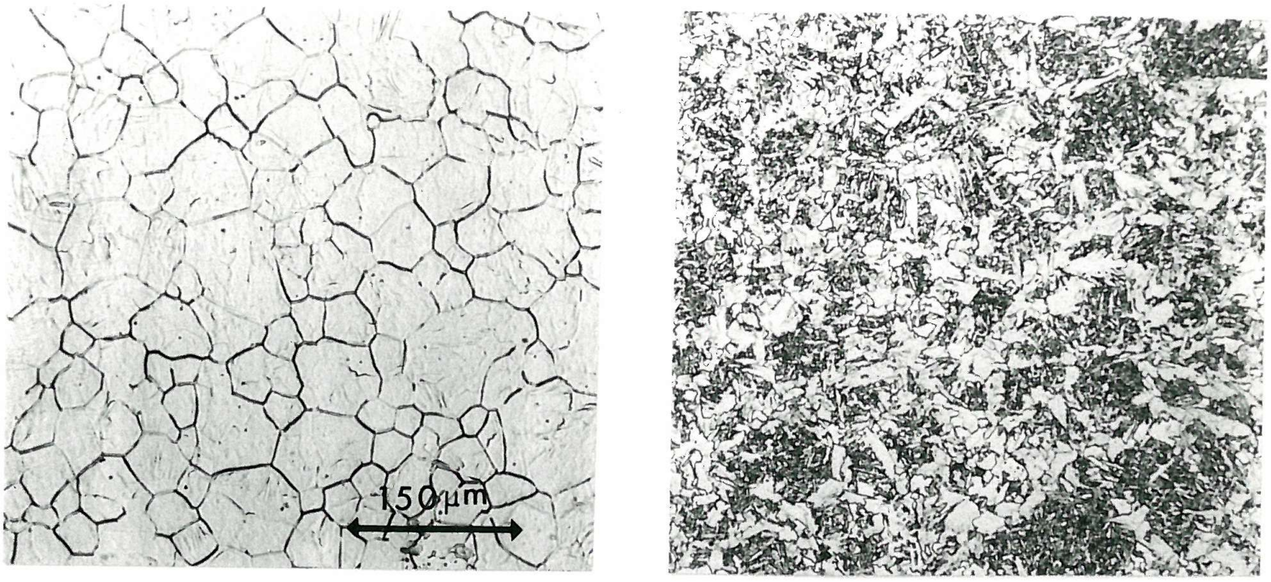

Thermal etch

Nital etch

Figure 4·6 M3D (100Sec. 1250°C)

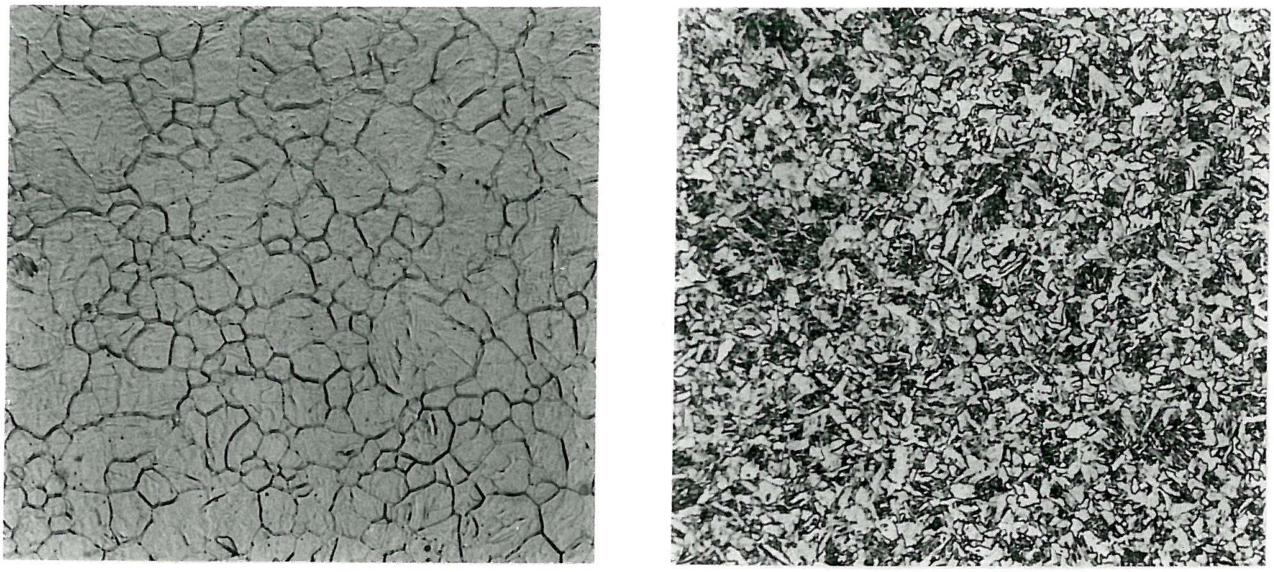

Thermal etch

Nital etch

Figure 4·7 M3E (100Sec.1150°C)

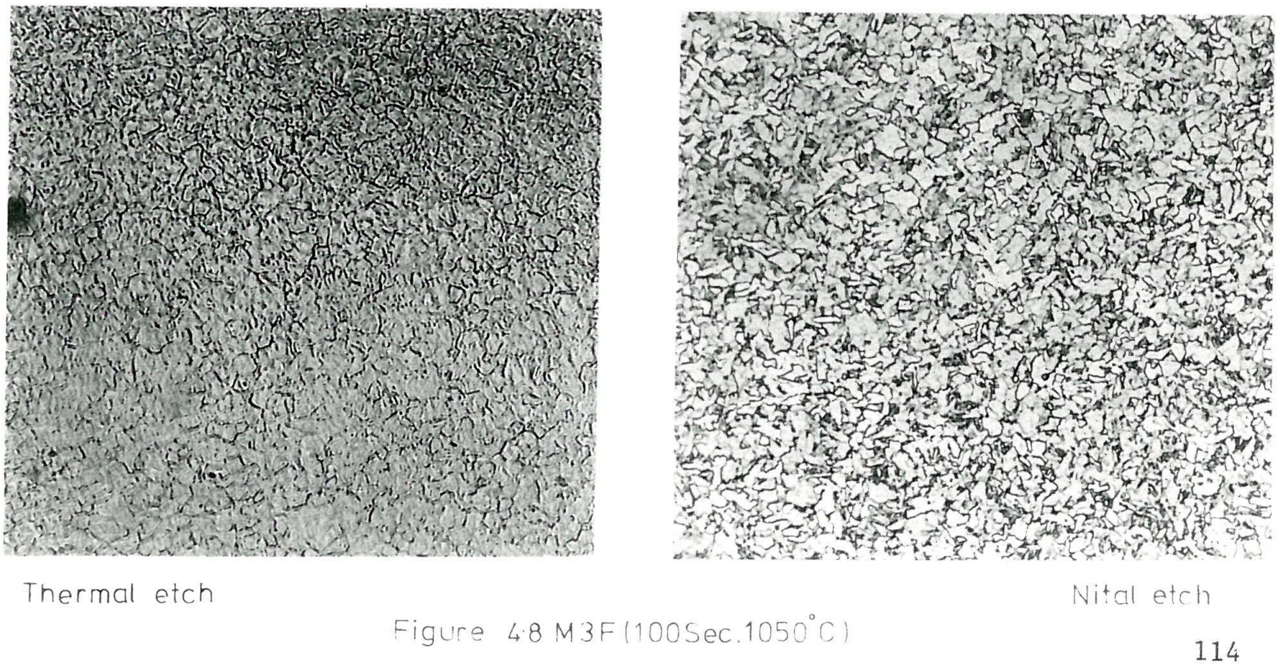

Thermal etch

Nital etch

Figure 4·8 M3F (100Sec.1050°C)

and nital etched γ structures (ASTM 3.9 and 4.1 respectively) suggests that the main thermally etched structure is in fact austenite.

In Figure 4.9 the grain coarsening results are plotted as grain size versus maximum heating temperature. For comparative purposes the results of a study of HAZ grain coarsening by Alberry and Jones [140] are also presented in this figure. It can be seen that there is a considerable difference in the γ grain growth characteristic of the two materials. In the case of the HAZ material initial grain growth in the first 10 sec. is very rapid and is followed by considerable further grain growth in the next 90 sec. period. In the case of the weld metal material, the initial grain growth in the first 10 sec. is much slower than that of the HAZ, and subsequent grain growth in the next 90 sec. period is extremely slow. (Compare the results for M3C (10 sec.) and M3D (100 sec.) at 1250°C in Figures 4.5 and 4.6.)

This marked difference in γ grain growth behaviour is similar to that caused by interactions with second phase particles as discussed in Chapter 2.

The results of the γ grain size measurements of other weld metals in the present investigation are given in Table 4.4. It can be seen that the two thermal cycles used for CCT diagram determinations produced similar γ grain sizes in the region of ASTM 5 to 6.

It can also be seen that the weld metal with the highest oxygen content, E5, (654 ppm) coarsened to the smallest mean grain size (ASTM 6.3) whereas the two vacuum remelted weld metals E0(r) and E5(r) coarsened to the largest mean grain sizes (ASTM 4.3 and 4.0 respectively).

This last point is important because although the two remelted materials E0(r) and E5(r) both attained similar grain sizes, their residual oxygen contents were vastly different (58 ppm and 278 ppm respectively).

It should also be noticed that the series of weld metals deposited with the iron powder containing electrodes (C-Mn-Ni series) have generally coarsened to slightly larger grain sizes than the iron powder free variety (C-Mn series), despite higher oxygen contents. Similarly the C-Mn submerged arc weld metal with high oxygen content (A5-511 ppm O) has coarsened slightly more than the medium oxygen content weld metal (A0-233 ppm O).

All these observations suggest that the size distribution of oxide inclusions is of major importance in controlling austenite grain

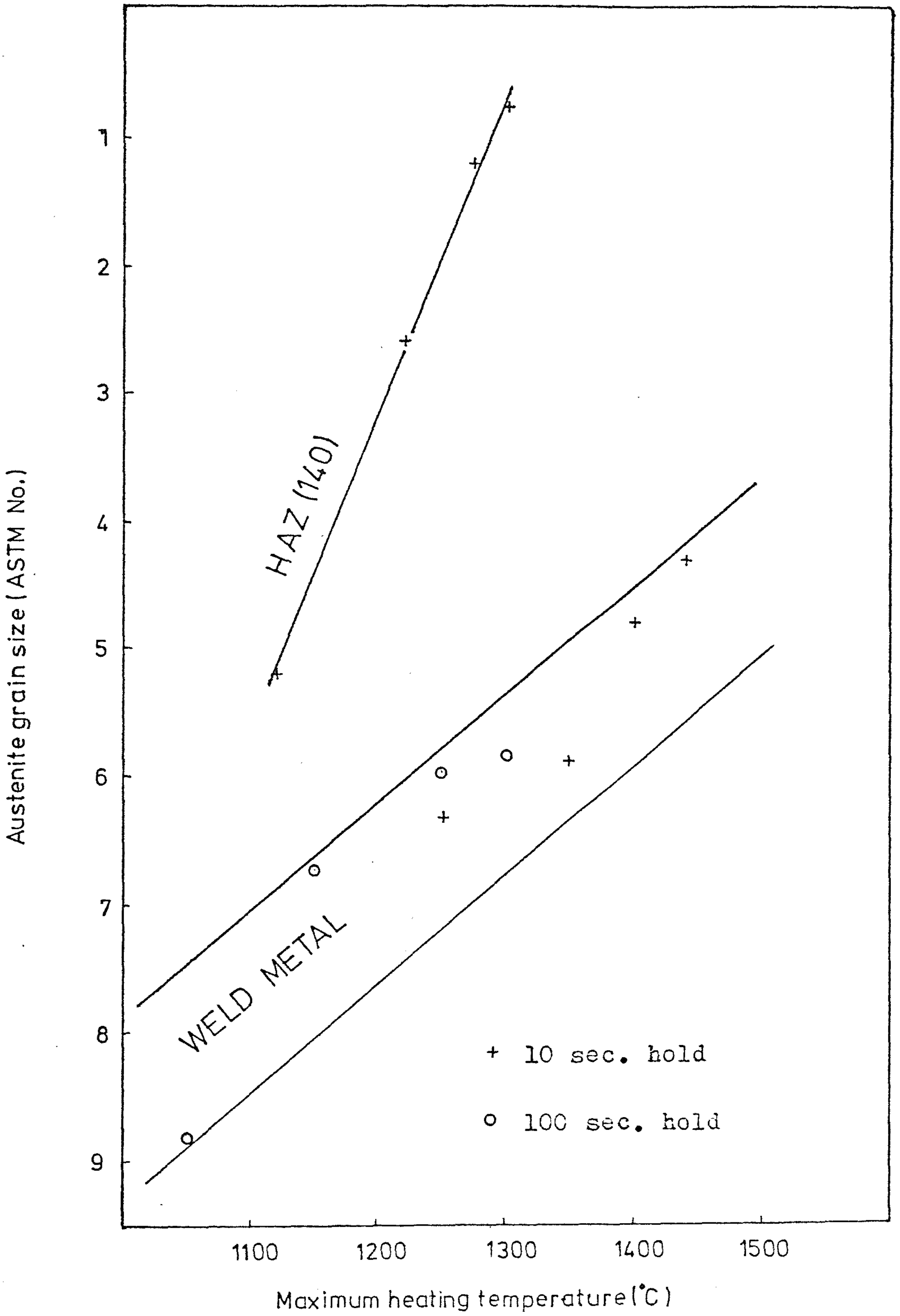

Figure 4.9 Austenite grain size versus maximum heating temperature.

coarsening behaviour, rather than the total oxygen content.

In an attempt to understand this effect Ferrante [161] measured the inclusion size distribution of materials E0, E0(r) and E5(r) using metallographic techniques on extraction replicas in the transmission electron microscope (TEM). The results of this investigation are shown in Figure 4.10, and it can be seen that the effect of remelting weld metal E0 has been to shift the inclusion size distribution to larger sizes as well as decreasing the volume fraction of inclusions. For example in weld metal E0 almost 60% of the inclusions have a diameter less than 0.5 µm before remelting, but after remelting only about 30% of the inclusions are less than 0.5 µm diameter.

This change in size distribution may be due to coalescence of small inclusions in the melt.

The results of the dilatometrically measured $\gamma \rightarrow \alpha$ transformation temperatures are plotted against austenite grain size (ASTM No.) in Figure 4.11. It can be seen that increasing austenite grain size decreases the $\gamma \rightarrow \alpha$ transformation temperature fairly uniformly in the range of grain sizes investigated. The magnitude of this depression is in the region of 25°C per ASTM No. for the 50% transformation temperature for this particular composition and cooling rate. It can also be seen that the overall transformation rate increases with increasing γ grain size.

4.5 Continuous Cooling Transformation Data

4.5.1 Cooling curves

Continuous cooling curves were obtained for all specimens (cylinders and thin discs) to allow construction of the 12 CCT diagrams. These curves are shown on the CCT diagrams (Figures 4.47 to 4.58) plotted as temperature versus log time. The cooling rates between 800°C and 500°C, calculated from each curve, are given at the base of each cooling curve on the CCT diagrams.

Due to the different mechanisms of cooling necessary to cover the complete range of cooling rates, not all cooling curves are of the same shape.

In the case of the Linseis dilatometer, the slow cooling rates obtained through the temperature controller are approximately linear. At faster cooling rates, however, the curves are of a Newtonian type due to the cooling effect of the quenching gas. The shape of the

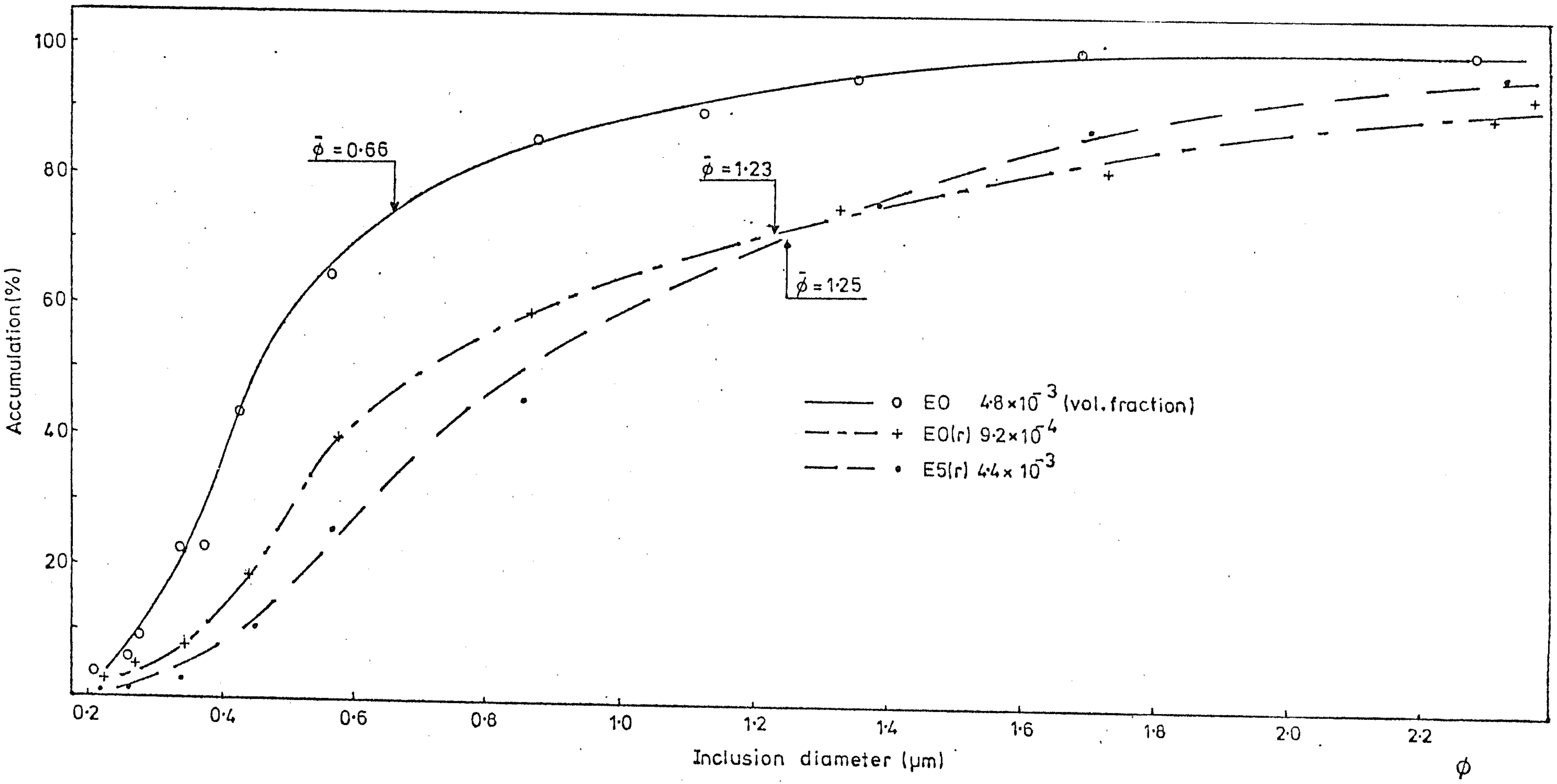

Figure 4.10 Cumulative inclusion size distributions for specimens E0, E0(r), and E5(r).

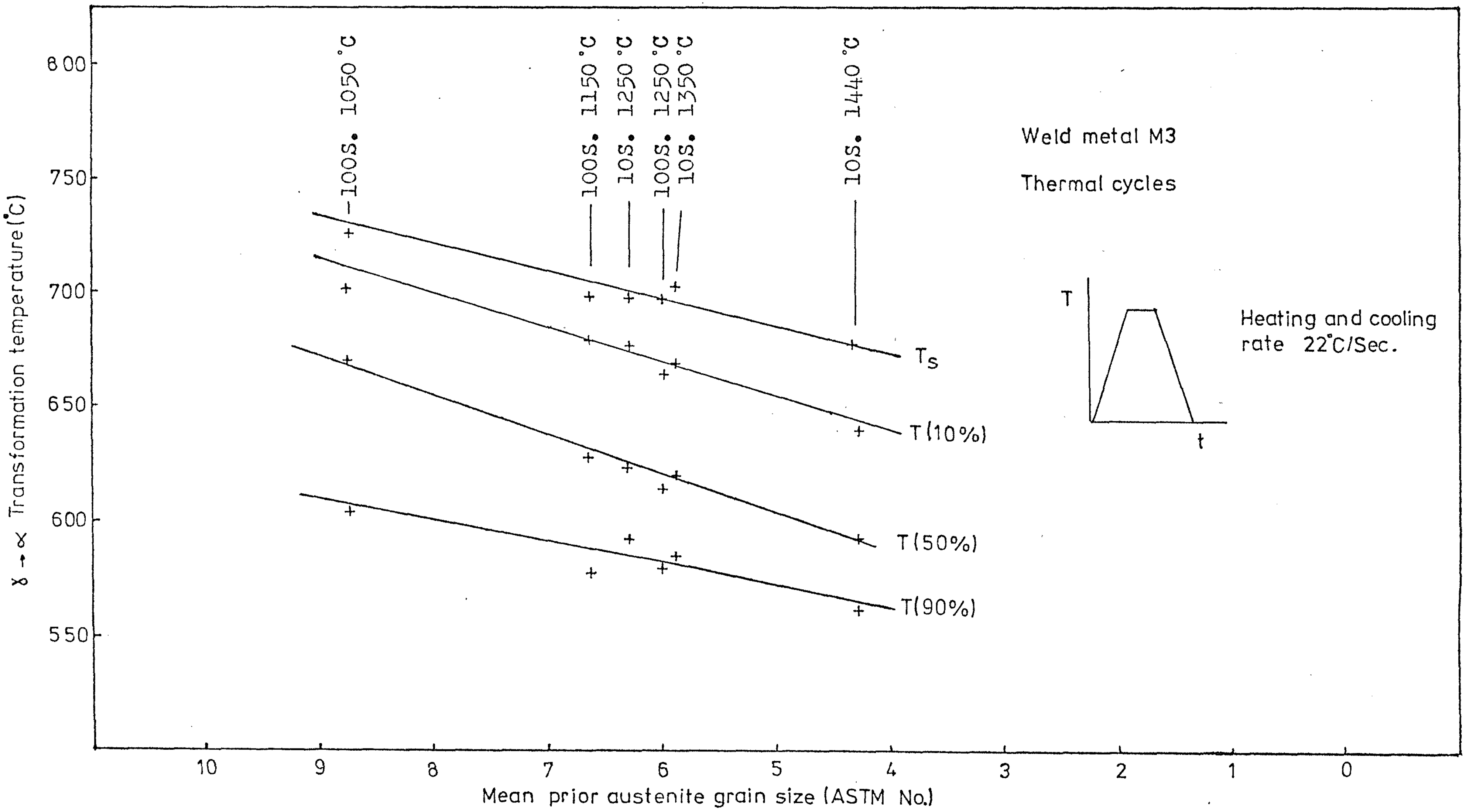

Figure 4.11 Influence of austenite grain size on $\gamma \rightarrow \alpha$ transformation temperatures.

cooling curves for specimens cooled at typical weld cooling rates, in the Linseis dilatometer, is shown in Figure 4.12. It can be seen that the cooling curves for these specimens is in good agreement with the original weld metal cooling curve throughout the γ → α transformation temperature regime.

In the case of the Theta dilatometer, the smaller thermal mass of the specimens allowed linear cooling to be achieved at all but the fastest cooling rates. Specimens cooled within the typical welding cooling rate range in the Theta dilatometer therefore had essentially linear cooling characteristics.

All specimens cooled at rates greater than about 1°C/sec showed thermal arrests on their cooling curves, due to the liberation of latent heat associated with the γ → α transformation. The clarity of these arrests seems to vary with specimen geometry, cooling rate and cooling media. Figure 4.13 shows cooling curves with thermal arrests for dilatometer specimens E0, E5, E0(r) and E5(r) (as welded and remelted conditions).

4.5.2 Continuous cooling dilatometry

The dilatometric data from each test was recorded directly onto an x-y recorder and presented as thermocouple e.m.f. versus specimen dilatation. Figures 4.14 and 4.15 show examples of this presentation for specimens E0, E5, E0(r) and E5(r) (as welded and remelted conditions).

In the majority of cases the smooth continuous curve produced during the γ → α transformation gave no indication of the start and finish of different transformation products. However, at fast cooling rates there was usually a clear indication of the start of the martensite reaction. Similarly at very slow cooling rates, most of the higher carbon weld metals (>0.1%C) showed a clear discontinuity corresponding to the pearlite reaction.

Interpretation of dilatometric data was discussed in detail in Chapter 2. The method of determining the start and finish of transformation is to determine the points at which the dilatation-temperature trace deviates from linearity. These points have been determined for each dilatometer specimen. Then, using the graphical construction described in Chapter 2, transformation temperatures representing 2½% and 97½% transformation have been calculated and plotted on the relevant cooling curves on the CCT diagrams. Values

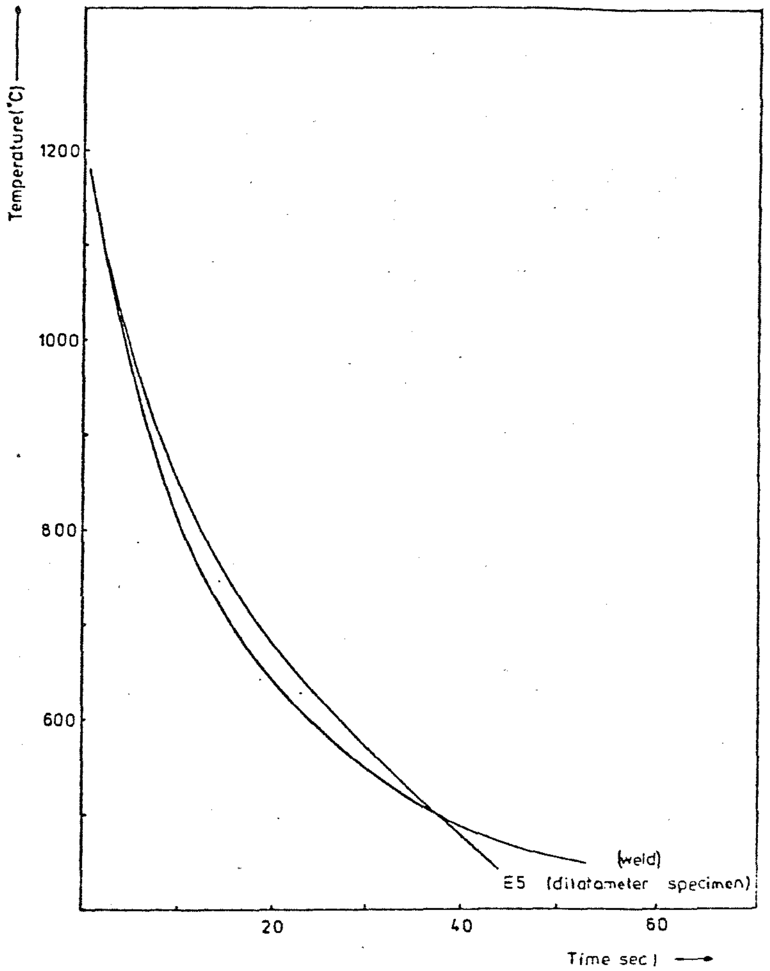

Figure 4.12 Comparison of original weld and weld simulated cooling curves (Linseis dilatometer).

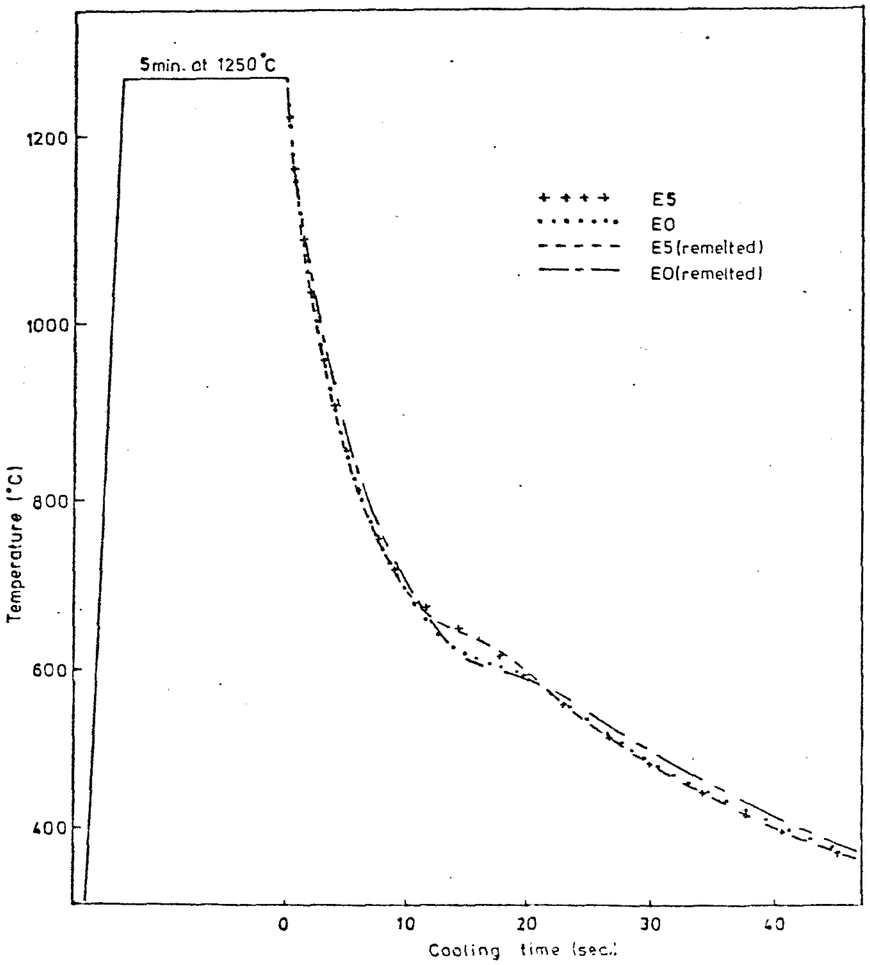

Figure 4.13 Thermal history of dilatometer specimens E0,E0(r),E5, and E5(r).

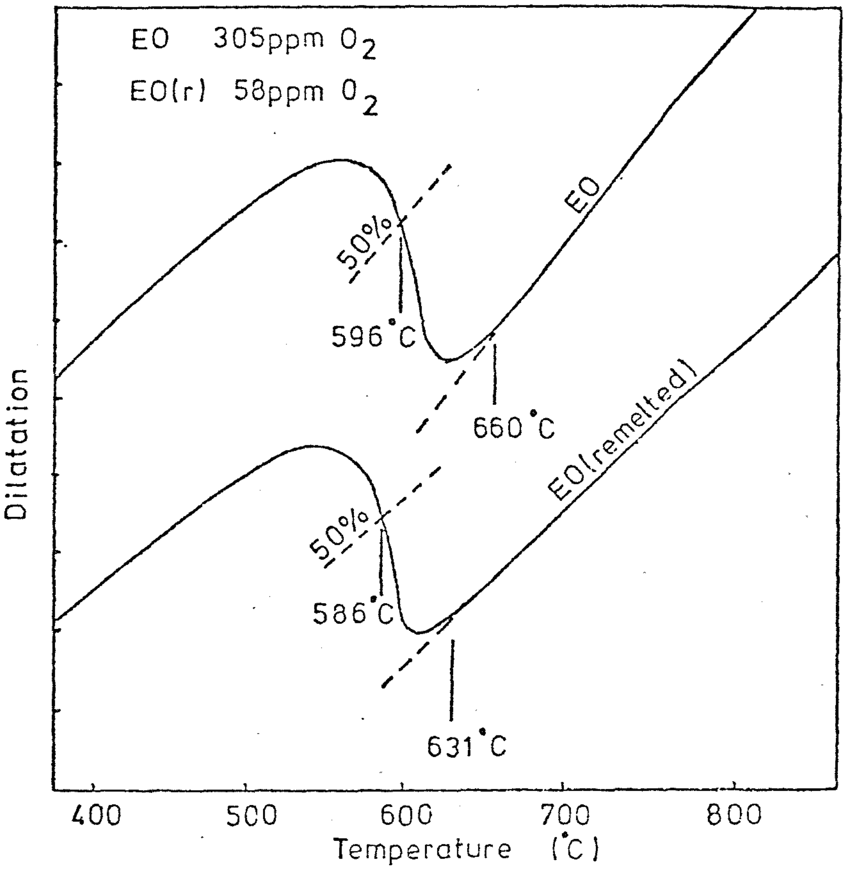

Figure 4.14 Dilatometric data for specimens EO and EO(r).

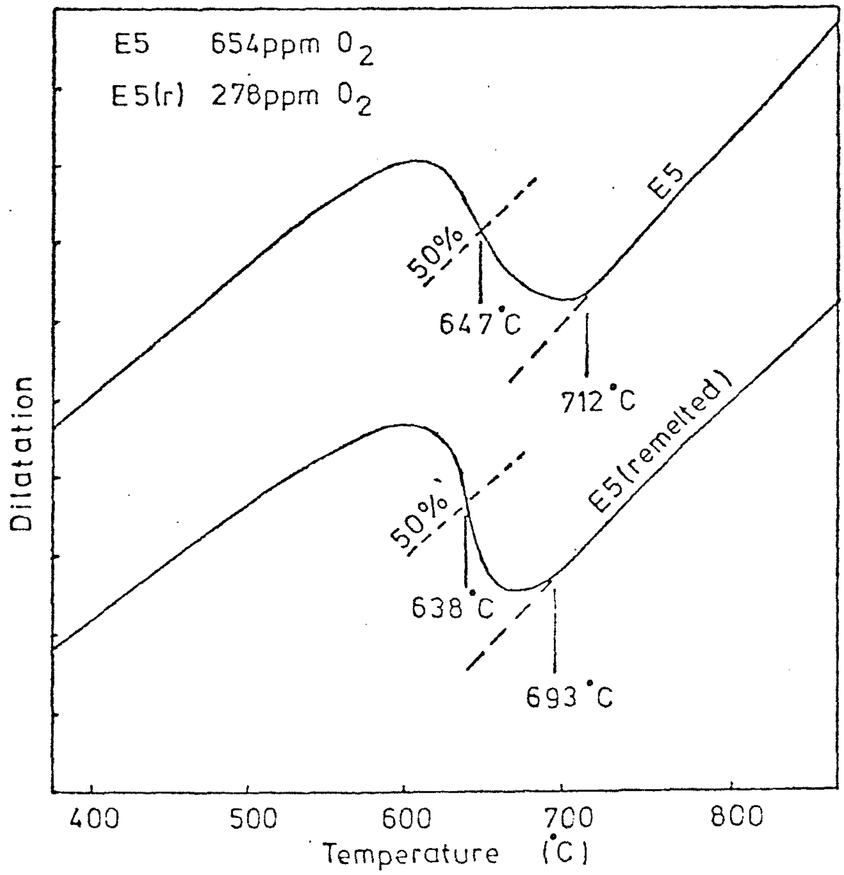

Figure 4.15 Dilatometric data for specimens E5 and E5(r).

of 2½% and 97½% were used in preference to the normal 1% and 99% to reduce scatter. The above data points, along with the pearlite and martensite data points available from some of the dilatometric traces, represent the parts of the CCT diagrams produced entirely by dilatometry.

4.5.3 Thermal analysis

All cooling curves relating to thermal analysis specimens produced distinct thermal arrests due to the liberation of latent heat associated with the $\gamma \rightarrow \alpha$ transformation. The temperature of the start of transformation (T_s) estimated from these arrests, are plotted directly onto the CCT diagrams.

Estimates of T_s, using the inverse rate method were not used as the necessary reference cooling curve for specimens not undergoing transformation were not available [162].

A detailed discussion of the thermal analysis technique and its associated errors is given in the appendix.

4.6 Optical Metallography

4.6.1 Qualitative examinations

Micrographs of the original weld metals used in the investigations are presented in Figures 4.16 to 4.29. These micrographs are considered representative of typical top run (i.e. as deposited) weld metal.

Detailed metallographic examinations were also carried out on all dilatometric and thermal analysis specimens in order to identify the various transformation products.

After studying every specimen in some detail, the following phases and morphologies were identified for presentation on the CCT diagrams. These are illustrated in Figures as indicated.

Polygonal ferrite (PF)	-	Polygonal or equiaxed at slow cooling rate. Grain boundary allotriomorphs at faster cooling rates (Figure 4.30).
Pearlite (P)	-	Pearlite or pearlitic carbides (Figure 4.30).

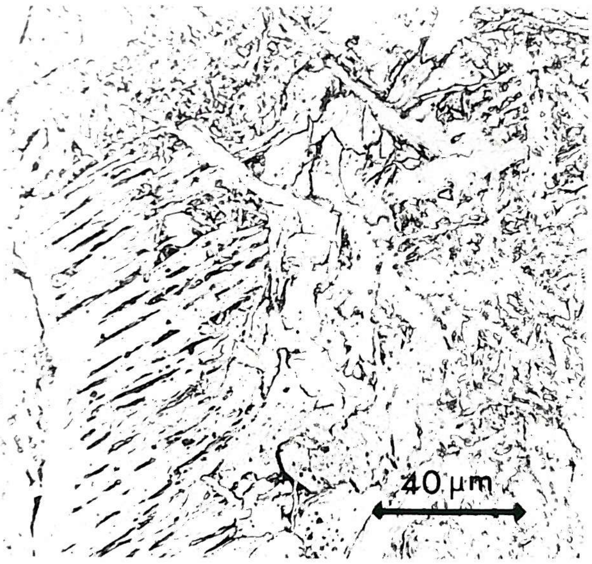

Figure 4·16 M1

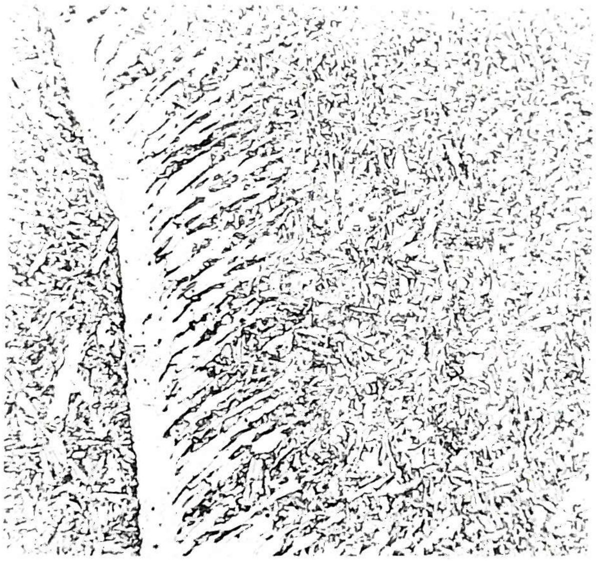

Figure 4·17 M2

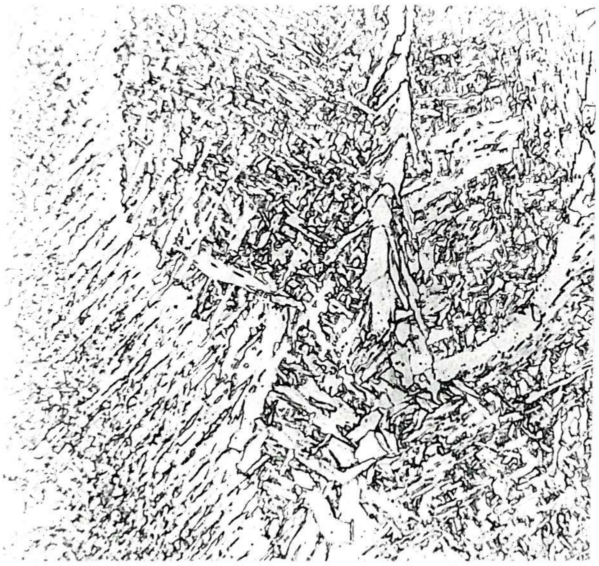

Figure 4·18 M3

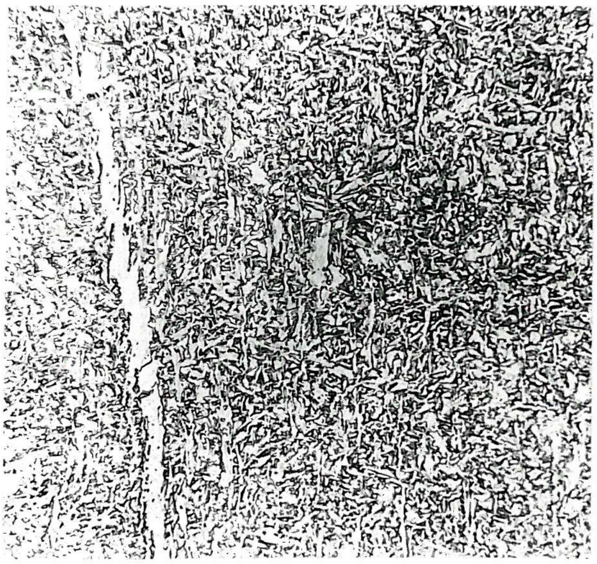

Figure 4·19 M4

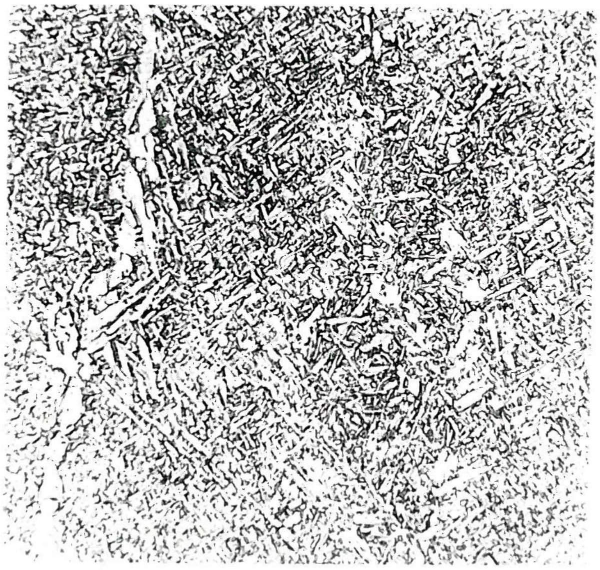

Figure 4·20 M5

Microstructure of as deposited
C-Mn MMA weld metals.
2% nital etch ×500

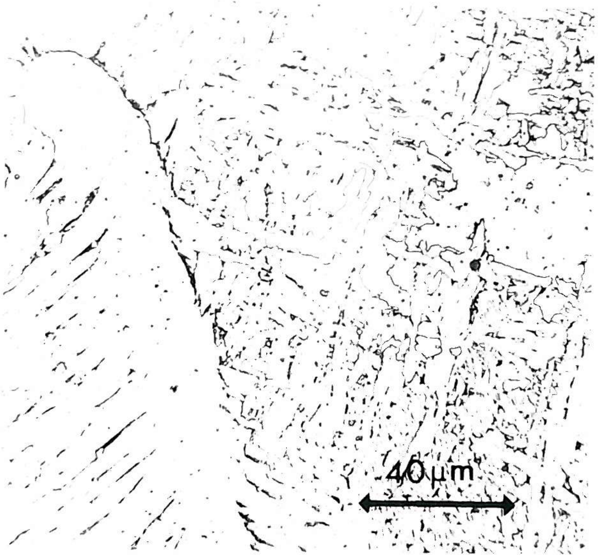

Figure 4·21 N1

Figure 4·22 N2

Figure 4·23 N3

Figure 4·24 N4

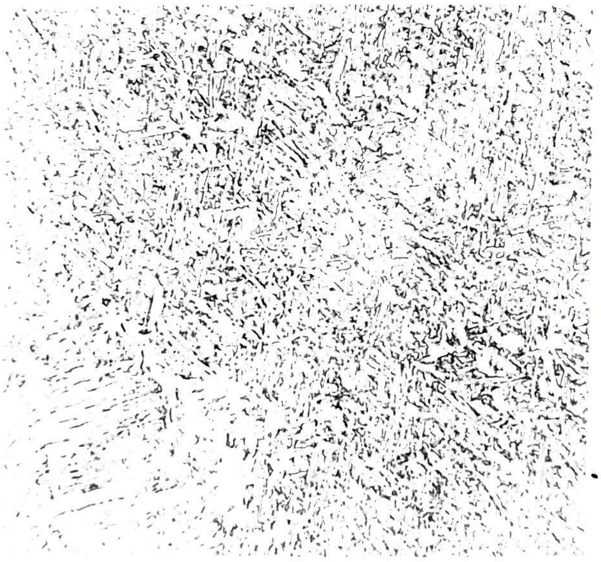

Figure 4·25 N4A

Microstructure of as deposited C-Mn-(Ni) MMA weld metals. 2% nital etch ×500

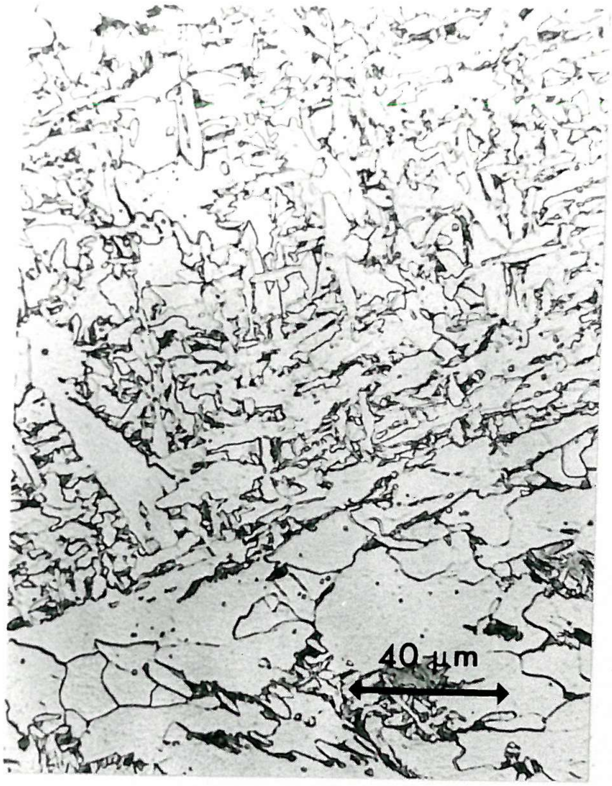

Figure 4·26 A0

Figure 4·27 E0

Figure 4·28 A5

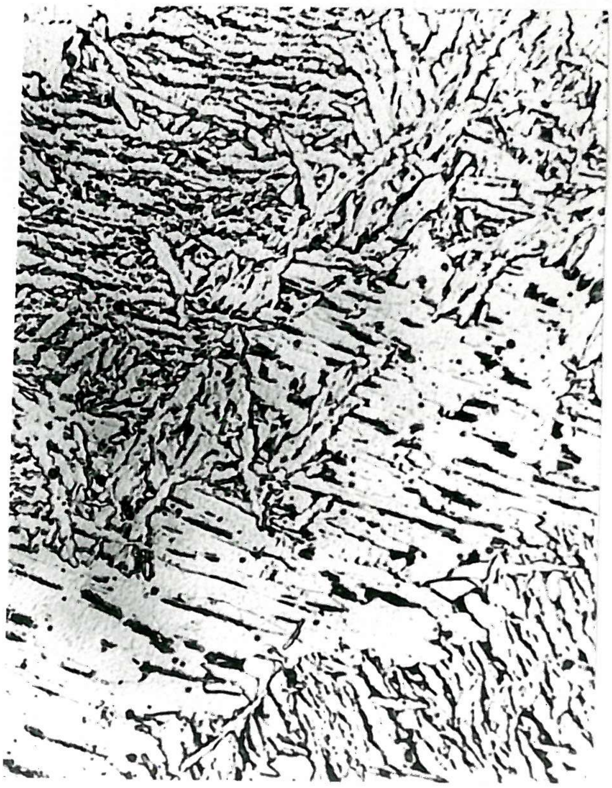

Figure 4·29 E5

Microstructure of as deposited C – Mn – (Nb) SA weld metals.
2% nital etch × 500

Ferrite Sideplates (FSP) - Sideplate structures growing directly from polygonal ferrite or grain boundary allotriomorphs, i.e. Widmanstätten secondary sideplates (Figure 4.34).

Acicular Ferrite (AF) - Intragranular product of fine interlocking ferrite grains separated by high angle boundaries, and aspect ratios from $\sim$3:1 to 10:1 (figure 4.32).

Corase Acicular Ferrite (CAF) - Refers to the intragranular product formed at slower cooling rates than acicular ferrite with large grain size and may be associated with carbides (Figure 4.33).

Lath Ferrite (LF) - Refers to the predominantly intragranular product resembling bainite which sometimes forms amongst acicular ferrite, or side-plate structures. Carbides may or may not be present (Figure 4.35).

Martensite (M) - Lath martensite (Figure 4.31).

When cooled at sufficiently slow cooling rates many of the weld metals under investigation transformed to an equilibrium polygonal ferrite - pearlite microstructure as illustrated in Figure 4.30. The amount of pearlite in the microstructure was in fairly good agreement with that predicted by the lever rule, as shown in Figure 4.36. In a few of the lowest hardenability weld metals there was also some evidence of occasional intergranular cementite films between polygonal ferrite grains.

As the cooling rate was progressively increased there was a tendency for polygonal ferrite grains to become refined and limited to prior austenite grain boundaries and triple points. This morphology is often referred to as grain boundary allotriomorphs and was a common feature of many of the weld metals studied.

The effect of progressively increasing cooling rate on the pearlite reaction was to reduce the amount of pearlite and eventually eliminate it completely from the microstructure. The structure of the pearlite also changed from parallel lamellar colonies to a more degenerate morphology with increasing cooling rate.

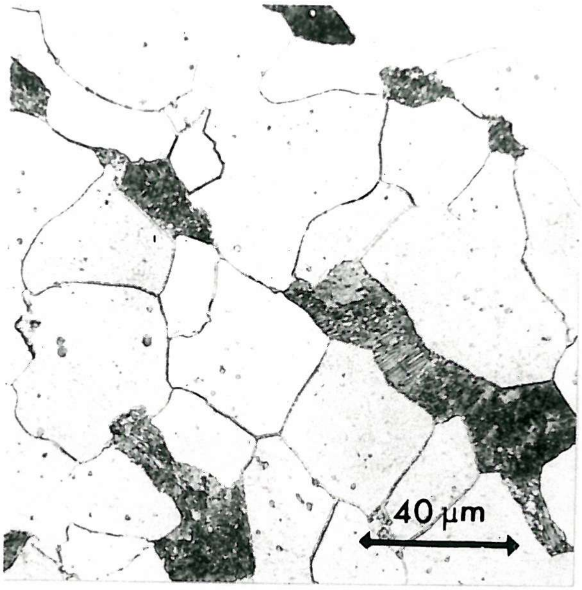

Figure 4·30 Polygonal ferrite and Pearlite (PF and P)

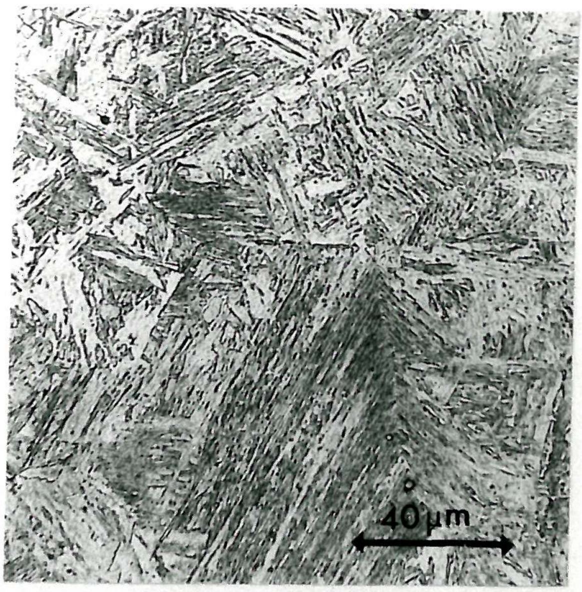

Figure 4·31 Lath Martensite (M)

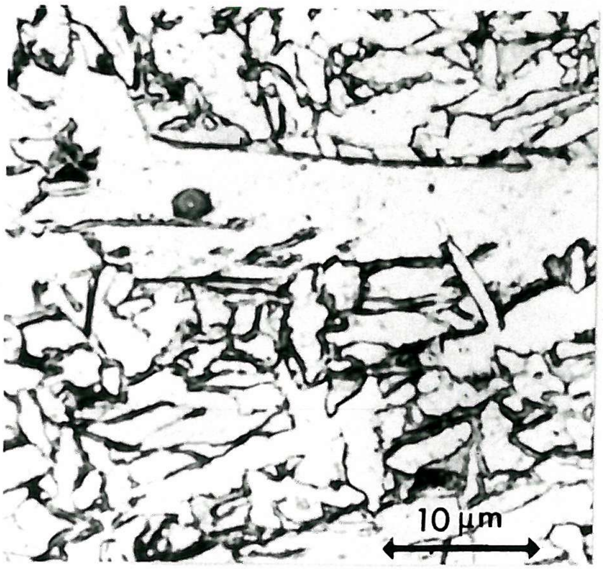

Figure 4·32 Acicular ferrite (AF)

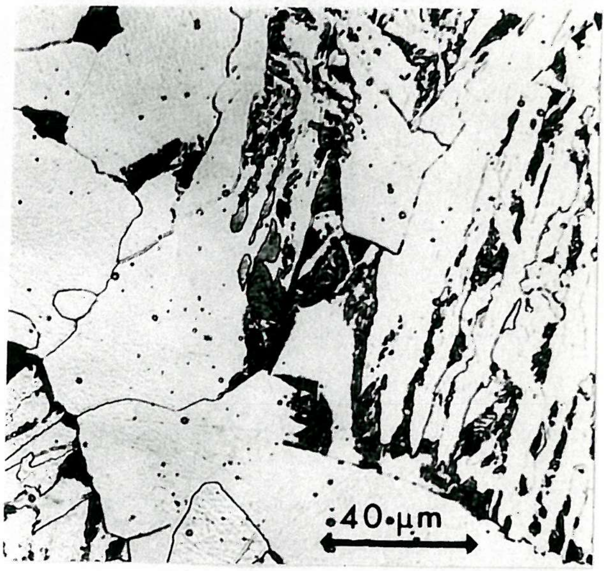

Figure 4·33 Coarse acicular ferrite (CAF)

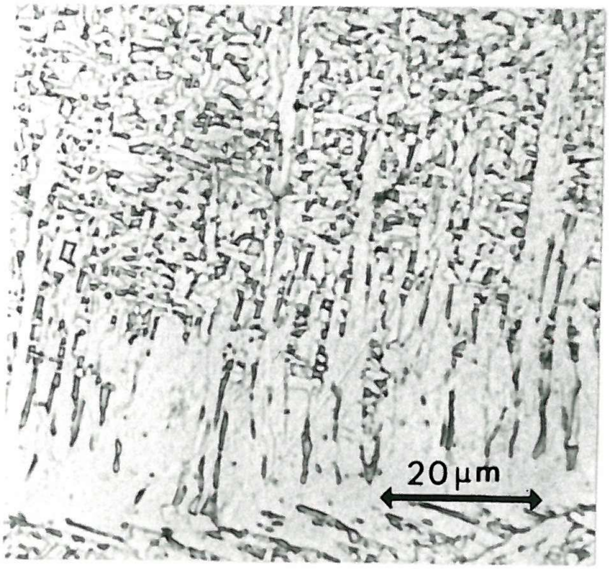

Figure 4·34 Ferrite sideplates (FSP)

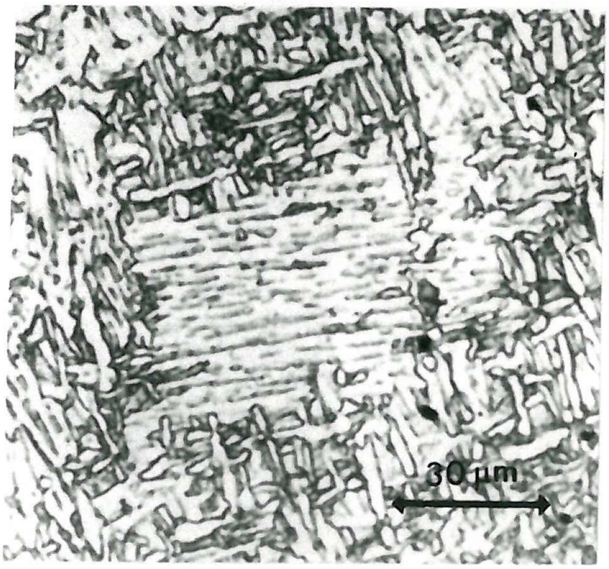

Figure 4·35 Lath ferrite (LF)

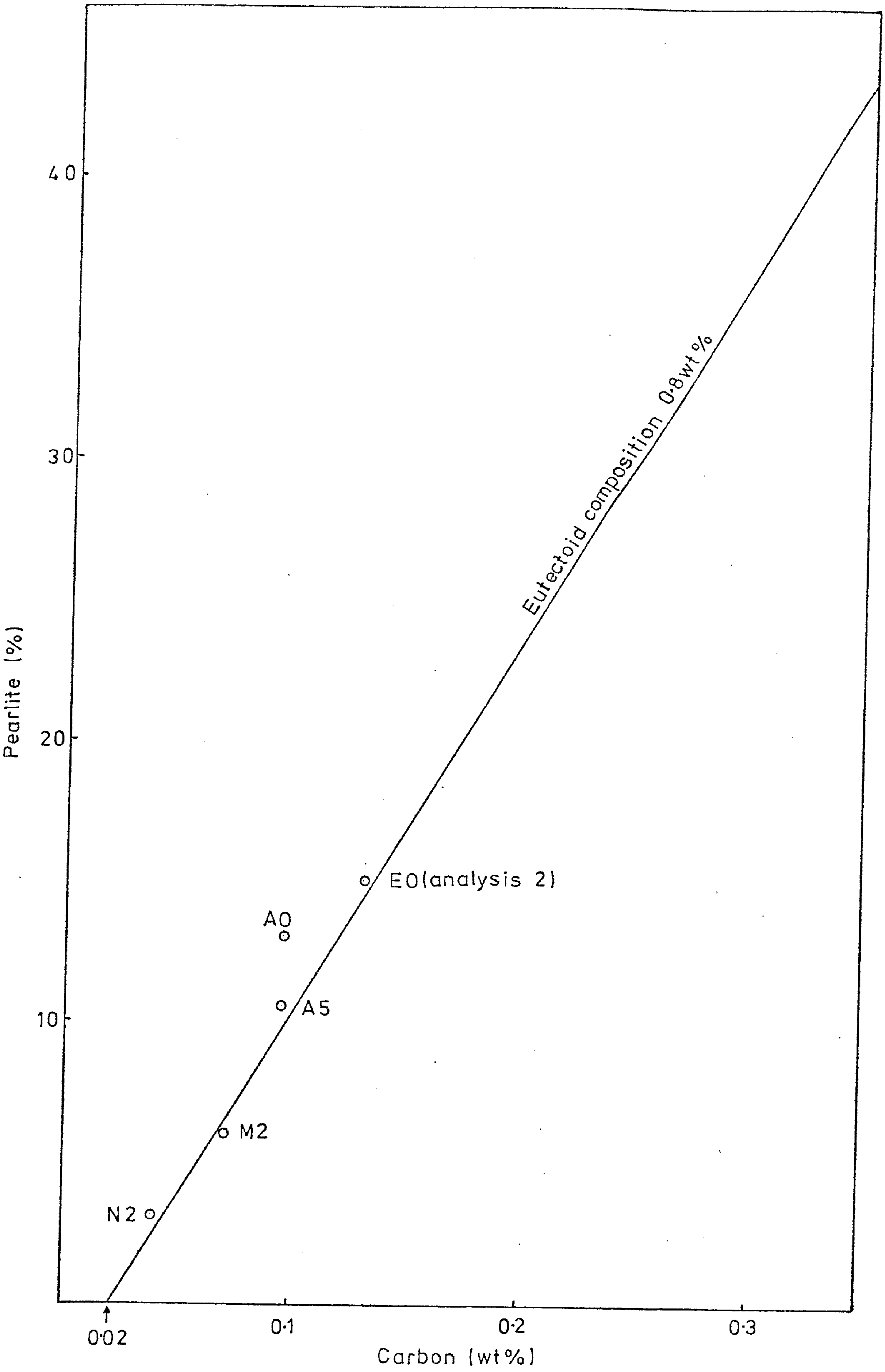

Figure 4.36 Relationship between carbon content and volume fraction of pearlite for slow cooled weld metals.

Most of the weld metals investigated appeared to show some tendency to develop Widmanstätten sideplate morphologies. In the majority of cases these structures could be identified as Widmanstätten Secondary sideplates which ranged from single, or multiple, coarse sideplates growing out of large polygonal ferrite grains at slow cooling rates, to fine colonies of secondary sideplates, growing out of grain boundary allotriomorphs, at faster cooling rates. In all cases, increased cooling rate tended to increase the ratio of sideplates to polygonal ferrite in the final microstructure.

When cooled at intermediate cooling rates almost all weld metals showed some evidence of intragranular transformation. The products described as acicular ferrite and coarse acicular ferrite accounted for the majority of these transformations and appeared to form as a continuous series of intragranular products on the CCT diagrams. Figure 4.32 illustrates a typical acicular ferrite microstructure consisting of fine interlocking ferrite grains (typically 1-3 μm), separated by high angle boundaries. The ferrite allotriomorph shown in this figure is also of interest as it shows a smoothly curved interface with the upper γ grain, but a ragged and irregular interface with the lower γ grain. This characteristic of allotriomorphs was discussed in section 2.2.5(a) of the literature review. Figure 4.33 shows coarse acicular ferrite produced at a much slower cooling rate in the same weld metal. This structure is much coarser than acicular ferrite and in this particular weld metal is associated with small regions of fine pearlitic carbides. In most of the weld metals there was a strong tendency for increased cooling rate to favour acicular ferrite at the expense of polygonal ferrite. There were some exceptions however. In the sideplate dominated weld metal (E5) increased cooling rate appeared to favour the sideplate reaction, and in the highly alloyed weld metals increased cooling rates favoured the lath ferrite structure.

The lath ferrite structure is shown in Figure 4.35 and consists of colonies of parallel laths of ferrite separated by retained austenite or carbides. Optical metallography and dilatometry suggest that this product is a form of upper bainite. From section 2.2.5(c) it would seem likely that lath ferrite may appear as any form of upper bainite depending on the weld metal constitution and cooling rate, (e.g. upper bainite, degenerate upper bainite, carbide free acicular bainite, granular bainite or bainite I, II or III).

Lath ferrite also occurred extensively in specimen E0(r) in which the oxygen content had been reduced to 58 ppm during remelting. Figures 4.37 and 4.38 illustrate the microstructures of E0 and E0(r) and show the dramatic microstructural change from fine acicular ferrite to lath ferrite caused by the removal of deoxidation products. Figures 4.39 and 4.40 show the microstructures of E5 and E5(r). In this case the reduced oxygen content has simply reduced the proportion of polygonal ferrite in favour of more sideplates and acicular ferrite.

4.6.2 Quantitative examinations

The results of the quantitative metallographic examinations of the original weld metals are given in Table 4.5. It can be seen that both manganese and nickel promote acicular ferrite development, at the expense of polygonal and sideplate ferrite, in the alloying ranges investigated. At the highest alloying levels lath ferrite and martensite development starts to become significant. In the case of the submerged arc C-Mn-(Nb) welds, niobium can be seen to promote acicular ferrite in the OP41TT flux series, but promotes sideplates in the 503 series.

The results of the quantitative examinations of the dilatometer specimens are presented on the relevant CCT diagrams (Figures 4.47 to 4.58). Due to the equiaxed grain structure of the reheated specimens, the relative proportions of grain boundary and intragranularly nucleated phases differs slightly from the original welds. However, the trends described above concerning the influence of Mn, Ni and Nb are identical.

The technique used to combine quantitative metallographic data and dilatometric data involves the use of a graphical construction and is described in Chapter 2. This procedure has been carried out to produce the data points dividing grain boundary and intragranularly nucleated products in the CCT diagrams.

The accuracy of the line dividing these products depends largely on the accuracy of the metallographic data and the graphical construction involved. In addition, it is unlikely that one reaction stops at precisely the same temperature the other reaction starts, but more likely the two reactions overlap for a certain temperature range. For these reasons the line dividing these products should not be taken as being absolute, but rather as a guide to the change in transformation behaviour.

Figure 4·37 E0

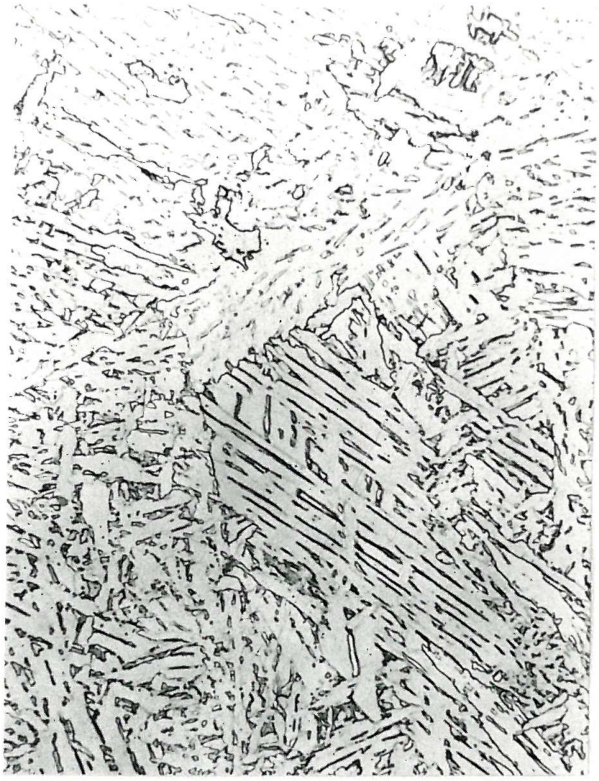

Figure 4·38 E0(remelted)

Figure 4·39 E5

Figure 4·40 E5(remelted)

Microstructure of weld simulated dilatometer specimens before and after remelting. 2% nital etch ×500

Weld Ident-ification	Transformation Product (%)					γ-grain size ($\bar{L}$)
	PF	FSP	AF + CAF	LF	M	
M1	31%	27%	42%	-	-	94µm
M2	15%	13%	72%			96µm
M3	21%	8%	70%	1%	-	95µm
M4	9%	9%	81%	1%	-	88µm
M5	8%	9%	79%	4%	-	44µm
N1	45%	30%	25%			132µm
N2	17%	19%	57%	7%		96µm
N3	15%	11%	66%	8%	-	75µm
N4	25%	18%	51%	6%	-	68µm
N4A	11%	10%	68%	8%	3%	64µm
A0	29%	4%	67%	-	-	93µm
E0	7%	2%	91%	-	-	82µm
A5	51%	2%	47%	-	-	80µm
E5	33%	58%	9%	-	-	85µm

TABLE 4.5: Results of Quantitative metallography for as deposited weld metals.

Similarly, the division between the polygonal and ferrite sideplate reactions cannot be defined absolutely as both products may be growing simultaneously over a certain temperature range. This dividing line is shown as a broken line representing the estimated temperature at which sideplates start to develop. No attempt has been made in the present investigation to divide the regions of lath ferrite, acicular ferrite or coarse acicular ferrite although the latter two could be divided by defining the limits of their grain sizes and aspect ratios.

The results of the prior austenite grain size measurements for reheated weld metals were given in Tables 4.3 and 4.4 and discussed in section 4.4. The results for the as deposited weld metals are given in Table 4.5. In the case of the C-Mn MMA weld metals there is no noticeable difference in prior austenite grain size with varying manganese content. Similarly, the C-Mn-(Nb) SA weld metals show no significant variation in austenite grain size, other than that expected due to experimental error. These results are very interesting because they seem to rule out the possibility that inclusion pinning is a significant factor in influencing as deposited austenite grain size. In the C-Mn series the oxygen content varied by ∼100 ppm across the manganese range. In the C-Mn-Nb series the oxygen content varied by ∼400 ppm due to the different flux systems used.

The results of the prior austenite grain size measurements for the C-Mn-Ni series are also very interesting. From Table 4.5 it can be seen that the austenite grain size decreases rapidly with increasing nickel content. This result is rather difficult to explain, but it suggests that the kinetics of the $\delta \rightleftharpoons \gamma$ reaction may be important at this carbon level (∼0.03 wt%C).

4.7 Quenching Out

The results of the quenching out investigations are shown in Figures 4.41 to 4.46. Figures 4.41 to 4.44 relate to specimens of EO cooled at 0.4°C/sec and quenched out from 650°C, 600°C and 550°C, and continuously cooled to room temperature, respectively.

Quenching out from 650°C, Figure 4.41 revealed a microstructure composed of a network of polygonal ferrite grains which have probably initially grown from the prior austenite grain boundaries. The intragranular regions of the austenite grains have transformed to a lower temperature transformation product during the quench (probably

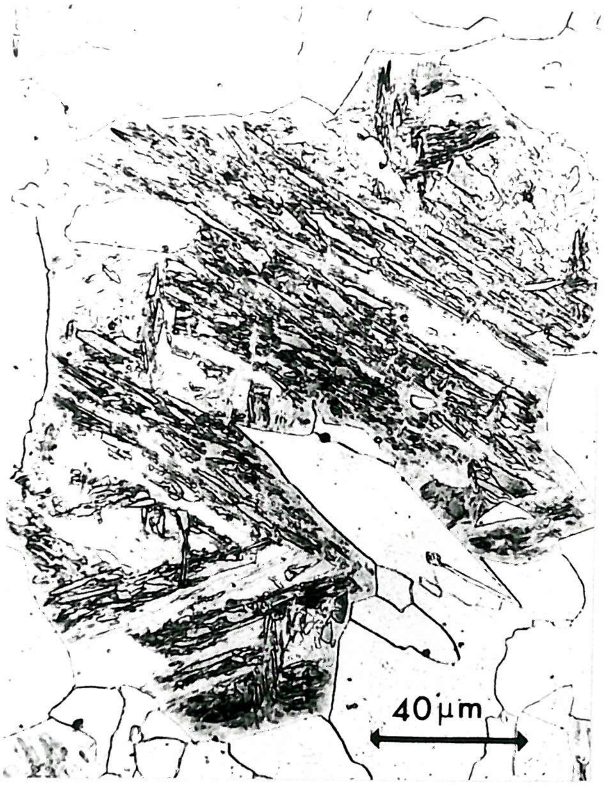

Figure 4·41 EO quenched out from 650°C

Figure 4·42 EO quenched out from 600°C

Figure 4·43 EO quenched out from 550°C

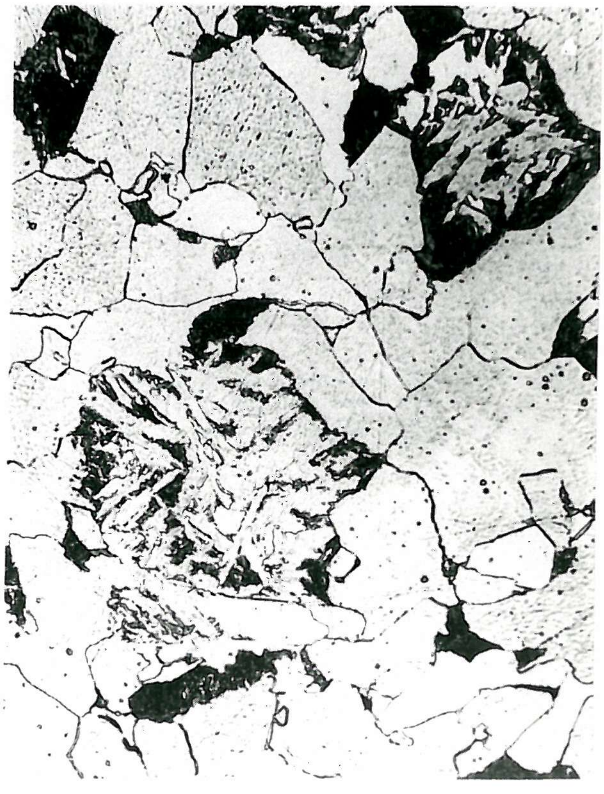

Figure 4·44 EO continuously cooled

Microstructure of weld metal EO after quenching out from various temperatures. Cooling rate 0·4°C/Sec. 2% nital etch ×500 martensite).

Quenching from 600°C, Figure 4.42, shows a similar structure, but this time a few regions of coarse acicular ferrite have nucleated and grown in the intragranular regions. Most of the remaining carbon enriched regions have transformed to martensite although a few small regions of pearlite (not illustrated)were observed.

Quenching from 550°C, Figure 4.43, shows slightly more intragranular CAF to be present and considerably more pearlite. Remaining regions have again transformed to martensite.

Finally, the specimen continuously cooled to room temperature has a microstructure of polygonal ferrite, with isolated intragranular areas of coarse acicular ferrite surrounded by pearlite or fine degenerate pearlitic carbides, (Figure 4.44).

The above observations give a good indication of the course of events during transformation at 0.4°C/sec. Initially, at about 750°C-700°C polygonal ferrite starts to nucleate and grow from prior γ grain boundaries. Between 650°C and 600°C coarse acicular ferrite nucleates and grows in the remaining enriched austenite regions. At about 600°C some of the carbon enriched regions start to transform to pearlite. By 550°C about half the enriched austenite has transformed to pearlite and between 550°C and room temperature the remaining areas transform to degenerate pearlite of pearlitic carbides. These observations are in good agreement with the predictions made from the CCT diagram (Figure 4.55).

A similar investigation was carried out at a cooling rate of 15°C/sec quenching out from 550°C, 500°C and 400°C and also continuously cooling to room temperature. Figure 4.45 shows the microstructure of the specimen quenched out from 550°C. Grain boundary ferrite clearly marks the prior austenite boundary with acicular ferrite in the intragranular regions. The slightly darker regions surrounding the acicular ferrite grains are thought to be martensite, formed during the quench.

Figure 4.46 shows the result of continuous cooling to room temperature. In this case virtually all the intragranular regions have transformed to acicular ferrite. Occasional small regions of pearlitic carbides and grain boundary carbides are also visible, mainly associated with the grain boundary ferrite. These carbides were also confirmed by Watson [57] in TEM investigations of similarly cooled weld metals.

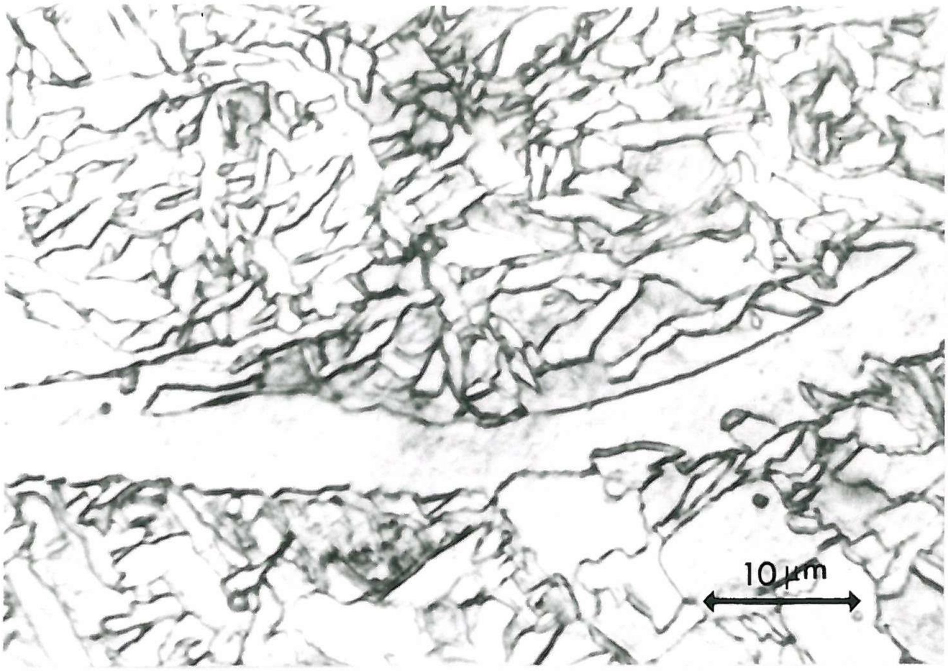

Figure 4·45 Microstructure of E0 quenched out from 550°C. Cooling rate 15°C/Sec. 2% nital etch × 2000.

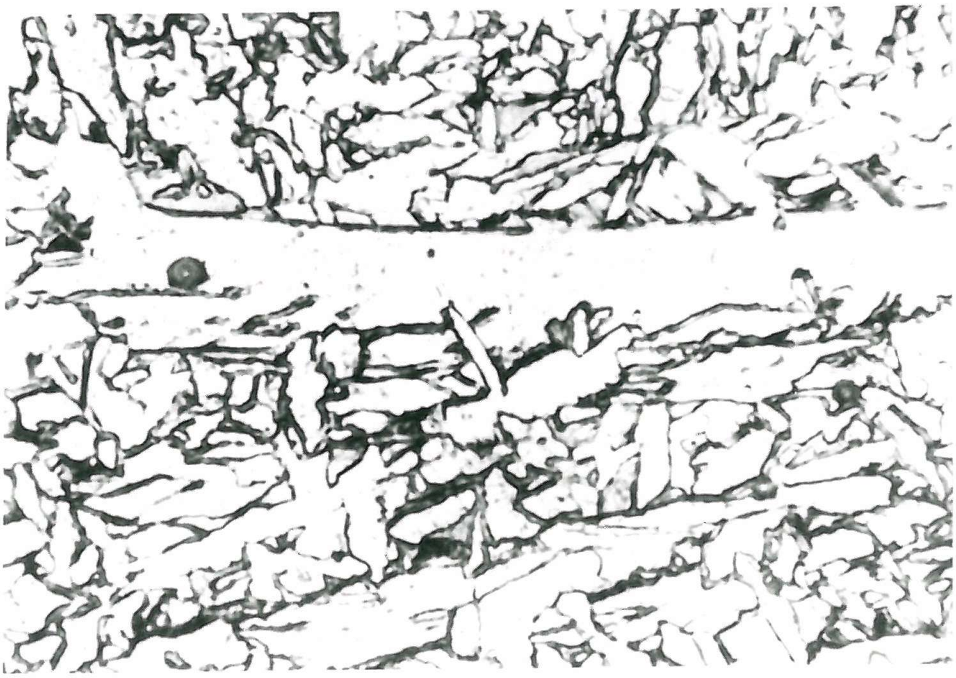

Figure 4·46 Microstructure of E0 continuously cooled to room temperature. Cooling rate 15°C/Sec. × 2000.

Quenching out from 500°C produced a similar microstructure to Figure 4.45 with slightly more acicular ferrite but no carbides. However, quenching out from 400°C did produce some optical evidence of carbides.

From these observations it was deduced that, although the quantity of carbides formed at 15°C/sec was small(<1%) the start of their transformation was probably between 500°C and 400°C.

4.8 Hardness Testing

The results of the Vickers hardness testing are presented directly below the CCT diagrams for ease of reference.

The effect of increasing cooling rate has generally been to increase the hardness of the transformation products.

4.9 CCT Diagrams

To enable the CCT data to be presented in a manner which is both suitable for welding applications and also comparable with existing CCT data it was decided to construct two types of CCT diagrams. The conventional type of diagrams are presented in Figures 4.47(b) to 4.58(b) in which transformation temperature is plotted against the time elapsed from the austenitising temperature, on a log scale. The alternative presentation is given in Figures 4.47(a) to 4.58(a) in which transformation temperature is plotted against log of the cooling rate between 800°C and 500°C. The micrographs associated with both types of CCT diagram are presented next to the diagrams (Figures 4.47(c) to 4.58(c)).

In the case of the conventional presentation, complete cooling curves have been drawn on the CCT diagrams in the temperature range 1250°C to 200°C. At the bottom of each cooling curve the 800 to 500°C cooling rate is given in °C/sec. Quantitative microstructural and Vickers hardness details can be obtained by drawing vertical lines from the CCT diagram to the microstructural "wedge" and hardness diagrams below. Chemical analyses, austenitising treatments and prior austenite grain sizes are also given on each CCT diagram.

In the case of the alternative presentation of CCT data there is no longer any need to know the complete weld metal thermal history from austenitisation. Instead transformation temperature is plotted directly against the cooling rate between 800°C and 500°C on a log scale. Each vertical line on the CCT diagram is therefore representative of one particular cooling rate. The quantitative microstructural information for each cooling rate is presented directly below the transformation temperature data. This presentation differs from the previous wedge diagrams and it should be noted that the total microstructure is obtained through summation of all the individual constituents at any given cooling rate. For ease of application to welding situations, the normal arc welding cooling rate range of $3^{o}C/sec$ to $30^{o}C/sec$ is indicated on the diagrams. Cooling times between $800^{o}C$ and $500^{o}C$ (Δt 800/500) are also presented.

In both varieties of CCT diagram the microstructural constituents are characterised using the notation system discussed in section 4.6. The six micrographs accompanying each CCT diagram have been selected at the following approximate cooling rates of $1^{o}C/sec$, $8^{o}C/sec$, $30^{o}C/sec$, $45^{o}C/sec$, $90^{o}C/sec$ and $>300^{o}C/sec$ to enable direct comparisons between different materials and cooling rates to be made.

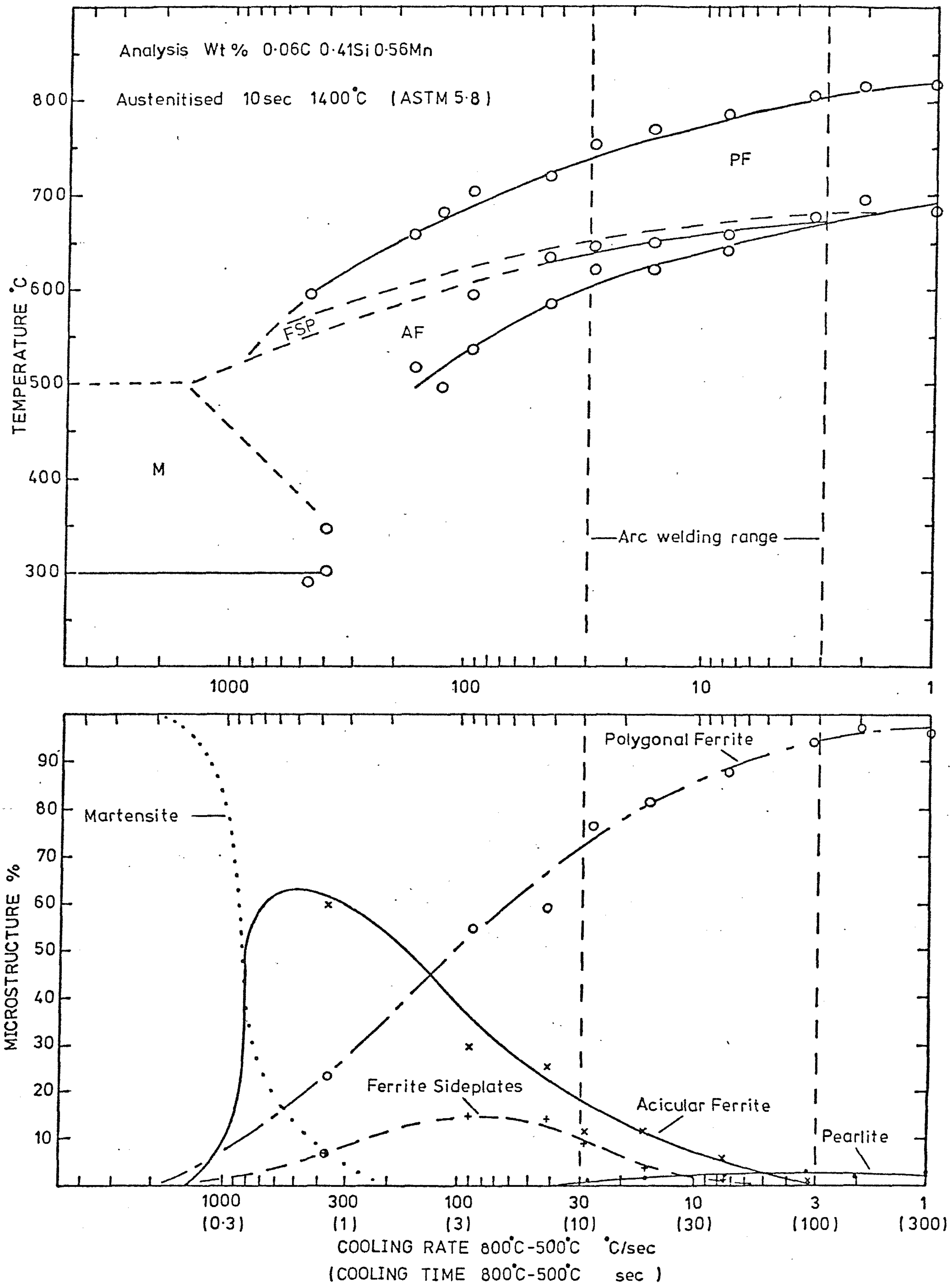

Figure 4.47(a) CCT diagram for weld metal M1.

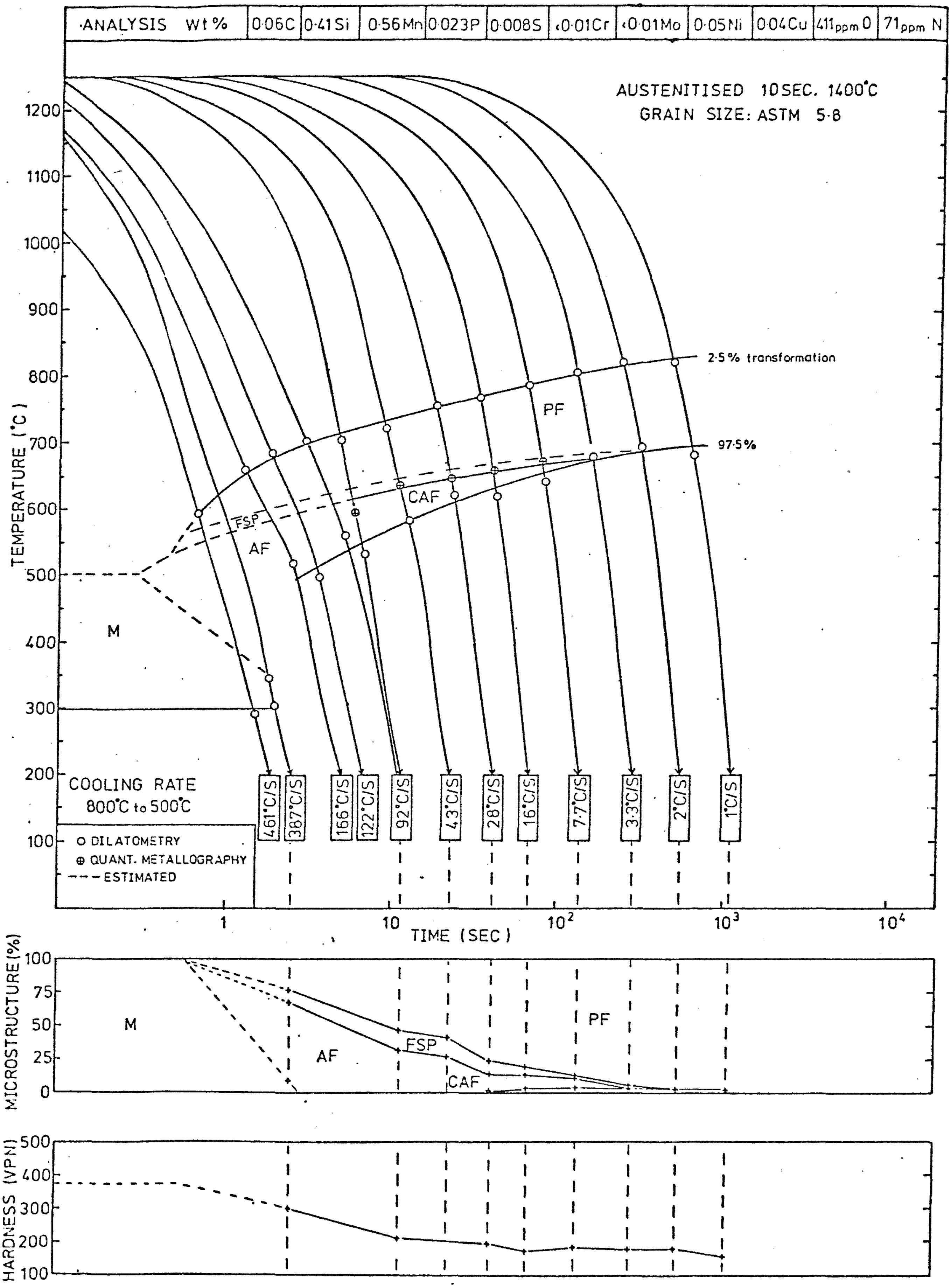

Figure 4.47(b) CCT diagram for weld metal M1.

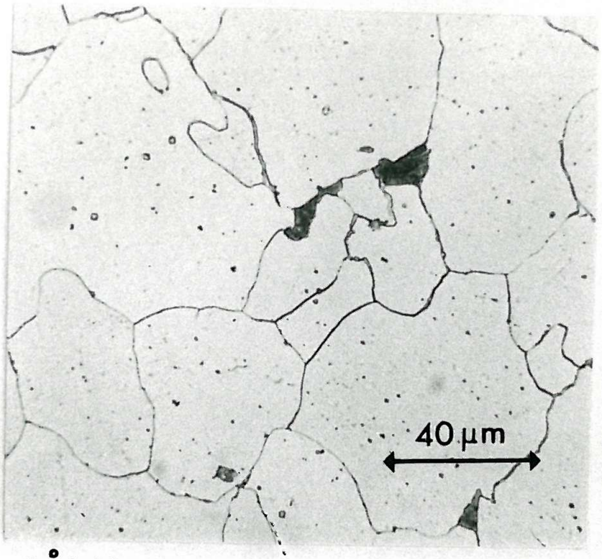

1 °C/Sec

7·7 °C/Sec

28 °C/Sec

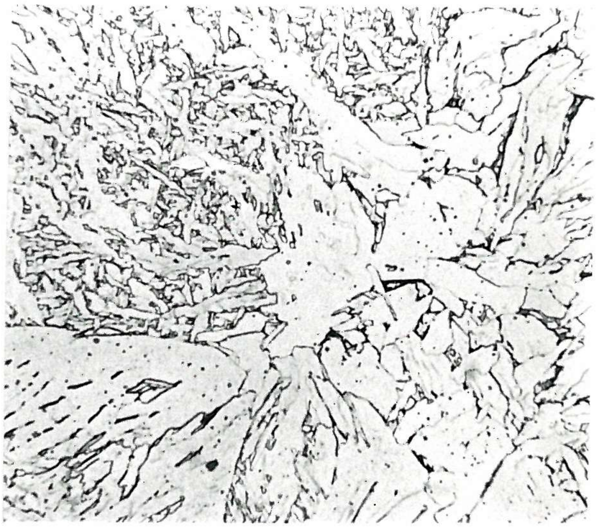

43 °C/Sec

92 °C/Sec

387 °C/Sec

Figure 4·47(c)

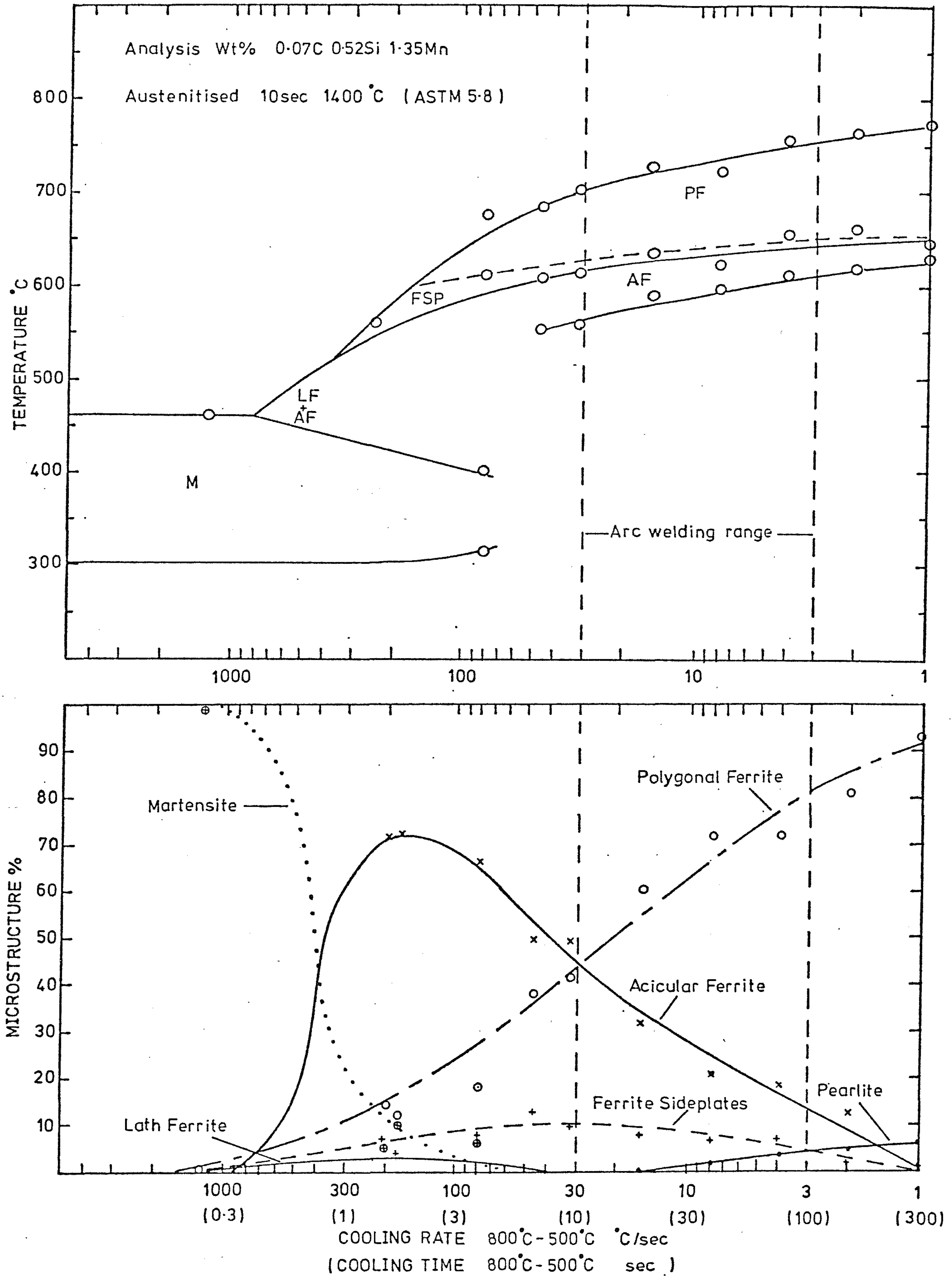

Figure 4.48(a) CCT diagram for weld metal M2.

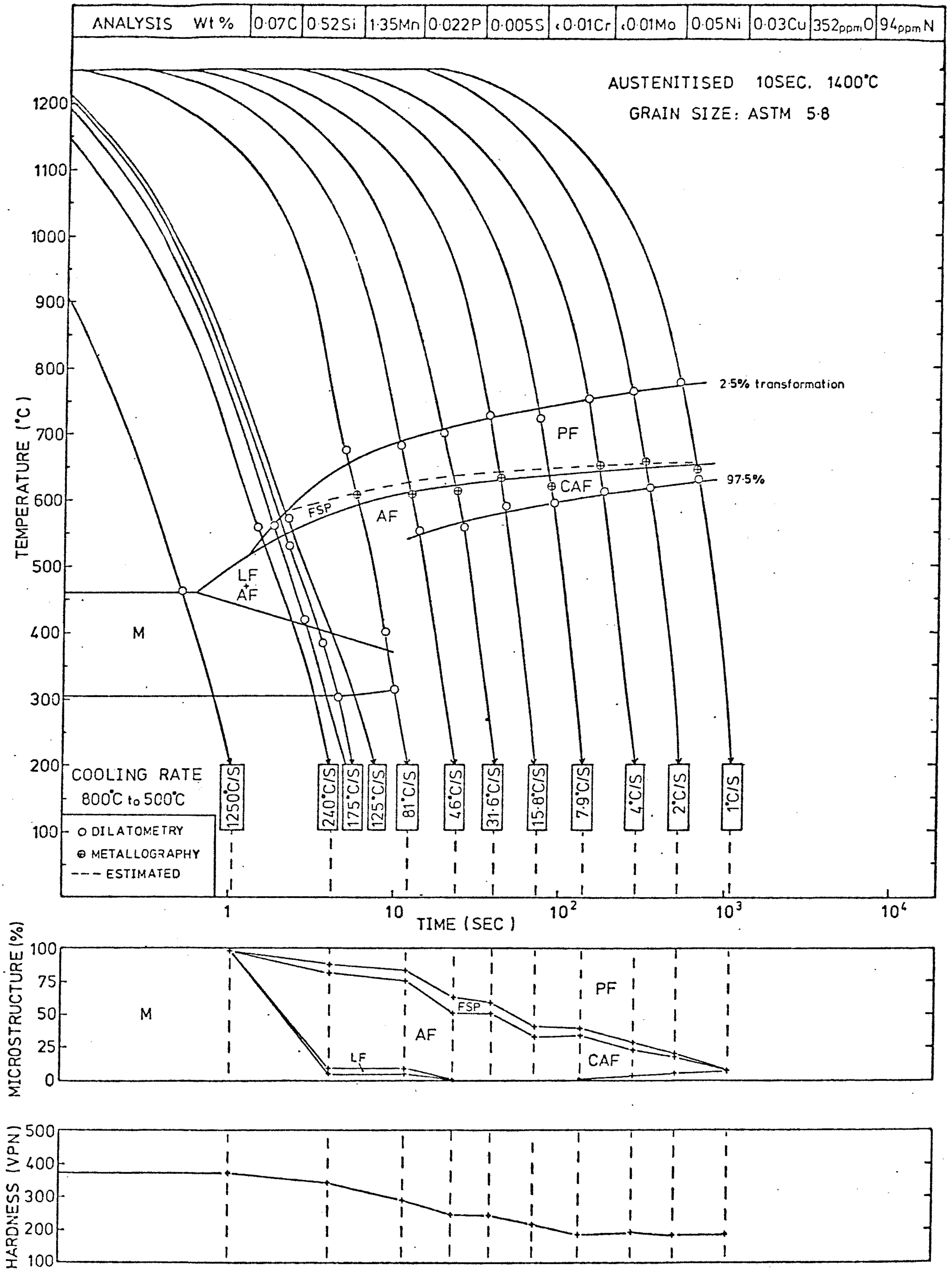

Figure 4.48(b) CCT diagram for weld metal M2.

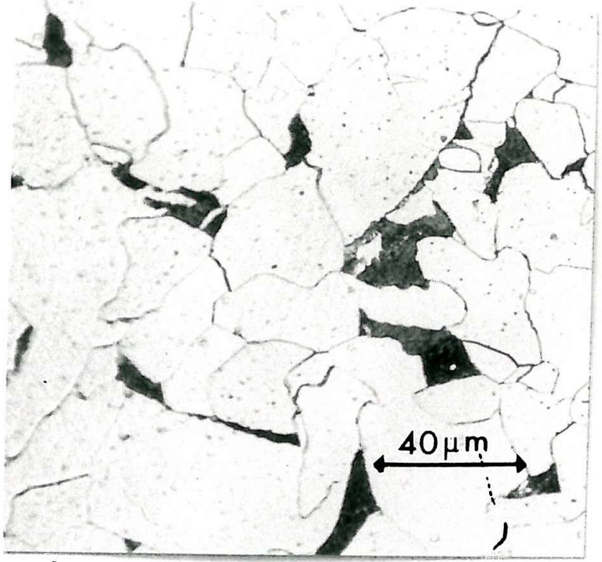

1°C/Sec

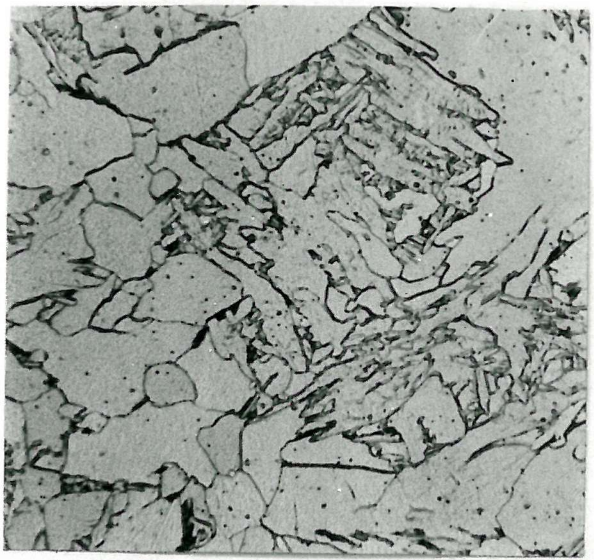

8°C/Sec

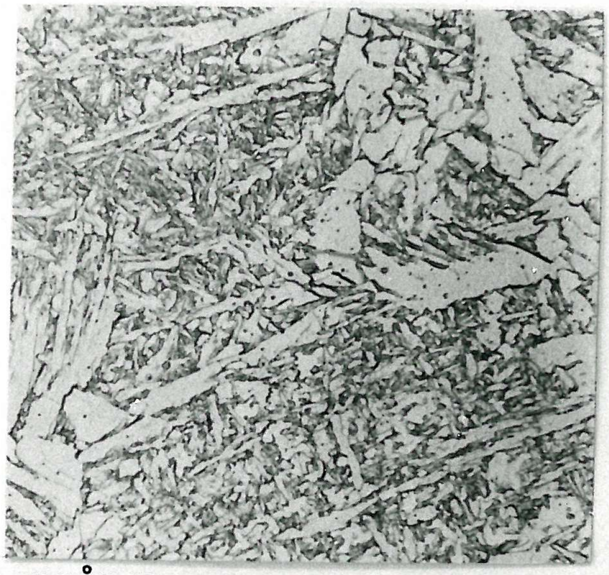

32°C/Sec

46°C/Sec

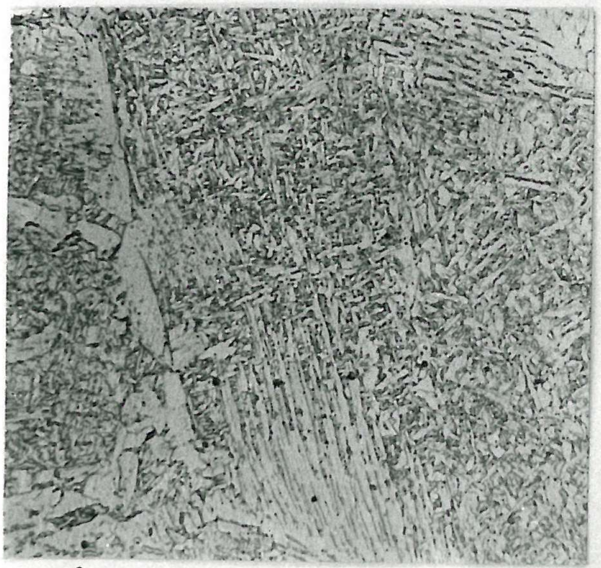

81°C/Sec

1250°C/Sec

Figure 4·48(c)

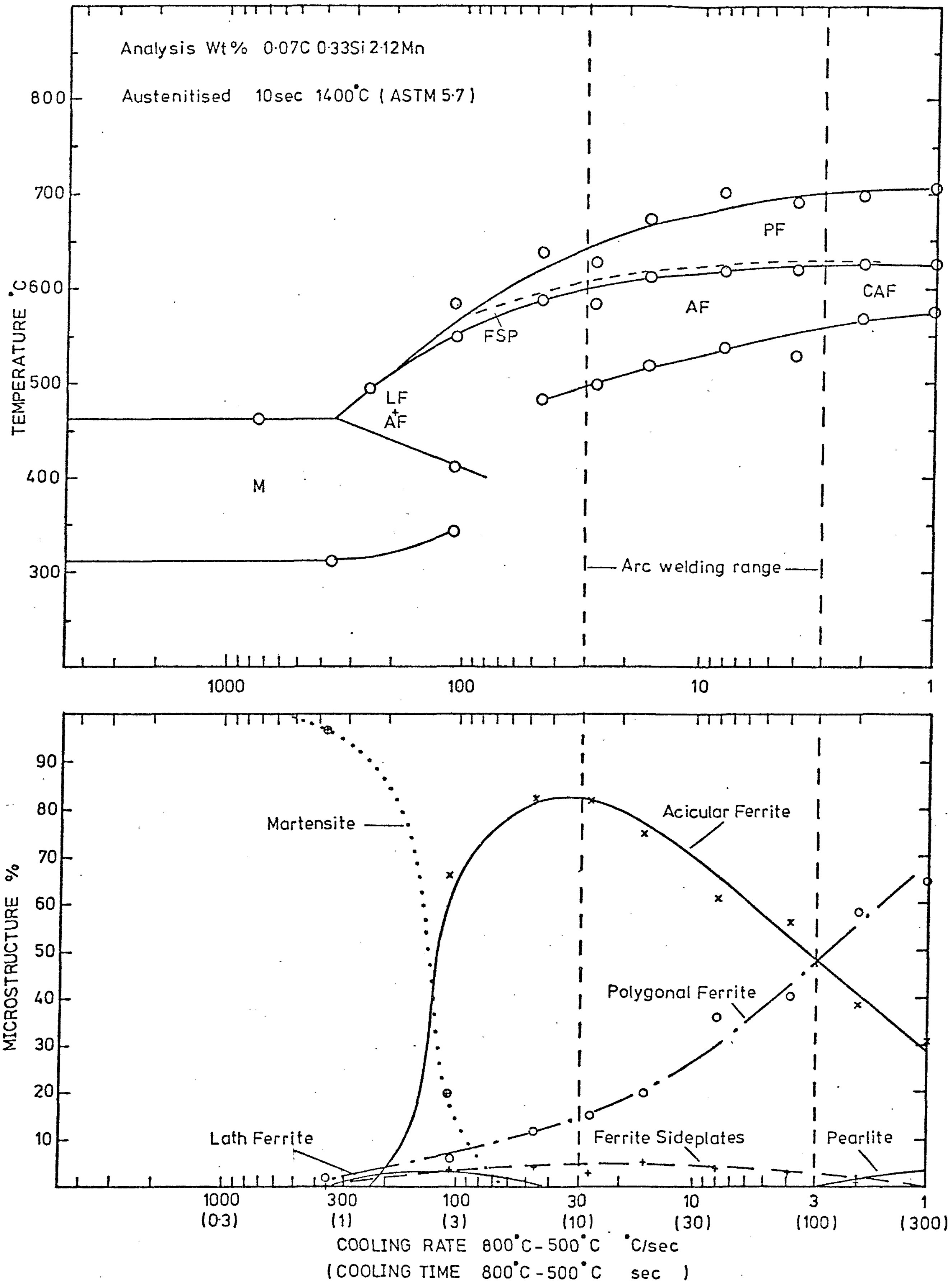

Figure 4.49(a) CCT diagram for weld metal M5.

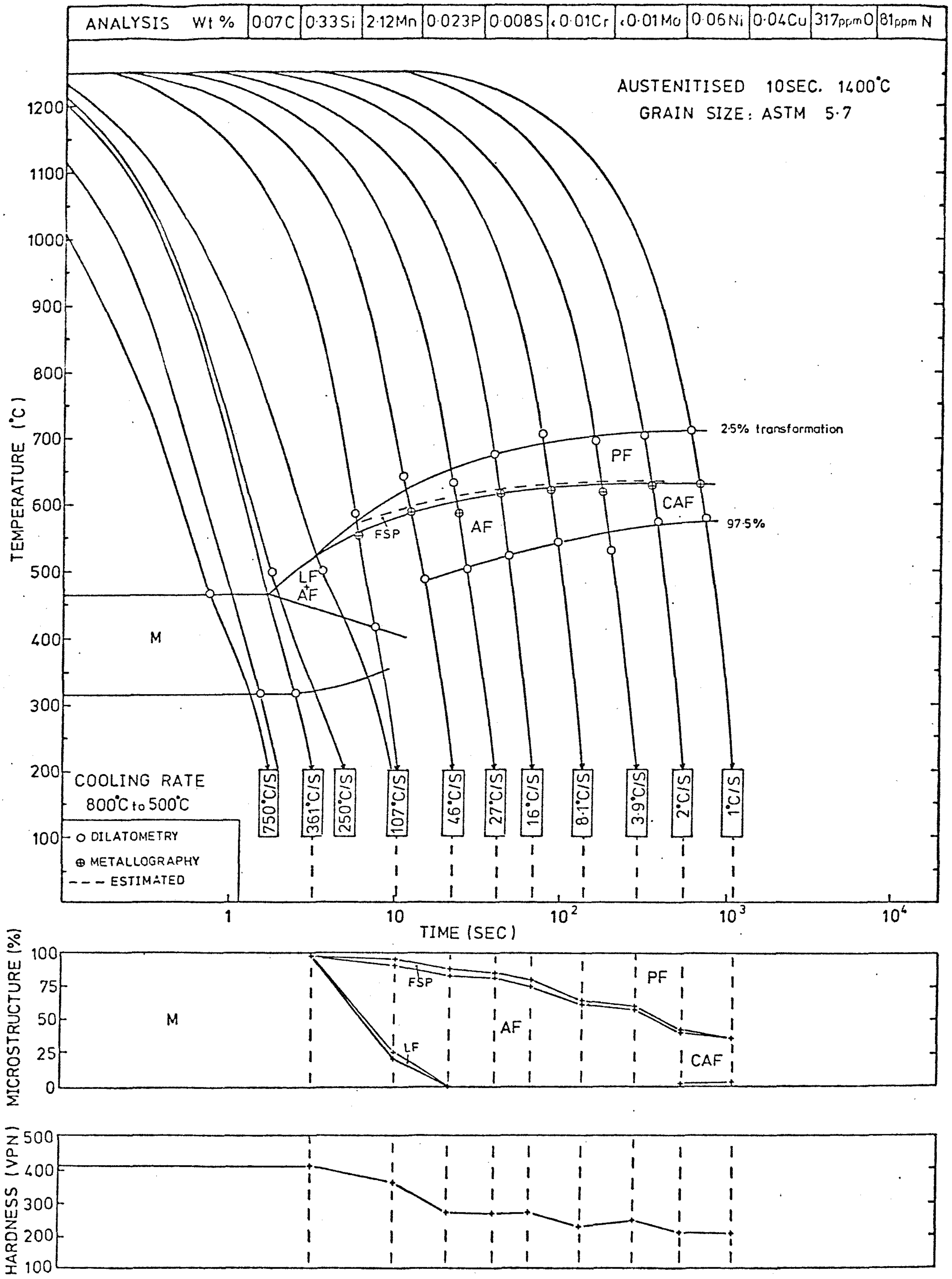

Figure 4.49(b) CCT diagram for weld metal M5.

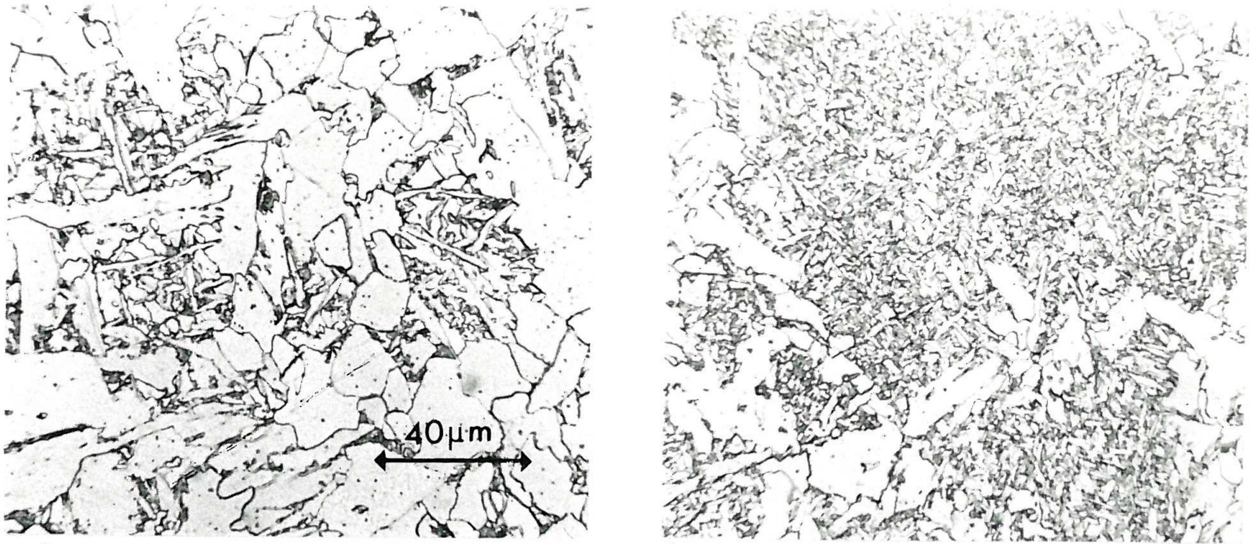

1°C/Sec 8·1°C/Sec

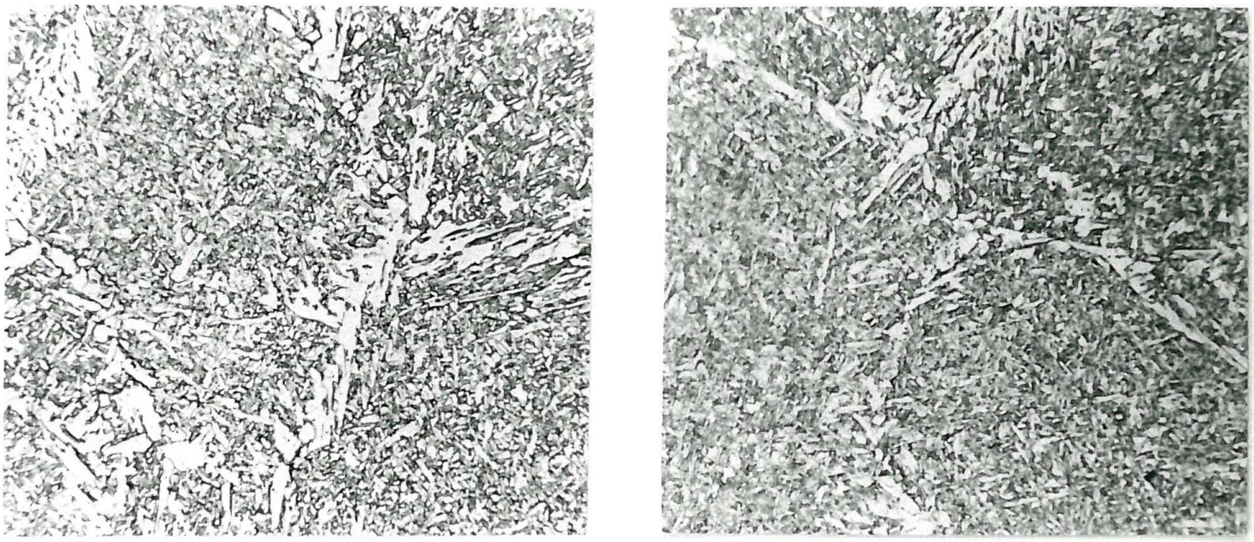

27°C/Sec 46°C/Sec

107°C/Sec 361°C/Sec

Figure 4·49(c)

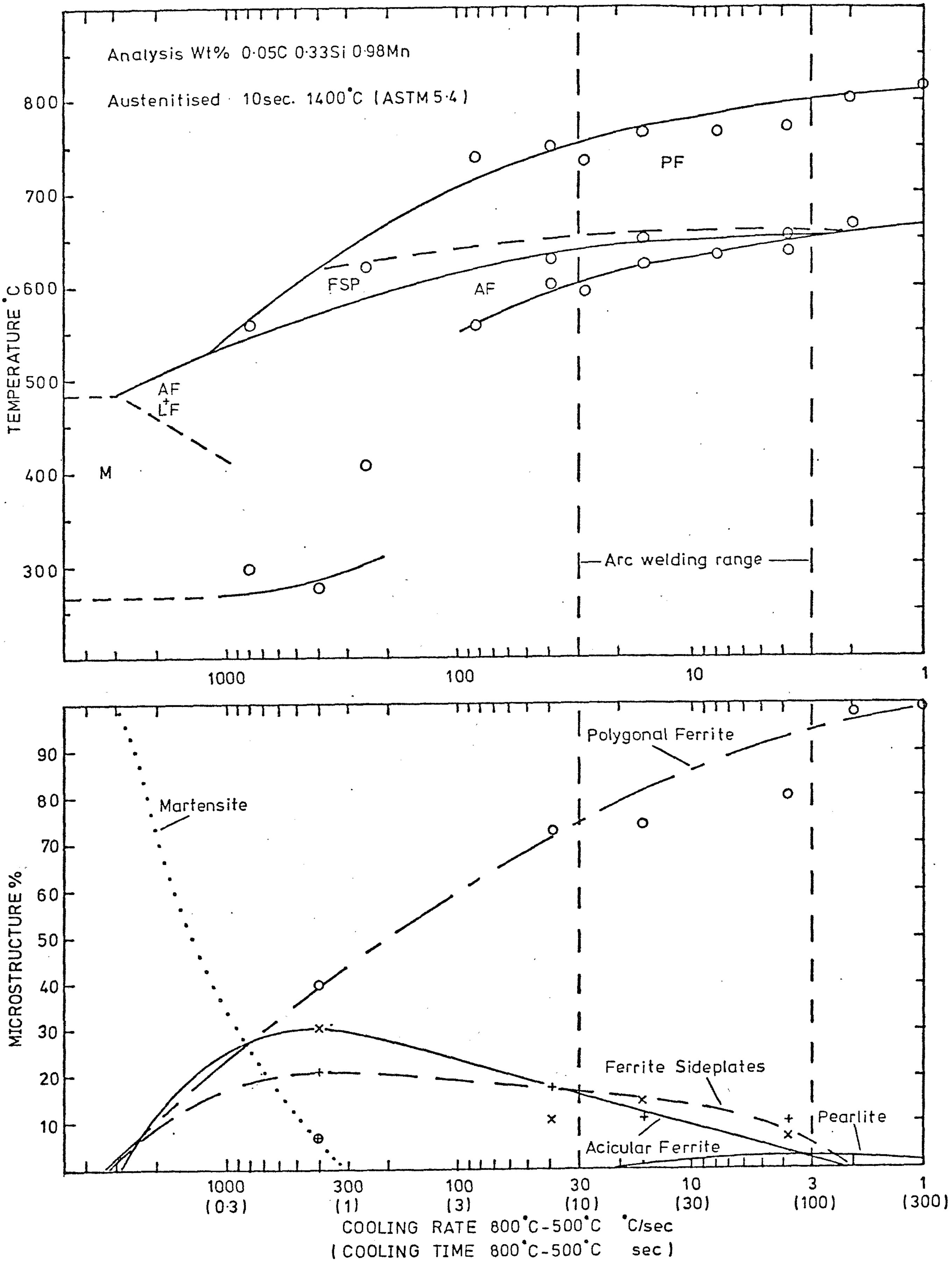

Figure 4.50(a) CCT diagram for weld metal N1.

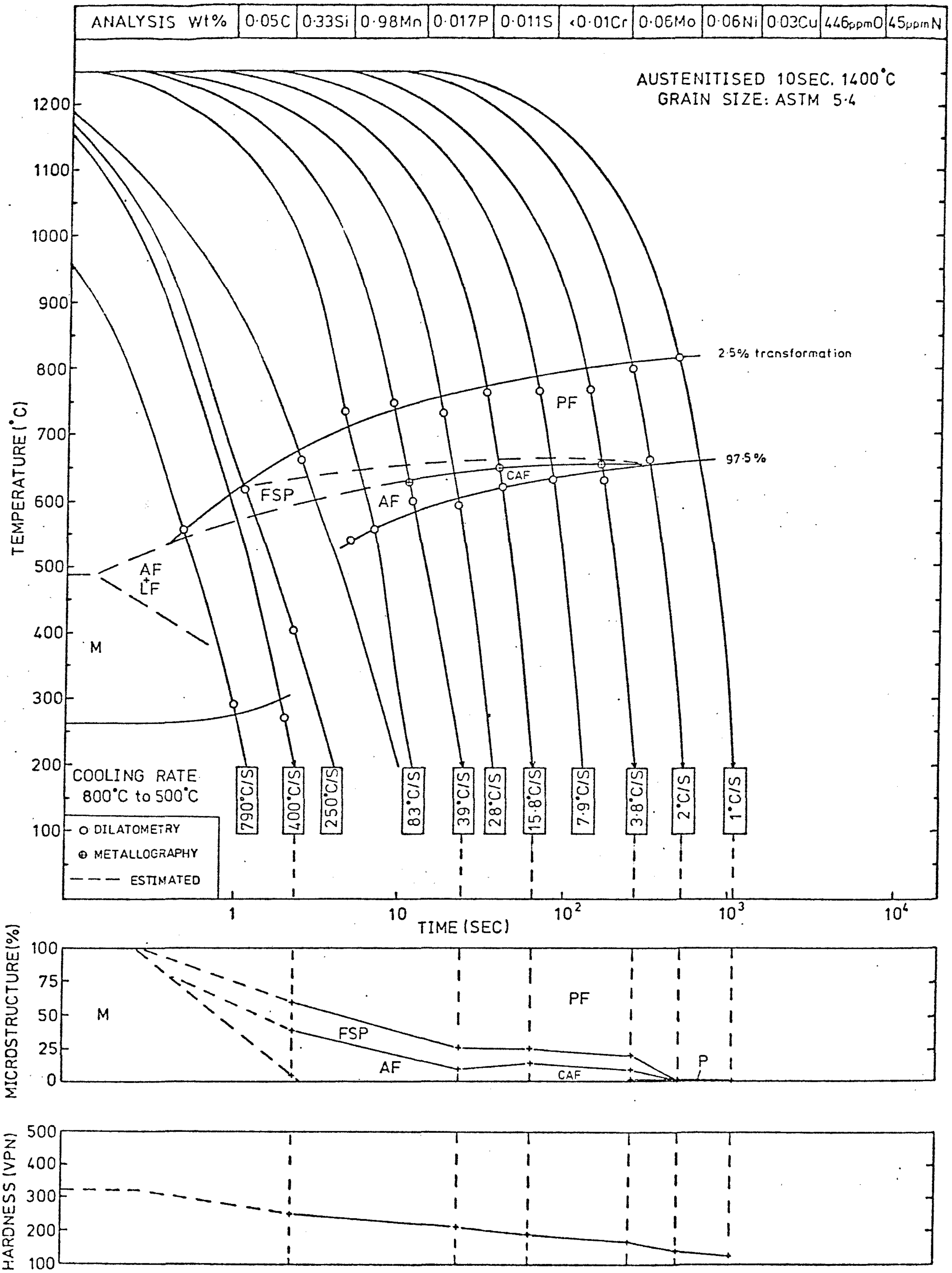

Figure 4.50(b) CCT diagram for weld metal N1.

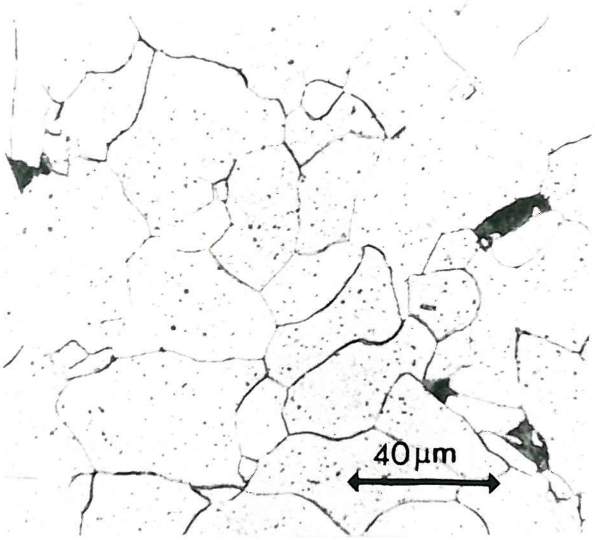

1°C/Sec

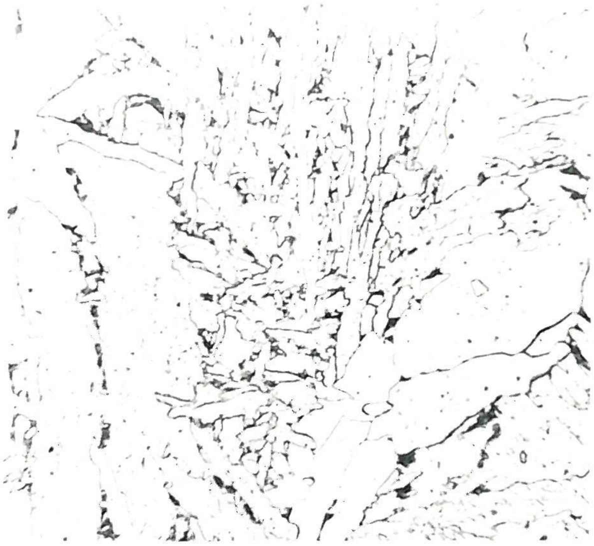

7·9°C/Sec

28°C/Sec

39°C/Sec

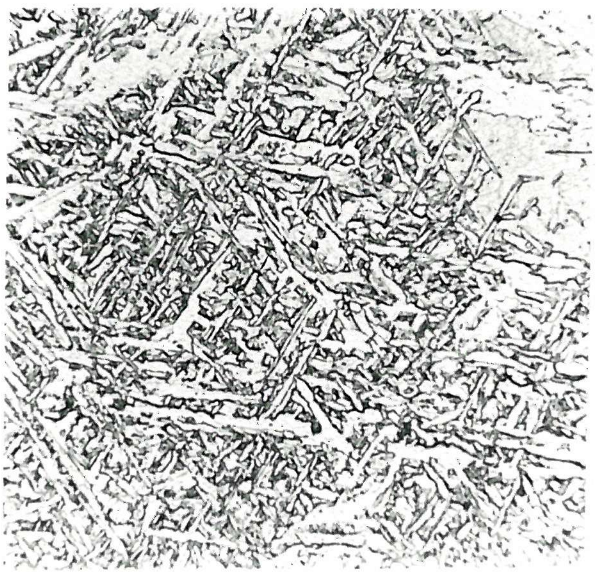

83°C/Sec

400°C/Sec

Figure 4·50(c)

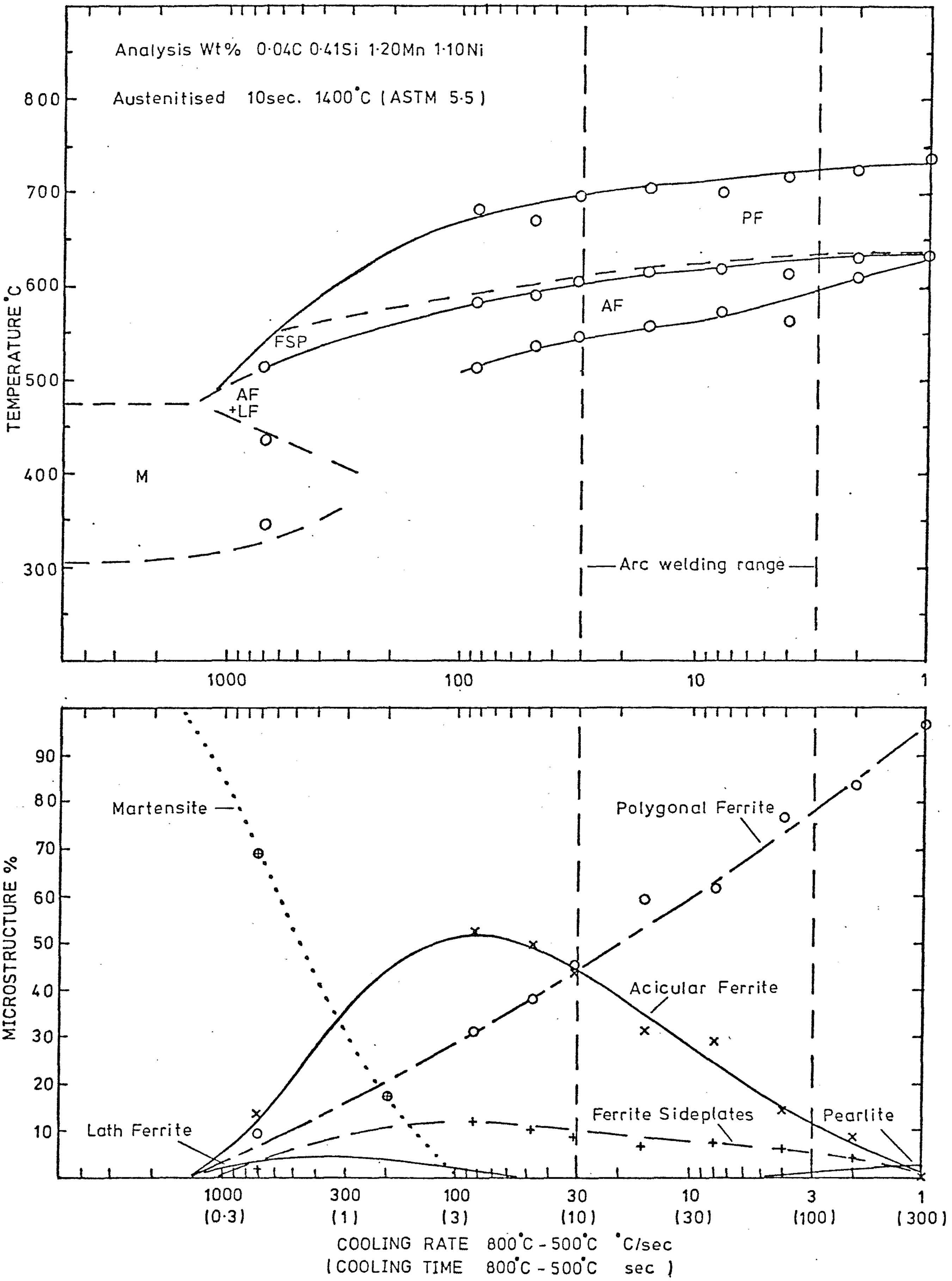

Figure 4.51(a) CCT diagram for weld metal N2.

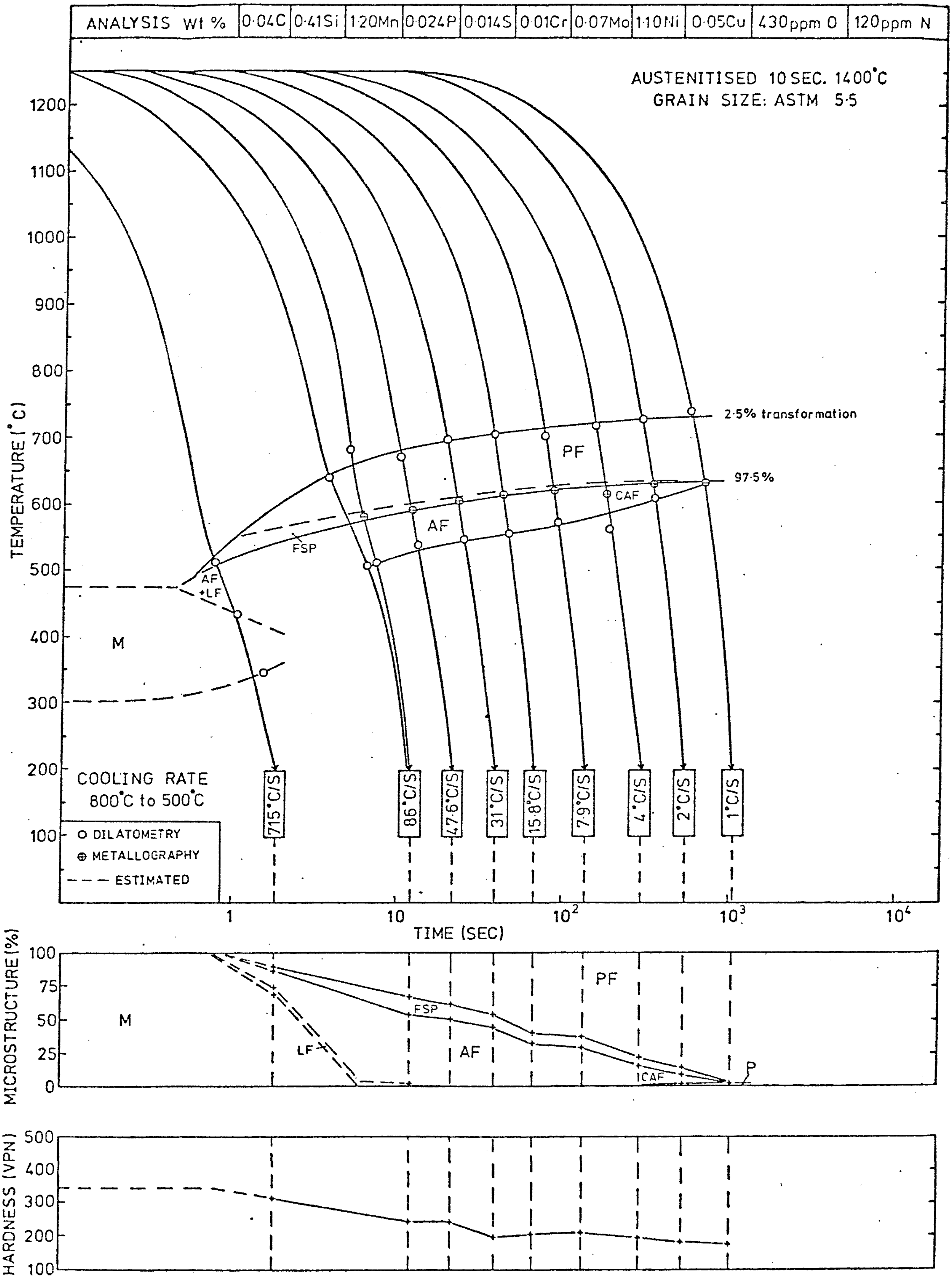

Figure 4.51(b) CCT diagram for weld metal N2.

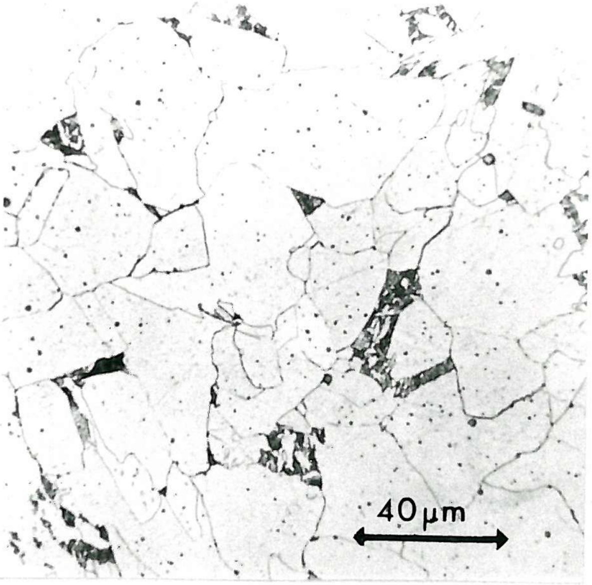

1°C/Sec

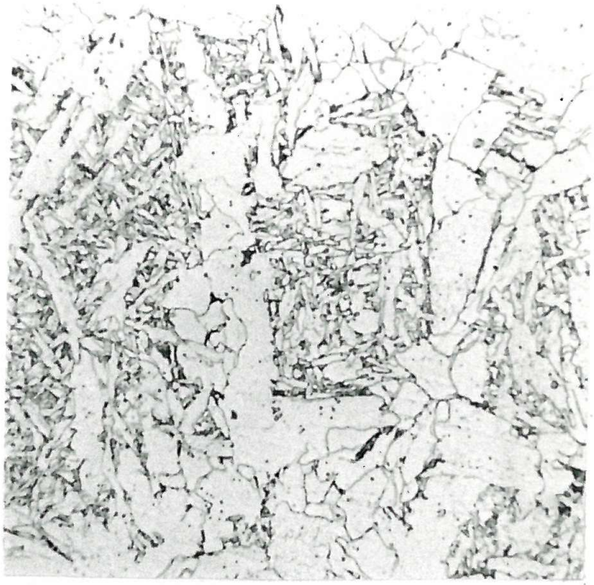

7·9°C/Sec

31°C/Sec

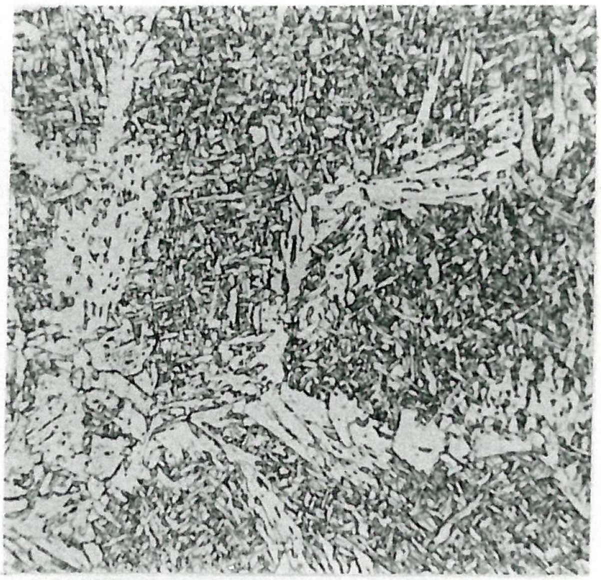

47·6°C/Sec

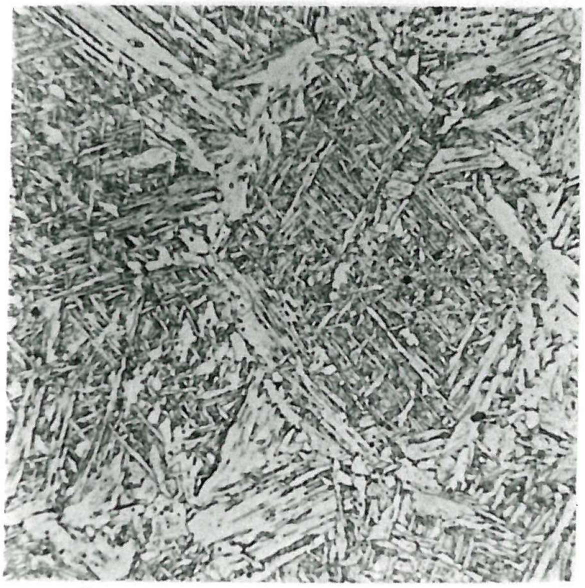

86°C/Sec

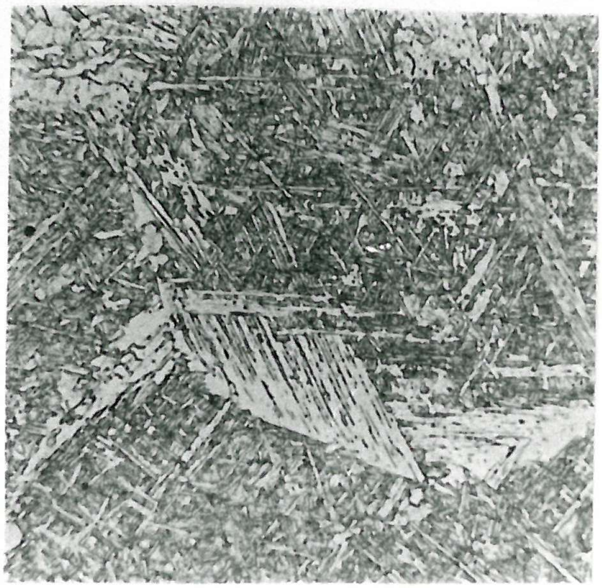

715°C/Sec

Figure 4·51(c)

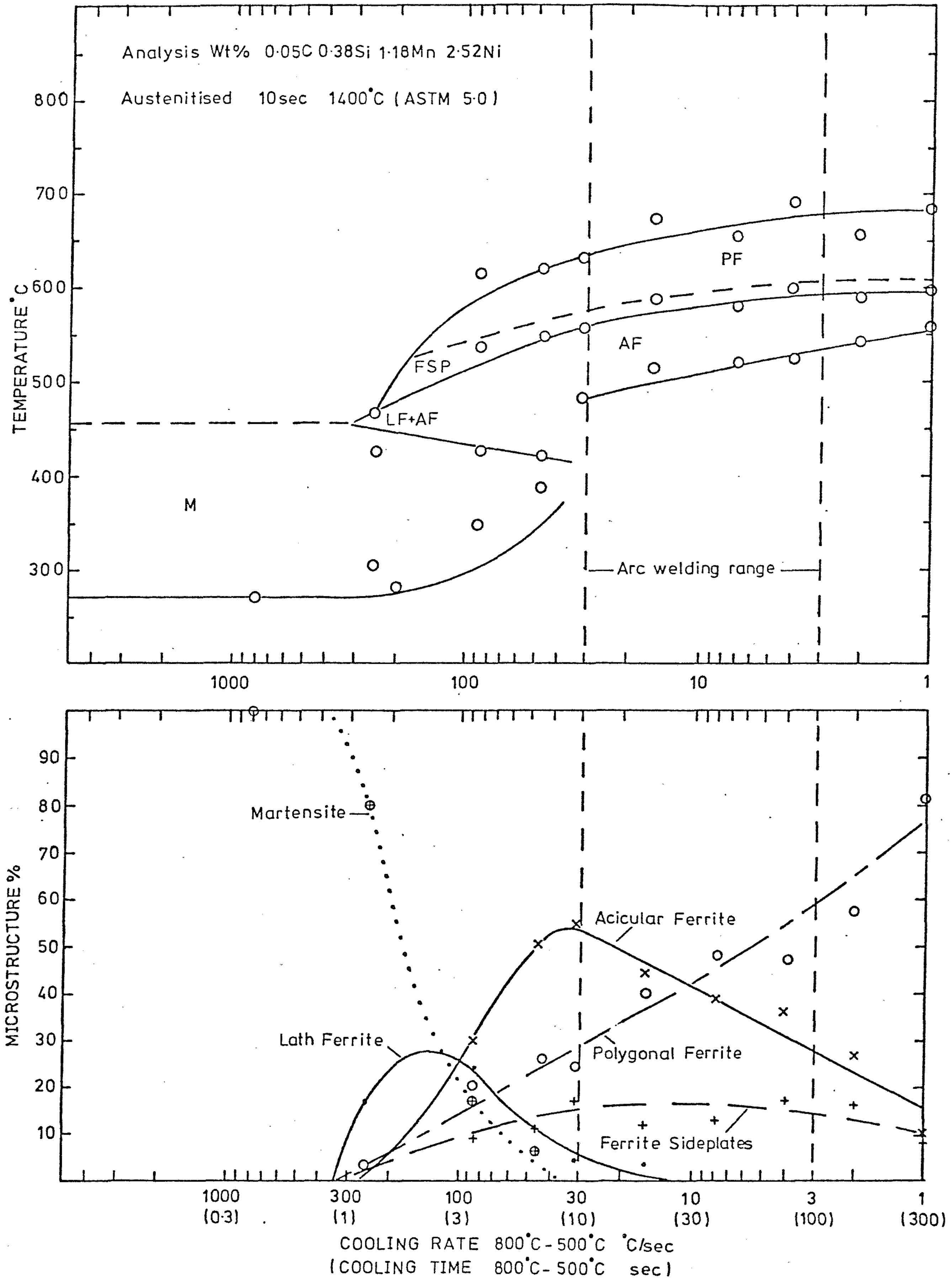

Figure 4.52(a) CCT diagram for weld metal N3.

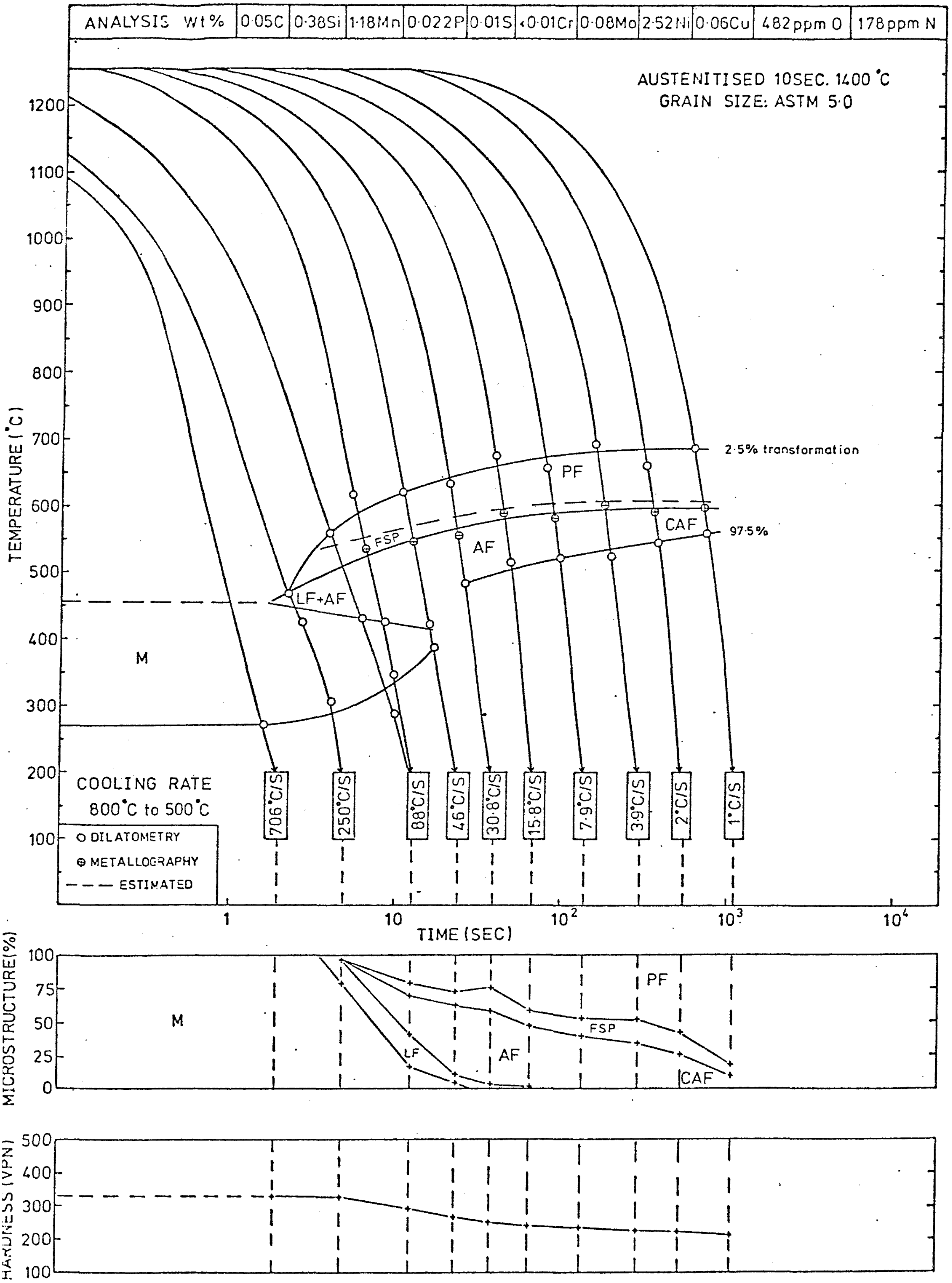

Figure 4.52(b) CCT diagram for weld·metal N3.

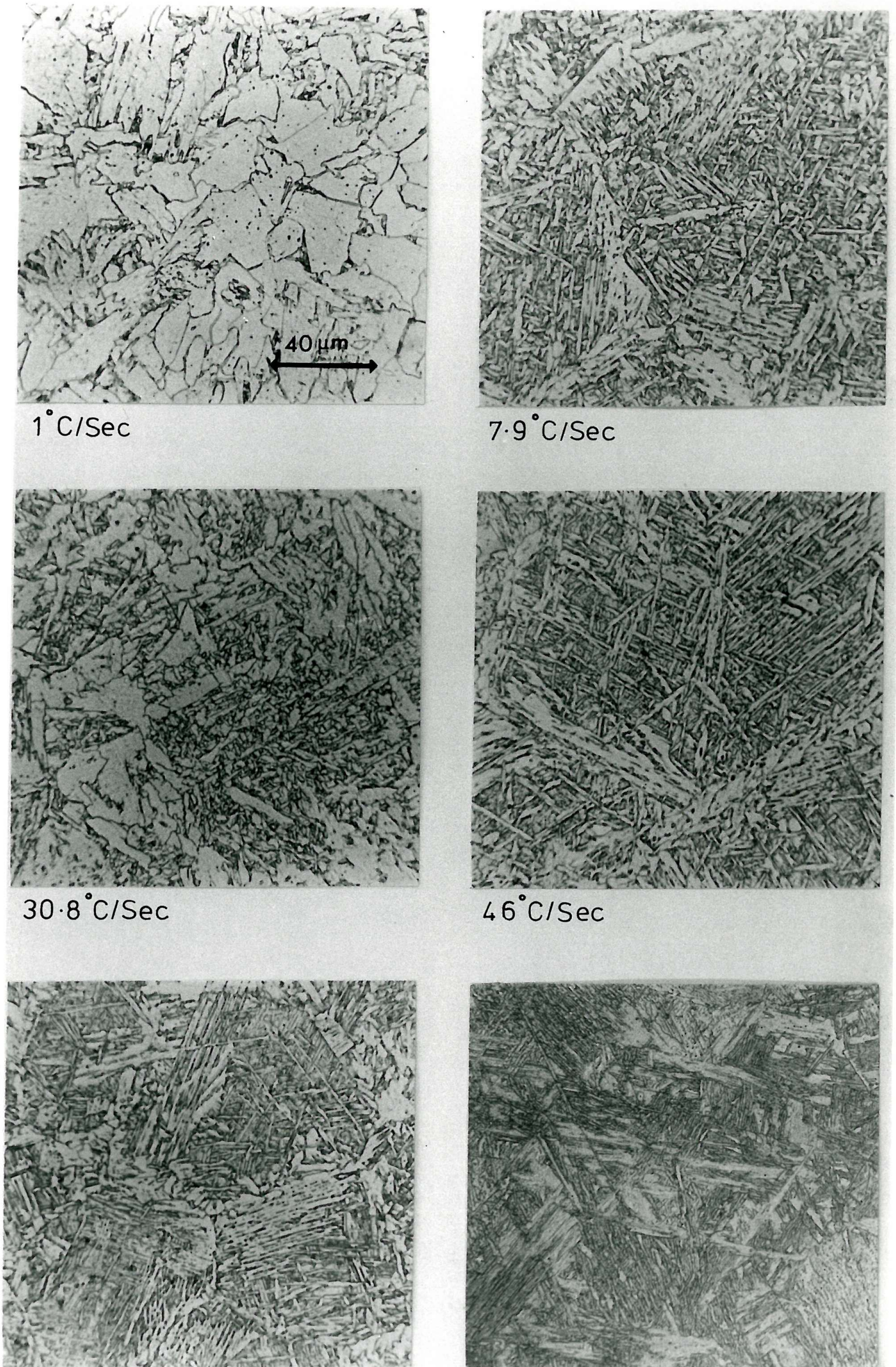

1°C/Sec

7·9°C/Sec

30·8°C/Sec

46°C/Sec

88°C/Sec

705°C/Sec

Figure 4·52(c)

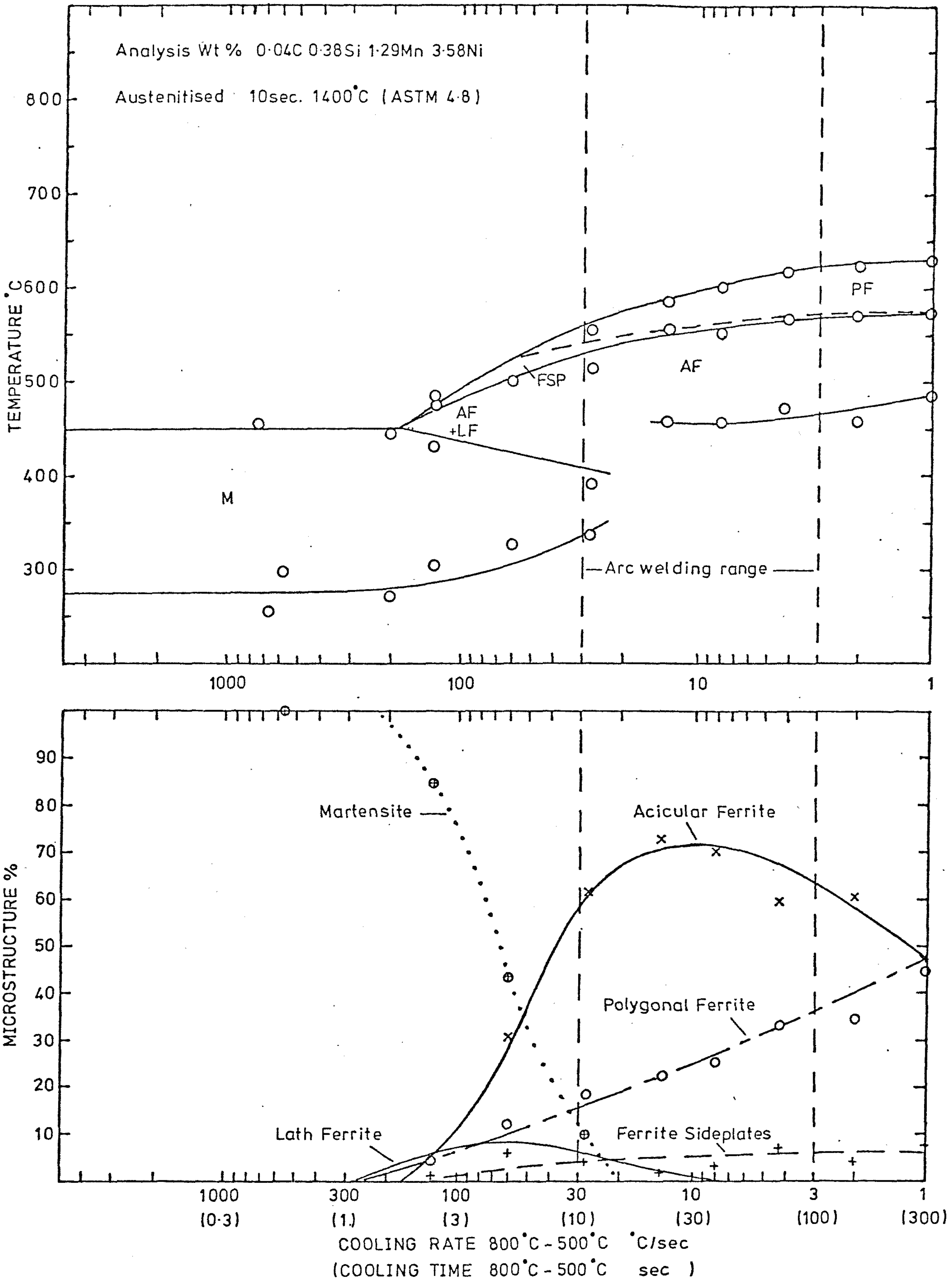

Figure 4.53(a) CCT diagram for weld metal N4A.

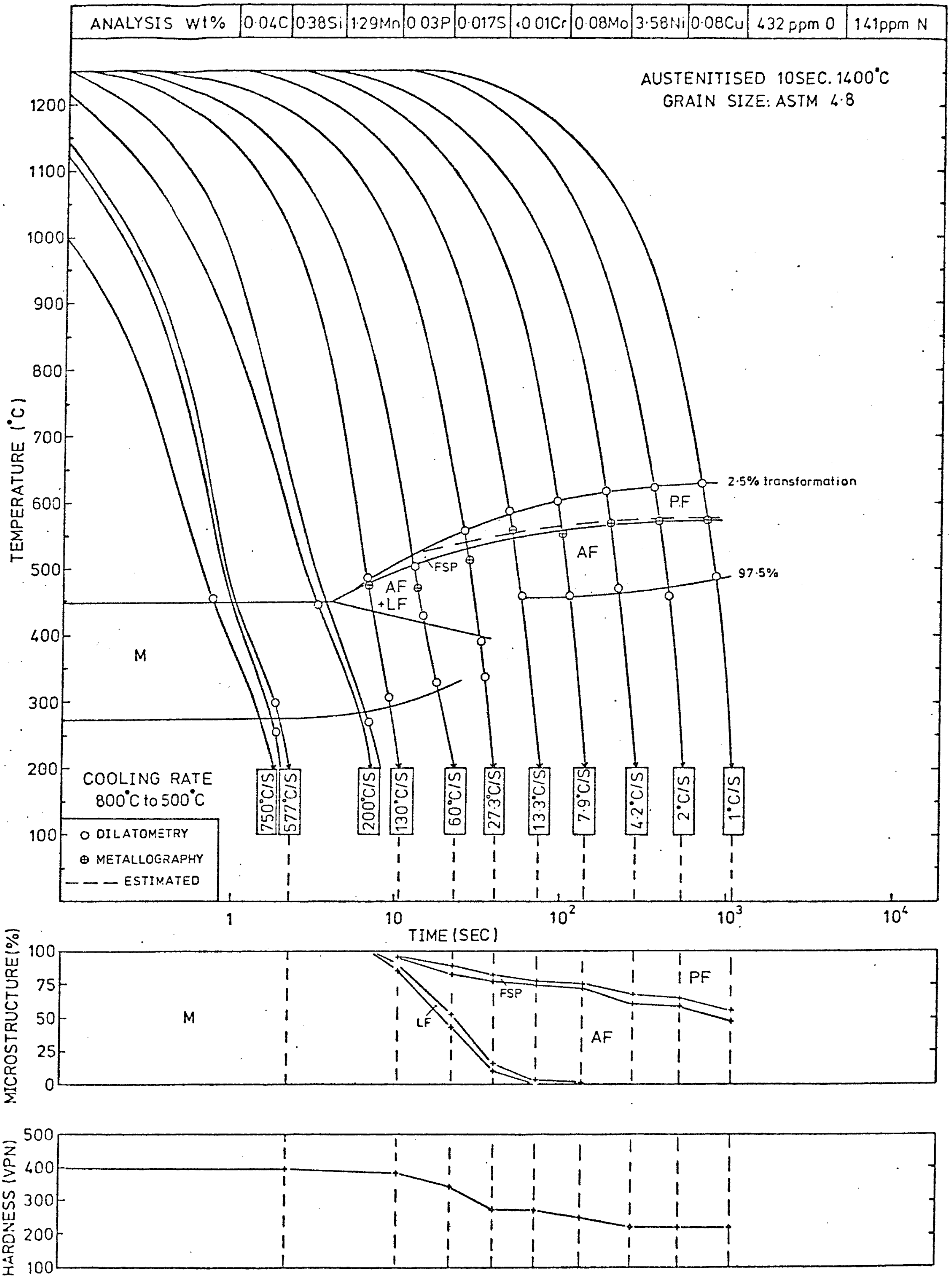

Figure 4.53(b) CCT diagram for weld metal N4A.

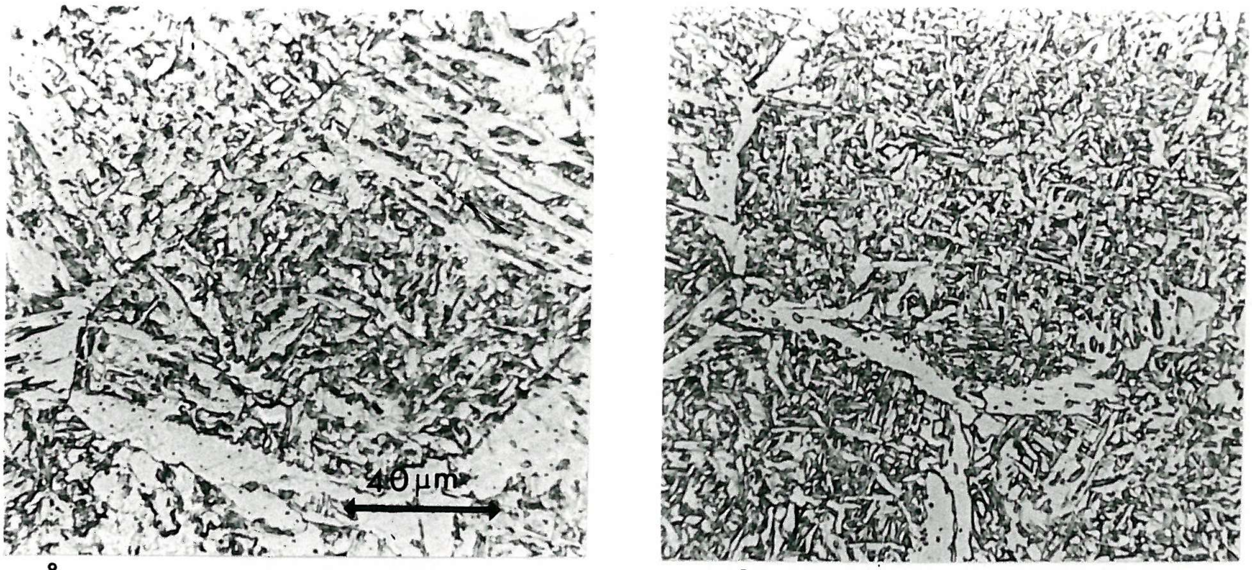

1°C/Sec

7·9°C/Sec

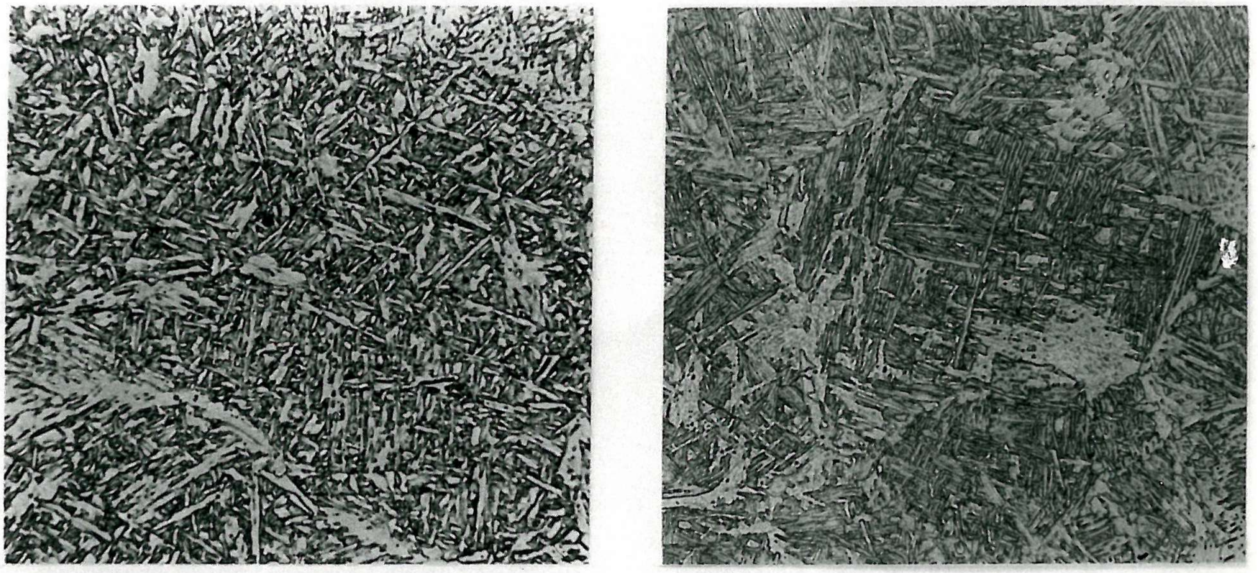

27·3°C/Sec

60°C/Sec

130°C/Sec

577 °C/Sec

Figure 4·53(c)

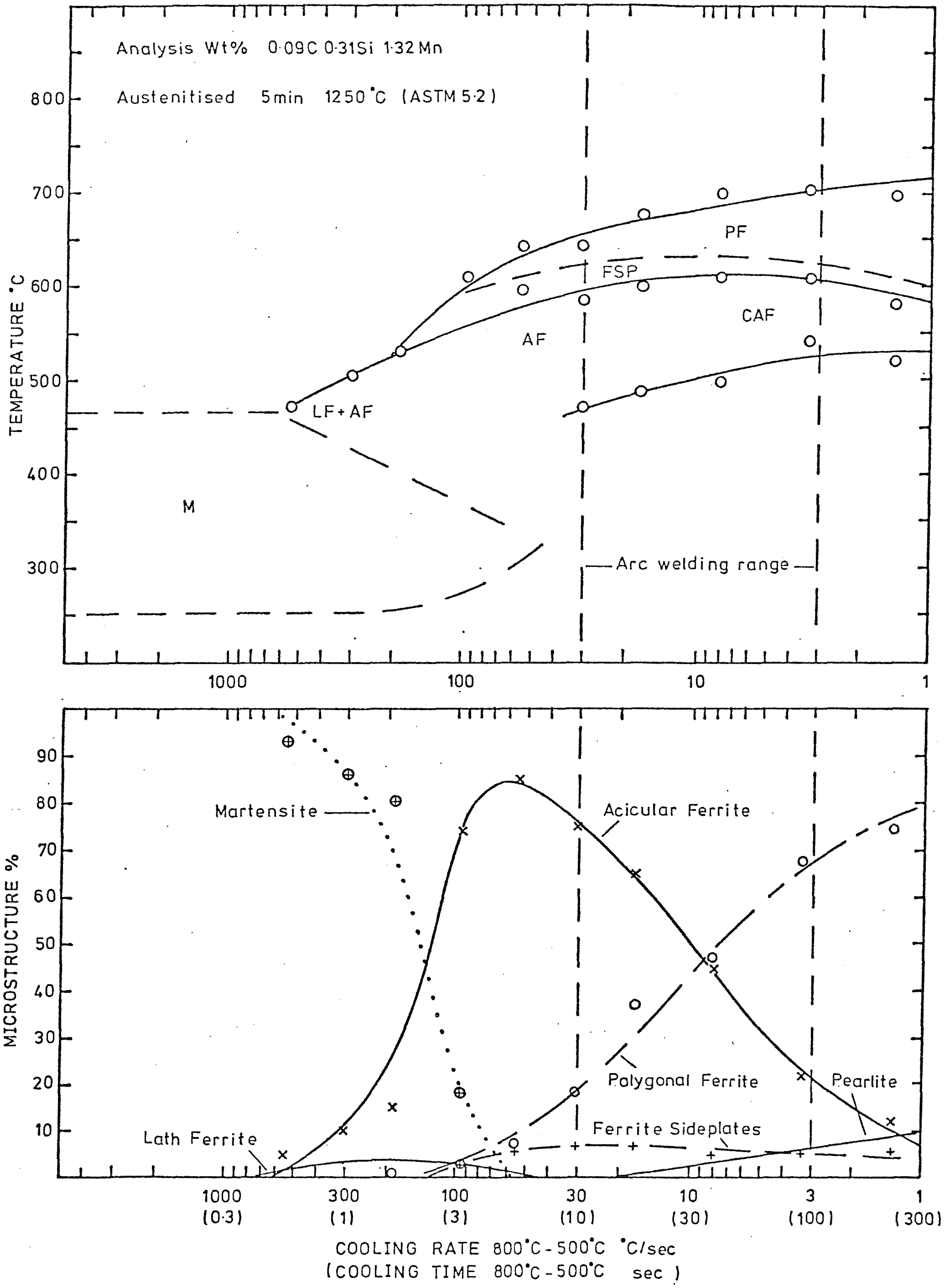

Figure 4.54(a) CCT diagram for weld metal AO.

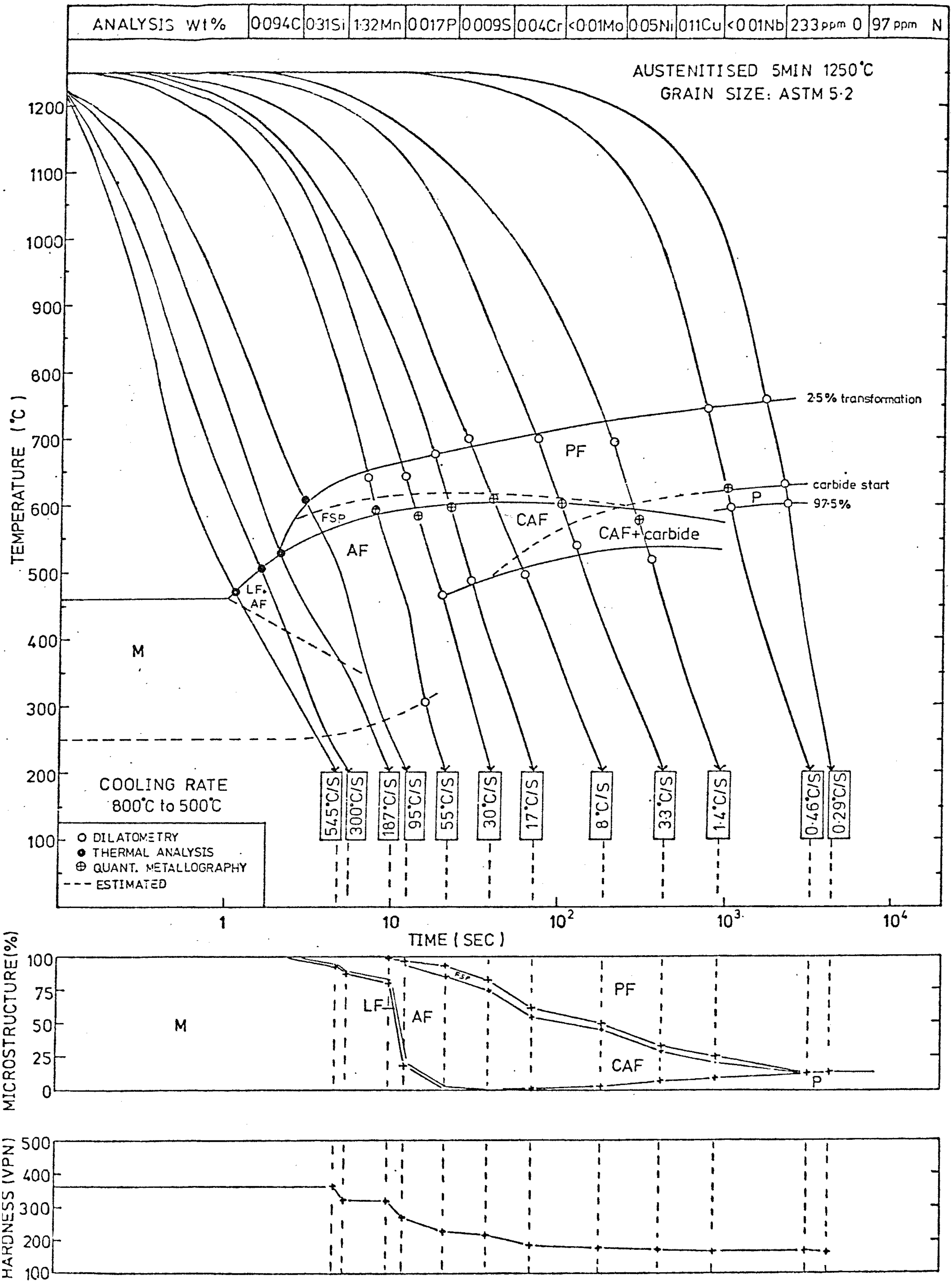

Figure 4.54(b) CCT diagram for weld metal AO.

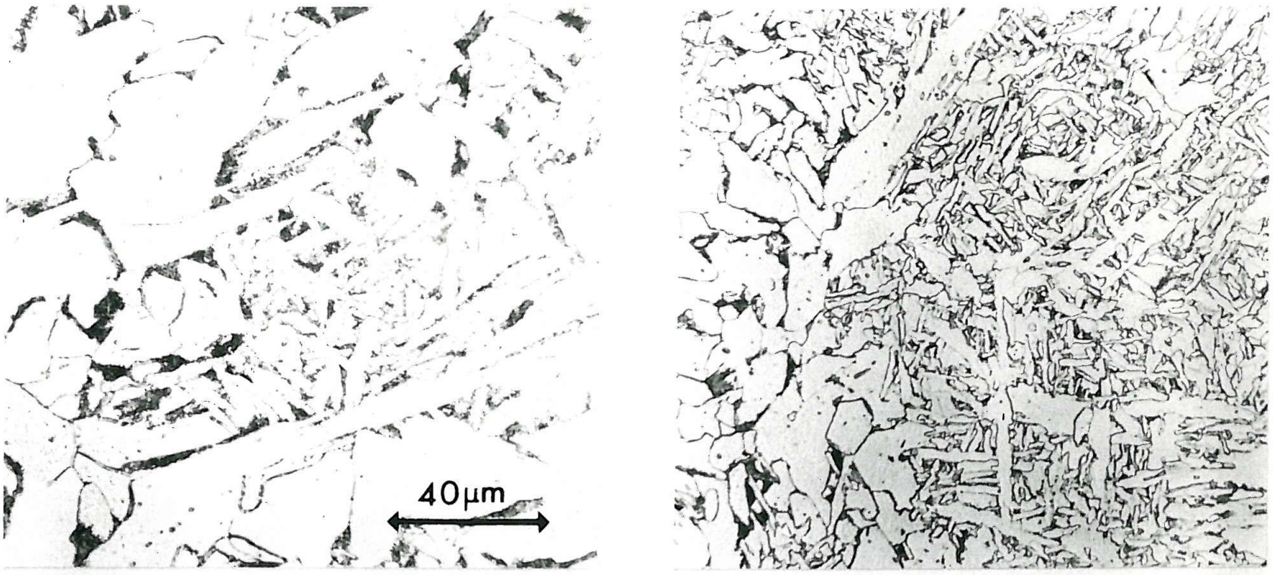

1·4 °C/Sec 8 °C/Sec

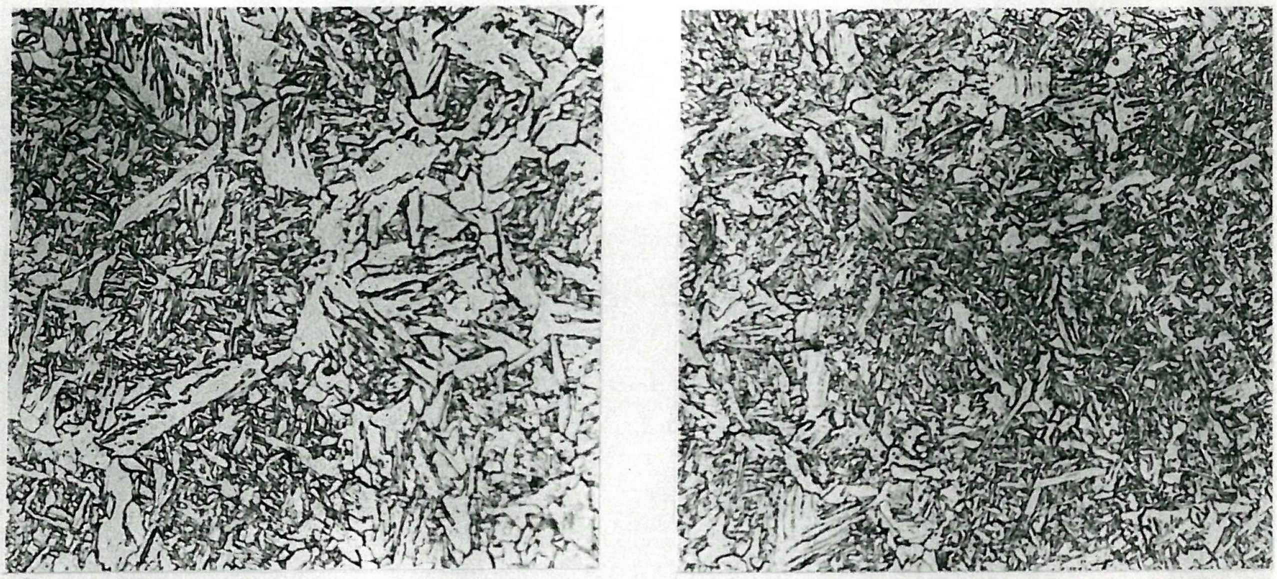

30 °C/Sec 55 °C/Sec

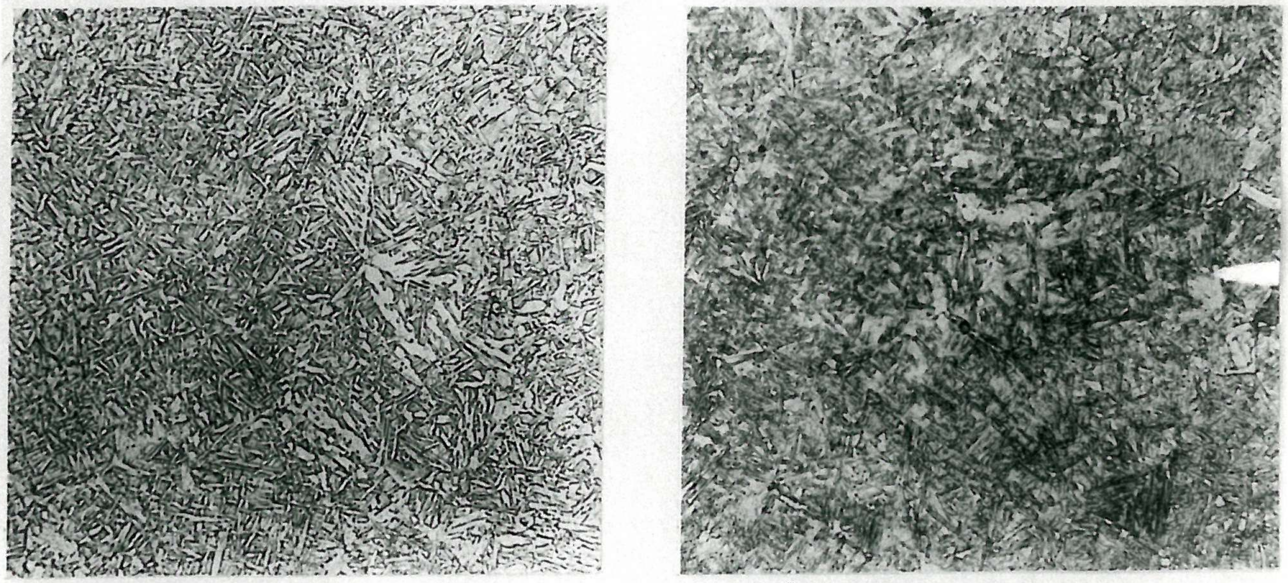

95 °C/Sec 545 °C/Sec

Figure 4·54(c)

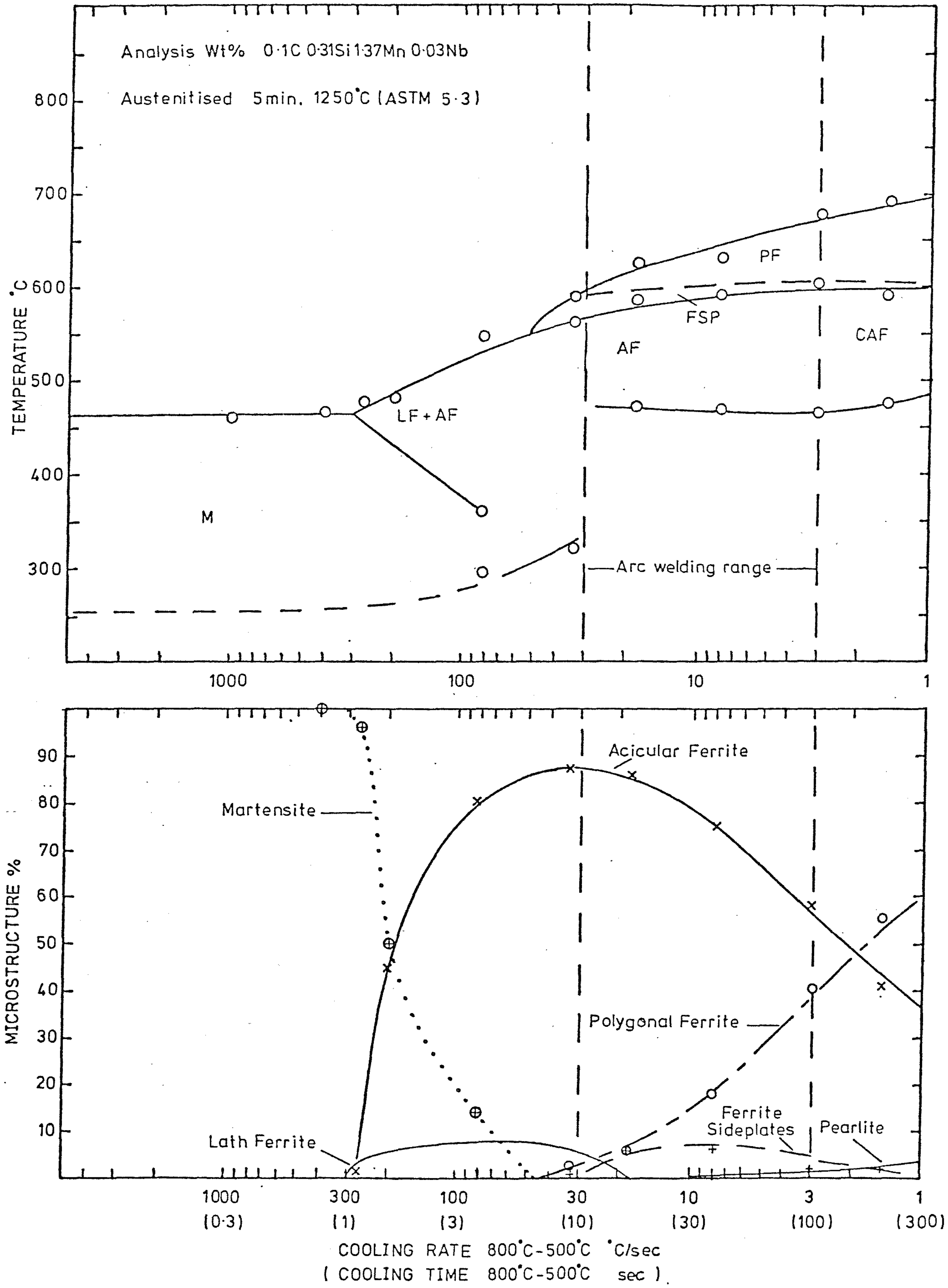

Figure 4.55(a) CCT diagram for weld metal EO.

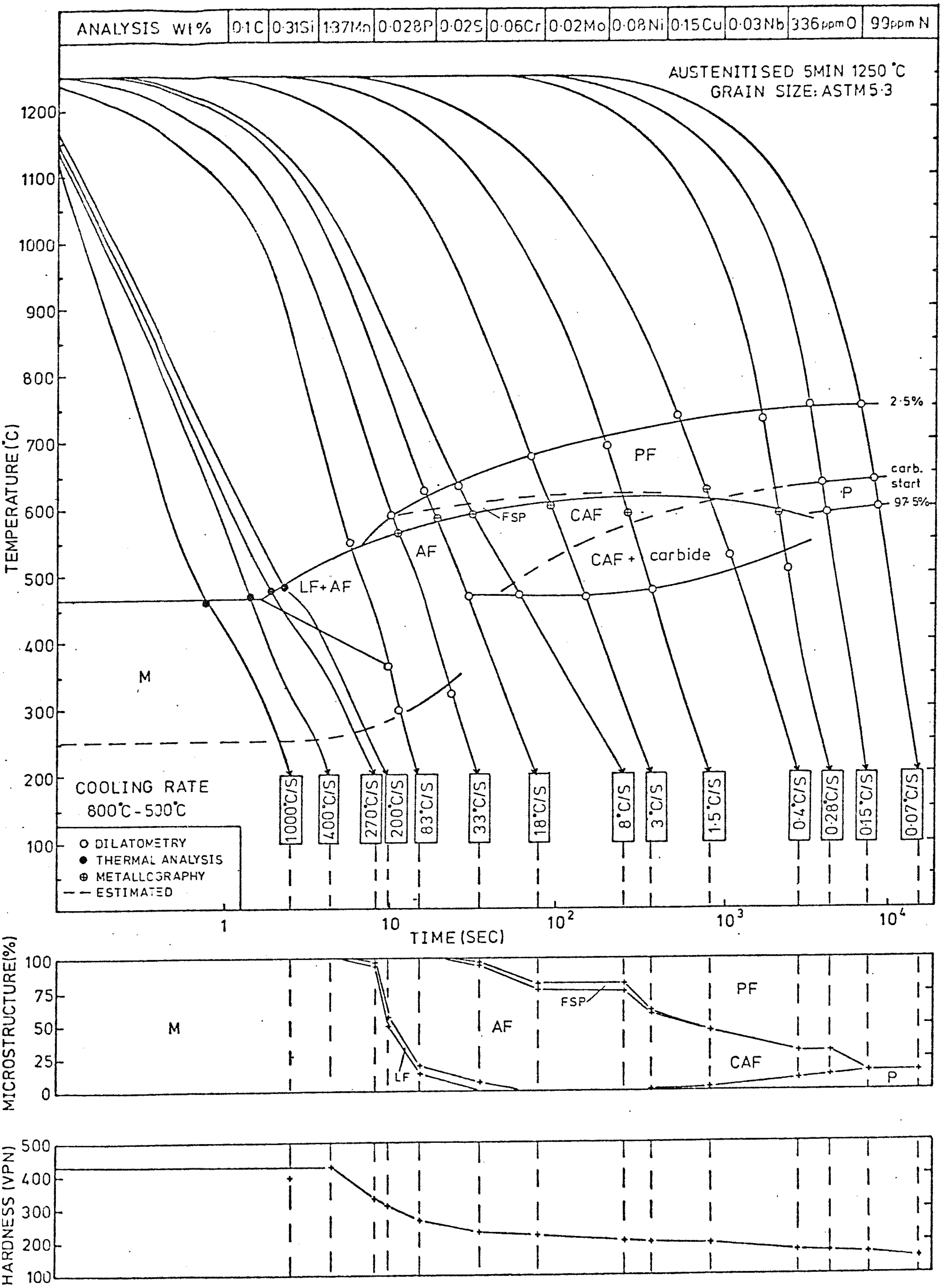

Figure 4.55(b) CCT diagram for weld metal E0.

1·5°C/Sec 8°C/Sec

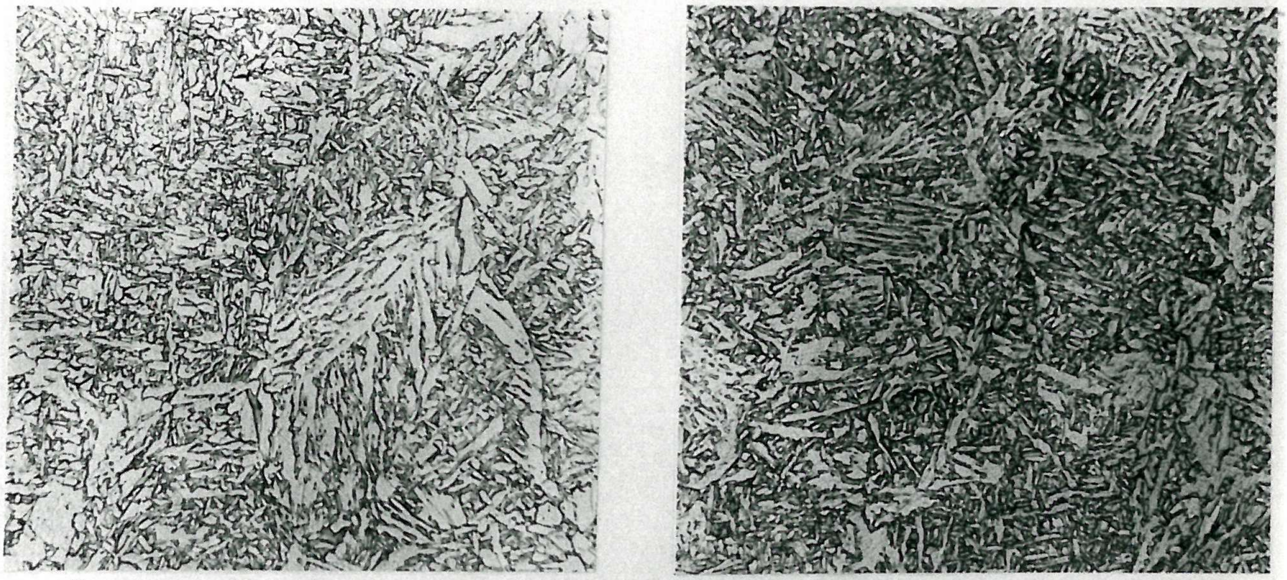

18°C/Sec 33°C/Sec

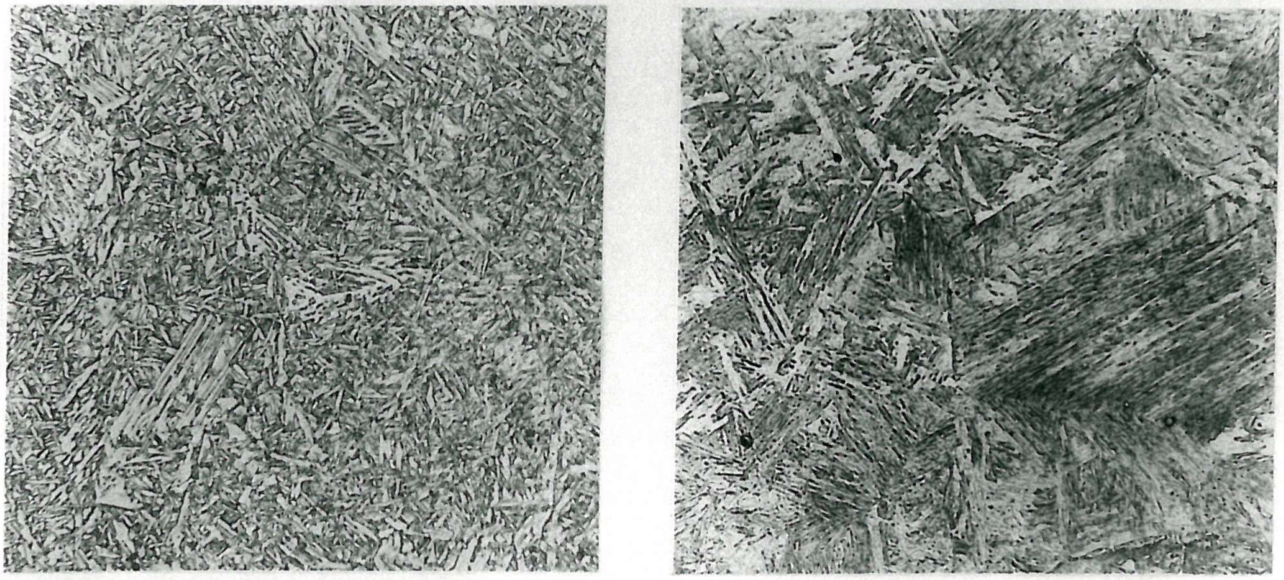

83°C/Sec 1000°C/Sec

Figure 4·55(c)

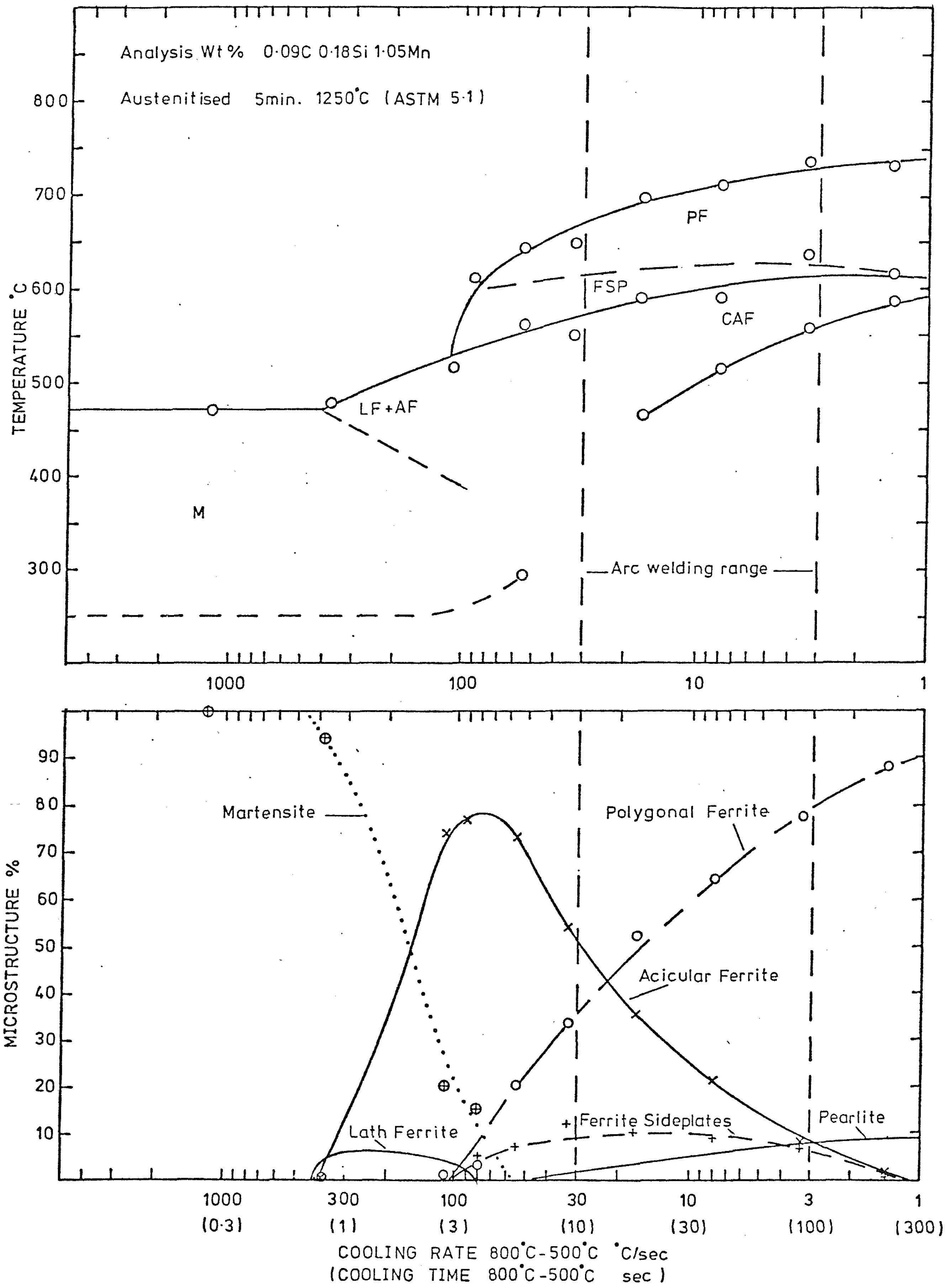

Figure 4.56(a) CCT diagram for weld metal A5.

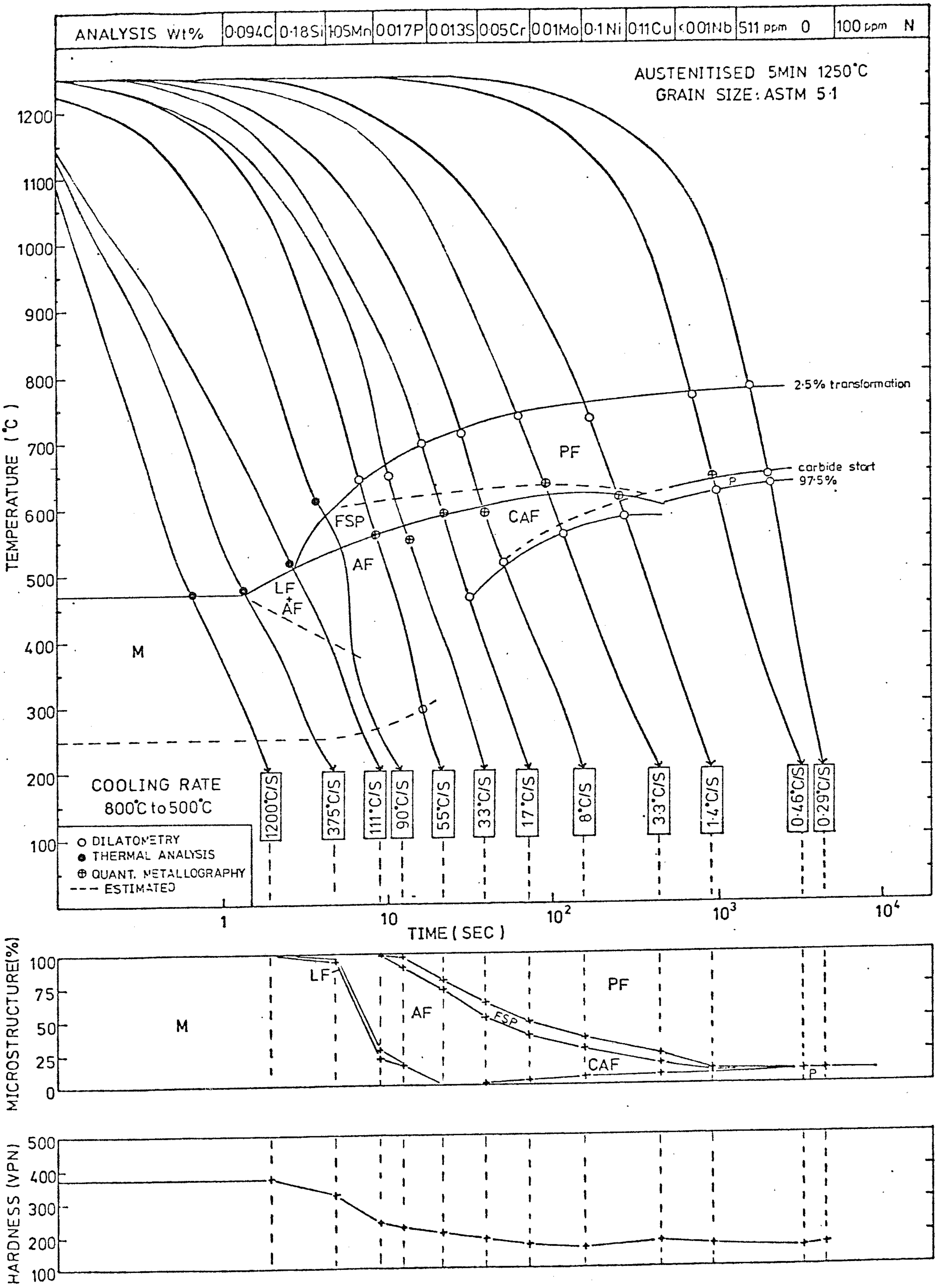

Figure 4.56(b) CCT diagram for weld metal A5.

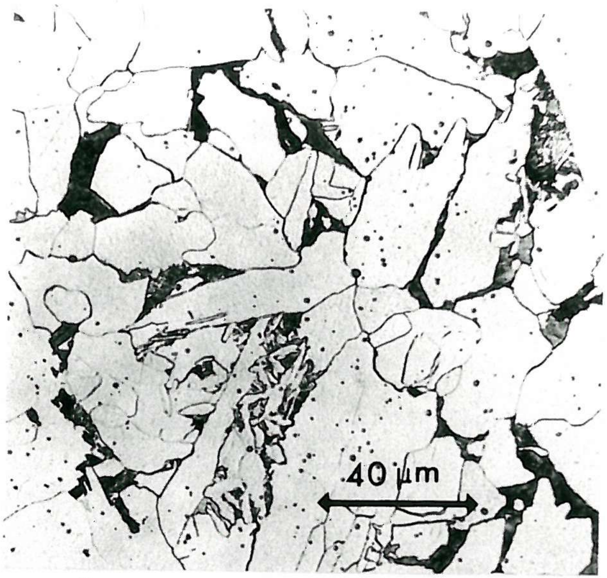

1·4°C/Sec

8°C/Sec

33°C/Sec

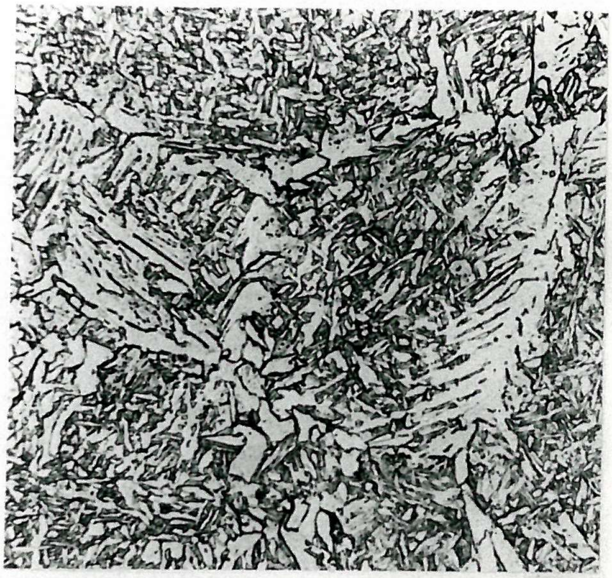

55°C/Sec

90°C/Sec

375°C/Sec

Figure 4·56(c)

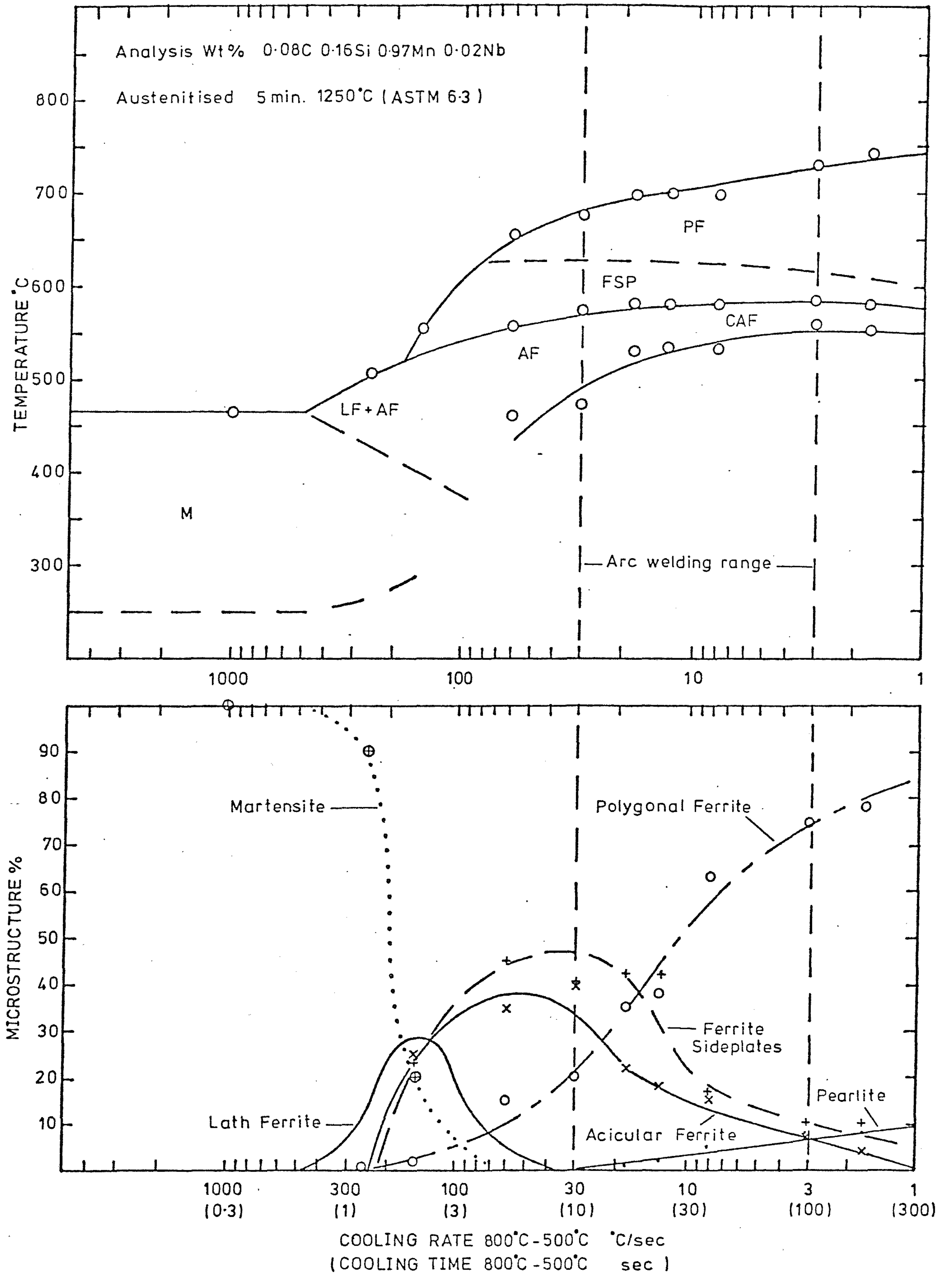

Figure 4.57(a) CCT diagram for weld metal E5.

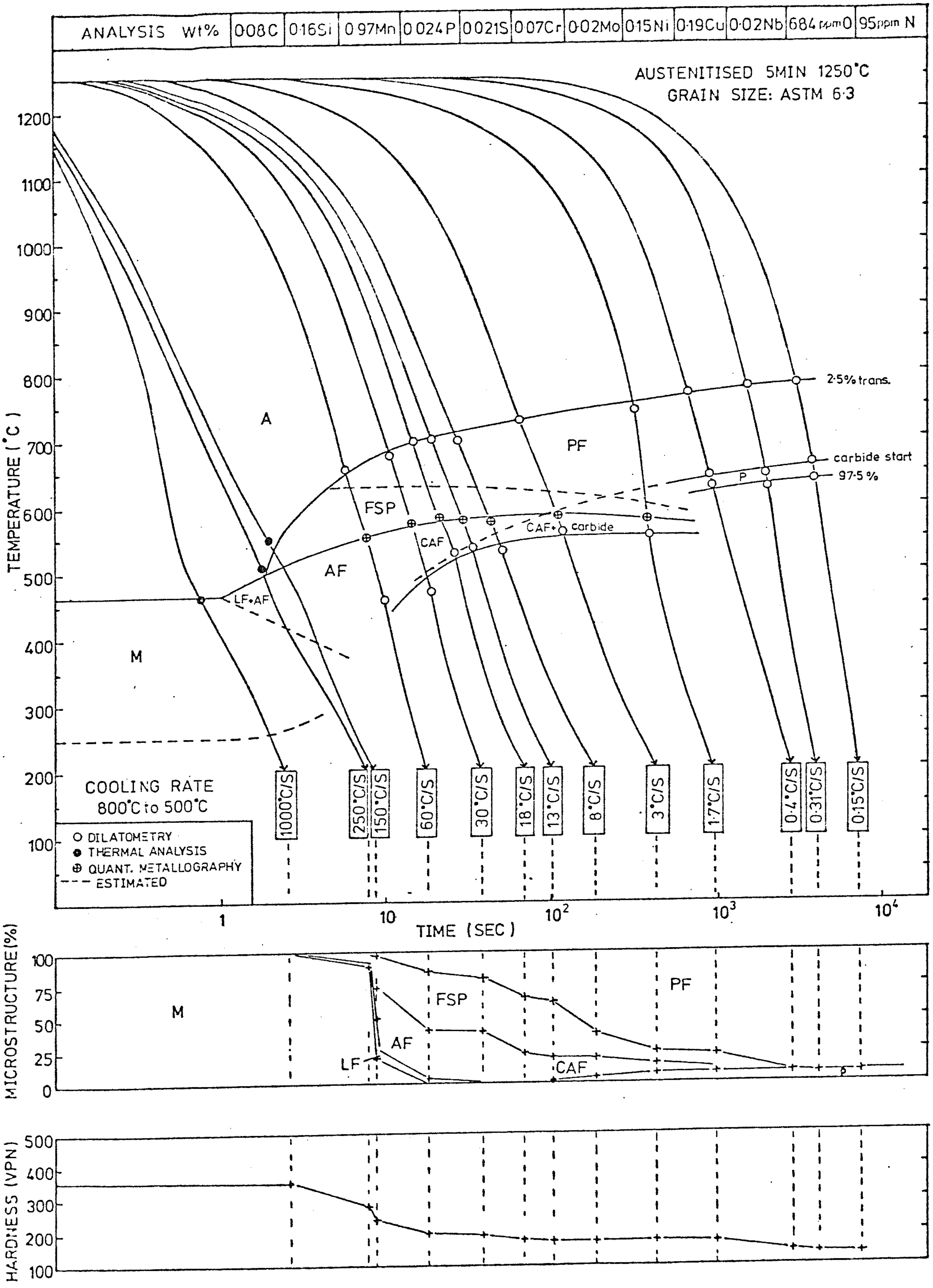

Figure 4.57(b) CCT diagram for weld metal E5.

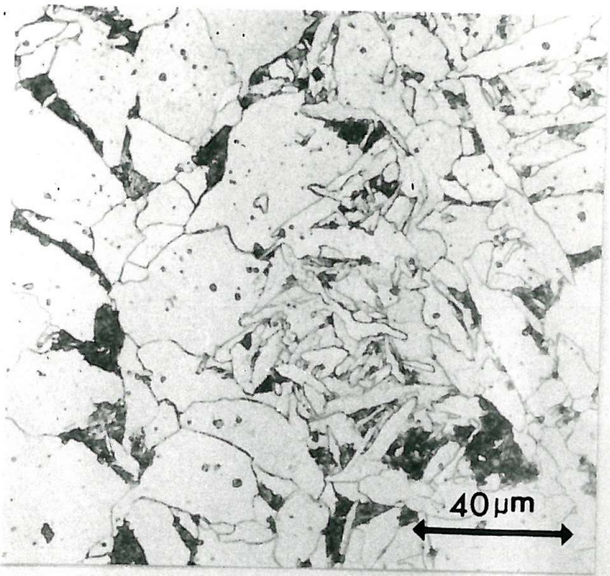

1·7 °C/Sec

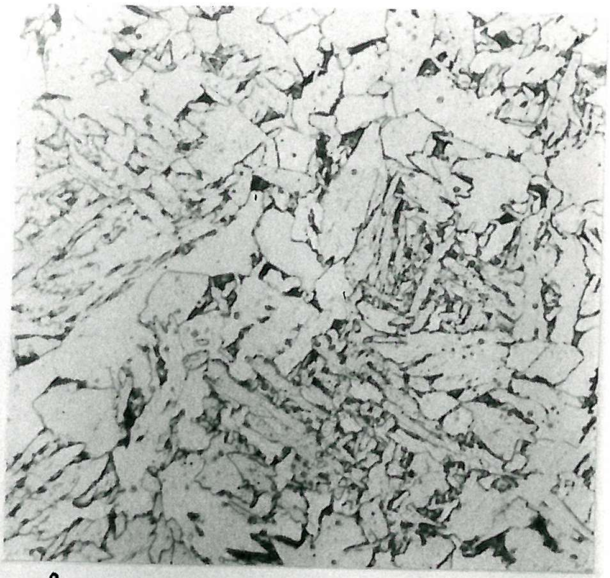

8 °C/Sec

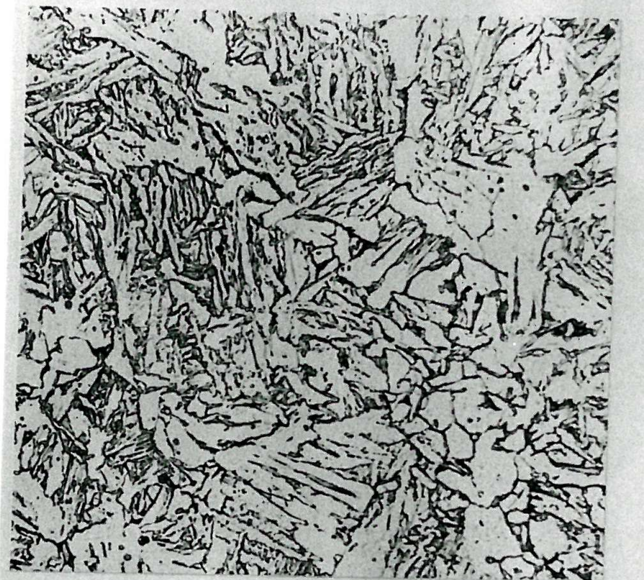

30 °C/Sec

60 °C/Sec

150 °C/Sec

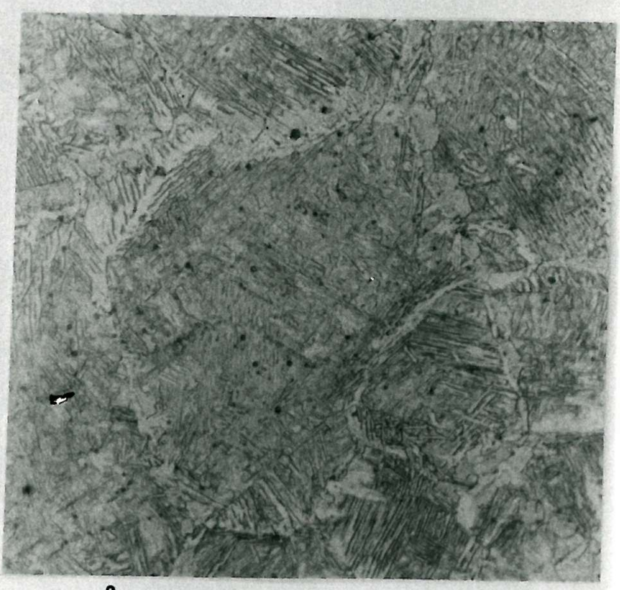

250 °C/Sec

Figure 4·57(c)

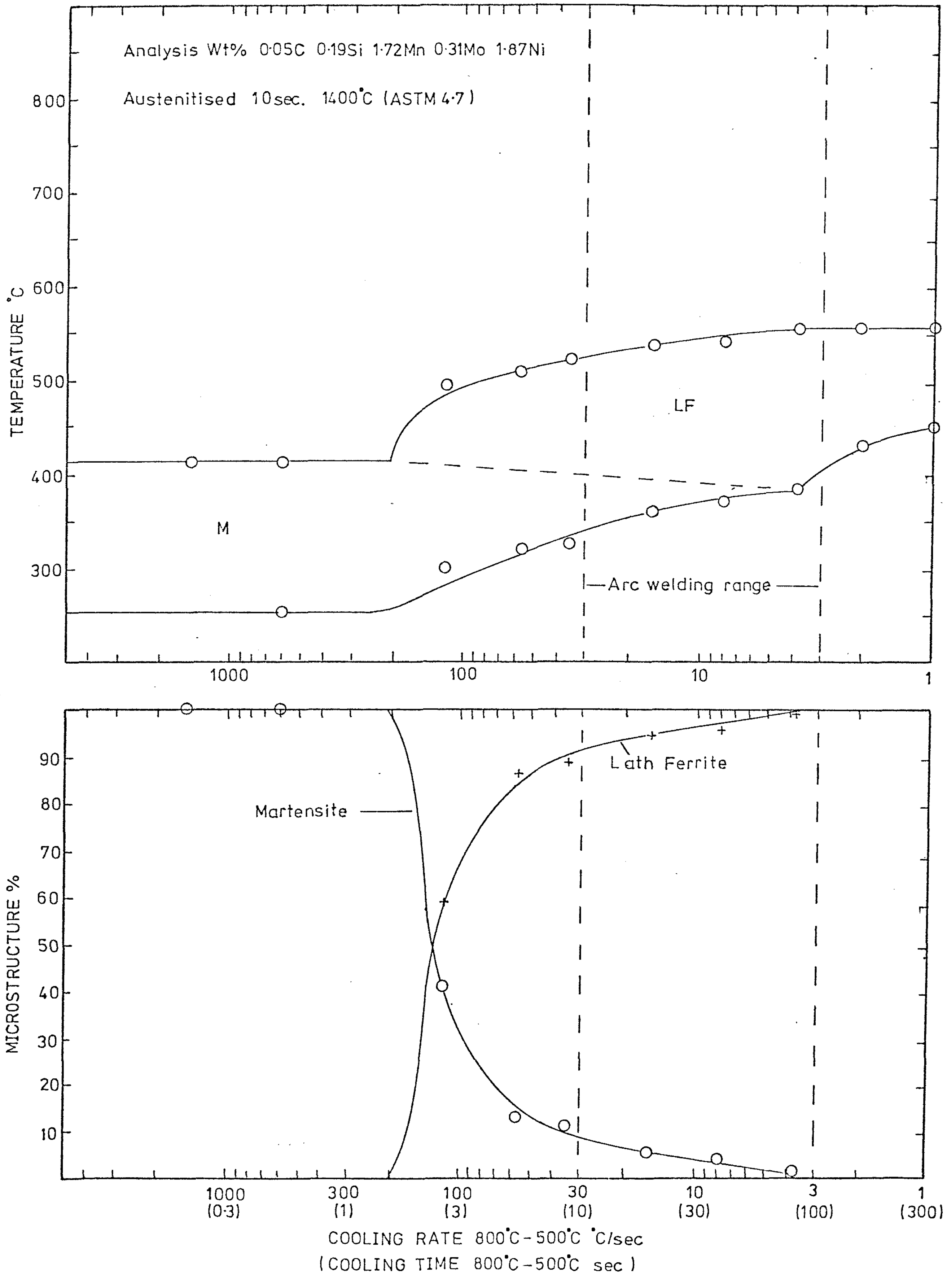

Figure 4.58(a) CCT diagram for weld metal NMo.

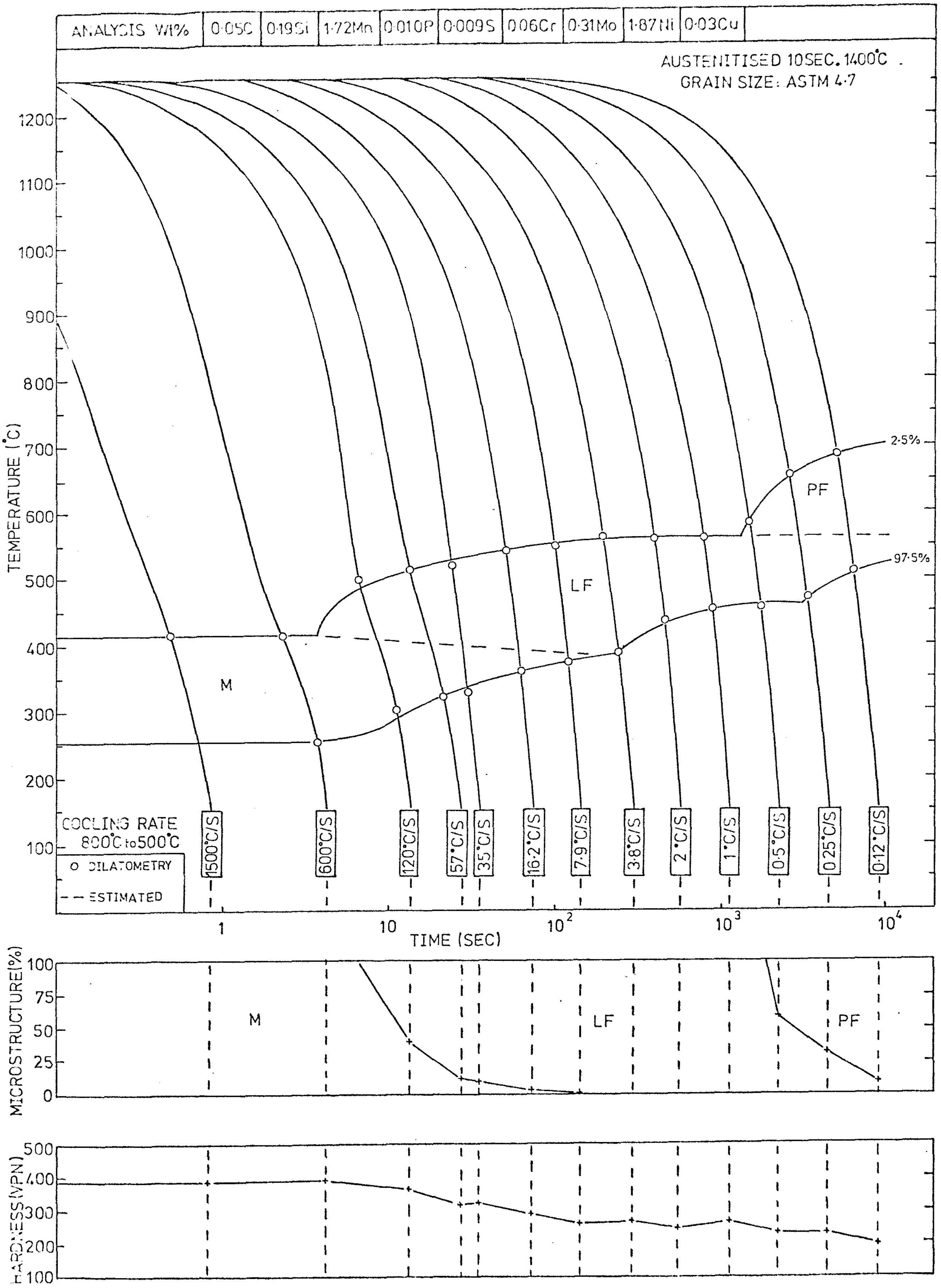

Figure 4.58(b) CCT diagram for weld metal NMo.

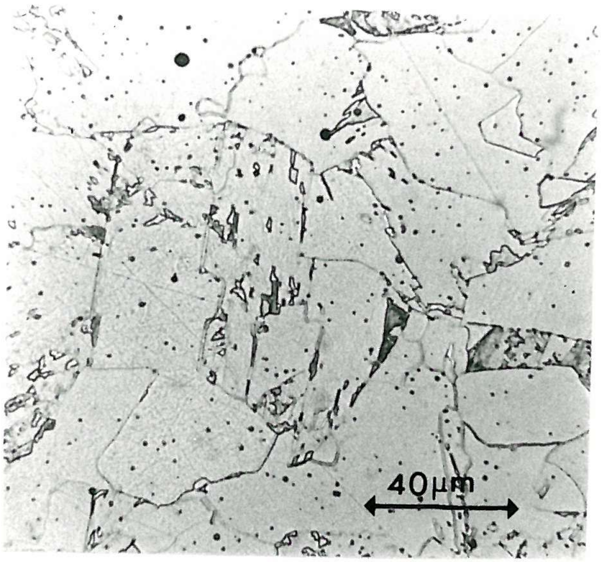

0·125 °C/Sec

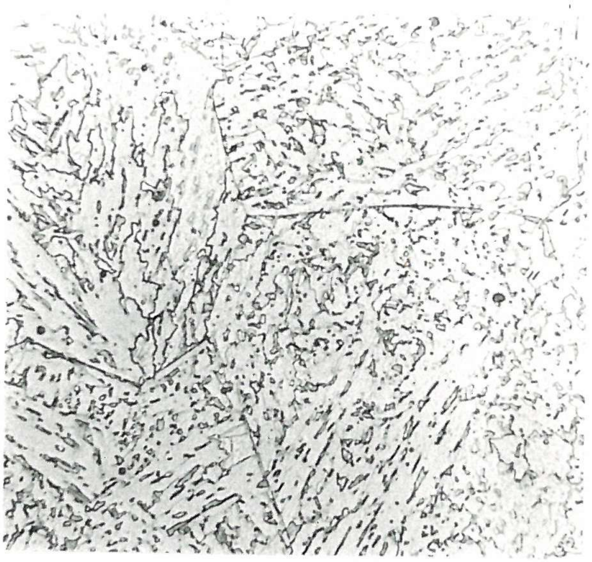

1 °C/Sec

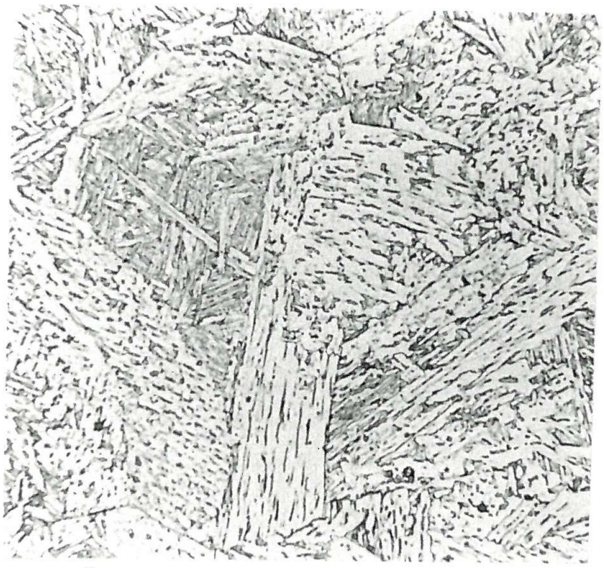

7·9 °C/Sec

35 °C/Sec

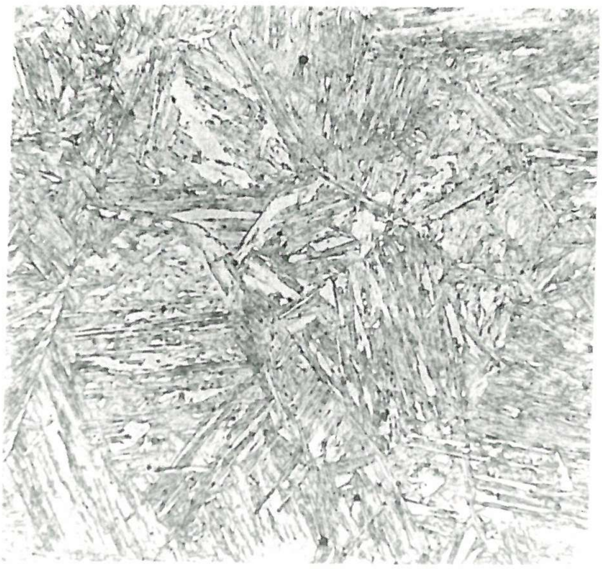

120 °C/Sec

600 °C/Sec

Figure 4·58(c)

CHAPTER 5: DISCUSSION

5.1 Introduction

The experimental work and results reported in the previous chapters have produced a series of twelve CCT diagrams applicable to weld metals. To enable the findings of the present work to be fully understood and compared with previous literature, this chapter will be divided into the following topics.

(1) Weld metal transformation products and CCT diagrams

The overall shape of the CCT diagrams and the relationships between various phases and morphologies will be discussed. Particular emphasis will be put on the effect of cooling rate within the welding range. The $\gamma \rightarrow \alpha$ transformation temperatures of polygonal, sideplate, acicular and lath ferrites will also be discussed and compared with the findings of sections 2.2 and 2.3 of the literature review.

(2) Influence of alloying and γ grain size on weld metal transformation behaviour

The influences of Mn, Ni, Nb, C, Mo, and prior γ grain size on CCT characteristics and resultant weld metal microstructures will be discussed. This information will then be compared with the data presented in section 2.4 of the literature review.

(3) Influence of inclusions on weld metal transformation behaviour

The influence of inclusions has been studied directly by using the remelting technique and has produced dramatic changes in transformation behaviour. In addition, the use of different flux systems has also shown significant differences in transformation behaviour. By comparing the present weld metal CCT diagrams with those for wrought steels of similar chemical composition a distinct hardneability shift is observed. All these factors confirm the view that inclusions are of fundamental importance to weld metal transformation behaviour. These findings are therefore discussed in relation to the various inclusion effects presented in section 2.5 of the literature review in an attempt to elucidate the influence of inclusions on weld metal transformations.

(4) Theoretical and Practical models describing weld metal transformation behaviour and its relationship to toughness

Using the experimental data generated in the current investigation, combined with the theoretical aspects of inclusions discussed in

Chapter 2 it should be possible to provide a new model for weld metal transformation behaviour. In the final section this model is developed and applied to several aspects of the literature.

The potential for using CCT diagrams to develop superior consumables for the future is also discussed in view of the findings of the current work.

5.2 Weld Metal Transformation Products and CCT Diagrams

5.2.1 CCT diagrams

The overall shape of the CCT diagrams produced in the current investigation is generally in good agreement with the schematic CCT diagram shown in Figure 2.6 of the literature review. However, in the real CCT diagrams there is no significant difference in transformation kinetics between the grain boundary ferrite (PF) and Widmanstätten secondary sideplate (FSP). This may be because these two forms of proeutectoid ferrite are inter-related morphologies and therefore form as a continuous series of products, with decreasing transformation temperature.

At faster cooling rates the CCT diagrams show a change in kinetic behaviour corresponding to the bainite reaction (LF). This feature is particularly noticeable in the C-Mn-Ni-Mo weld metal (Figure 4.58) where the proeutectoid reaction is limited to very slow cooling rates. The bainite nose is a distinguishable feature in all the CCT diagrams and generally corresponds to B_s temperatures between 500°C and 600°C.

An interesting feature of the CCT diagrams is the occurrence of either lath ferrite or acicular ferrite within the bainite field. In the more highly alloyed weld metals lath ferrite is the predominant morphology, but in lower alloy weld metals acicular ferrite usually predominates. In many of the weld metals studied both morphologies occurred. Generally, slower cooling rates favoured acicular ferrite, whilst faster cooling favoured the lath ferrite morphology.

Comparing a weld metal CCT diagram with a weld HAZ CCT diagram of similar chemical composition reveals some interesting similarities. Figure 5.1 shows a CCT diagram applicable to a weld HAZ. In this diagram the conventional ferrite, pearlite and martensite regions are shown, in addition to three constituents in the bainite region - lower bainte (LB), upper bainite (UB) and bainitic ferrite (BF).

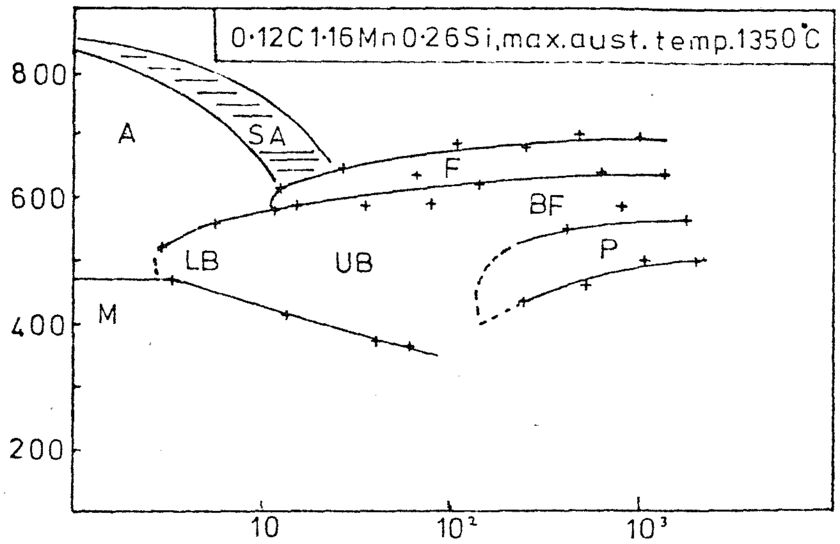

Figure 5.1 Weld HAZ CCT diagram after Kunitake (97).

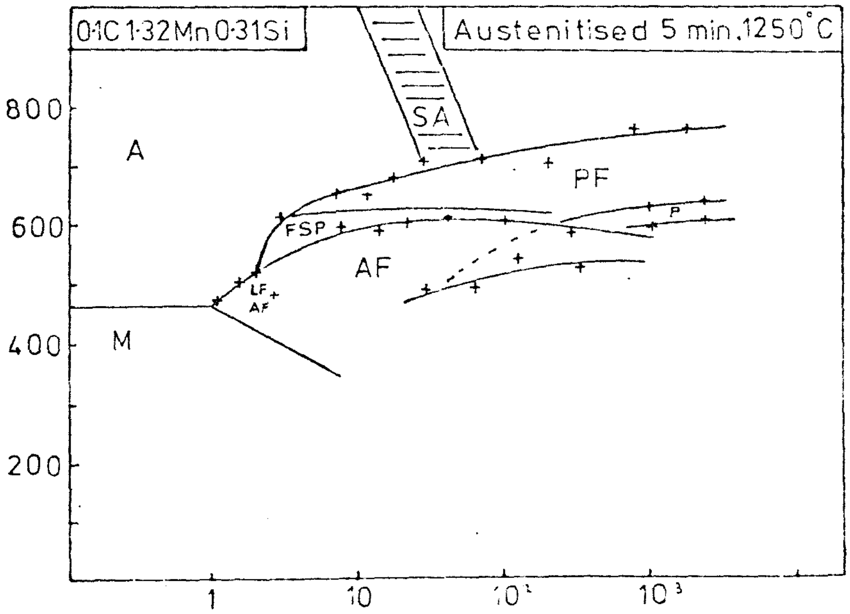

Figure 5.2 Weld metal CCT diagram (AO).

Figure 5.2 shows a CCT diagram applicable to weld metal of similar composition as above. Again three constituents are identified in the bainite region, i.e. lath ferrite (LF), acicular ferrite(AF) and coarse acicular ferrite (CAF). By comparing both CCT diagrams it can be seen that in terms of transformation temperatures and times, acicular and coarse acicular ferrite in weld metals occur in the same region as upper bainite and bainitic ferrite in HAZ's. Similarly, lath ferrite corresponds to lower bainite.*

Clearly there are distinct morphological differences between weld metal and HAZ transformation products. Nevertheless, the above similarities in terms of transformation kinetics does suggest that lath ferrite, acicular and coarse acicular ferrite are all simply morphological variants of the bainite reaction.

Further evidence for this view comes from a comparison of the maximum lath ferrite and acicular ferrite start temperatures with those predicted by the Steven and Haynes [163] formula for B_s temperature. Table 5.1 shows the correlation between measured LF_s or AF_s temperature and calculated B_s temperature, for four of the more highly alloyed weld metals. In view of the fact that the Steven and Haynes formula only has a 90% certainty of predicting B_s to ±25°C, Table 5.1 would seem to provide a reasonable correlation between the AF_s and B_s temperatures. Unfortunately at the lower hardenability of the other weld metals, the Steven and Haynes formula is no longer applicable and predicts much higher B_s temperatures than are found experimentally. This may be due to the lack of very low carbon steels in the original Steven and Haynes data base.

5.2.2 Transformation products within the normal welding range

5.2.2(a) Polygonal or grain boundary ferrite

In the literature review (section 2.2.6(a)) it was concluded that grain boundary ferrite in weld metals is identical to the proeutectoid ferrite morphology described as grain boundary allotriomorphs in the Dubé classification system. This conclusion was reached on the grounds of similar transformation temperatures, preferred nucleation sites, grain shapes, dislocation densities, and

---

NOTE: *In the Japanese literature lower bainite corresponded to Bainite III (see section 2.2.4(c)).

Weld Metal	B_s (^oC)	AF_s (^oC)
0.07C 2.12Mn	618	630
0.05C 1.18Mn 2.52Ni	610	595
0.04C 0.29Mn 3.58Ni	564	575
0.05C 1.72Mn - 1.87Ni 0.31Mo	563	557(LF)

TABLE 5.1: Correlation between Steven and Haynes B_s temperatures and measured AF_s temperatures.

Specimen Code	Austenite Grain Size (µm) (mean linear intercept $\overline{L}$)	
	Measured	Calculated
E0	49	47
E0(r)	72	925
E5(r)	78	197

TABLE 5.2: Correlation between measured and calculated austenite grain size, based on classical pinning theories.

the equilibrium partitioning of carbon and manganese at the transformation interface.

In the current investigation the CCT data provides an estimation of the typical ranges of PF_s temperatures to be expected in weld metals. These values obviously depend on cooling rate, alloying and austenite grain size.

For a typical basic flux MMA weld metal of composition 0.07 wt%C, 0.52 wt%Si, 1.35 wt%Mn subjected to a weld simulation thermal cycle, the values range from 760°C (Δt^{800}_{500} = 100 sec) to 700°C (Δt^{800}_{500} = 10 sec). These values are in good agrement with those recently presented by Christensen and Simonsen [99], van Nassau and Hullu [164] and Gaillard et al [165], for similar materials.

5.2.2(b) Sideplate structures

Sideplate development in weld metals is generally accepted as being an extension of the proeutectoid grain boundary ferrite reaction discussed in the previous section. Observations in the literature have noted similarities in transformation temperature, morphology, dislocation density and growth rate with the morphology termed Widmanstätten secondary sideplates in the Dubé system (section 2.2.6(b)). Unfortunately sideplate development in weld metals is complicated by the interactions of inclusions, alloying, austenite grain size, and cooling rate and it has therefore been difficult to postulate a mechanism to explain all the observations in the literature. Notable problem areas are the promotion of sideplates by high oxygen contents and the development of sideplates in some niobium bearing weld metals, but not in others.

In examining the influence of high oxygen content on microstructure, Cochrane and Kirkwood [129] observed an increase in $\gamma \rightarrow \alpha$ transformation temperature and suggested that this promoted Widmanstätten sideplate growth. The mechanism postulated is shown in Figure 5.3 and involves direct nucleation of ferrite on inclusions in the γ grain boundary. Due to anisotropy of diffusion fields around these nuclei, subsequent sideplate development follows as described by the Townsend and Kirkaldy [23] model of Widmanstätten sideplate formation.

Lazor and Kerr [166] have recently criticised the above model on the grounds that inclusion spacing does not correlate with the observed sideplate spacing. However, it should be remembered that

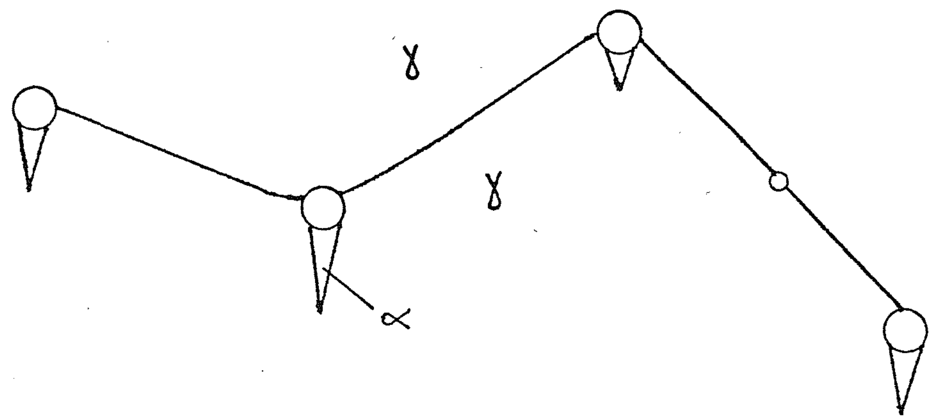

Figure 5.3 Schematic model for sideplate nucleation in high oxygen weld metals after Cochrane and Kirkwood (129).

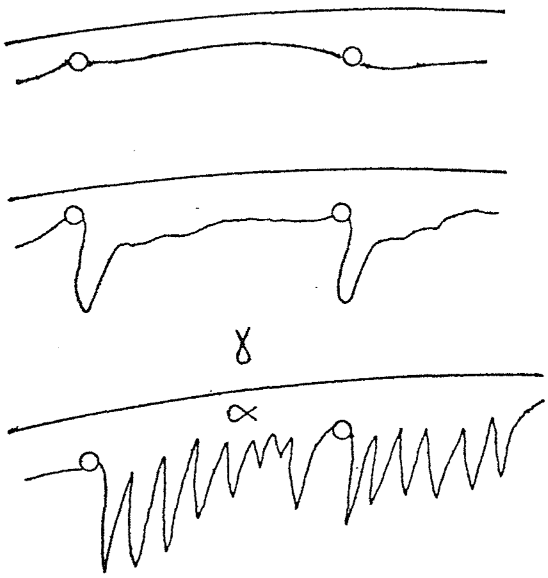

Figure 5.4 Model for the effect of inclusions on sideplate formation after Lazor and Kerr (166).

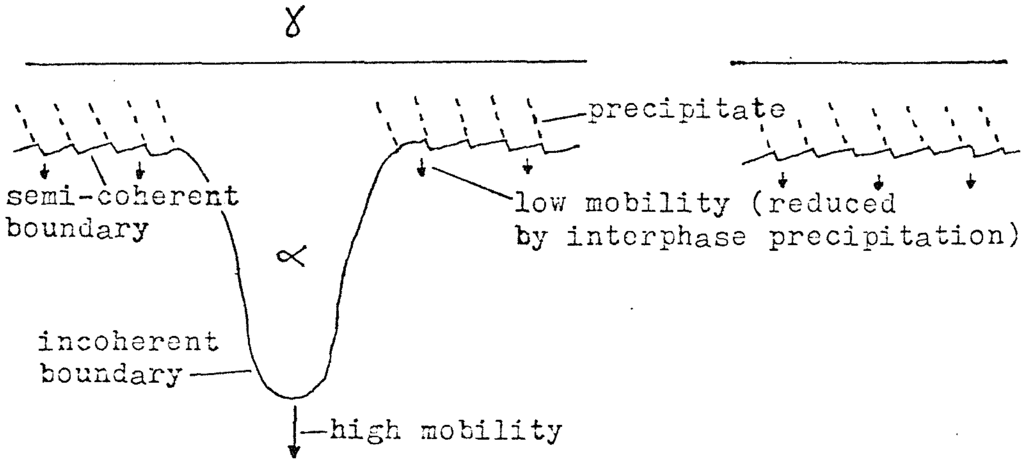

(a) Intermediate transformation temperature (incoherent and semi-coherent boundaries).

(b) Low transformation temperature (mainly semi-coherent boundaries).

Figure 5.5 Model showing the effect of interphase precipitation on sideplate development.

the diffusional sideband spacing will control the sideplate spacing rather than the inclusions themselves.

Lazor and Kerr [166] then suggested that inclusions may obtstruct the $\gamma \rightarrow \alpha$ interphase boundary as shown in Figure 5.4. This produces anisotropy of surface tensions and non-uniform growth rates which eventually produce colonies of sideplates. A criticism of this theory is the magnitude of the inclusion-interface interaction. Although grain boundary pinning is an important factor when boundaries are migrating by surface tension effects it is doubtful whether or not it is significant in retarding a transformation boundary driven by free energy of transformation.

In view of the fact that it has been shown that inclusions can catalyse grain boundary nucleation (section 2.5.4(e)), it would seem likely that Cochrane and Kirkwood's original model for sideplate development is reasonably correct. However, whether it is the initial interface shape or interface crystallography which influences sideplate development remains open to debate.

Another area of interest to the current discussion is the influence of niobium on sideplate development. From the results relating to niobium bearing weld metals contained in the following section, and similar reports in the literature, it would seem that niobiums influence is highly dependent on transformation temperature, (i.e. the hardenability and flux system of the consumables used in welding). The general concensus of opinion, for SA welding situations, is that in high oxygen/low hardenability systems niobium promotes sideplate structures, but in low oxygen/higher hardenability systems, niobium promotes acicular ferrite, although the sideplate to polygonal ferrite ratio may also increase in these systems [57][167]. In an attempt to explain these phenomena Harrison et al [75] suggested that interphase precipitation of Nb(CN) may be an important factor in limiting the development of grain boundary ferrite. An illustration of this model is shown in Figure 5.5. In this model it is assumed that the allotriomorph γ/α interfaces consist of a mixture of high energy incoherent and low energy semi-coherent boundaries.

At low transformation temperatures (Figure 5.5(b)) the interfaces are predominantly of the low energy type, as discussed in section 2.2.4(b), and migrate by the lateral movement of ledges. Interphase precipitation of Nb(CN) at these ledges impedes the boundary migration resulting in lower proportions of grain boundary ferrite as shown in the CCT diagrams (Figures 5.14 and 5.15).

At higher transformation temperatures (Figure 5.5(a)) the interfaces contain a greater proportion of incoherent boundaries, which will be appreciably more mobile than the restricted semi-coherent regions at elevated temperatures. The net result is automatic sideplate development as shown in Figure 5.5(a). Further development of these sideplates may then be enhanced by the Townsend and Kirkaldy diffusion model previously discussed.

The above model may now be extended to give a more general model for sideplate initiation in weld metals. In section 2.2.5(a) it was noted that faceting of the grain boundary allotriomorph interface tends to increase with decreasing transformation temperature. This leads to a morphological progression of the allotriomorph from smooth to ragged, to blocky, and eventually to the development of sawteeth and sideplates. It is difficult to define specific temperatures for these variations but evidence in the literature suggests that the changes occur in the temperature range 800°C to 700°C, under isothermal conditions.

The influence of the allotriomorph interface type on sideplate development may now be considered for three different temperature regimes during continuous cooling of weld metals as shown in Figure 5.6.

(1) <u>High $\gamma \rightarrow \alpha$ transformation temperature (Typically 775°C-725°C)</u>

At high transformation temperatures the γ/α interface will be mainly incoherent and mobile as shown in Figure 5.6(a). This results in more or less uniform migration of the interface and very little tendency towards sideplate development. An example of this type of behaviour is shown by the weld metal of composition 0.06 wt%C, 0.41 wt%Si, 0.56 wt%Mn (figure 4.47(a)) which starts to transform at ∿750°C (Δt_{500}^{800} = 10 sec) and develops a microstructure containing about 75% polygonal ferrite and only 10% ferrite sideplates.

(2) <u>Intermediate $\gamma \rightarrow \alpha$ transformation temperature (Typically 725°C-675°C)</u>

At intermediate transformation temperatures the γ/α interfaces will consist of a mixture of incoherent and semi-coherent regions. In this temperature regime the incoherent boundaries are more mobile than the semi-coherent boundaries and this will automatically lead to sideplate development, as shown in Figure 5.6(b). Examples of this type of behaviour are the high oxygen weld metals discussed in the literature and certain weld metals susceptible to interphase precipitation as previously discussed. An example of this type of behaviour is the weld metal of composition 0.08 wt%C, 0.16 wt%Si, 0.97 wt%Mn,

(a) High Temperature

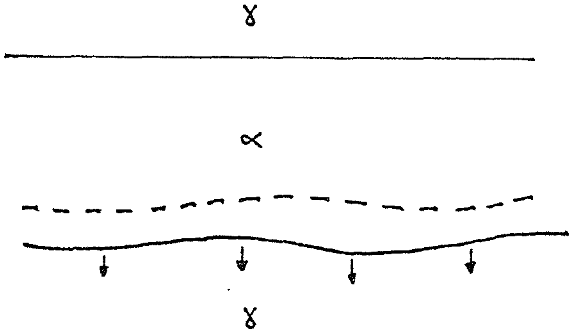

γ/α interphase boundary incoherent and mobile.

(b) Intermediate Temperature

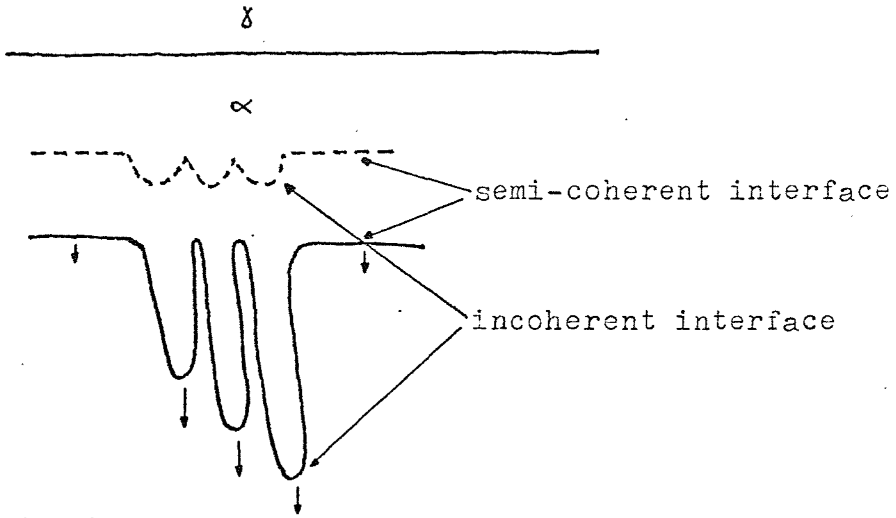

γ/α interphase boundaries consisting of semi-coherent and incoherent regions. Incoherent regions are more mobile in this temperature regime.

(c) Low Temperature

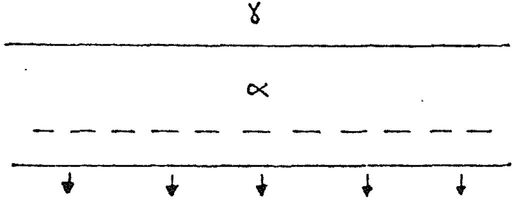

γ/α interphase boundaries mainly semi-coherent and mobile.

Figure 5.6 Model showing the influence of interphase boundary mobility on sideplate development.

0.02 wt%Nb, 0.07 wt%O (Figure 4.57(a)), which starts to transform at 675°C (Δt_{500}^{800} = 10 sec) and develops a microstructure containing about 50% sideplates and only 20% polygonal ferrite.

(3) Low $\gamma \rightarrow \alpha$ transformation temperature (Typically below 675°C)

At low transformation temperatures the γ/α interfaces will be largely semi-coherent and become increasingly mobile (Figure 5.6(c)). In this temperature regime the mobility of these boundaries is of similar order to diffusionally controlled incoherent boundaries. This results in a reduced tendency towards sideplate development, although as before interphase precipitation may inhibit movement of the semi-coherent boundaries and therefore encourage sideplate development. An example of transformation behaviour in this temperature regime is the weld metal of composition 0.07 wt%C, 0.33 wt%Si, 2.12 wt%Mn (figure 4.49(a)) which starts to transform at ∿640°C (Δt_{500}^{800} 10 sec) and develops 15% polygonal and only 5% sideplate ferrite within the proeutectoid ferrite phase field.

The above model shows how the nature of the intial γ/α interphase boundary may play an important role in initiating sideplate structures in weld metals. Clearly any alloying additions which retard the mobility of semi-coherent interphase boundaries through interphase precipitation may favour sideplate development if transformations are occurring within the "susceptible" temperature regime. Oxygen content may influence sideplate development simply through its influence on transformation start temperatures.

The final extent to which sideplates develop in the microstructure will depend on their transformation rate and the time interval before lower temperature transformation products start to dominate the transformation reaction.

5.2.2(c) Acicular ferrite

According to the literature (section 2.2.6(c)) acicular ferrite is a fully intragranular, fine grained morphology, consisting of highly dislocated acicular grains, separated by high angle grain boundaries. Previous investigators have shown that acicular ferrite develops during continuous cooling at lower temperatures than Widmanstätten sideplates, but at higher temperatures than lath ferrite (bainite). Thus it is not immediately apparent whether acicular ferrite is a low temperature extension of the proeutectoid reaction, or a high temperature extension of the bainite reaction.

The results of the current investigation confirm the view that acicular ferrite forms at lower transformation temperatures than Widmanstätten ferrite. However the distinction between lath ferrite and acicular ferrite is more dependent on cooling rate than transformation temperature in weld metals which exhibit both morphologies. A similar cooling rate dependence of bainite morphology was also observed by Habraken and Economopoulos [38] in wrought low carbon low alloy steels. In this investigation a large range of low alloy steels were found to develop bainite, with a parallel lath morphology during fast cooling, but a more irregular granular morphology at slower cooling rates. The actual morphology of Habraken's granular bainite differs markedly from acicular ferrite in terms of acicularity. In view of this, acicular ferrite is not considered to be a true granular bainite, but rather an alternative morphological variant of the bainite reaction, which develops from extensive independent intragranular nucleation.

Further evidence of the bainitic nature of acicular ferrite comes from the following observations.

(1) Correspondence of the AF_s temperature with the Stevens and Haynes B_s temperature for the more highly alloyed weld metals (Table 5.1).

(2) Very high dislocation densities.

(3) Occurrence of Nb(CN) precipitation within the bainitic ferrite on stress relieving [65]. This suggests initial supersaturation during transformation.

(4) Surface relief effects (Figure 4.2).

Unfortunately it is difficult to be emphatic that all acicular ferrite is totally bainitic in character. Evidence for the proeutectoid nature of acicular ferrite comes from the occurrence of regions of highly enriched austenite which often accompany the phase. The presence of such regions shows that carbon rejection has occurred either during or immediately subsequent to acicular ferrite transformation. If these enriched regions transform to pearlite during transformation, then the previous ferrite reaction must be considered to be proeutectoid in nature. However, if these regions remain untransformed or transform to martensite-austenite (MA constituent), the nature of the ferrite reaction will be inconclusive, as both upper bainite and Widmanstätten ferrite cause austenite enrichment.

Evidence of the proeutectoid nature of coarse acicular ferrite was given in section 4.7 of the results chapter using the "quenching out" technique. From Figures 4.42 and 4.43 it can be seen that coarse acicular ferrite develops at a higher transformation temperature than pearlite thus suggesting it is proeutectoid in character. Unfortunately these optical micrographs are not absolutely conclusive because most of the large pearlitic carbides are associated with the polygonal proeutectoid ferrite, rather than the coarse acicular ferrite. A more detailed examination of the fine carbides associated with the coarse acicular ferrite is required to resolve this question. Other factors which suggest that acicular ferrite may be proeutectoid in nature are as follows:-

(1) Morphological similarities to intragranular Widmanstätten plates discussed in section 2.2.5(a).

(2) Tendency for carbon enrichment of austenite during proeutectoid reaction to depress B_s temperature more than W_s temperature as reaction proceeds.

(3) Surface relief effects.

From the information obtained in the current investigation it seems likely that acicular ferrite formed in higher hardenability weld metals and at fast cooling rates under the "bainite" nose is definitely bainitic in character. There is, however, the possibility that acicular ferrite formed at higher transformation temperature (through lower hardenability or slow cooling rates) may have a more Widmanstätten character. Ideally acicular ferrite should be examined under isothermal conditions to determine whether it is a truly proeutectoid or truly bainitic phase.

The various theories relating to acicular ferrite nucleation will be discussed in detail in section 5.4, which considers the influence of inclusions on weld metal transformation behaviour.

5.2.2(d) Lath ferrite

According to the literature (section 2.2.6(d)),lath ferrite consists of fine parallel laths of ferrite, separated by carbide precipitates, or MA islands. Laths have an extremely high dislocation density and are separated by low angle boundaries. The transformation temperature of lath ferrite is generally believe to be low, (below 500°C according to Choi and Hill [55]). The above evidence suggests that lath ferrite is a form of upper bainite in which the adjacent enriched austenite may or may not transform.

In the current investigation weld metal of composition 0.05 wt%C, 0.19 wt%Si, 1.72 wt%Mn, 0.31 wt%Mo. 1.87 wt%Ni (Figure 4.58) transformed to a very high proportion of lath ferrite throughout the typical arc welding cooling rate range. The LF_s temperature can be seen to be in excellent agreement with the Stevens and Haynes B_s temperature (Table 5.1) which is further evidence that this morphology is in fact upper bainite. In most of the other weld metals the proportion of lath ferrite is low, particularly within the welding range. For example weld metal of composition 0.05 wt%C, 0.38 wt%Si, 1.18 wt%Mn, 2.52 wt%Ni (Figure 4.52) starts to transform intragranularly at $\sim 560^{\circ}C$ (Δt_{500}^{800} = 10 sec.) and develops 55% acicular ferrite and only 5% lath ferrite. Increasing the cooling rate however, promotes lath ferrite and at Δt_{500}^{800} = 3 sec. the intragranular transformation starts at $\sim 510^{\circ}C$ and produces almost equal proportions of acicular ferrite, lath ferrite and martensite.

The above cooling rate dependence of lath ferrite development is a feature observed in many of the weld metals, and has important practical implications. For example, a weld metal optimised for use at high heat input or with pre-heat may develop significant quantities of lath ferrite, or even martensite, if used under low heat input conditions, or without pre-heat. Alternatively, dilution from the parent metal by elements with a strong influence on hardenability may also encourage lath ferrite development if the weld metal is already highly alloyed.

In the current investigation lath ferrite also occurs in the remelted weld metal with the lowest oxygen content ($\sim$58 ppm). Details of this experiment are discussed in section 5.4, but it should be noted that complete removal of oxygen causes a change in microstructure from acicular to lath ferrite. This suggests that the oxygen rich deoxidation products have a strong influence in nucleating acicular ferrite, and that the change in morphology from acicular to lath ferrite is nucleation controlled. If this assumption is correct the tendency towards lath ferrite development at fast cooling rates or high hardenability must be explained in terms of more favourable nucleation rates. Presumably the side-by-side sympathetic nucleation of parallel bainitic laths dominates over independent nucleation of individual acicular ferrite laths at very high levels of supercooling.

5.2.3 Influence of cooling rate on $\gamma \rightarrow \alpha$ transformation behaviour

By studying the CCT diagrams (Figures 4.47 to 4.58) the following influences of cooling rate on weld metal transformation behaviour can be observed.

In general the overall effect of increasing cooling rate is to lower transformation temperatures. In the current investigation the only exception to this type of behaviour is the C-Mn-Ni-Mo weld metal, which develops bainite over a wide range of cooling rates, and has almost constant transformation characteristics within the typical welding range.

In most weld metals depression of transformation temperature, due to increased cooling rates, reduces the quantity of grain boundary nucleated phases and favours intragranular morphologies such as coarse acicular ferrite, acicular ferrite, or lath ferrite. The exception to this rule is the high oxygen, niobium bearing weld metal (Figure 4.57), which produces a more or less constant quantity of grain boundary nucleated ferrite (PF + FSP), over a wide range of cooling rates. This is due to the extensive development of sideplates in this weld metal, which is enhanced by increased cooling rates. Owing to the faster growth rate of sideplates, a greater proportion of this morphology develops, than would be expected for allotriomorphs over the same temperature drop.

Increasing cooling rate progressively suppresses the carbide reactions. At slow cooling rates pearlite is formed, but with increasing cooling rate transformation temperature is progressively depressed and the amount of pearlite decreases and becomes degenerate in nature. Faster cooling rates tend to eliminate the reaction completely but may give rise to areas of retained austeinite or martensite/austenite (MA) which may transform to carbides on subsequent reheating (e.g. stress relieving treatments).

Cooling rate also has an important influence on the intragranular reaction. As previously discussed,faster cooling rates often tend to promote lath ferrite and martensite, although the exact extent of this effect seems to depend on alloying and nucleation characteristics of the weld metal.

Increasing cooling rate has the effect of refining acicular ferrite grain size, and conversely decreasing cooling rate favours the development of coarse acicular ferrite (CAF).

These general observations of the effect of cooling rate on transformation behaviour may now be made more specific by considering typical weld metal cooling rates. For ease of discussion an order of magnitude of cooling rate will be considered - from $3^{\circ}C/sec$ to $30^{\circ}C/sec$ (i.e.Δt_{500}^{800} 's between 100 sec and 10 sec). This range of cooling rates is typical for arc welding and covers most S.A. and M.M.A. situations.

Figure 5.7 shows the above cooling rate range for three weld metals with significantly different transformation characteristics. Figure 5.7(a) relates to a 3.5 wt%Ni, basic flux, weld metal which is clearly optimised for high heat input or pre-heated welding conditions.

At a slow cooling rate (Δt_{500}^{800}=100 sec), the grain boundary nucleated transformation starts at $\sim 624^{\circ}C$ and results in ∿35% polygonal ferrite and 5% sideplates. On further cooling the remaining 60% of the austenite transforms to acicular ferrite in the temperature range $575^{\circ}C$ to $475^{\circ}C$. From a toughness point of view this microstructure should be reasonably good, because it is not embrittled by either pearlite, lath ferrite, or martensite.

At a fast cooling rate (Δt_{500}^{800}=10 sec), the grain boundary reaction commences at $\sim 560^{\circ}C$ and is followed by the intragranular reaction at $\sim 530^{\circ}C$. This results in a microstructure consisting of 15% polygonal ferrite, 5% sideplates, 60% acicular ferrite, 8% lath ferrite and 12% martensite. Obviously at the faster cooling rate this particular weld metal is not optimised for toughness, due to the presence of both lath ferrite (bainite) and martensite.

It is interesting to note that at this relatively high alloy level, the high proportion of acicular ferrite is maintained over an appreciable range of cooling rates. This is a very useful characteristic for high heat input welding situations. It can also be seen from Figure 5.7(a) that although this particular weld metal may remain in the proeutectoid ferrite transformation regime for some time (∿20 sec at Δt_{500}^{800}=100 sec), there is little tendency towards sideplate development. This reinforces the view that the nature of the γ/α interface plays an important role in initiating sideplates as discussed in section 5.2.2(b).

Figure 5.7(b) relates to a basic flux, C-Mn weld metal containing 1.35 wt%Mn.

At a slow cooling rate (Δt_{500}^{800}=100 sec), the grain boundary reaction starts at $\sim 760^{\circ}C$ and results in ∿80% polygonal ferrite and 5% sideplates. On further cooling, the remaining transformation to

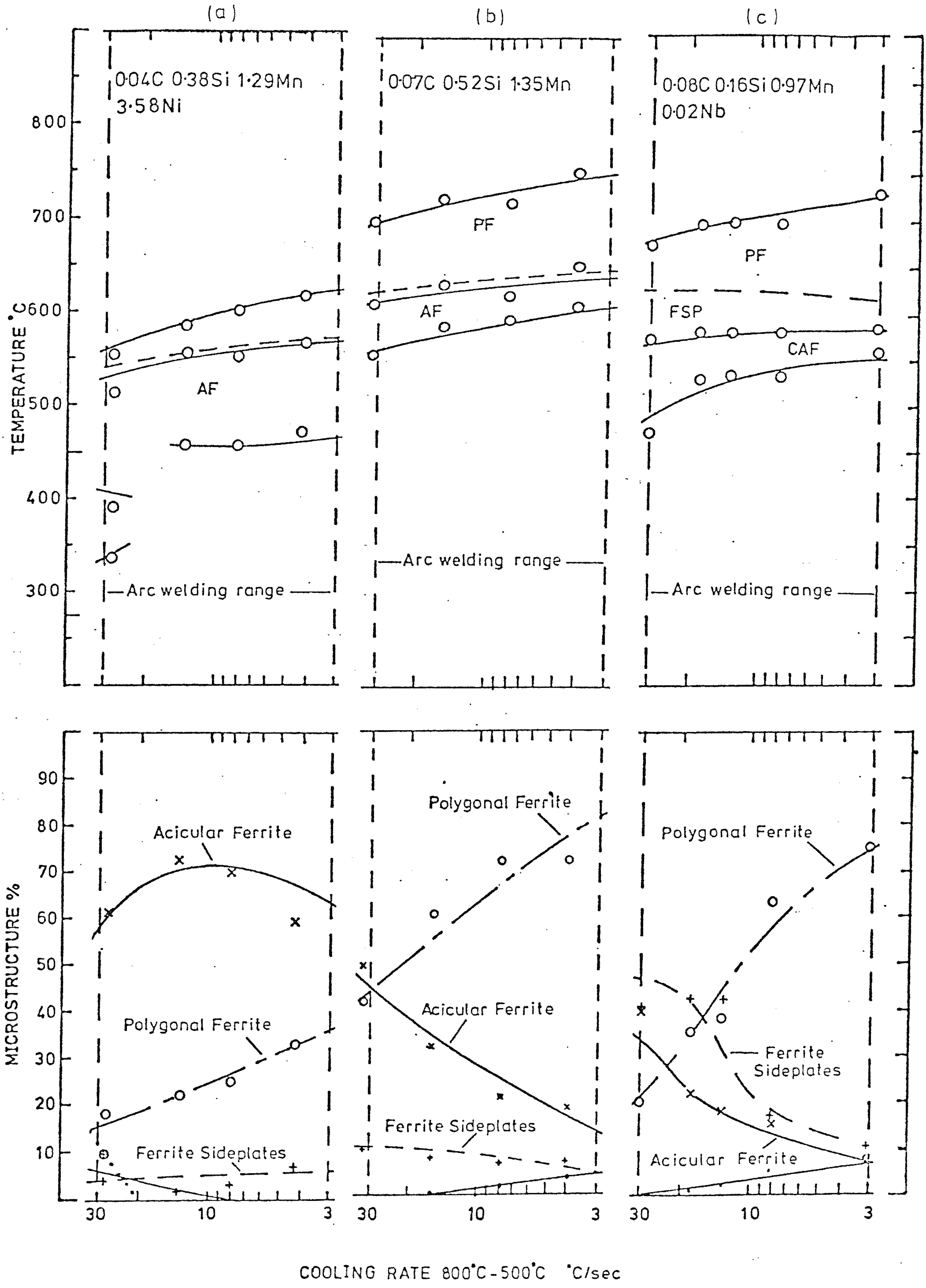

Figure 5.7 Influence of cooling rate on $\gamma \rightarrow \alpha$ transformation and microstructural development for three different types of weld metals.

coarse acicular ferrite and pearlitic carbides occurs in the temperature range ~640°C to 610°C.

At a fast cooling rate (Δt_{500}^{800} = 10 sec) the grain boundary reaction commences at ~700°C resulting in ~45% polygonal ferrite and 10% sideplates and the remaining intragranular transformation produces 45% acicular ferrite between ~620°C and 560°C.

In this particular weld metal the microstructure produced at high heat inputs is clearly not optimised for toughness due to the small quantity of acicular ferrite and the occurrence of a high volume fraction of pearlitic carbides (~5%). At low heat inputs the microstructure should be reasonably good from a toughness point of view due to the absence of embrittling phases such as pearlite, lath ferrite or martensite. However, the proportion of acicular ferrite is only 45%.

It should be noted that the C-Mn weld metal just discussed is much more sensitive to cooling rate changes than the previous 3.5% Ni weld deposit. This implies that C-Mn weld metals will only be optimised for toughness over a fairly narrow band of cooling rates. If this implication is correct, the optimum manganese content for high heat input SA welding will be significantly greater than for low heat input MMA welding situations, provided other factors such as prior grain size and chemistry remain constant.

Figure 5.7(c) relates to a high oxygen-niobium bearing SA weld metal of composition 0.08 wt%C, 0.97 wt%Mn, 0.02 wt%Nb.

At a slow cooling rate (Δt_{500}^{800}=100 sec), the grain boundary nucleated reaction starts at 730°C and results in the development of 75% polygonal ferrite and 10% sideplates. On further cooling the remaining 15% austenite transforms to almost equal proportions of coarse acicular ferrite and pearlitic carbides between 590°C and 550°C.

At a fast cooling rate (Δt_{500}^{800}=10 sec), the grain boundary reaction starts at 680°C resulting in 20% polygonal ferrite and almost 50% sideplates. This is followed by the intragranular reaction which commences at 570°C and the remaining 30% austenite transforms to acicular ferrite.

Clearly the transformation behaviour of the high oxygen-niobium bearing weld metal differs considerably from the previous basic flux C-Mn and C-Mn-Ni varieties, in terms of sideplate development. At the slower cooling rates the transformation behaviour is not that dissimilar from the C-Mn weld metal. However at faster cooling rates, sideplate development dominates the transformation. The model postulated in section 5.2.2(b) to describe sideplate development predicts a very high susceptibility to sideplate development for transformations starting in the 725°C - 675°C temperature regime. This susceptibility is further increased by the influence of niobium, which also makes sideplate development more likely at lower transformation temperatures, due to interphase precipitation. In the weld metal under discussion, at $\Delta t_{500}^{800}=10$ sec, transformation starts at 680°C, which is within the dangerous region predicted for sideplate initiation. However the C/Mn weld metal previously discussed also starts within this temperature regime but produces only 15% sideplates. An additional factor must therefore be involved in influencing the continued development of sideplates. By comparing Figures 5.7(b) and (c), it can be seen that there is a significant difference in the temperature at which the intragranular transformation commences, (620°C for C/Mn as opposed to 570°C for high O_2/Nb). Thus, in the C/Mn weld metal, sideplate development is interrupted by the intragranular reaction at a fairly early stage. In the high oxygen-niobium weld metal, on the other hand, sideplate development is not interrupted until a substantial amount of transformation has occurred. The above observation is extremely important because it implies that the potency of intragranular nucleation sites may be varied from one weld metal to another. This possibility will be discussed in more detail in the section on the influence of inclusions, (section 5.4).

It must be remembered that all the previous discussions relate to CCT diagrams and give results which are applicable to reheated weld metal specimens. These values should also be reasonably accurate in describing transformation behaviour in coarse grained regions of reheated weld metals in multipass welds, (i.e. close to the fusion line). To describe transformation behaviour in the as deposited regions a correction factor is required to account for differences in austenite grain size and shape.

It must also be remembered that the previous comments on weld metal toughness are based entirely on microstructural considerations. These simplified assumptions neglect other factors such as solution strengthening, strain ageing, precipitation or grain boundary embrittlement which if present, mitigate against good toughness in the so called "optimum" microstructure.

5.2.4 Summary

The previous section has been primarily concerned with a discussion of weld metal CCT diagrams and the influence of cooling rate on weld metal transformation behaviour.

Some of the more salient points arising from this discussion are summarised below.

(1) Experimentally determined CCT diagrams for weld metals are in general agreement with the schematic CCT diagram presented in the literature review. The overall shapes of these diagrams are similar to those applicable to HAZ's, although the bainite region is replaced by a region in which either acicular ferrite or lath ferrite develops. In general terms lath ferrite replaces acicular ferrite at fast cooling rates, high alloy contents, or when suitable nucleation sites for acicular ferrite are removed.

(2) Grain boundary ferrite in weld metals is equivalent to the morphological variety of the proeutectoid ferrite reaction known as grain boundary allotriomorphs.

(3) Sideplate structures in weld metals are for the most part equivalent to the morphological variety of the proeutectoid reaction known as Widmanstätten secondary sideplates. Their development is influenced by chemical composition, cooling rate and austenite grain size and is enhanced by high oxygen contents. The initial development of sideplate structures can be explained in terms of the type and mobility of the $\gamma \rightarrow \alpha$ interphase boundaries. This is in turn controlled by the transformation temperature and factors such as interphase precipitation.

The final extent of sideplate development depends on the time available for growth before the intragranular reaction occurs.

(4) Acicular ferrite is a fully intragranular, fine grained transformation product which is known to confer good mechanical properties to weld metals.

The bainitic nature of acicular ferrite is evident from the good correspondence between AF_s and B_s temperatures particularly in the more highly alloyed weld metals. Further evidence of its bainitic nature comes from its high dislocation density and the occurrence of certain precipitation reactions within acicular ferrite grains during stress relieving.

Evidence for the proeutectoid nature of acicular ferrite formed in lower hardenability weld metals comes from its morphological similarity to intragranular Widmanstätten plates, and the occurrence of carbon enrichment between acicular ferrite laths.

(5) The low temperature lath ferrite structure in weld metals is identical to upper bainite in terms of both transformation temperatures and morphology.

(6) Cooling rate has many influences on the transformation behaviour of weld metals, as discussed in section 5.2.3. In basic flux C-Mn-(Ni) weld metals increasing cooling rate generally has the following effects:

(a) Transformation temperatures are depressed.
(b) The proportion of grain boundary nucleated products decreases.
(c) The intragranular acicular ferrite becomes refined.
(d) The pearlite reaction is suppressed.
(e) At very fast cooling rates or high alloy contents, lath ferrite and martensite are formed.

5.3 Influence of Alloying and Austenite Grain Size on Weld Metal $\gamma \rightarrow \alpha$ Transformation Behaviour

5.3.1 Influence of manganese

By comparing the three CCT diagrams produced from the C-Mn series of MMA weld metals, it should be possible to deduce the effect of manganese on weld metal transformation behaviour at any given cooling rate. Obviously to do this accurately, all other variables such as prior austenite grain size and weld metal chemistry must be kept as constant as possible.

Figure 5.8 shows CCT diagrams for weld metal materials M1 (0.56 wt%Mn), M2 (1.35 wt%Mn), and M5 (2.12 wt%Mn), superimposed to show the influence of manganese. For simplicity only the 2½% and 97½% transformation lines are presented.

It can be seen that the prior austenite grain sizes of each material are virtually identical (ASTM 5.7, 5.8 and 5.8) and that variations in the following elements are minimal - C,P,S,Cr,Mo,Ni,V and Cu. However, it should be noted that variations in silicon and oxygen content may be significant. In the case of silicon, the

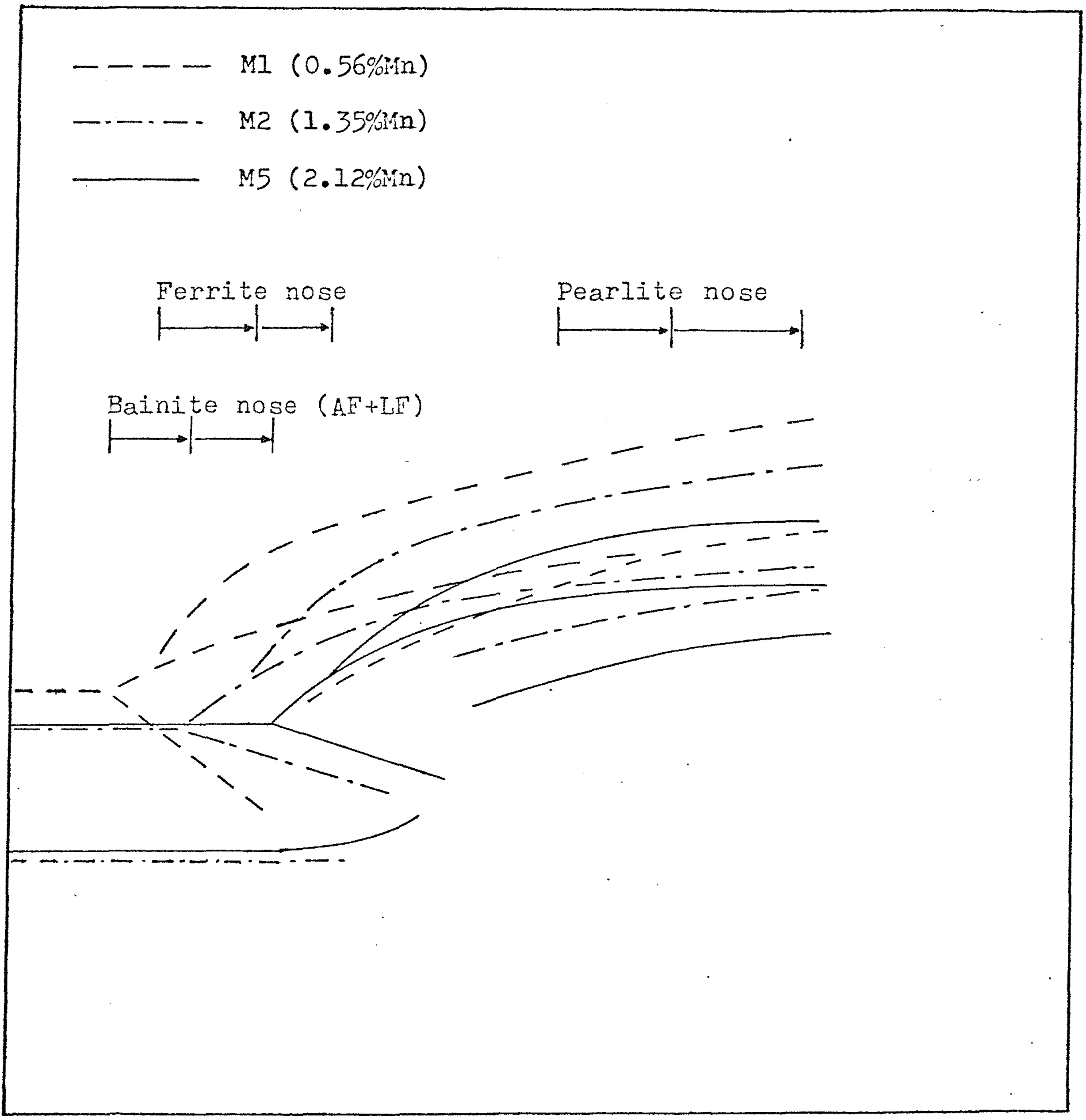

Figure 5.8 CCT diagrams M1, M2, and M5 superimposed to show the influence of manganese.

variation between weld metals M2 and M5 is almost 0.2 wt%. In the case of oxygen, there is a decrease in oxygen content with increasing manganese content, which amounts to approximately 100 ppm between M1 and M5 (Figure 4.1).

The effect of superimposing the three CCT diagrams shows that transformation temperatures are depressed at almost all practical cooling rates by manganese. The values of martensite transformation temperatures are likely to be subject to quite large experimental errors (see Appendix) so little emphasis will be placed on them. The M_s temperature presented for M1 (0.56%Mn) is an estimate based on the Andrews formula [168].

The influence of manganese on transformations within the typical arc welding cooling rate range is best illustrated by referring to Figure 5.9. This combined transformation temperature and microstructure diagram shows that manganese depresses all transformation temperatures throughout the arc welding range.

From Figure 5.9 it can be seen that all polygonal ferrite start temperatures are depressed to a greater extent than the corresponding acicular ferrite start temperatures with increasing manganese additions. This results in progressively less polygonal ferrite and more acicular ferrite in the final microstructure.

It can also be seen from Figure 5.9 that the addition of manganese gradually suppresses the formation of pearlite at typical welding cooling rates. In the 0.56 wt%Mn alloy, pearlite is present at all welding cooling rates, but in the 2.12 wt%Mn alloy it is completely suppressed.

From Figure 5.9 it can also be seen that manganese has little effect on the maximum quantity of ferrite sideplates formed in the final microstructure. However, manganese does control the cooling rates at which the sideplates are replaced by other transformation products through its effect on hardenability.

An important point of interest is the high proportion of acicular ferrite, produced at high cooling rates, in the 0.56 wt%Mn weld metal. In a recent report it was suggested that there may be a critical Mn content, of about 1.1 wt%, above which weld metal microstructures are predominantly acicular ferrite [130]. Clearly manganese is important in developing acicular ferrite microstructures, but the actual manganese level required is also highly dependent on cooling rate.

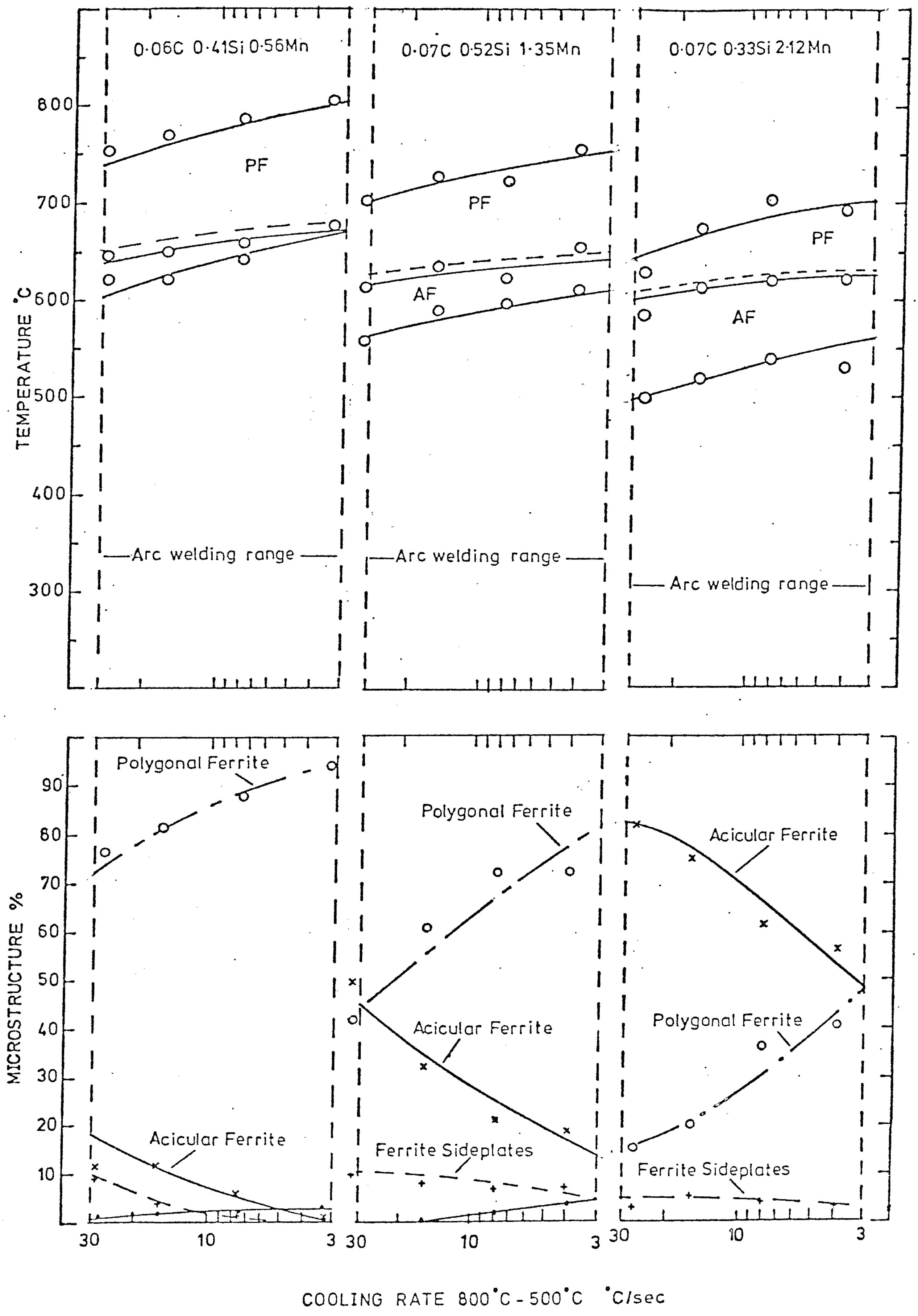

Figure 5.9 Influence of manganese on weld metal transformation behaviour within the typical arc welding cooling rate range.

Figure 5.10 shows the influence of manganese on polygonal ferrite and acicular ferrite start temperatures, at a cooling rate of $3^{o}C/sec$ (Δt_{500}^{800}=100 sec). For comparative purposes the calculated M_s and B_s temperatures, based on the Andrews and Steven and Haynes formulae, have also been included in this figure.

It is interesting to note that extrapolation of the data in Figure 5.10 implies that a 100% acicular ferrite microstructure could be produced at about 4 wt%Mn, with a transformation start temperature of about 565°C. However, according to Choi and Hill, high manganese levels eventually produce the low temperature lath structure, (Upper bainite). This latter effect suggests that above some critical level of manganese, the PF_s and AF_s lines no longer apply (Figure 5.10), and transformations proceed as described by the B_s line. Obviously the actual level of alloying at which this occurs is important from a practical point of view, as it sets the upper alloying limit for acicular ferrite development.

5.3.2 Influence of nickel

By comparing the four CCT diagrams produced from the C-Mn-Ni series of MMA weld metals it should be possible to deduce the effect of nickel at any cooling rate.

Figure 5.11 shows the outlines of CCT diagrams for weld metals N1 (0.06 wt%Ni), N2 (1.10 wt%Ni), N3 (2.52 wt%Ni) and N4A (3.58 wt%Ni), superimposed to show the influence of nickel. It can be seen that nickel has depressed transformation temperatures throughout the range of CCT diagrams in a similar manner to manganese.

The prior austenite grain sizes vary slightly throughout the series (ASTM 5.4, 5.5, 5.0 and 4.8) althought his variation is probably within experimental error. The following elements in the chemical analyses are also within reasonably close limits throughout the series - C,Si,P,S,Cr,Mo,V,Cu and O. Variations in Mn, particularly between N1 (0.98 wt%Mn) and N4A (1.29 wt%Mn) will undoubtedly be significant in affecting transformation temperatures.

The influence of nickel on transformations within the typical arc welding cooling rate range is best illustrated by referring to Figure 5.12. As in the case of manganese, nickel also depresses transformation temperature throughout the arc welding cooling rate range. Again it can be seen that the polygonal ferrite start temperatures are depressed more than the corresponding acicular ferrite

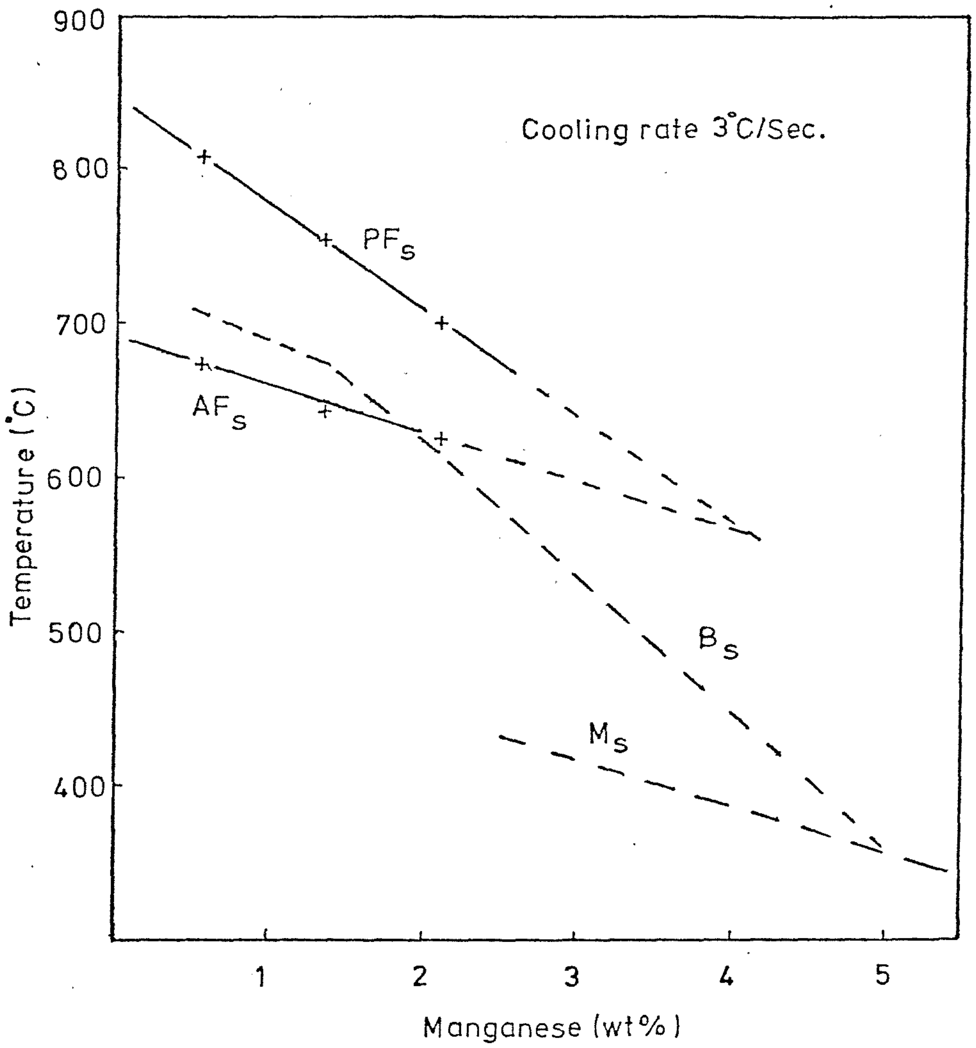

Figure 5.10 Influence of manganese on transformation start temperatures for PF, AF, B, and M, at a cooling rate of 3 °C/Sec.

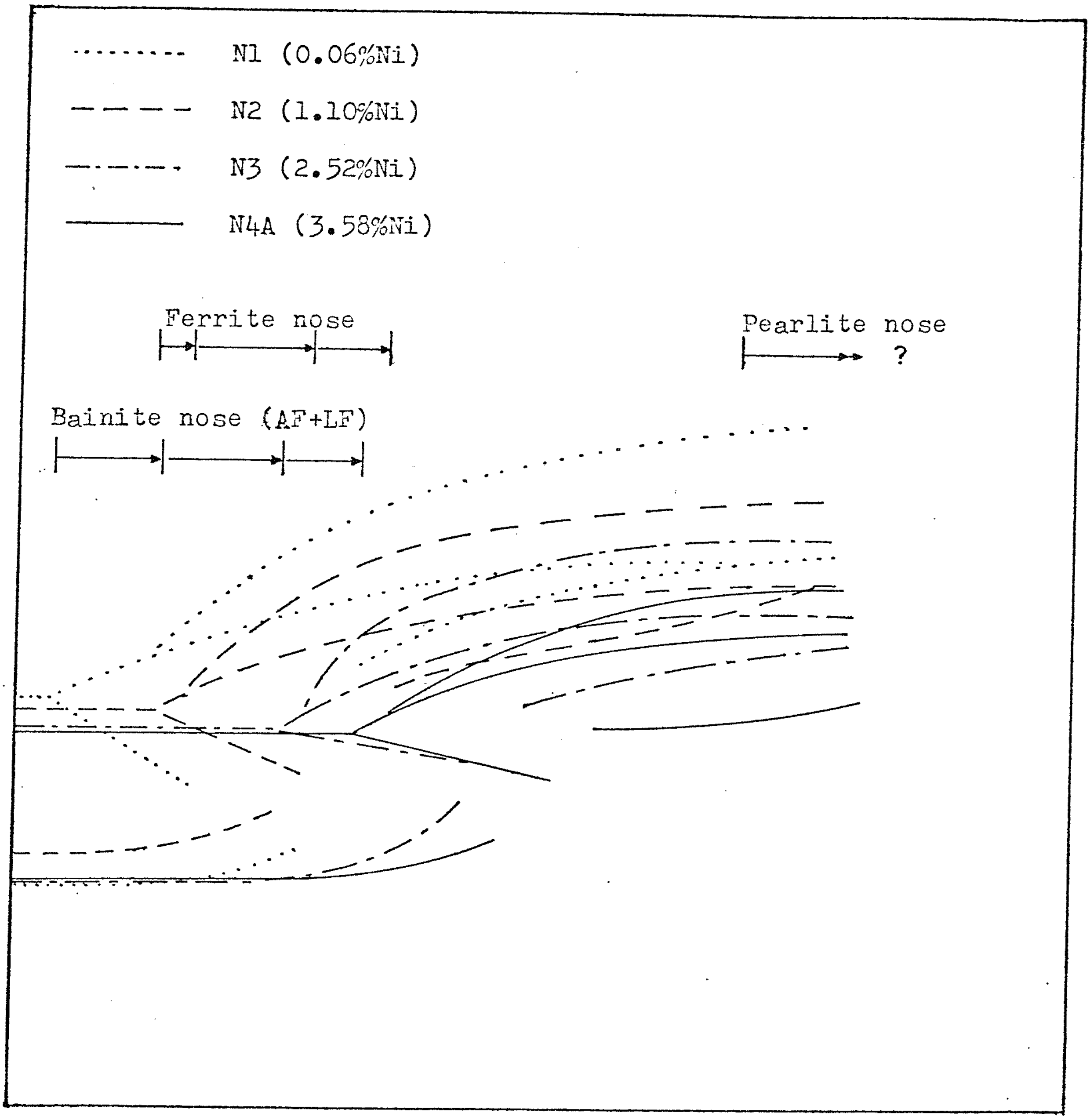

Figure 5.11 CCT diagrams N1, N2, N3, and N4A superimposed to show the influence of nickel.

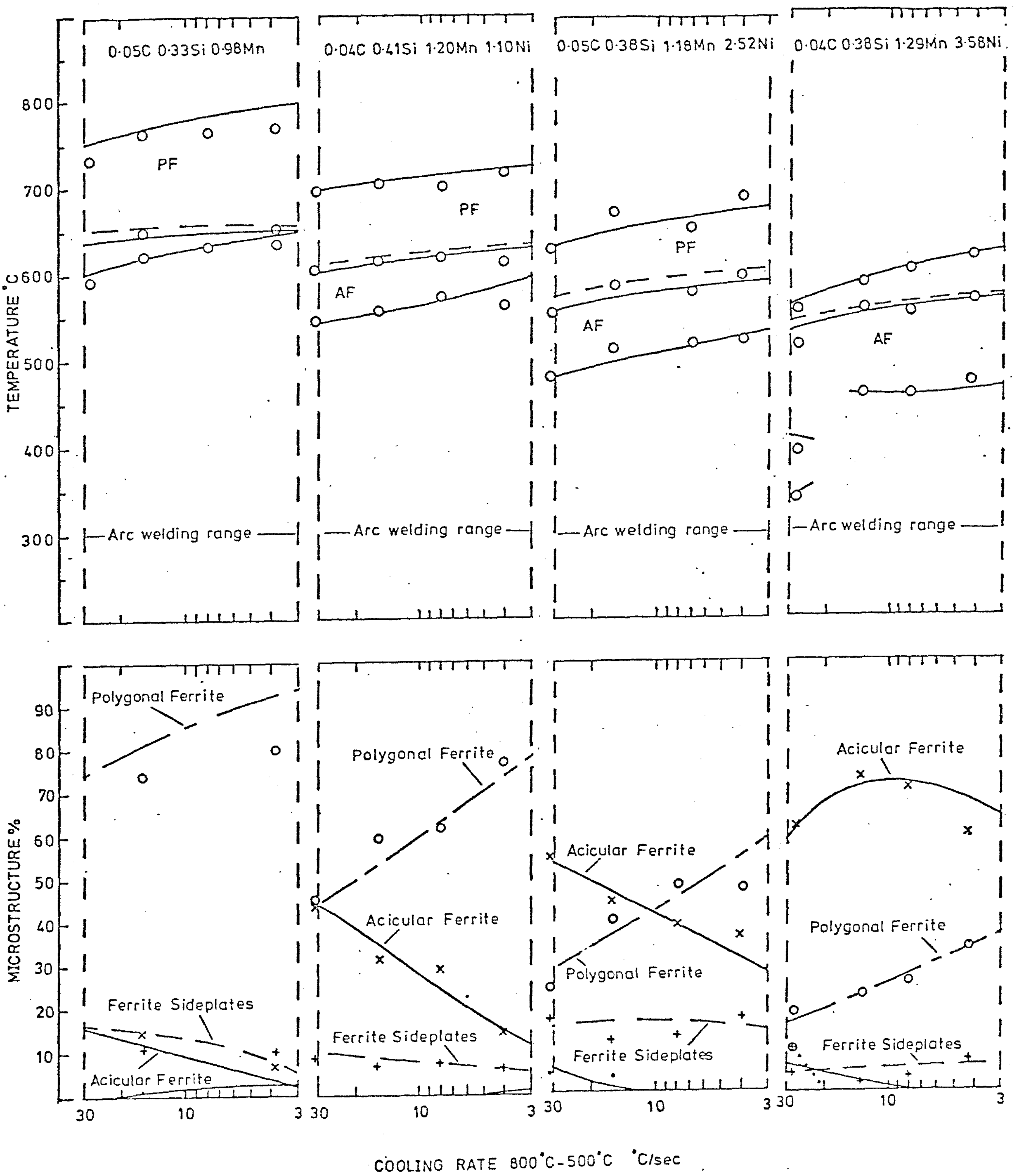

Figure 5.12 Influence of nickel on weld metal transformation behaviour within the typical arc welding cooling rate range.

start temperatures at the same cooling rates. This has the effect of progressively increasing the quantity of acicular ferrite in the microstructure at the expense of polygonal ferrite. It can be seen that for the 3.6 wt%Ni weld metal a certain amount of martensite may be formed within the welding cooling rate range. Transformations to pearlite react in much the same way as in the C-Mn series by being sensitive to movement of the complete CCT diagram relative to the welding cooling rates. A rather unexpected result is the large quantity of sideplates in weld metal N3 relative to the other nickel bearing weld metals. It should also be noted that some lath ferrite occurs at the faster welding cooling rates in both the 2.5 wt%Ni and 3.5 wt%Ni weld metals.

Figure 5.13 shows the influence of nickel on polygonal and acicular ferrite start temperatures at a cooling rate of 3^{o}C/sec. It is interesting to note the similarity between this figure and Figure 5.10 which related to manganese. As with manganese it appears that nickel eventually eliminates the polygonal ferrite reaction. By extrapolation this should occur at about 5.75 wt%Ni and a transformation temperature of about 520^{o}C at this particular cooling rate. However, as with manganese, there may be a change to lath ferrite before 100% acicular ferrite is reached. Again it is not clear at what level of alloying this occurs.

By comparing Figures 5.10 and 5.13 it can be seen that manganese has a stronger weight for weight influence in suppressing the polygonal ferrite reaction than nickel. This is in agreement with the findings of the literature review (section 2.4.3) concerning the effects of these elements on hardenability, (Figure 2.15).

5.3.3 Influence of niobium

By comparing the relevant CCT diagrams it should be possible to deduce the effect of niobium on weld metal transformations at the two hardenability levels produced by the two flux systems.

The effect of Nb at higher hardenability can be deduced by comparing CCT diagrams A0 and E0. Both these diagrams refer to the OP41TT flux system, and the prior austenite grain sizes were almost identical (ASTM 5.2 and 5.3). A detailed comparison of the chemical analyses shows E0 to contain more of the impurity elements than A0. However, judging by the results discussed in Chapter 2, the combined effect of all these impurities is likely to be less than the

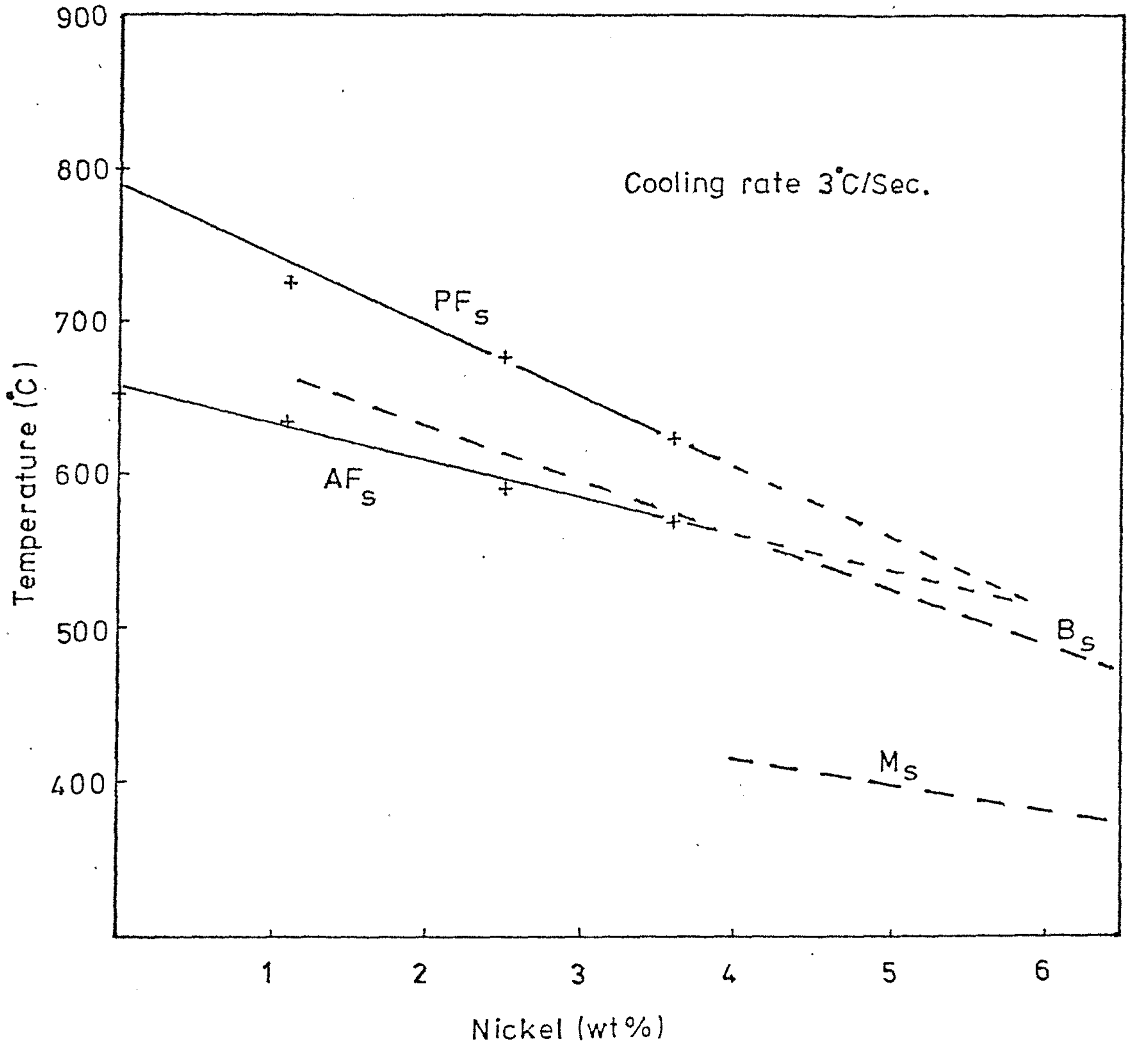

Figure 5.13 Influence of nickel on transformation start temperatures for PF, AF, B, and M, at a cooling rate of 3°C/Sec.

influence of niobium.

In Figure 5.14 the outlines of CCT diagrams A0 and E0 are superimposed to show the effect of niobium at a weld metal manganese content of approximately 1.35 wt% (OP41TT flux).

It can be seen that niobium has a strong effect on overall hardenability, moving the whole CCT diagram to the right. Moreover, for any fixed cooling rate transformation temperatures are depressed by niobium in all but the slowest cooled regions of the CCT diagram. In addition the ferrite and pearlite reactions are both suppressed relative to the rest of the CCT diagram.

The influence of niobium on transformations within the typical arc welding cooling rate range is best illustrated by referring to Figure 5.15. From this figure it can be seen that niobium has depressed the polygonal and acicular ferrite start temperatures at all cooling rates within the arc welding range. This depression of transformation temperature is more pronounced for polygonal ferrite than for acicular ferrite and results in a reduction in the amount of polygonal ferrite formed and an increase in the quantity of acicular ferrite. At the fastest cooling rates the quantities of secondary sideplates are also reduced as the grain boundary ferrite structures start to die out. From the diagram it can also be seen that the pearlite reaction is noticeably suppressed by niobium.

The effect of niobium at slightly lower hardenability may be deduced by comparing CCT diagrams A5 and E5 which relate to the 503 flux system.

Unfortunately, the different grain coarsening behaviour of these two weld metals resulted in a discrepancy in prior austenite grain sizes (ASTM 5.1 and 6.4). Close comparison of the chemical compositions shows that the niobium bearing weld metal contains slightly less of the major elements C, Mn and Si, but slightly more of the impurity elements, Ni, Cr, Cu etc. According to the hardenability results discussed in the literature review, these variations should more or less cancel each other, so that the overall hardenabilities of both weld metals are very similar.

Figure 5.16 illustrates the outlines of CCT diagrams A5 and E5, and shows the effect of Nb at lower hardenability, produced with the 503 flux system. It can be seen that the two diagrams are very similar, particularly within the welding cooling rate range. Obviously

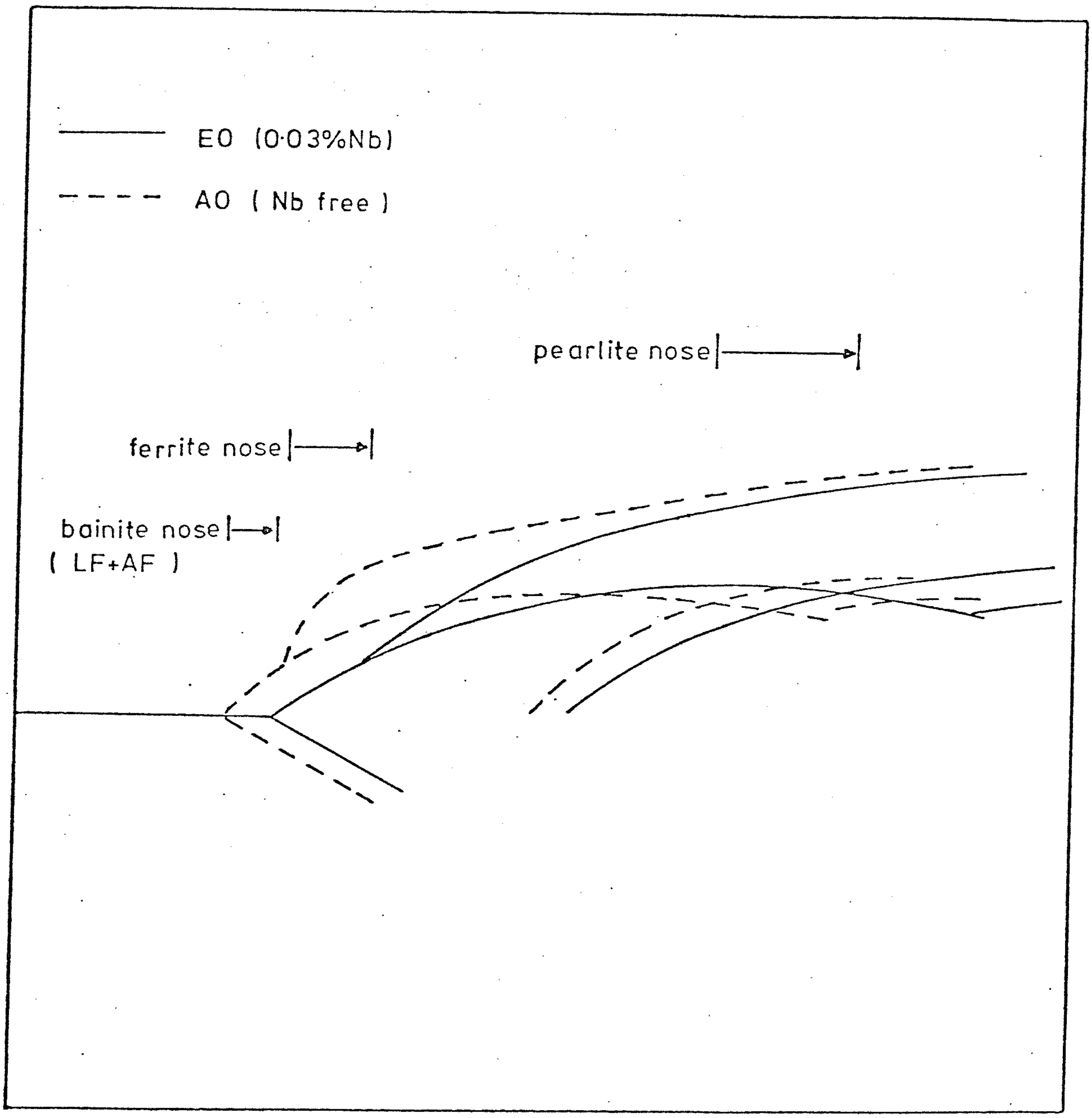

Figure 5.14 CCT diagrams AO and EO superimposed to show the influence of nibium at a baseline composition of 0.1wt%C,1.35wt%Mn,0.31wt%Si, (OP41TT flux).

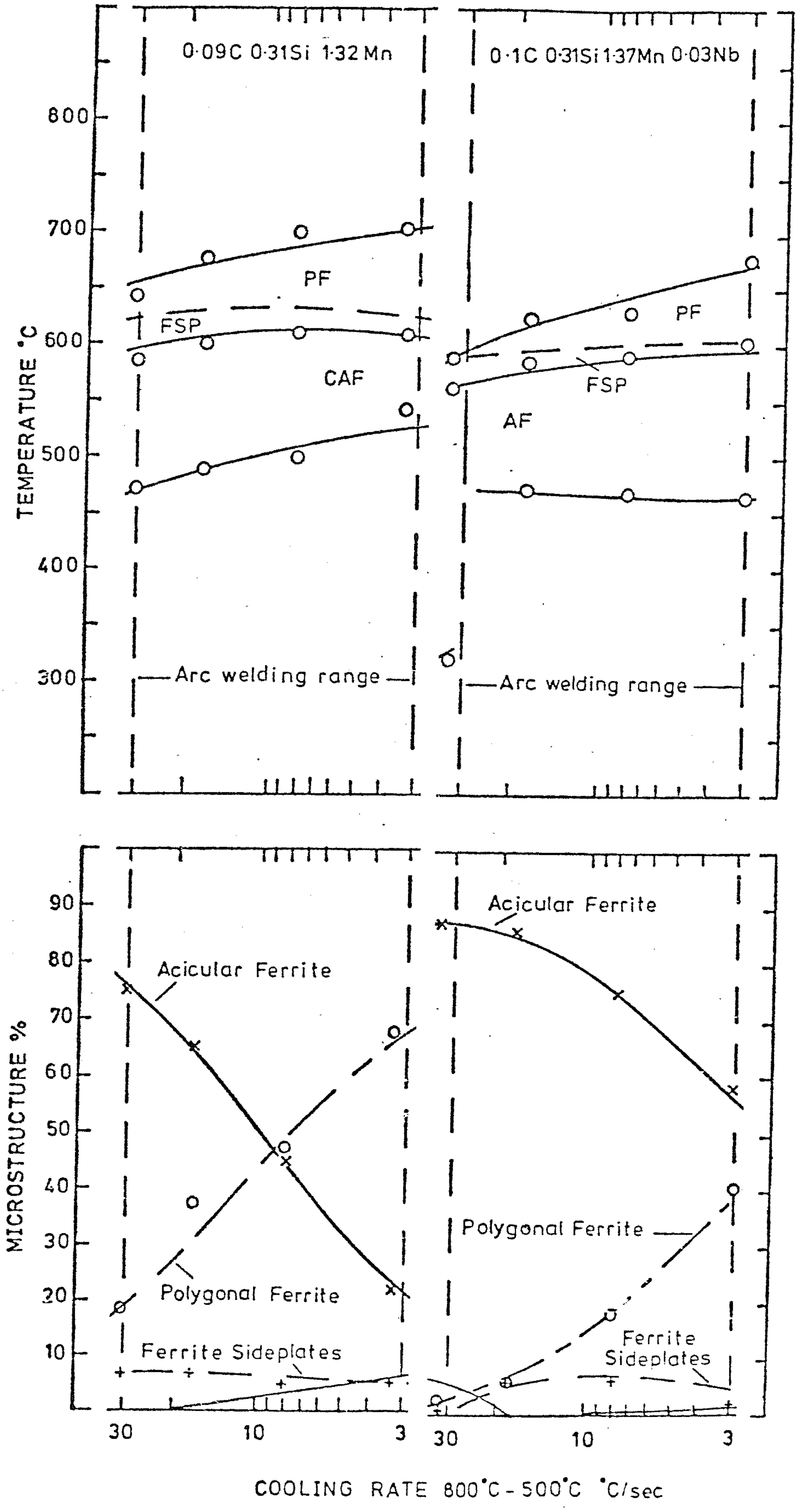

Figure 5.15 Influence of niobium on weld metal transformation behaviour within the typical arc welding cooling rate range. (OP41TT flux)

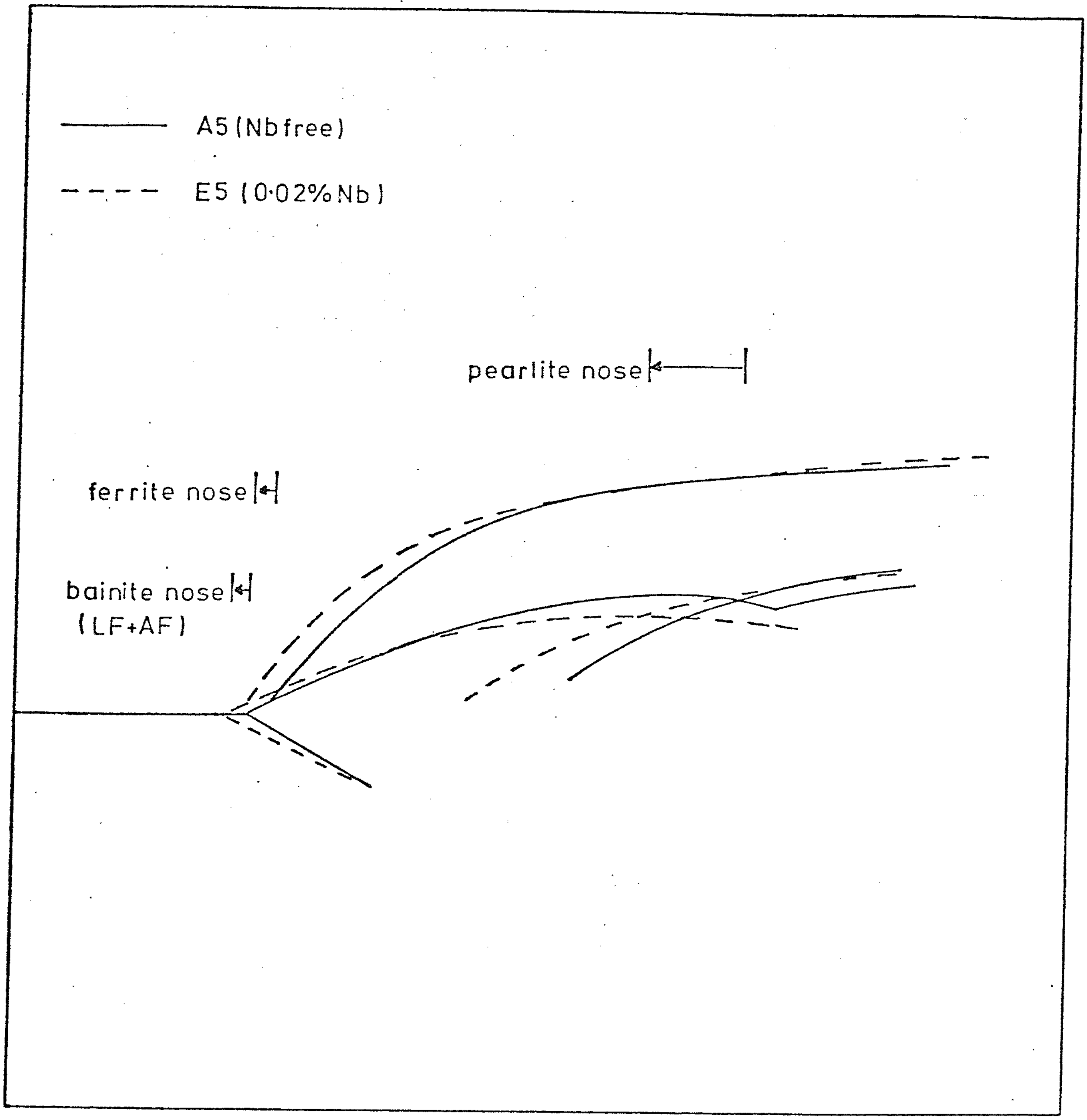

Figure 5.16 CCT diagrams A5 and E5 superimposed to show the influence of niobium at a baseline composition of 0.09wt%C,1.0wt%Mn,0.15wt%Si, (503 flux).

no direct conclusions can be drawn from Figure 5.16 due to the variations in prior austenite grain size. However, it may be argued that the γ grain size difference is being exactly balanced by the Nb content. The results discussed in section 4.4 give some indication of the effect of prior γ grain size on transformation temperatures, and these results can therefore be used indirectly to give an indication of the influence of niobium on transformation temperature. Using this analysis one can estimate that the increase in transformation temperature due to a decrease in prior austenite grain size (ASTM 5.1 to ASTM 6.4) is exactly balanced by the depression of transformation temperature caused by 0.02 wt%Nb. From Figure 4.11 this depression in transformation temperature should amount to $\sim 20^{\circ}$C at a cooling rate of 22°C/sec. Obviously the errors involved in this last analysis are likely to be high. Nevertheless, the influence of niobium is again found to be one of depression of transformation temperatures.

The influence of niobium on transformations within the typical arc welding cooling rate range, for the lower hardenability weld metals, is shown in Figure 5.17. The most important feature of this figure is the widening of the sideplate region of the CCT diagram resulting in increasing proportions of sideplates at the expense of polygonal and acicular ferrite. As previously discussed the errors involved in comparing these CCT diagrams are large due to austenite grain size and alloy variations. However, there does seem to be some evidence that niobium has had a strong influence on depression of the AF_s temperature at the slower cooling rates. This accounts for the increase in sideplates at the expense of acicular ferrite. The increase in sideplates at the expense of polygonal ferrite on the other hand was discussed in section 5.2.2(b) and was believed to be related to the occurrence of Nb(C,N) interphase precipitation.

5.3.4 Influence of carbon

By comparing CCT diagrams N1, M2 and A0 it should be possible to deduce the influence of carbon on weld metal transformation behaviour. N1 is a MMA weld metal of composition 0.05 wt%C, 0.33 wt% Si 0.98 wt%Mn, M2 is a MMA weld metal of composition 0.07 wt%C, 0.52 wt%Si, 1.35 wt%Mn, and A0 is a SA deposit of composition 0.095 wt%C, 0.31 wt%Si, 1.32 wt%Mn. All three welds were deposited under basic flux systems.

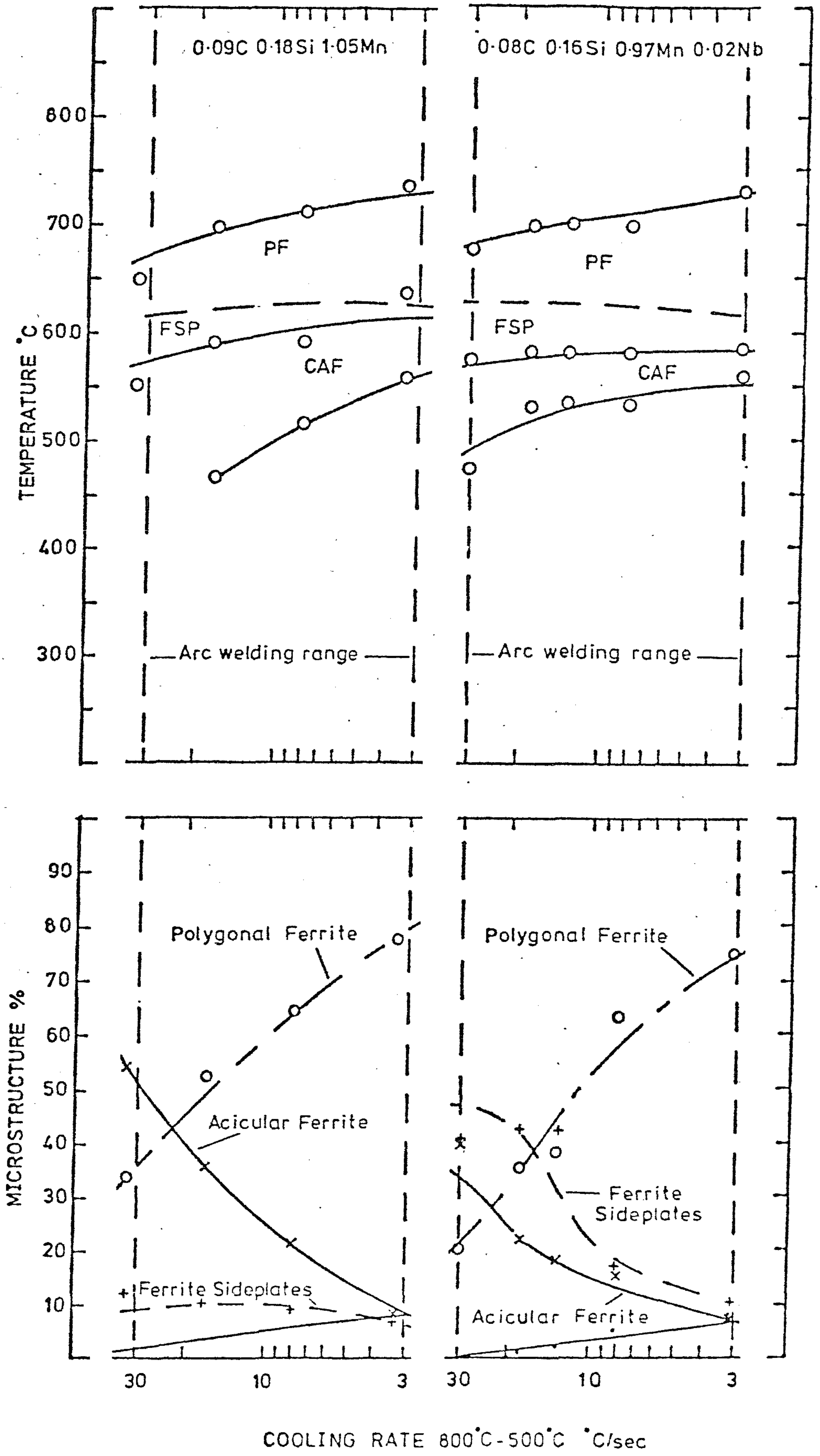

Figure 5.17 Influence of niobium on weld metal transformation behaviour within the typical arc welding cooling rate range.(503 flux)

Figure 5.18 shows the outlines of these three CCT diagrams superimposed to show the influence of carbon. It can be seen that carbon has depressed transformation temperatures in all regions of the CCT diagram in a similar manner to manganese and nickel. The Ms temperature data should be treated with caution, as two of the values are calculated, whilst the third value is subject to experimental errors (see Appendix). Prior austenite grain sizes vary very slightly between the three diagrams (ASTM 5.2, 5.4 and 5.8). However, in terms of transformation temperatures, this error is probably less significant than the errors due to manganese and silicon variations.

A very noticeable influence of carbon is its ability to delay the end of transformation. This is presumably related to increased carbon enrichment, which causes transformations to pearlite or CAF and carbides to occur at lower temperatures.

The influence of carbon on transformations within the typical arc welding cooling rate range is best illustrated by referring to Figure 5.19. This diagram shows depression of the polygonal ferrite start temperatures relative to acicular ferrite start temperatures. This reults in increased development of acicular ferrite.

In the range under investigation carbon appears to have little influence on sideplate development. Contrary to expectations carbon appears to reduce separation of the bainite and pearlite noses.*

The quantity of pearlite developed in the equilibrium structure however, is proportional to the carbon content as shown in Figure 4.36.

Figure 5.20 shows the influence of carbon on polygonal and acicular ferrite start temperatures at a cooling rate of 3°C/sec. The data points for M2 and A0 are taken from the relevant CCT diagrams. The third pair of data points relate to weld metal N1, and have been corrected for a small variation in manganese content, (Figure 5.10).

From Figure 5.20 it can be seen that carbon influences the PF_s and AF_s temperatures in a similar manner to both Mn and Ni, although its weight for weight influence is clearly much greater.

5.3.5 Influence of molybdenum

In the current investigation only one weld metal was examined which contained molybdenum. This was a C-Mn-Ni-Mo type, of composition 0.05 wt%C, 1.72 wt%Mn, 1.87 wt%Ni, 0.31 wt%Mo, developed for use in the nuclear power industry.

From examination of the CCT diagram (Figure 4.58) it can be

---

*NOTE: In this context the pearlite nose is taken to be the position at which less than ∿1 vol% pearlite is observed optically.

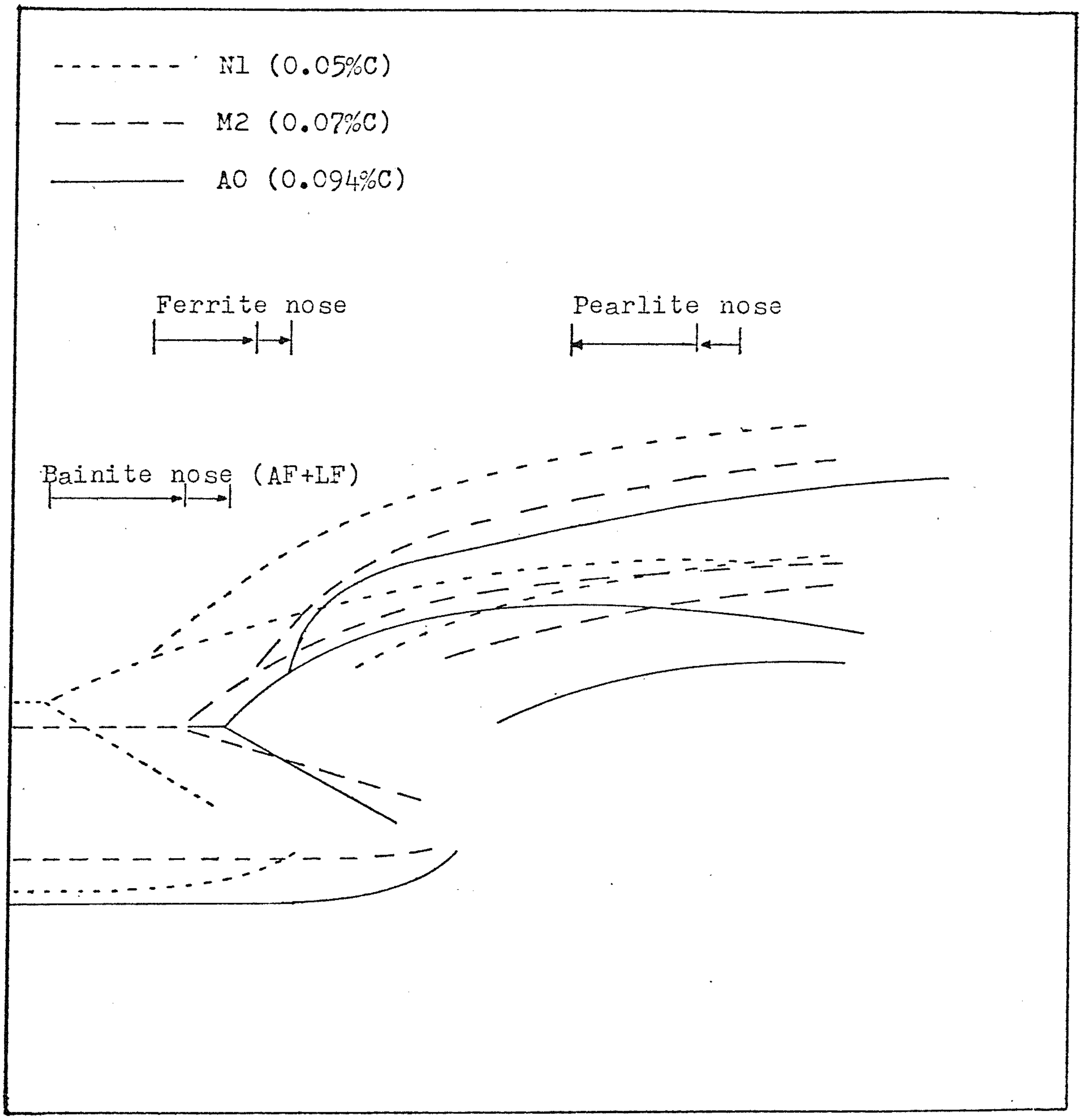

Figure 5.18 CCT diagrams N1, M2, and AO superimposed to show the influence of carbon.

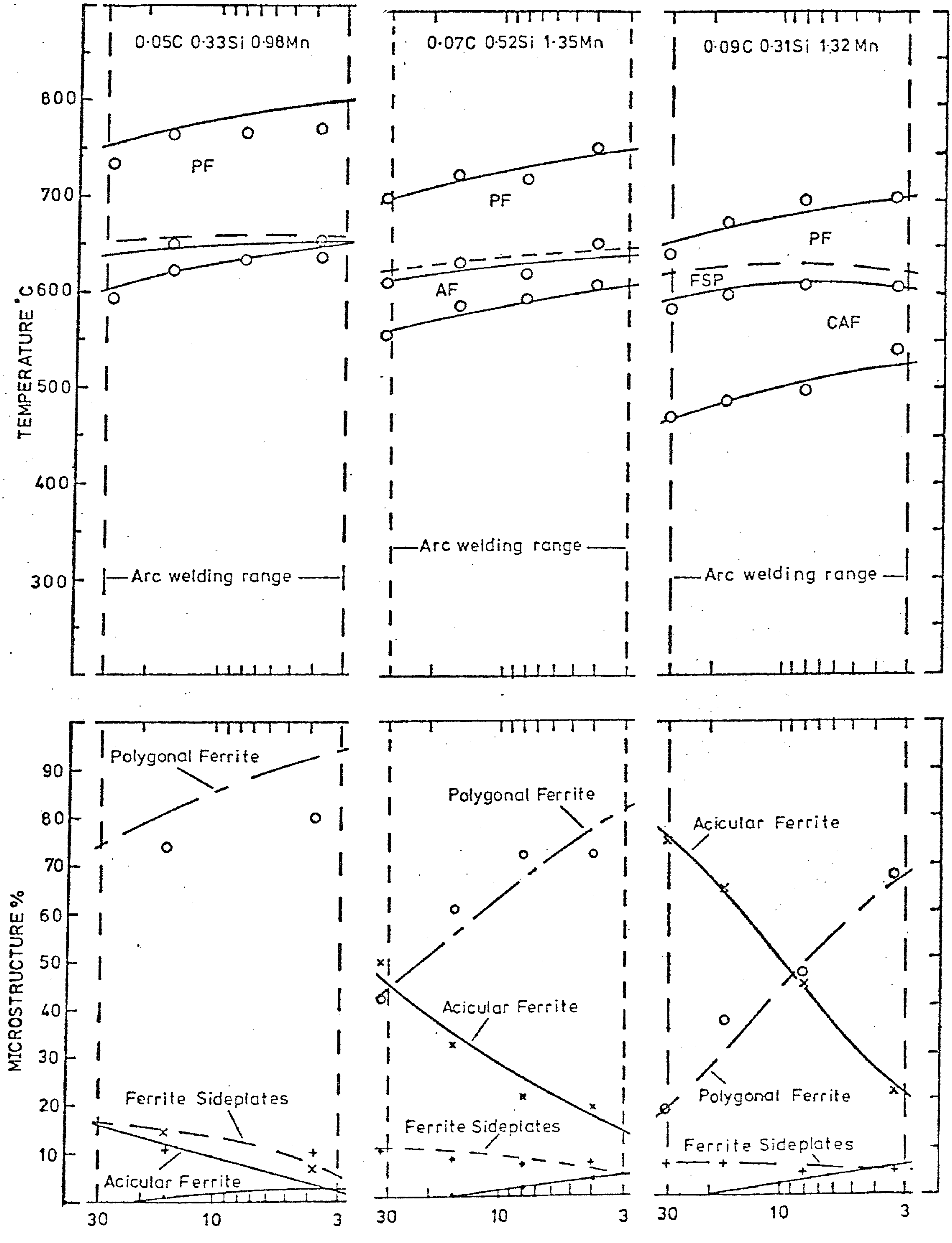

Figure 5.19 Influence of carbon on weld metal transformation behaviour within the typical arc welding cooling rate range.

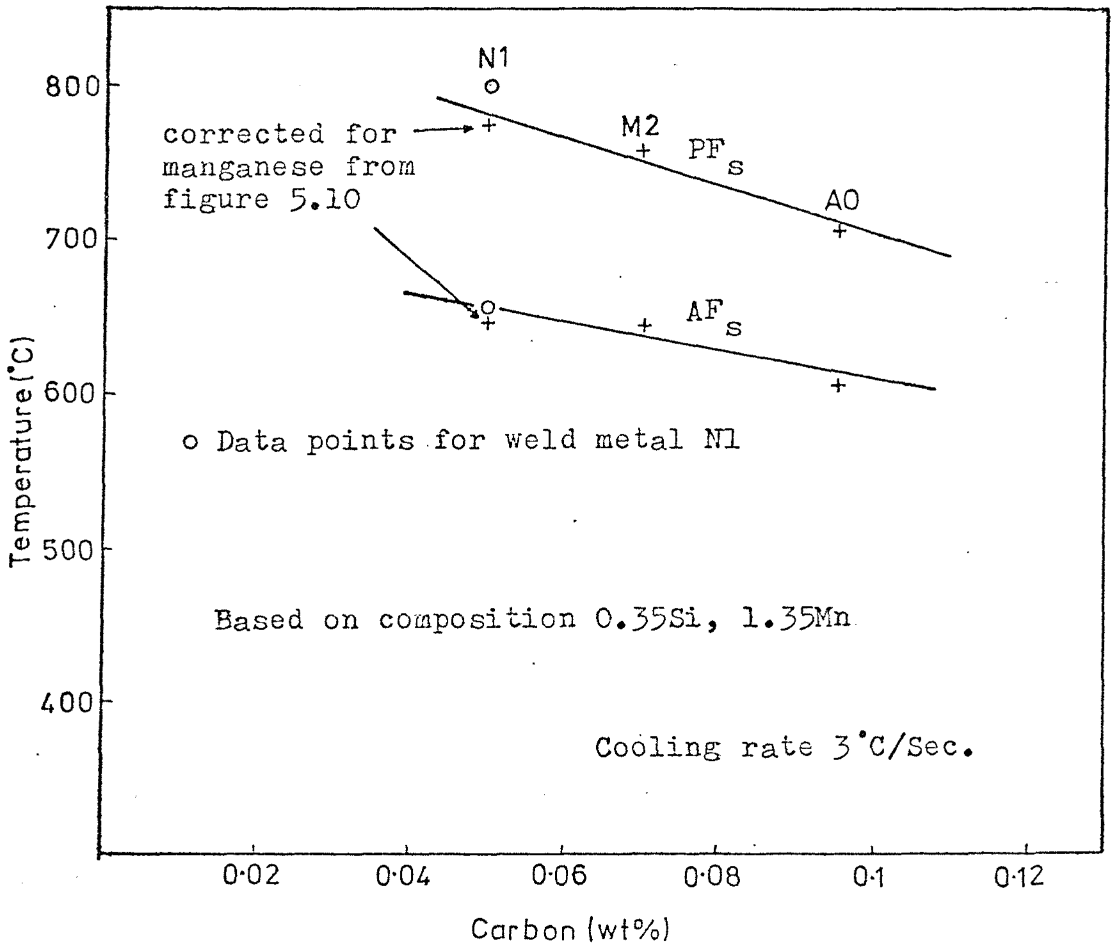

Figure 5.20 Influence of carbon on transformation start temperatures for PF and AF at a cooling rate of 3°C/Sec.

seen that the transformation behaviour of this weld metal is unlike any of the other compositions examined. Over the entire welding cooling rate range there is very little variation in transformation temperatures and a substantially lath ferrite (upper bainite) microstructure is developed.

Clearly the lack of systematic data for molybdenum bearing weld metals makes it difficult to estimate the influence of this element on transformation temperatures. However, it does seem that Mo has acted as predicted in the literature review and produced a very clear separation of the ferrite and bainite noses.

The ability of Mo to suppress the grain boundary ferrite reaction makes it a very useful addition for producing microstructures with a high proportion of acicular ferrite. This ability is already utilised in the Mo-Ti and Mo-Ti-B type submerged arc consumables which have been shown to produce very attractive mechanical properties. If Mo is used in more highly alloyed weld metals as in the C-Mn-Ni-Mo material studied, the microstructure will be predominantly upper bainite at typical welding cooling rates. One might expect the impact properties of such a structure to be inferior to the equivalent acicular ferrite structure in the as welded condition due to relatively large distances between high angle grain boundaries.

Clearly further systematic CCT studies are required to define the influence of molybdenum on weld metal transformation behaviour.

5.3.6 Influence of prior austenite grain size

The influence of prior austenite grain size on weld metal transformation temperatures is shown in Figure 4.11. It can be seen that the Ts, 10%, and 50% transformation temperatures are all depressed by between 10°C and 20°C per ASTM No.

This figure is in agreement with the findings of the literature review (section 2.4.5) and confirms that prior austenite grain size has a powerful influence on transformation temperature.

The change in microstructure associated with changes in austenite grain size can be seen in Figures 4.3 to 4.8. Clearly the smaller austenite grain structures transform to a fine grained polygonal ferrite dominated structure, whereas the larger austenite grain structures are dominated by acicular ferrite. This difference in behaviour can be explained in terms of nucleation site density and supercooling using classical nucleation theory.

Because fine grained austenite contains a high density of favourable primary heterogeneous nucleation sites (i.e. a large γ grain boundary area), a high rate of grain boundary nucleation will occur at a relatively low degree of supercooling. The transformation start temperature will therefore be high, and because the γ grain size is small, little growth is required before the polygonal ferrite grains grow to impingement. The net result is a fine grained polygonal ferrite microstructure developed at a fairly high transformation temperature.

A coarse grained austenite, on the other hand, contains far fewer primary nucleation sites (i.e. small γ grain boundary area) and therefore requires a much larger degree of supercooling to produce a detectable nucleation rate. The transformation start temperature will therefore be lower, and because the γ grain size is large, the polygonal ferrite grains are unlikely to grow to impingement unless the cooling rate is very slow. As cooling continues the intragranular regions remain untransformed until supercooling eventually reaches a level at which copious heterogeneous nucleation becomes favourable at secondary nucleation sites within the austenite grains. The net result is a mixed microstructure consisting of a small proportion of polygonal ferrite delineating the prior austenite grain boundaries and a large proportion of intragranular acicular ferrite.

From above it therefore appears that austenite grain size has two important influences on weld metal transformation behaviour.

(1) Prior austenite grain size influences the transformation start temperature by altering the availability of grain boundary nucleation sites.

(2) Prior austenite grain size influences the ratio of grain boundary to intragranular transformation products through its influence on intragranular supercooling. This also depends on other factors such as cooling rate, alloying and the potency of intragranular nucleation sites.

5.3.7 Summary

In the previous section the influence of Mn, Ni, Nb, C, Mo and prior austenite grain size on weld metal transformation behaviour has been discussed. This information, combined with that in the literature review, is summarised as follows:

(1) Manganese is a strong austenite stabiliser and depresses

transformation temperatures in all regions of the CCT diagram. According to the literature manganese moves both the bainite and pearlite noses to longer times, but has little effect on separating them. In weld metals increasing manganese has been shown to promote acicular ferrite at the expense of polygonal ferrite and ferrite side-plates, and to refine the acicular ferrite grain size.
In the current work, all the above factors have been confirmed, although there is evidence that manganese has a very mild effect on separation of the bainite and pearlite noses, (see Figure 5.33).
In terms of the development of weld metal microstructures, the current work provides a useful source of systematic, quantitative data on the influence of manganese in basic flux C-Mn systems.

(2) Nickel is an austenite stabiliser but has less influence on transformation temperature than manganese. According to the literature there is some evidence that nickel causes a slight separation of the bainite and ferrite-pearlite noses. In weld metals, observations suggest that nickel refines the ferrite grain size.
All the above factors are reproduced in the current work. The influence of nickel on separation of the bainite and pearlite noses is confirmed (see Figure 5.34). This probably explains the greater tendency to develop the low temperature lath structure at high nickel contents.
In terms of weld metal microstructural development nickel works through its influence on transformation temperature in a very similar manner to manganese. Again the current work provides a useful source of systematic, quantitative, data on the influence of Ni in basic flux C-Mn-Ni systems.

(3) Niobium is a ferrite stabiliser and a very powerful carbide forming element. Although there is little data in the literature relating to niobium's influence on TTT diagrams, it does seem that niobium causes a separation of the bainite and ferrite-pearlite noses. Niobium also has a very strong influence on hardenability. In weld metals niobium has been shown to promote acicular ferrite in some cases and side-plate or lath structures in others.
In the current work the effect of niobium, has been studied at two

hardenability levels. In weld metal of base composition 0.1 wt%C, 1.35 wt%Mn, 0.31 wt%Si, niobium has been shown to increase hardenability and strongly suppress both the ferrite and pearlite reactions. This results in a decrease in the grain boundary ferrite content of the weld metal microstructure in favour of acicular ferrite. The acicular ferrite is also slightly refined due to depression of its transformation temperature.

In weld metal of base composition 0.09 wt%C, 1.0 wt%Mn, 0.15 wt%Si, niobium is also believed to have depressed transformation temperatures. In this case, however, niobium favoured the development of a predominantly sideplate type microstructure. At both hardenability levels niobium seems to influence transformation behaviour by interfering with the development of grain boundary ferrite.

(4) Carbon is a strong austenite stabiliser and has a powerful influence on movement of the bainite and pearlite noses to longer times, but has little tendency to separate them.

In weld metals carbon content influences the volume fraction of carbides in the microstructure. Carbon may also refine grain size through its influence on transformation temperatures.

In the current work, carbon has been shown to have a very strong influence on transformation temperatures. At slow cooling rates the amount of pearlite developed is in good agreement with the lever rule. At welding cooling rates the amount of pearlite formed depends on the position of the pearlite nose. Again, the current work provides useful, quantitative data on the influence of carbon on the transformation behaviour of basic flux C-Mn weld metals.

(5) Molybdenum is a ferrite stabiliser and has a very strong tendency to separate the bainite and ferrite noses. Molybdenum also has a strong influence on hardenability.

In the current work molybdenum has been shown to produce a clear separation of the bainite and ferrite noses. This resulted in a predominantly lath ferrite (upper bainite) microstructure in the C-Mn-Ni-Mo weld metal when cooled in the welding cooling rate range.

(6) Prior austenite grain size influences transformation temperatures by controlling the availability of grain boundary

nucleation sites. In addition austenite grain size influences the type and variety of transformation products developed through its influence on intragranular supercooling.

5.3.8 Calculation of $\gamma \rightarrow \alpha$ transformation start temperatures for C-Mn-(Ni) weld metals

In the previous sections CCT data has been used to determine the influence of Mn, Ni, Nb, C and Mo on weld metal transformation temperatures. This information may be summarised as shown in Figure 5.21 which shows the weight for weight influence of C, Mn and Ni on weld metal transformation start (T_s) temperatures, at a cooling rate of 30°C/sec ($\Delta t_{500}^{800}=10$ sec). It should be noted that this figure is similar to Figure 2.15, which shows the weight for weight influences of alloying elements on hardenability.

For simplicity Figure 5.21 may be reduced to the following equation:-

$$T_s(\text{at } \Delta t_{500}^{800} = 10 \text{ sec}) = 910-1800C-65Mn-52Ni \qquad (5.1)$$

where T_s is the transformation start temperature (°C) at a cooling rate of 30°C/sec ($\Delta t_{500}^{800} = 10$ sec).

The above equation is based on a simple summation of the individual linear regression coefficients for C, Mn, and Ni shown in Figure 5.21.

The equation is applicable to C-Mn-(Ni) weld metals deposited under basic flux systems.

To test the validity of the above equation it has been applied to all 9 C-Mn-(Ni) compositions investigated in the current work and eleven other compositions investigated by Christensen [99] and Van Nassau [164]. The resulting correlation between calculated and measured values is shown in Figure 5.22.

It can be seen that all the dilatometrically determined results lie within the ±25°C scatter band. It is interesting to note that almost all the results obtained by thermal analysis lie outside the scatter bands. The majority of these results are some 30°C to 40°C lower than the calculated values and this may be an indication that the thermal analysis technique is somewhat less sensitive than dilatometry in locating the transformation start temperature.

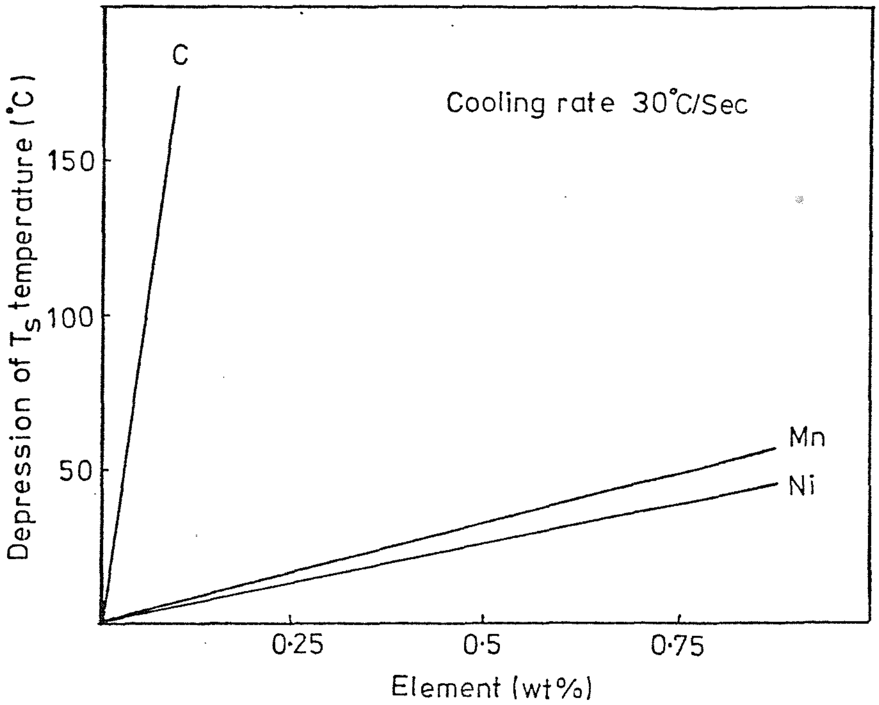

Figure 5.21 Weight for weight influence of C, Mn, and Ni on depression of weld metal T_s temperatures.

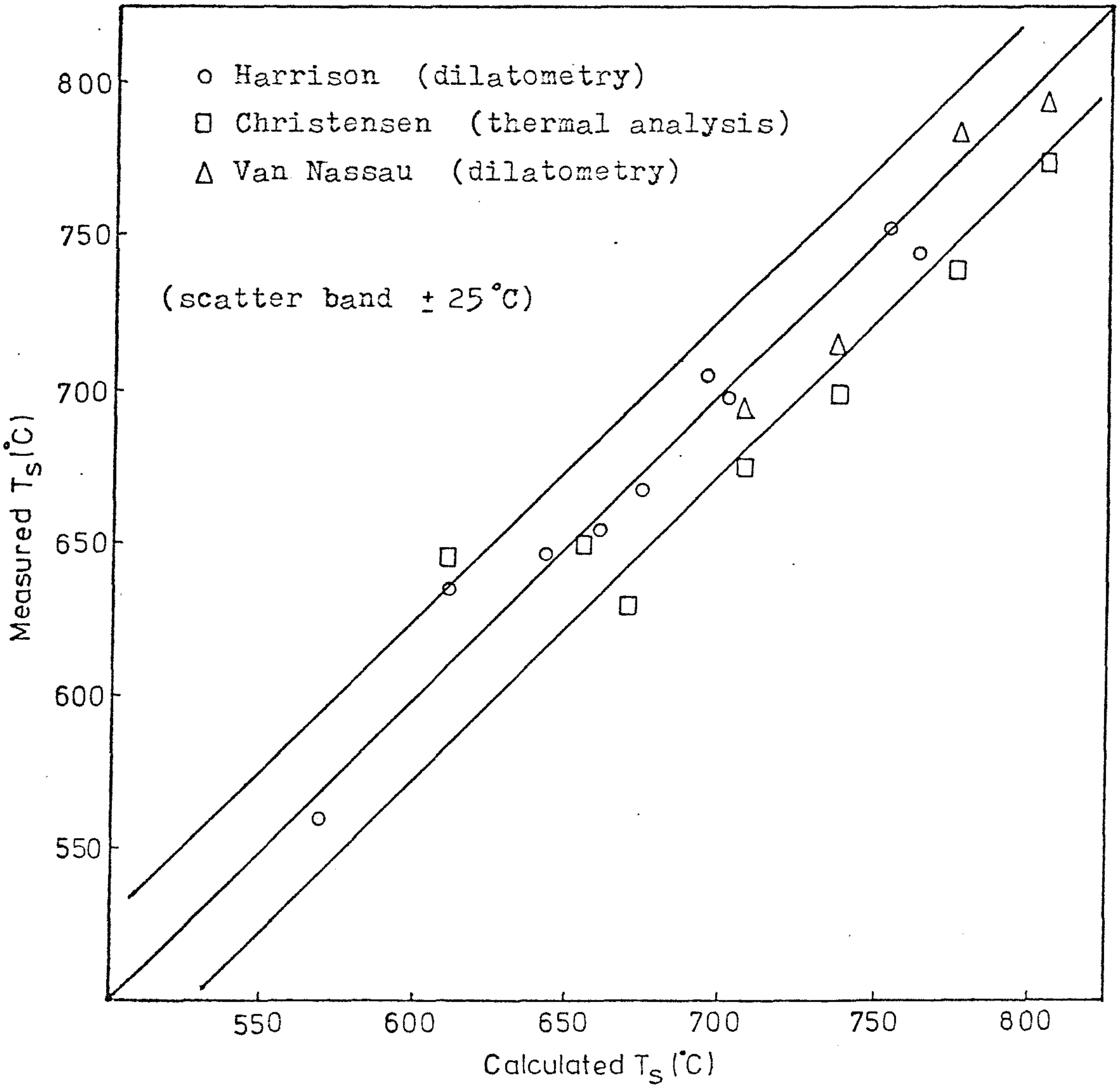

Figure 5.22 Correlation between measured and calculated T_s temperatures for C-Mn-(Ni) weld metals.

5.4 Influence of Oxygen-Rich Inclusions on Weld Metal $\gamma \rightarrow \alpha$ Transformation Behaviour

5.4.1 Remelting experiment

The remelting experiment provides a means of isolating the influence of oxygen content, without causing significant variations in other alloying elements. In the current work the analytical oxygen content is considered to be synonymous with the volume fraction of oxygen-rich inclusions due to the virtual insolubility of oxygen in solid iron (86 ppm at 1500°C)[169].

From the dilatometric results obtained for weld metal E5 (Figure 4.15), it can be seen that reducing the oxygen content by about half reduces the $\gamma \rightarrow \alpha$ transformation start temperature by almost 20°C. From the microstructural observations of Figures 4.39 and 4.40 it can be seen that this reduction in transformation temperature results in a reduction in the amount of the high-temperature polygonal ferrite and an increase in the amount of lower temperature morphologies (ferrite sideplates and acicular ferrite). Comparing the prior austenite grain sizes of specimens E5 and E5 (remelted) (Table 4.4), shows that partial removal of inclusions has enabled a larger grain size to develop in specimen E5 (remelted), during the austenitizing cycle.

The dilatometric results for weld metal E0 (Figure 4.14), show that almost complete removal of oxygen depresses the transformation start temperature by almost 30°C. Again comparison of the prior austenite grain sizes of specimens E0 and E0 (remelted), (Table 4.4), reveals an increased γ grain size due to the removal of the oxygen-rich inclusions.

The microstructural change associated with this reduction in transformation temperature is shown in Figures 4.37 and 4.38. This dramatic change in microstructure from acicular to lath ferrite suggests that oxygen-rich inclusions influence the nucleation characteristics of weld metals in addition to interacting with γ grain boundaries.

In both weld metals (E0 and E5) it is clear that removal of oxygen-rich inclusions reduces the pinning of austenite grain boundaries and allows larger austenite grains to be become established. Owing to the change in the grain boundary area available, these larger grains subsequently transform at slightly lower temperatures during continuous cooling.

From above it is clear that weld metal inclusions interact with austenite grain boundaries and thereby alter transformation temperatures via a prior grain size relationship. However, what is less clear is the influence of inclusions in altering nucleation characteristics. The very distinct change in microstructure from acicular ferrite to lath ferrite caused by almost complete removal of inclusions is qualitative evidence of a nucleation effect. The quantitative nature of this effect may be estimated by comparing the depression of the T_s temperatures of the remelted and unremelted specimens, when subjected to identical changes in austenite grain size.

Figure 5.23 shows depression of T_s temperatures as a function of the change in prior austenite grain size for normal and remelted weld metals. The normal weld metal shown in Figure 5.23 refers to M3 (0.06 wt%C, 0.33 wt%Si, 1.57 wt%Mn, 0.03 wt%O) which was used to study the influence of austenite grain size on transformation temperatures, (Figure 4.11 and section 5.3.6). The results for the remelted weld metals E0(r) and E5(r) deviate strongly from the results for the normal weld metal indicating that there is an additional effect other than that due to grain size alone. This influence is of a similar order to the prior grain size effect and is assumed to be a nucleation effect related to the presence of inclusions.

A most interesting feature of Figure 5.23 is that the vectors representing the nucleation effects have opposite signs for the two remelted weld metals. In the case of E0(r) the nucleation vector is negative, indicating lower nucleating power than the normal weld metal. This is understandable, since virtually all the inclusions were removed during remelting ($\sim$58 ppm O_2). The nucleation effect vector for E5(r) however, is positive, and this requires a little further explanation.

The oxygen content of E5(r) is 278 ppm and is therefore quantitatively very similar to the "normal" weld metal, M3 (295 ppm O). The observed difference in nucleation efficiency is therefore considered to be related to the inclusion size distribution rather than the overall oxygen content.

Unfortunately the detailed inclusion size distribution for weld M3 is not available, but it is assumed to be similar to E0 (similar chemistry and flux systems). Figure 4.10 shows the inclusion size distributions for E0, E0(r) and E5(r). From this figure it is clear that remelting shifts the entire size distribution curve to

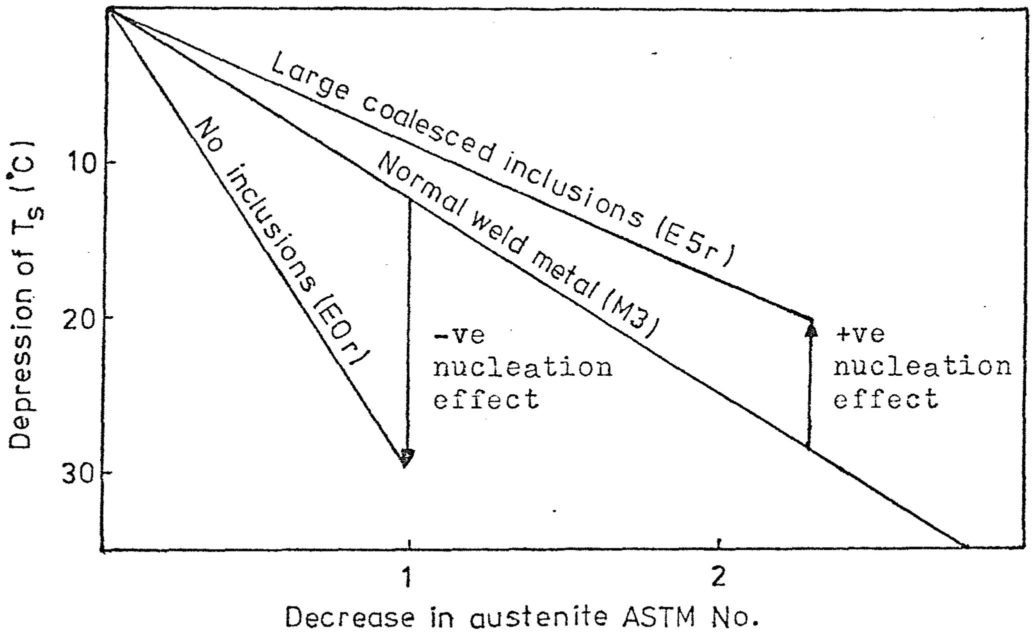

Figure 5.23 Influence of austenite grain size on depression of T_s temperature for normal and remelted weld metals.

larger inclusion sizes. The mean inclusion diameter increases from about 0.6 μm to about 1.2 μm. the increase in nucleation efficiency of E5(r) can now be understood in terms of the greater inclusion/matrix surface area available for nucleation. As Figure 5.23 is concerned with T_s temperatures it is assumed that the inclusion interfacial area in contact with austenite grain boundaries is the controlling factor, through the calalytic mechanism discussed in section 2.5.4(e). It is to be expected therefore that nucleation at inclusions located in grain boundaries becomes more favourable as the inclusion diameter increases, because this effectively increases the availability of these very favourable nucleation sites.

In the case of weld E5(r) the mean inclusion diameter is about double that of the "normal" weld metal, whilst the volume fraction of the two distributions is about the same. It would therefore be expected that the nucleation efficiency of E5(r) would be greater than for the "normal" weld metal, M3, as is in fact shown in Figure 5.23.

Having seen that inclusions can exert a strong influence on weld transformation kinetics it is interesting to compare weld metal hardenability with the hardenability of wrought steels of similar chemical composition. If due account is taken of prior austenite grain size and chemistry, this comparison should provide further evidence of the enhanced nucleation characteristics of weld metals.

5.4.2 Hardenability of weld metals

By critically comparing the weld metal CCT diagrams of the present work with identical wrought CCT diagrams from the literature, it should be possible to assess whether or not significant differences in kinetic behaviour exist between wrought and weld deposited materials. To do this CCT diagrams based on the regression equations of Maynier et al [109] discussed in Chapter 2 will be used. This approach allows CCT diagrams of identical composition to be calculated and suitable allowances for prior austenite grain size to be made.

Figure 5.24 compares the critical cooling velocities (CCV's) for transformation to a 100% martensite microstructure in weld metals and wrought steel of identical composition. Weld metals A0 and A5 have been used to avoid complications due to alloying or micro-alloying effects. The CCV's predicted from regression equations refer to cooling rates at 700°C. CCV's taken from the weld metal CCT diagrams refer to cooling rates from 800°C to 600°C. Grain size is

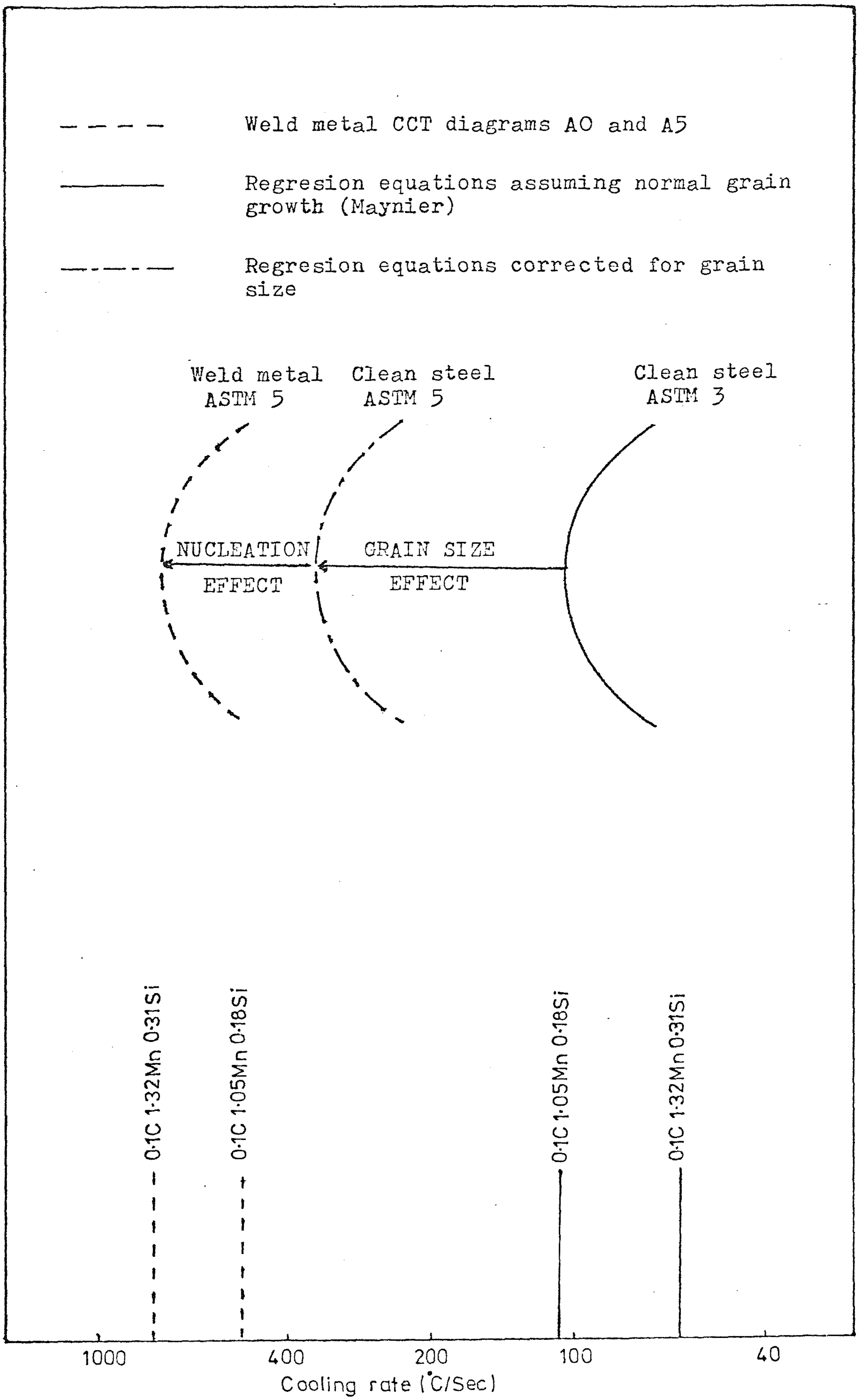

Figure 5.24 CCV's for transformation to 100% martensite showing the difference in hardenability between weld metal and clean steel.

taken into account in the regression equations through the austenitising parameter (P_A) which assumes normal grain growth. In the case of the weld metals, austenitised for 5 minutes at 1250°C, grain size of A0 and A5 were ASTM 5.2 and ASTM 5.1 respectively.

From Figure 5.24 it can be seen that the overall hardenabilities of the weld metals are much less than the predicted values for wrought steels of identical composition. For example, the weld metals must be cooled at about 500 to 800°C/sec to transform to 100% martensite whereas almost identical wrought materials need only be cooled at 60°C to 100°C/sec for the identical transformation, having been austenitised under identical conditions.

The above behaviour is also observed when comparing real CCT diagrams for weld HAZ's and weld metals of similar composition. Figure 5.25 shows this effect for a Nb bearing HSLA steel and its equivalent weld metal. Figure 5.26 shows the same effect for simple C-Mn compositions. Figure 5.27 shows the hardenability shift occurring between 3.5 wt%Ni wrought steel and weld metal materials. The latter example is subject to errors due to differences in C and Mn content. However, from the previous regression equation it can be calculated that the overall hardenability of the weld metal should be greater than the wrought material and in fact the opposite is observed.

From the above comparisons, it can be seen that weld metal hardenability, measured in terms of 100% martensite formation, is significantly less than for the equivalent wrought material. Obviously a major contribution to this hardenability shift is the difference in austenite grain sizes developed during austenitisation. However, this is not the only factor influencing the hardenability shift. If suitable allowances are made for differences in austenite grain growth, by using the regression equation, there is always a residual hardenability shift.

This effect is illustrated in vector form in Figures 5.24, 5.25, 5.26 and 5.27 and is assumed to represent the magnitude of the additional nucleation effect as discussed in the previous section.

Unfortunately, in the current work there is insufficient data to confirm the influence of austenite grain size on hardenability, as predicted by the regression equation. This is a major shortcoming as it makes a quantitative differentiation between the grain size and any additional nucleation effect difficult. However, the regression equation was based on 63 selected CCT diagrams for low alloy steels and according to Maynier was justified for 210 CCT diagrams including

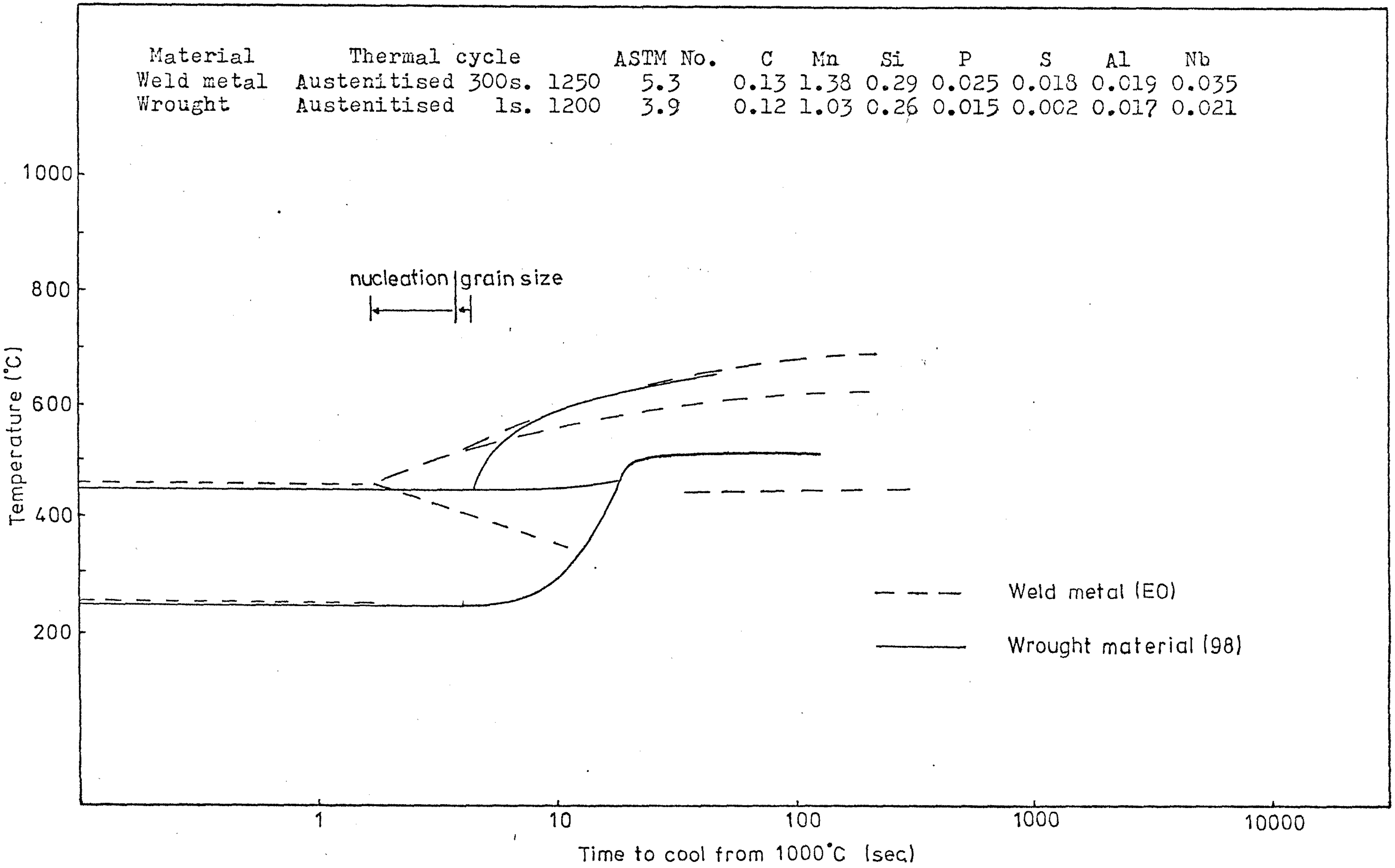

Material	Thermal cycle	ASTM No.	C	Mn	Si	P	S	Al	Nb
Weld metal	Austenitised 300s. 1250	5.3	0.13	1.38	0.29	0.025	0.018	0.019	0.035
Wrought	Austenitised 1s. 1200	3.9	0.12	1.03	0.26	0.015	0.002	0.017	0.021

Figure 5.25 Hardenability shift between Nb bearing HSLA steel HAZ and weld metal.

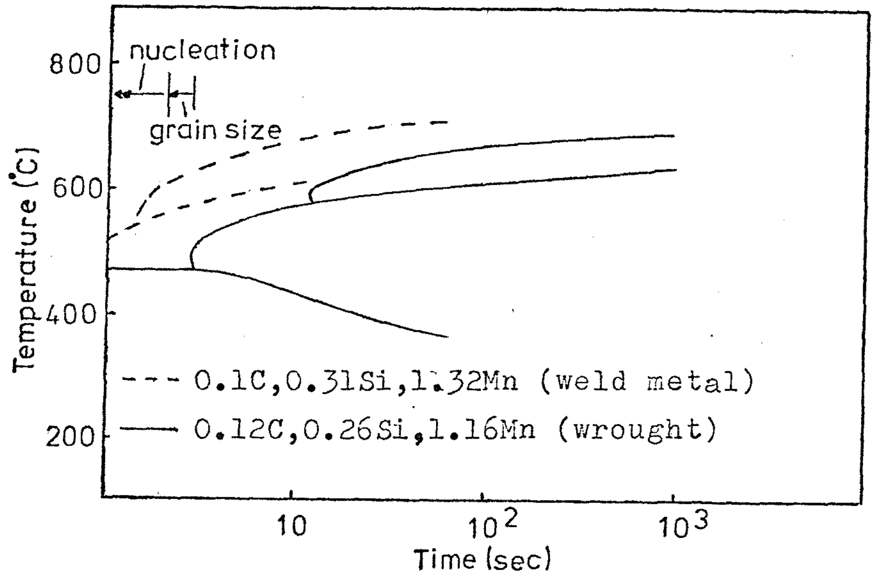

Figure 5.26 Hardenability shift between C-Mn steel HAZ and weld metal.

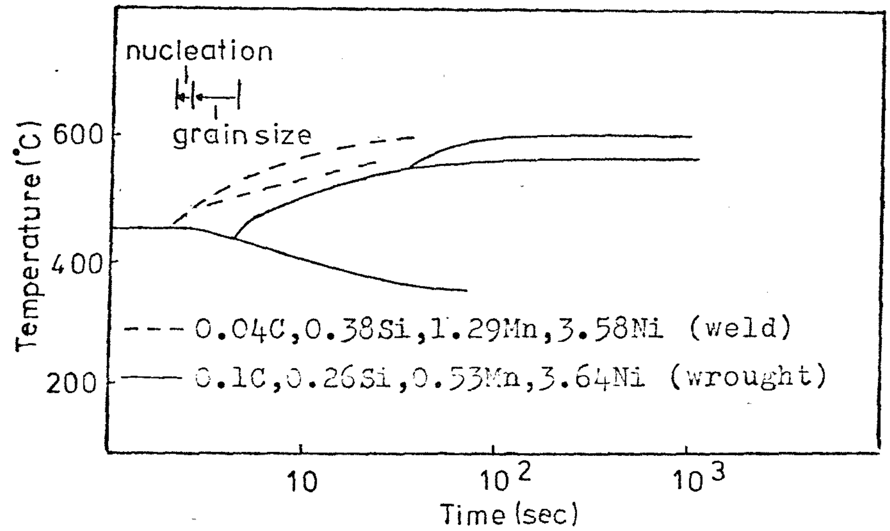

Figure 5.27 Hardenability shift between 3.5%Ni steel HAZ and weld metal.

those by Inagaki and Baker for welding situations. At the time of publication this covered practically all CCT diagrams available in the literature.

If one assumes that the regression equation is essentially correct there is ample evidence to suggest that weld metals have a lower hardenability than their equivalent wrought steel counterparts, even assuming identical austenite grain sizes. On this basis it is proposed that inclusions alter re-heated weld metal transformation kinetics in two ways.

(1) By pinning austenite grain boundaries and thereby increasing the proportion of primary nucleation sites, (grain boundary corners, edges and faces).

(2) By a direct effect on nucleation caused by:-
  (a) Increasing the efficiency of primary nucleation sites (inclusions in grain boundaries).
  (b) Substantially increasing the number of secondary intragranular, nucleation sites (inclusions or dislocation sub-structure).

The above effects will now be discussed in more detail.

5.4.3 Grain boundary pinning in reheated weld metals

In section 2.5.2(a) the theory of grain boundary pinning was reviewed and it was shown that a modified classical Zener theory could be successfully applied to weld metals. This theory can now be tested for the inclusion distributions and grain growth data relating to the remelting experiment.

The grain boundary pinning formula predicts a limiting grain radius (Ro) given by:-

$$\frac{Ro}{r} = \frac{A}{\beta f} \qquad (5.2)$$

where β = $0.125 \ln 40\ \rho/r$

r = particle radius

ρ = "unrestricted" grain size

f = volume fraction of particles

A = constant

The value of the constant A is uncertain and values ranging from 1.33 (Zener theory) to 0.44 (Hellman theory) have been quoted in the literature. The inclusion size distributions and volume fractions of samples E0, E0(r) and E5(r) are given in Figure 4.10. Carrying out a simplified calculation based on mean values for E0 and assuming A=0.885 (average of literature values)

$\bar{r}$ = 0.33 µm

f = 4.8×10^{-3} (based on the mean inclusions size and number of inclusions /unit volume)

ρ = 850 µm [143]

we have from equation (5.2)

$\bar{R}_o$ = 42 µm

and from equation (3.2)

$\bar{L}_o$ = 47 µm

A more detailed calculation may be carried out by considering mean particle sizes and volume fractions for small increments over the entire particle size distribution. In this case the limiting grain size is given by:-

$$R_o = \frac{A}{\bar{\beta}(f_1/r_1 + f_2/r_2 + \ldots\ldots f_n/r_n)} \qquad (5.3)$$

where $\bar{\beta}$ is a mean correction factor.

The result of this calculation for weld metal E0 gives a limiting grain diameter, $\bar{L}_o$=43 µm. It can be seen, therefore, that the error involved in carrying out the simplified calculation, based on mean values, is small.

Table 5.2 compares the calculated and measured austenite grain sizes of specimens E0, E0(r) and E5(r) based on the simplified calculation. It can be seen that weld metal E0, which is typical of a SA weld metal deposited under a basic flux, has reached its calculated limiting grain size after 5 mins. at 1250°C. Any continued holding at this temperature would not be expected to cause further grain growth.

Weld metal E0(r) on the other hand has a calculated limiting grain size of 925 µm, due to its much lower oxygen-rich inclusion content (58 ppmO). After 5 mins. at 1250°C this material has a measured grain size of only 72 µm.

Continued holding at 1250°C would therefore be expected to result in continued grain growth towards the limiting grain size. However, it is clear that grain growth is still severely restricted in this specimen. One possible reason for this is the presence of additional second phase particles not accounted for in the previous calculation. Although remelting reduced the oxygen content from 305 ppm to 58 ppm, the nitrogen content only decreased from 91 ppm to 84 ppm. Thus, fine nitride particles may also provide a contribution in restricting grain growth in this weld metal.

Weld metal E5(r) behaved in a similar manner to E0(r) and coarsened to an austenite grain size of 78 μm after 5 mins. at 1250°C. Continued holding at 1250°C would be expected to produce further grain growth towards the limiting size of 197 μm. Again the previous comments concerning the possible additional influence of nitrides may also be important for this weld metal.

In general the grain growth behaviour of weld metals may be summarised in the form of the schematic diagram shown in Figure 5.28. This diagram shows that "clean" HAZ material will coarsen to very large grain sizes in high heat input welding situations whereas an average weld metal will reach a limiting grain size. Figure 5.28 is similar to Figure 4.9, in which the results of the current investigation for weld metals are compared with the grain growth behaviour of HAZ's.

5.4.4 Ferrite nucleation

In section 2.5.4 most of the common heterogeneous sites for ferrite nucleation in weld metals were considered. In all cases the activation energy barrier for nucleation is reduced by physical means. This occurs either by elimination of an existing interface or by using pre-existing interfaces in the new embryo nuclei. The following sites seem to provide attractive sites for ferrite nucleation in weld metals on this basis.

(1) Austenite grain boundaries
(2) Inclusion substrates
(3) Sub-grain boundaries or dislocation boundaries

In addition to purely physical considerations, chemical and strain effects also play an important role in ferrite nucleation. For example chemical variations influence nucleation by altering the value of ΔG_V (free energy for nucleation). Such effects are likely to occur to some extent in areas of solute segregation caused during solidification. In addition, chemical effects may also be important in weld metals if local chemical variations occur in the immediate vicinity of the deoxidation products.

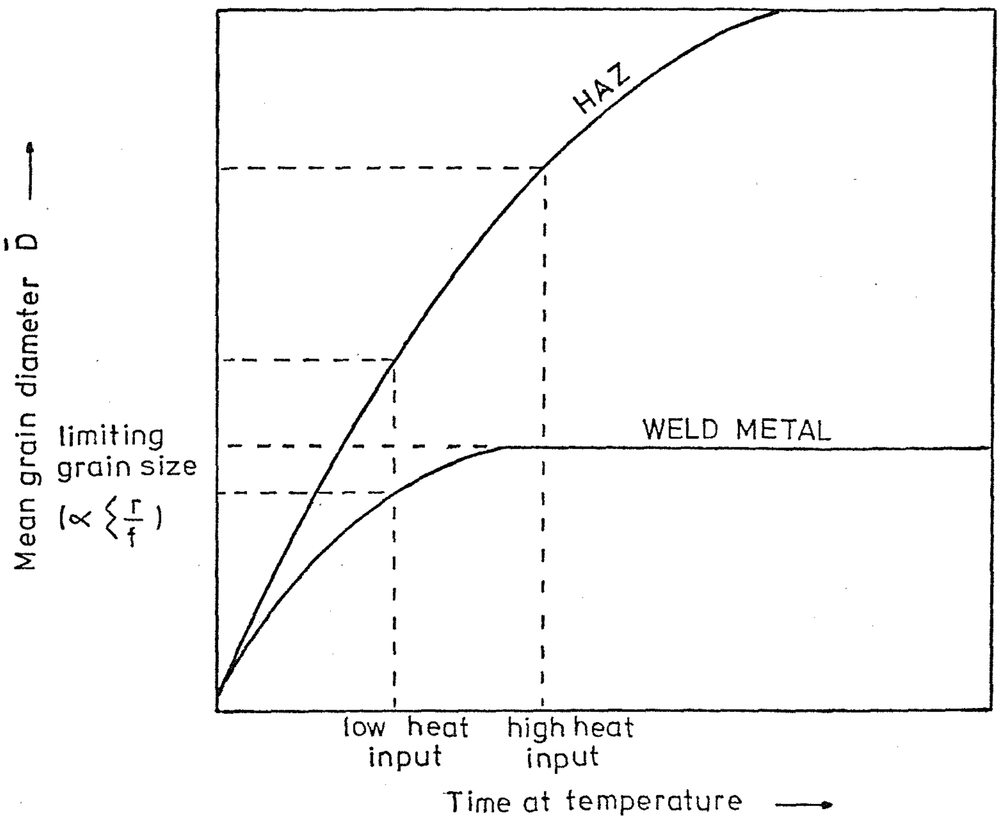

Figure 5.28 Influence of pinning on grain growth behaviour.

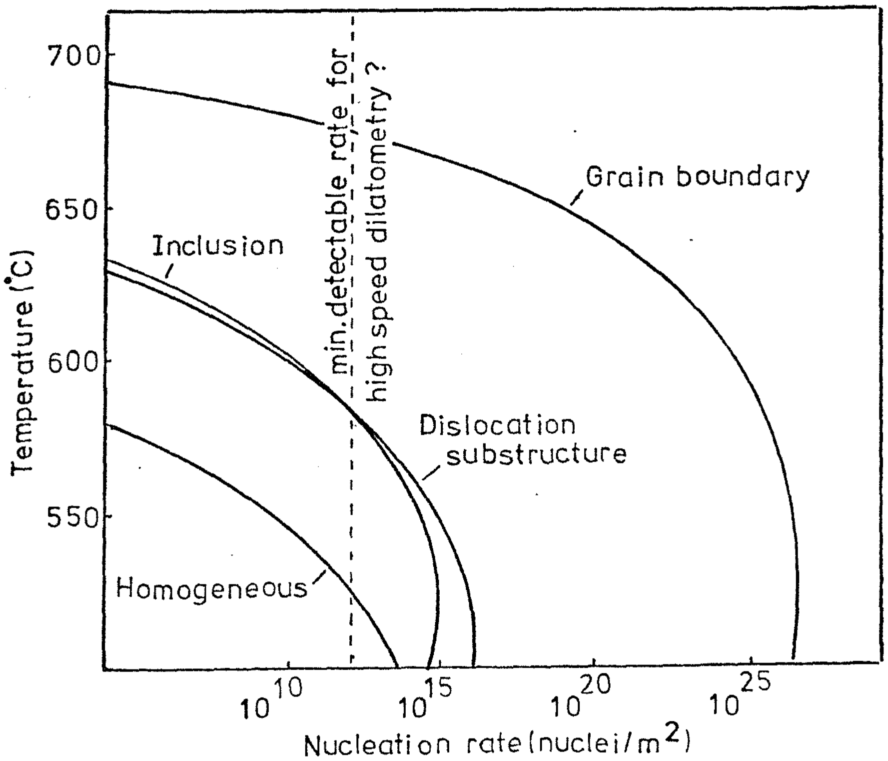

Figure 5.29 Ferrite nucleation rate versus temperature for various heterogeneous sites.

Strain effects must also be taken into account when considering ferrite nucleation in weld metals. In section 2.5.3 it was shown that hard inclusions could provide a potent source for dislocation generation during cooling, by the differential thermal contraction mechanism . This may have the effect of producing an extensive sub-structure within the austenite prior to transformation, which may provide additional sites for ferrite nucleation.

The localised stress around each inclusion also influences nucleation directly, by altering the value of the strain energy term and therefore altering ΔG.

Clearly as the $\gamma \rightarrow \alpha$ transformation represents about a four per cent volume expansion, it will be less thermodynamically favourable for nucleation to occur in the region of high compressive stress (i.e. the inclusion/matrix interface) as opposed to an equivalent region under neutral or tensile stresses.

These considerations will now be discussed in more detail.

5.4.4(a) Physical effects

In Figure 2.29 most of the heterogeneous nucleation sites were compared in terms of their normalised activation energy barriers for nucleation. This type of analysis gives an indication of the most energetically favourable sites, but unfortunately does not necessarily indicate which are the most dominant sites during continuous cooling. To get a true indication of the latter, it is necessary to also consider the number of nucleation sites and the extent of the undercooling during transformation.

From classical nucleation theory, the rate of nucleation, N, may be expressed as:-

$$N = \omega c \exp \left(\frac{-\Delta G^*}{KT}\right) \qquad (5.4)$$

where ω is a frequency factor.

c is the number of atoms in contact with the nucleation site.

Using an analysis similar to that of Sharma and Purdy [170], nuclation rates have been calculated as a function of temperature for the most likely nucleation sites i.e. grain boundaries, inclusion substrates and dislocation sub-boundaries. Figure 5.29 shows the results of this preliminary analysis.

From Figure 5.29 it can be seen that grain boundaries are the dominant nucleation sites over the entire temperature range studied. Unfortunately it is difficult to estimate the minimum detectable nucleation rate during continuous cooling dilatometry. If one assumes this is about 10^8 nuclei/cm^2 per sec at a typical weld cooling rate it can be seen that reasonable results are predicted from Figure 5.29. For example ferrite nucleation at the grain boundary would be detected at about 673°C followed by intragranular nucleation at dislocation sub-boundaries or inclusions substrates at about 575 to 580°C. In the purely hypothetical case of their being no heterogeneous sites, homogeneous nucleation would occur at about 507°C.

The above transformation temperatures compare favourably with experimental values for a weld metal of similar composition (0.1 wt%C, 1.0 wt%Mn) cooled at about 30°C/sec. In this case (Figure 4.56) grain boundary ferrite is detected (2½% transformation) at about 668°C followed by intragranular acicular ferrite at 575°C.

The above results clearly show that an equivalent rate of intragranular ferrite nucleation may be produced on either the inclusion substrates or the dislocation substructure at a very similar temperature. If this is true it may explain why some investigators have been unable to account for the acicular ferrite phase as an entirely inclusion nucleated transformation product, particularly in terms of the ratio of inclusions to acicular ferrite grains. Unfortunately it must be appreciated that the theoretical calculations cannot be considered to be completely rigorous. Clearly the assumptions concerning the existence of a dislocation substructure are open to debate. In addition there are other shortcomings, particularly in the assumptions concerning embryo shape and interfacial energy terms. For simplicity the value of 0.075 J/m^2 suggested by Sharma has been used. Clearly this implies the embryo shape to consist very largely of coherent or semi-coherent interfaces. However, in view of the low transformation temperature and crystallographic nature of acicular ferrite, these assumptions may not be too unreasonable.

5.4.4(b) Chemical effects

When considering ferrite nucleation in the vicinity of weld metal inclusions, the possibility of local chemical inhomogenity influencing nucleation cannot be ruled out. Recent advances in high resolution microanalysis techniques have enabled analysis of material close to the inclusion-matrix interface. However, since the critical ferrite nucleus diameter is in the order of only 100 Å the region of material of interest is currently below the limit of resolution of most microanalysis techniques.

It should be appreciated that only relatively small concentrations of elements such as titanium (∿0.7 wt%), aluminium (∿0.63 wt%) or phosphorus (∿0.17 wt%) are required to stabilise ferrite [172]. Any minor inhomogenity of these elements close to the inclusion interface may therefore have a strong influence on the thermodynamics of ferrite nucleation.

5.4.4(c) Strain effects

In section 2.5.3 it was calculated that the maximum compressive stress generated around certain inclusions during cooling could exceed the yield stress of the material. As austenite decomposition is sensitive to both temperature and pressure, it is of interest to consider whether or not these stresses could influence ferrite nucleation at the inclusion interface.

Figure 5.30 shows the influence of pressure on the iron-carbon diagram for a 0.44%C steel. Clearly increasing pressure has a strong effect on retarding austenite decomposition. From section 2.5.3(a) a radial compressive stress of about 185 MPa (∿2 kilobars) may exist at the inclusion matrix interface. This may locally reduce the $\gamma \rightarrow \alpha$ transformation temperature by about 10°C. This last point is important because although previous calculations predicted almost simultaneous nucleation on inclusions and dislocation sub-structures, it would seem that the sub-structure may provide the slightly more favourable nucleation sites. There is some practical evidence to support this hypothesis. For example in a study of the microstructure and toughness of HSLA steel weld metals, Barritte and Edmonds [76] noted that often two adjacent inclusions would seem to act as a single ferrite nucleation site. The authors suggested that the tessallated stresses around the inclusions may be influencing the ferrite nucleation process in some way.

From the previous discussion it would seem that the inclusion/matrix interfaces would be less favourable nucleation sites from the stress point of view. However, the regions of neutral stress between two inclusions may provide favourable nucleation sites,

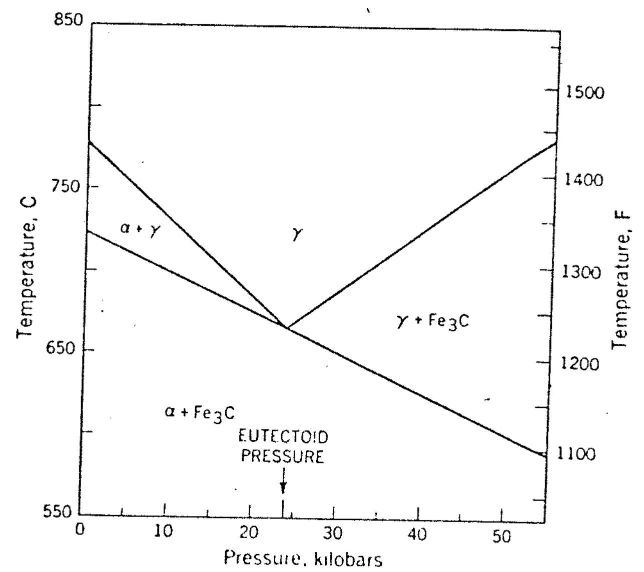

Figure 5.30 Influence of pressure on the iron - carbon phase diagram for a 0.44wt%C steel (173).

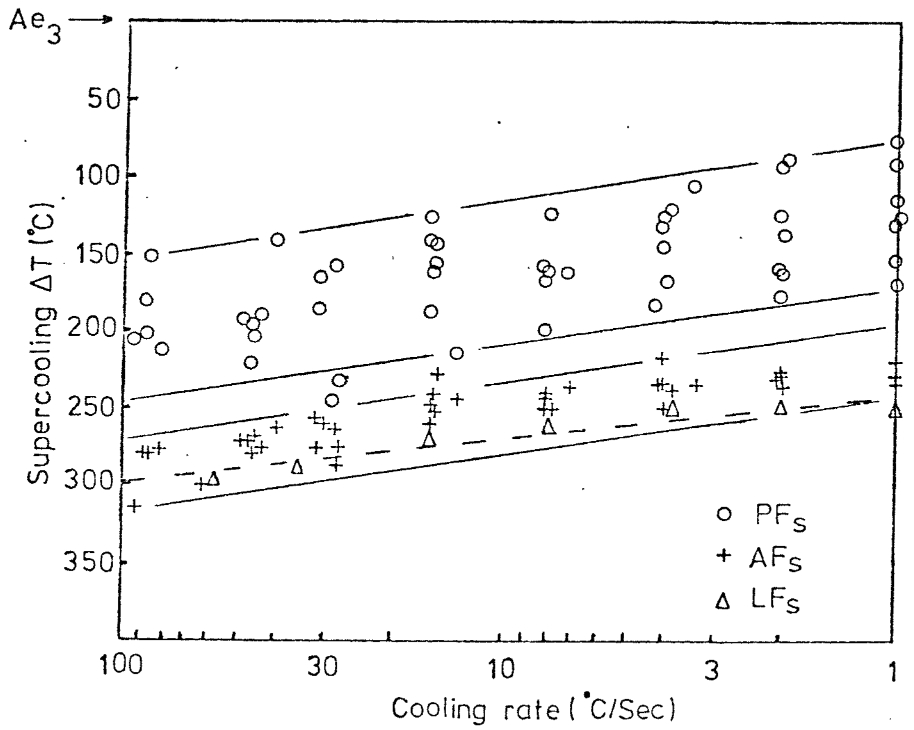

Figure 5.31 Relationship between supercooling (Andrews Ae$_3$ - measured T_s), cooling rate, and microstructure for weld metals M1,M2,M5,N1,N2,N3,N4A,and NMo.

particularly if they are associated with suitable heterogeneous nucleation sites such as dislocation boundaries.

5.4.5 Summary

In the previous section the experimental evidence concerning the influence of oxygen-rich inclusions on weld metal transformation behaviour has been examined, and discussed in relation to the ideas developed in section 5 of the literature review. The most interesting points arising from this discussion are summarised as follows:-

(1) In reheated weld metals, inclusions interact with austenite grain boundaries and restrict normal grain growth. This results in higher $\gamma \rightarrow \alpha$ transformation temperatures for weld metals than for identical "clean" steels, subjected to the same weld thermal cycle. This is due to the increased availability of favourable grain boundary nucleation sites in the smaller γ grain structure.

(2) Grain boundary pinning in reheated weld metals generally follows the classical theory of Zener, although further work is required to define an accurate correlation factor. At very high or very low oxygen contents the simple theory clearly breaks down.

(3) There is no evidence in the current work to suggest that oxygen content influences as deposited austenite grain size.

(4) The microstructural change from acicular ferrite to lath ferrite caused by complete removal of inclusions is clear qualitative evidence of an inclusion related nucleation effect.

(5) Detailed comparison of HAZ and weld metal CCT diagrams and careful consideration of the influence of grain size on transformation temperatures in remelted and unremelted weld metals gives direct quantitative evidence of an inclusion related nucleation effect.

(6) The current experimental evidence supports the views raised in the literature review that inclusions directly influence ferrite nucleation in two ways.

  (a) Inclusions located in grain boundaries can catalyse grain boundary nucleation by the mechanism discussed in section 2.5.4(e). It is assumed that the magnitude of this effect will be proportional to the surface area of inclusions associated with the grain boundary. In this respect, high oxygen content weld metals will have the maximum catalytic effect.

(b) Intragranular inclusions may act as heterogeneous sites for ferrite nucleation by the mechanism discussed in section 2.5.4(b). However, it is doubtful whether this mechanism can entirely account for the nucleation of fine grained acicular ferrite. Clearly the potency of inclusion substrate nucleation will depend critically on local chemistry and strain effects in the surrounding matrix. Hard, highly straining inclusions such as the alumina rich variety found in basic flux weld metals may actually be less efficient nucleation sites than the softer silicate types produced in acidic flux systems. This is due to the magnitude of the radial compressive stress at the inclusion-matrix interface which should inhibit nucleation. However, hard highly straining inclusions are expected to substantially increase the dislocation density of the austenite matrix, through the differential thermal contraction mechanism discussed in section 2.5.3. This may therefore provide additional heterogeneous nucleation sites in the form of a dislocation substructure. If this occurs it could be envisaged that the very high nucleation rate required to develop fine grained acicular ferrite, occurs from extensive nucleation of ferrite on both the dislocation substructure and inclusions at almost the same degree of supercooling.

5.5 Models Relating to Weld Metal γ - α Tranformation Behaviour

5.5.1 Theoretical model describing weld metal microstructural development

In the previous three sections it has become clear that weld metal microstructural development is complex and influenced by many factors. The following model is therefore only considered to be a general overview of weld metal transformation behaviour.

Weld metal microstructure may be considered to be influenced by the following four variables.

(1) Cooling rate
(2) Chemical composition
(3) Austenite grain size
(4) Deoxidation products (Inclusions)

All these variables are inter-related in the welding process and are influenced by wire and plate composition, flux type, and welding process variables such as arc energy, preheat, and weld geometry etc.

In the most general terms, microstructural development may be expressed by the following equation:

Thermodynamics + Kinetics → Supercooling → Microstructure

The four major variables may therefore be considered in terms of their influence on thermodynamics and kinetics as follows:-

(1) Cooling rate has a direct influence on thermodynamics during continuous cooling transformations by influencing the degree of supercooling reached prior to transformation. Cooling rate also influences the amount of time available for transformations to occur at any given temperature.

(2) Chemical composition influences thermodynamics by altering the Ae_3 temperatures (i.e. γ or α stabilisation), and also influences kinetics through its influence on hardenability.

(3) Austenite grain size influences the kinetics of primary nucleation, (availability of grain boundary nucleation sites).

(4) Inclusions influence the kinetics of secondary nucleation (availability of intragranular nucleation sites).

It should be noted that in reheated weld metals the inclusions will interact with γ grain boundaries and therefore alter the austenite grain size. However, from the present work there is no evidence to suggest that inclusions significantly alter the γ grain size of as deposited weld metals.

Influence of supercooling on microstructural development

As previously discussed the thermodynamic driving force for the $\gamma \rightarrow \alpha$ transformation is determined by the degree of supercooling prior to transformation. This supercooling is in turn influenced by alloying, cooling rate and the nucleation site density.

Figure 5.31 shows the relationship between the degree of constitutional supercooling (Ae_3-T_S), cooling rate and microstructure for the seven MMA C-Mn and C-Mn-Ni weld metals, and the single SA C-Mn-Ni-Mo weld metal studied in the current investigation. Clearly polygonal ferrite and acicular ferrite can be divided in terms of supercooling from Ae_3. Lath ferrite or upper bainite can be seen to develop within the same band of constitutional supercooling as acicular ferrite, although generally towards the bottom of this band.

Figure 5.31 may now be used as a basis for describing the influence of cooling rate, γ grain size and alloying on weld metal transformation behaviour.

During continuous cooling from Ae_3 the degree of supercooling, ΔT, continually increases. Eventually a certain value is reached at which the thermodynamic driving force is great enough to produce a detectable nucleation rate at the most favourable nucleation sites (i.e. the γ grain boundaries). If the cooling rate is slow, there may then be sufficient time for the ferrite to grow and the transformation may go to completion before the degree of supercooling becomes much greater in intragranular regions.

If on the other hand the cooling rate is fast, the primary ferrite will continue to grow, but the degree of supercooling at the grain interior will rapidly increase until the thermodynamic driving force is great enough to produce secondary nucleation at intragranular sites. Two factors are very important in influencing this continued increase in ΔT at the intragranular regions. These are the γ grain size and the extent of carbon rejection from the primary ferrite into the surrounding austenite. Clearly if the austenite grains are small and the carbon enrichment large, the degree of constitutional supercooling at the grain interior will not increase rapidly and may in fact even decrease as the transformation proceeds. In such cases the primary grain boundary ferrite reaction is likely to dominate the transformation. However, if the γ grain size is large, as is usually the case with as deposited weld metals, the intragranular supercooling will soon reach the necessary value for intragranular nucleation, and the intragranular transformation product will dominate.

From above it can be seen that the relative proportions of grain boundary nucleated and intragranularly nucleated products depends largely on the degree of supercooling and the rate at which this degree of supercooling is achieved. Thus for any particular weld metal composition, both the cooling rate and γ grain size will play a major role in determining the final proportion of grain boundary and intragranular transformation products.

Clearly alloying also has an important rôle in determining transformation behaviour through its influence on constitutional supercooling. In section 2.3 both the thermodynamic influences in terms of α or γ stabilisation and the kinetic influences in terms of hardenability were discussed. As we are considering transformations in terms of supercooling from Ae_3 it becomes apparent that both these factors are important.

Austenite stabilising elements such as Mn and Ni depress both the Ae_3 and the actual continuous cooling transformation start temperatures and therefore have a relatively mild influence on supercooling. These elements do however, slow down the ferrite transformation (probably by the solute drag mechanism) and therefore allow the supercooling to reach a level at which intragranular nucleation dominates the transformation. This produces large proportions of acicular ferrite in the final microstructure of basic flux weld metals.

Ferrite stabilising elements, on the other hand, such as Mo, Nb and V and to a lesser extent Cr increase Ae_3 whilst decreasing actual transformation temperatures. These elements therefore have a very powerful influence on supercooling and this often has the effect of increasing the degree of supercooling to the point where true parallel lath bainitic transformation products dominate the microstructure. In addition certain powerful ferrite stabilisers are known to strongly suppress the high temperature ferrite reaction, which again promotes bainitic microstructures. An example of this type of behaviour is the C-Mn-Ni-Mo weld metal discussed in the previous sections.

The previous considerations regarding the influence of cooling rate, γ grain size and alloying on supercooling and microstructural development may now be used to produce a general model of weld metal transformation behaviour.

Figure 5.32 is a schematic model showing the influence of cooling rate, γ grain size and alloying on supercooling, and also showing the relationship between supercooling, nucleation rate, and microstructure for various nucleation sites. The relationship between ΔT and nucleation rate for different nucleation sites is based on Figure 5.29. Clearly several assumptions must be made concerning the major nucleation sites of the various microstructural types. These assumptions are as follows:-

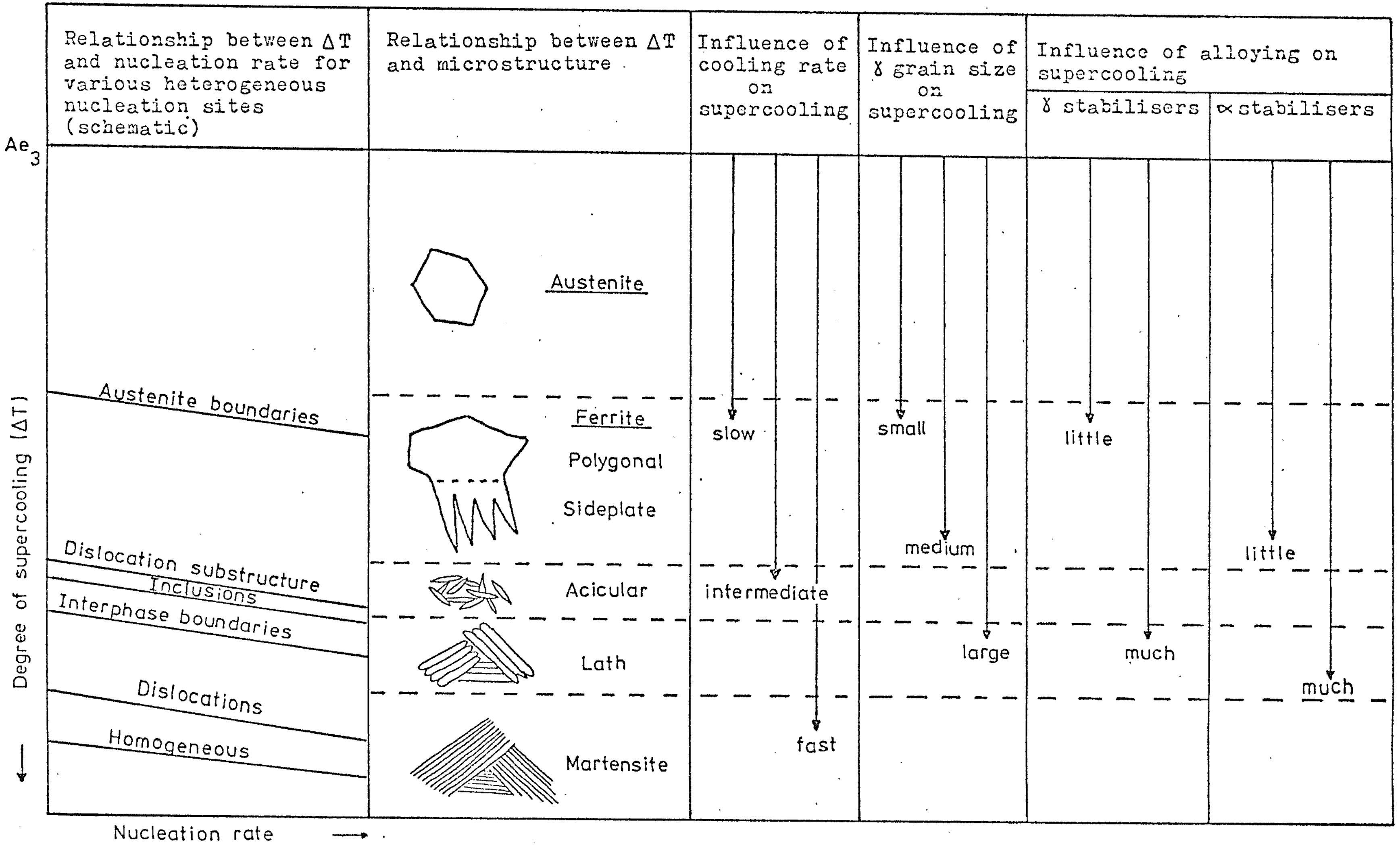

Figure 5.32 Schematic model showing the influence of cooling rate, γ grain size, and alloying on supercooling and also showing the relationship between supercooling, nucleation rate, and microstructure for various nucleation sites.

(1) The majority of polygonal ferrite grains are nucleated at austenite grain boundaries.

(2) The majority of acicular ferrite grains are nucleated either on the dislocation substructure or inclusions.

(3) The majority of lath ferrite grains are sympathetically nucleated from other laths. This reaction requires a precursor nucleation reaction such as nucleation at grain boundaries, substructure or inclusions.

(4) The majority of lath martensite is dislocation nucleated.

These assumptions do not preclude the possibility that some microstructural types nucleate on more than one of the above nucleation sites. For example in the case of the low temperature transformation products there is little doubt that nucleation could occur on several different types of site, provided site saturation had not already occurred during a precursor reaction. However, the previous assumptions are clearly a simplification and are intended to apply to the majority of each microstructural type as it develops during continuous cooling.

The influence of cooling rate, γ grain size and alloying on supercooling are shown in vector form in Figure 5.32. The actual magnitude of each of these vectors will depend on the particular circumstance envisaged.

For example a combination of fast cooling rate, large γ grain size and much alloying will produce a very large degree of supercooling and will almost certainly produce martensite. On the other hand, slow cooling rate, small γ grain size and little alloying will produce a mild supercooling resulting in polygonal ferrite development. Any intermediate mixture of cooling rate, γ grain size and alloying is likely to produce intermediate supercooling and may produce sideplates, acicular ferrite or lath ferrite, or all three.

It should be remembered that the vectors represent the maximum degree of supercooling reached and therefore show the lowest transformation product that may be formed in each case. This implies that all higher transformation products may also form to some extent during continuous cooling. The exact extent to which higher temperature transformation products develop, will depend on cooling rate, alloying and nucleation site density and such information is ideally presented in the form of a CCT diagram.

So far the model has only been used to explain the interactions between cooling rate, γ grain size and alloying on supercooling and microstructure. The other important variable in weld metals is the inclusion content and this must now be considered.

Complete removal of the inclusions from a weld metal removes both the direct sites (inclusion substrates) and indirect sites (dislocation substructure) for acicular ferrite nucleation. Figure 5.32 may therefore be modified by removing these nucleation sites and their corresponding acicular ferrite supercooling regime. The modified model should now be applicable to "clean" steels and should describe transformation behaviour of HAZ's or very low oxygen content weld metals of similar composition.

The modified model now predicts that any combination of cooling rate, γ grain size and alloying which results in intermediate supercooling will encourage the development of sideplate or lath ferrite structures. The previous experimental work in which a weld metal was de-gassed, and the discussion in section 5.4.1 confirms this view of events.

By way of interest the model may also be adjusted to account for microstructural development in thermomechanically worked steels of similar composition. In this case an extensive dislocation substructure is introduced into the austenite by warm working. Figure 5.32 is applicable to this situation provided the line represented the inclusion nucleation sites is neglected. It can therefore be seen that careful control of supercooling, through alloying and cooling rate can produce an acicular ferrite type of microstructure, nucleated mainly on the dislocation sub-structure, (i.e. the acicular ferrite steels).

One of the most interesting aspects of weld metal transformation behaviour is the influence of flux type on microstructural development.

In the literature it has been noted that SA weld metals deposited under acidic fluxes often have a predominately sideplate type microstructure whereas those of almost identical chemical composition deposited under basic fluxes develop acicular ferrite. The main factor which seems to influence this change is the oxygen content, which is in turn a reflection of the oxygen-rich inclusion population. When dilatometry is carried out to measure the $\gamma \rightarrow \alpha$ transformation temperatures it is noted that high oxygen weld metals transform at appreciably higher temperatures [129][76]. This is thought to be partly due to development of smaller γ grain sizes, due to greater grain boundary/particle interactions in the high oxygen weld metal, during re-austenitisation. However, in as deposited weld metals the austenite grain size is determined by the size of the original solidification grain structure and the transformation characteristics of the subsequent $\delta \rightarrow \gamma$ phase transformation. In the current investigation, as deposited γ grain size measurements for high and low oxygen weld metals show little variation, and therefore suggest that pinning is not an important factor during their development.

If this is so it is interesting to see how the model of transformation behaviour can be used to explain the change in microstructure brought about the different flux systems.

In section 2.5.3(a) it was shown that the glassy manganese-silicate type of inclusions, produced under acidic fluxes, were much less efficient in generating thermal contraction stresses than the alumina rich inclusion types of the basic fluxes.

In section 2.5.4(e) it was shown that nucleation at boundaries in contact with inclusions was much more energetically favourable than nucleation at either boundaries or inclusions alone. The combination of both these above factors can now be applied to the model describing transformation behaviour.

In the case of basic flux weld metals which contain hard alumina rich inclusions, differential contraction stresses operate during cooling to produce an extensive dislocation sub-structure. The previous model shown in Figure 5.32 was constructed to describe the transformation behaviour of such materials.

From Figure 5.32 it can be seen that by producing a certain intermediate degree of supercooling in the intragranular regions it is possible to obtain a very high nucleation rate on both the sub-structure and the inclusions simultaneously. This will therefore result in a very fine acicular ferrite grain size. Unfortunately factors such as local chemical variations, local stress concentrations, and interactions between sub-boundaries and inclusions, make it difficult to put values on the relative contributions from direct (inclusion substrate) and indirect (dislocation sub-structure) nucleation.

In the case of acidic flux, high oxygen content, weld metals the manganese silicate inclusions have much less potential for producing large thermal contraction stresses during cooling. The model of transformation behaviour should therefore be modified for these materials by removing the line representing sub-structure nucleation.

It can now be seen that for a similar intermediate degree of supercooling the acidic flux weld metals will have a much lower intragranular ferrite nucleation rate than the equivalent basix flux weld metal. As a result fine grained acicular ferrite will not develop in these materials.

Another factor which is important in these materials is the catalytic influence of inclusions associated with γ grain boundaries. In section 2.5.4(e) it was shown that such inclusions were even more favourable sites for ferrite nucleation than the grain boundaries themselves. This implies that high oxygen weld metals require less supercooling to initiate the grain boundary reaction than the equivalent clean steel of identical grain size. If this is so, these materials will clearly have much more time for development of grain boundary nucleated transformation products before the intragranular reaction occurs. This may explain why high oxygen weld metals are usually dominated by grain boundary nucleated transformation products such as ferrite sideplates.

5.5.2 Practical utilisation of CCT data to optimise weld metal microstructure and mechanical properties

The major aim of this thesis has been to produce a rational understanding of weld metal microstructural development. With this understanding it should be possible to produce reliable, reproducible weld metals in which the microstructure can be optimised to confer the best possible combination of mechanical properties to the weld.

The experimental work discussed in the previous chapters has helped to elucidate the various factors controlling microstructural development and has provided the basis for the model of transformation behaviour presented in the previous section. However, it is the actual CCT diagrams which provide the essential source of detailed microstructural data for optimising mechanical properties. In the final sections an example of how CCT data may be used to optimise weld metal toughness will be given, using the data applicable to C-Mn and C-Mn-Ni MMA weld metals, deposited under a basic flux system.

5.5.2(a) Toughness of coarse grained reheated C-Mn weld metals deposited under basic flux systems

In terms of optimising toughness, the CCT diagrams may be useful if certain assumptions are made. The first assumption is that toughness is controlled entirely by the quantity and distribution of the various $\gamma \rightarrow \alpha$ transformation products. This assumption is obviously an over simplification, but is made on the grounds that other influences such as solution strengthening, precipitation, strain ageing etc., may be, to some extent, varied independently of microstructure. These other factors can therefore be considered additional factors in the toughness equation.

Having accepted the first assumption, the various $\gamma \rightarrow \alpha$ transformation products must be ranked in some order of toughness. By drawing on previous experience of weld metal structure-properties relationships [171][57] it is assumed that a high proportion of acicular ferrite is favourable in terms of toughness. Small quantities of martensite or pearlite are considered to be very detrimental and cause embrittlement. The other three structures, polygonal, sideplate and lath ferrite are also considered to be poor, from a toughness point of view. This is thought to be due to their having relatively few high angle grain boundaries and therefore little resistance to propagating cleavage cracks, and also having generally large structural units.

Using the previous assumptions the influence of manganese on optimum weld metal toughness is shown as a function of cooling rate in Figure 5.33. It should be noted that Figure 5.33 is only strictly applicable to reheated weld metals situated close to the fusion line. An adaptation of this diagram for as deposited weld metal will be presented later. In Figure 5.33 the right hand diagonal line represents the position of the pearlite nose on the CCT diagrams. At all cooling rates to the right hand side of this line, increasing quantities of pearlite will be developed which will have an increasingly detrimental influence on toughness. The left hand diagonal line represents the position at which detectable quantities of martensite form in the microstructure. At all cooling rates to the left of this line increasing quantities of martensite will be developed which will also be detrimental to toughness. The region between the martensite and pearlite lines represents the range of composition and cooling rate in which the enriched austenite either remains untransformed or transforms to bainite or martensite-austenite. It is assumed that the region of maximum toughness will be found within this region. The exact position is expected to be a compromise

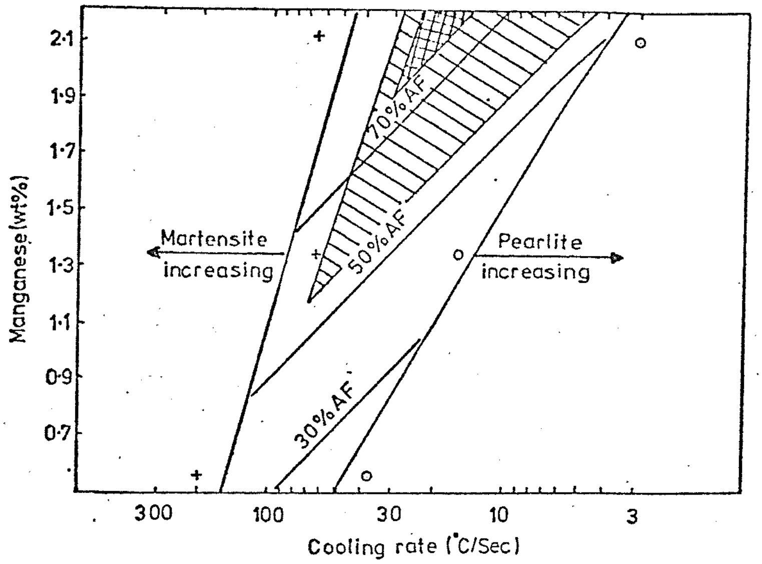

Figure 5.33 Optimum toughness regimes in reheated C-Mn weld metal.

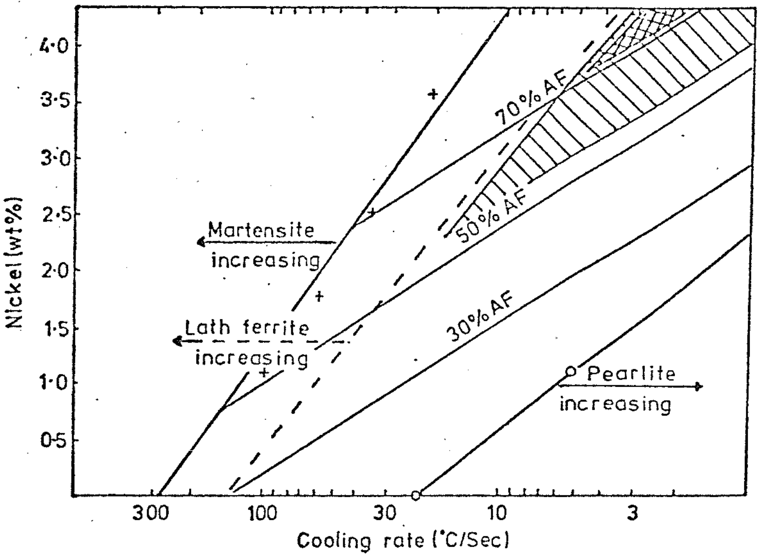

Figure 5.34 Optimum toughness regimes in reheated C-Mn-Ni weld metal.

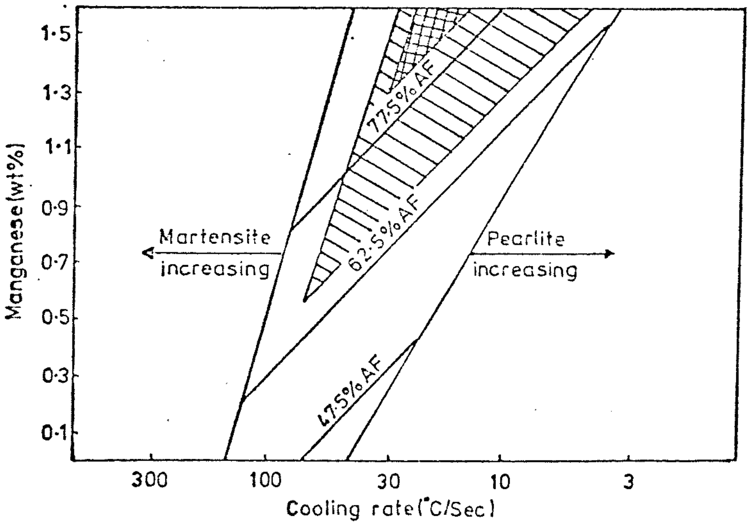

Figure 5.35 Optimum toughness regimes in as deposited C-Mn weld metal.

between increasing proportions of acicular ferrite and increasing proportions of M-A which are believed to have opposing influences on toughness. The shaded areas in Figure 5.33 are estimates of the regions of optimum toughness for the dilatometer specimens. It can be seen that at a cooling rate of 30°C/sec (Δt^{800}_{500} = 10 sec) the optimum manganese content is estimated to be ∿1.9 wt%Mn. At cooling rates typical of high heat input welding the optimum manganese content is expected to be somewhat higher. Unfortunately there is insufficient data in the current investigation to predict this upper value.

5.5.2(b) Toughness of coarse grained reheated C-Mn-Ni weld metals deposited under basic flux systems

Figure 5.34 shows the influence of nickel on optimum weld metal toughness, based on the assumptions described in the previous section. It can be seen that this figure is of similar format to the figure relating to manganese (Figure 5.33). In the case of the nickel series of weld metals, the region in which M-A forms is much larger. This is probably a consequence of the generally higher levels of alloying of the C-Mn-Ni series of weld metals. Again the areas expected to produce the best toughness are shaded and are a compromise between increasing acicular ferrite and increasing M-A contents. An additional complication in the C-Mn-Ni weld metals is the development of significant quantities of lath ferrite. The cooling rates and compositions at which these structures start to develop is shown by the dotted line in Figure 5.34. Optimum toughness is assumed to occur to the right hand side of this line, where the lath structure does not occur.

It can be seen from Figure 5.34 that the optimum nickel content for good toughness at a cooling rate of 30°C/sec is estimated at about 1.8 wt%Ni. This value increases to about 4.0 wt%Ni at a cooling rate of 3°C/sec. Again it must be emphasised that the above values are only applicable to reheated weld metals and are not applicable to as deposited material. It should also be appreciated that the optimum values will vary if the other alloying levels (i.e. C and Mn) are altered.

5.5.2(c) Adaptation of CCT data to predict optimum toughness transformation regimes in as deposited C-Mn basic flux weld metals

The previous analysis of CCT data gives a reasonable estimate of the relationship between alloying, cooling rate and microstructure in reheated C-Mn-(Ni) dilatometer specimens. In order to adapt this type of data to as deposited weld metals it is necessary to correct for different austenite grain sizes and shapes.

From section 5.3.6 it is known that austenite grain size influences transformation behaviour in terms of both transformation temperatures and the ratio of grain boundary nucleated, to intragranularly nucleated products. Two corrections must therefore be made to Figure 5.33 to make it applicable to as deposited C-Mn structures. Firstly a grain size correction must be made by comparing the mean grain diameters of the equiaxed and columnar grain structures, relating to the reheated and as deposited materials respectively. As there is a relationship between the influence of alloying and γ grain size, in terms of transformation temperatures, the grain size correction may be applied directly to Figure 5.33 by making the appropriate shift in alloy content. For manganese this correction has been calculated to be $\sim$0.6 wt%.

To correct for the difference in γ grain shape it is necessary to calculate the difference in grain boundary area to grain volume ratios. For simplicity this has been done by assuming spherical grains in the equiaxed structure and cylindrical grains with an aspect ratio of 3:1 in the columnar structures. This analysis shows that there is approximately 25% more grain boundary area in the equiaxed structure and therefore a correction must be made to the proportion of grain boundary nucleated phases shown in the CCT diagrams. Figure 5.33 (applicable to C-Mn dilatometer specimens) may now be redrawn for as deposited weld metals, and is shown as Figure 5.35.

From this figure it can be seen that the optimum manganese content for good toughness in as deposited C-Mn basic flux weld metals, at a cooling rate of $\sim 30^{\circ}$C/sec, should be about 1.3 wt%Mn. Clearly at slower cooling rates, the optimum manganese content would be expected to increase, although there is insufficient data in the current investigation to predict any actual values.

A similar analysis could be carried out for the C-Mn-Ni series of CCT diagrams although this would be further complicated by the unknown influence of grain size and transformation temperature on the position of the lath ferrite or upper bainite nose.

CHAPTER 6: CONCLUSIONS

The conclusions drawn from the present work can be divided into three main categories covering the following topics: CCT diagrams and transformation products; alloying elements and prior austenite grain size; and grain boundary pinning and ferrite nucleation.

The conclusions relating to CCT diagrams and weld metal transformation products may be summarised as follows:-

(1) CCT diagrams can be produced to accurately describe weld metal transformation behaviour. With such diagrams it is possible to divide weld metal transformation products into two categories.

  (a) Transformation products nucleating and growing from prior austenite grin boundaries. These products form at the highest transformation temperatures and consist of polygonal ferrite, grain boundary allotriomorphs and Widmanstätten sideplates.

  (b) Transformation products nucleating and growing in the intragranular regions of prior austenite grains. These products form at lower temperatures and consist of acicular ferrite, coarse acicular ferrite and lath ferrite.

The overall shapes of weld metal CCT diagrams are similar to those applicable to HAZ's, although the bainite region is replaced by a region in which either acicular ferrite or lath ferrite develops. In general terms lath ferrite replaces acicular ferrite at fast cooling rates, high alloy contents, or when suitable nucleation sites for acicular ferrite are removed.

(2) Grain boundary ferrite in weld metals is equivalent to the morphological variety of the proeutectoid ferrite reaction known as grain boundary allotriomorphs.

(3) Sideplate structures in weld metals are for the most part equivalent to the morphological variety of the proeutectoid reaction known as Widmanstätten secondary sideplates.

(4) Acicular ferrite is a fully intragranular, fine grained transformation product. Although the results of the current investigation are not conclusive, the weight of evidence suggests that acicular ferrite is bainitic in nature.

(5) The low temperature lath structure in weld metals is identical to upper bainite in terms of both transformation temperatures

and morphology.

(6) Cooling rate has many influences on weld metal transformation behaviour. In basic flux acicular ferrite type weld metals, increasing cooling rate generally has the following effects:
   (a) Transformation temperatures are depressed.
   (b) The proportion of grain boundary nucleated products decreases.
   (c) The intragranular acicular ferrite becomes refined.
   (d) The pearlite reaction is suppressed.
   (e) At very fast cooling rates or high alloy contents, lath ferrite and martensite are formed.

The conclusions relating to the influence of alloying elements and prior austenite grain size may be summarised as follows:-

(1) Manganese is a strong austenite stabiliser and has a moderate influence on hardenability. In the current investigation manganese has been shown to depress transformation temperatures in all regions of the CCT diagram and to promote acicular ferrite at the expense of polygonal ferrite and ferrite sideplates. There is also evidence that manganese has a very mild effect on separation of the bainite and pearlite noses.

(2) Nickel is an austenite stabiliser, but has less influence on hardenability and transformation temperatures than manganese. In the current investigation nickel has been shown to depress transformation temperatures in all regions of the CCT diagram in a similar manner to manganese. This results in increased proportions of acicular ferrite at the expense of polygonal ferrite and ferrite sideplates. There is also clear evidence of a slight separation of the bainite and pearlite noses.

(3) Niobium is a ferrite stabiliser and has a very strong influence on hardenability. In the current work the effect of niobium has been studied at two hardenability levels. In weld metal of base composition 0.1 wt%C, 1.35 wt%Mn, 0.31 wt%Si, niobium has been shown to increase hardenability and strongly suppress both the ferrite and pearlite reactions. This results in a decrease in the grain boundary ferrite content of the weld metal microstructure in favour of acicular ferrite. The acicular ferrite is also slightly refined due to depression of its transformation temperature. In weld metal of base composition 0.09 wt%C, 1.0 wt%Mn, 0.15 wt%Si, niobium is also believed to have depressed transformation temperatures. In

this case however, niobium favoured the development of a predominantly sideplate type microstructure.
At both levels of hardenability niobium seems to influence transformation behaviour by interfering with the development of grain boundary ferrite.

(4) Carbon is a strong austenite stabiliser and has a very powerful influence on hardenability and transformation temperatures. In the current investigation carbon has been shown to depress transformation temperatures in all regions of the CCT diagram. This results in increased proportions of acicular ferrite at the expense of polygonal ferrite and ferrite sideplates. At slow cooling rates the amount of pearlite developed is in good agreement with that predicted by the lever rule. However, at welding cooling rates the amount of pearlite formed depends on the position of the pearlite nose.

(5) Molybdenum is a ferrite stabiliser and has a strong influence on hardenability. In the current investigation, molybdenum has been shown to have a strong influence on the separation of the bainite and ferrite noses. This resulted in a predominantly lath ferrite (upper bainite) microstructure in the C-Mn-Ni-Mo weld metal when cooled in the welding cooling rate range.

(6) Prior austenite grain size influences transformation behaviour in two ways.
    (a) Transformation start temperatures are influenced directly by the availability of heterogeneous grain boundary nucleation sites, (i.e. grain boundary area).
    (b) The ratio of grain boundary nucleated, to intragranularly nucleated transformation products, is influenced by prior austenite grain size through its influence on intragranular supercooling.

The conclusions relating to grain boundary pinning and ferrite nucleation may be summarised as follows:-

(1) In reheated weld metals, inclusions interact with austenite grain boundaries and restrict normal grain growth. This results in higher $\gamma \rightarrow \alpha$ transformation start temperatures for weld metals than for identical "clean" steels subjected to identical weld simulation thermal cycles.

(2) Grain boundary pinning in reheated weld metals generally follows the classical theory of Zener, although further work is required

to define an accurate correlation factor. Unfortunately the simple theory breaks down at very high and very low oxygen contents.

(3) There is no evidence in the current work to suggest that oxygen content influences as deposited austenite grain size.

(4) There is considerable evidence in the current work to suggest that the nucleation characteristics of weld metals are strongly influenced by inclusions. The hypothesis presented in the present work suggests that inclusions alter nucleation in the following ways:

  (a) Inclusions located in grain boundaries catalyse grain boundary nucleation by providing very thermodynamically favourable nucleation sites. These sites reduce the activation energy barrier for nucleation not only by the elimination of an existing area of austenite grain boundary, but also by providing an area of inert substrate in the critical ferrite nucleus.

  (b) Intragranular inclusions may act as heterogeneous sites for ferrite nucleation by the mechanism proposed by Ricks and Howell, although localised chemical and strain effects are clearly important factors.
  Certain types of inclusions provide potent sources of dislocation generation through the differential thermal contraction mechanism. The large increase in dislocation density produced by this mechanism may provide additional sites for ferrite nucleation. This may be an important factor in the development of acicular ferrite microstructures.

Suggestions for future work

The CCT diagrams produced in the current work have provided much useful and relevant data on the transformation characteristics of C-Mn, C-Mn-Ni, and C-Mn-Nb weld metals. It is therefore proposed that this technique be extended to investigate the influences of Cr, Mo, V, Ti, and B on weld metal transformation behaviour. In this respect financial support is currently being sought from the S.E.R.C. to study the influences of Cr and Mo on the transformation behaviour of creep-resisting Cr-Mo weld metals.

In the current work a model based on CCT data was proposed, to predict the relationship between alloying, cooling rate, microstructure, and optimum toughness. Clearly it would be very useful to test this model practically. Future work on the correlation of microstructure versus mechanical properties relationships in both weld deposited and weld simulated materials should therefore be given a high priority.

A point of both practical and scientific interest raised in the current work is the influence of inclusions on weld metal transformation behaviour. Clearly some further critical experiments are required in this area. For example there is currently some debate surrounding the influence of inclusions on as deposited austenite grain size. In view of this debate, an investigation into the influences of inclusions, and also alloying, cooling rate, and delta ferrite grain size, on the $\delta \rightarrow \gamma$ phase transformation, using high temperature dilatometry would be very useful.

Critical experiments are also required to elucidate the inclusion related nucleation effects. For example a very careful transformation study of a high oxygen content and clean steel of otherwise identical chemical composition would be very informative. Such a study would involve the construction of two CCT diagrams from identical austenite grain sizes and should confirm the hardenability shift and inclusion nucleation effects discussed in the current work.

Finally, although many thousands of research hours have already been devoted to the study of the acicular ferrite microstructures, there is still no truly definitive evidence regarding the transformation mechanism of this product. CCT diagrams have helped to elucidate the relationship between acicular ferrite and the other transformation products during continuous cooling. However, for truly definitive evidence of the nature of acicular ferrite, it may prove necessary to study the transformation under isothermal conditions.

REFERENCES

1. H.C. COTTON, The Metallurgist and Materials Technologist, 7, 403, (1979).
2. FOOTHILLS PIPE LINES (YUKON) LTD., Engineering specification No. P-100. Calgary, (1978).
3. C.H. ENTREKIN, Jr., Metallography, 12, 295, (1979).
4. J.M. GRAY and H. STUART, in "Development of Superior Notch Toughness in High-Dilution Weldments of Microalloyed Steel", Niobium Products Company Ltd., CBMM, Araxá, Minas Gerais, Brasil, (1980).
5. P.E. BRETZ, B.L. BRAGLIA and R.W. HERTZBERG, in "Weldments: Physical Metallurgy and Failure Phenomena", Proc. Conf., General Electric Company, Schenectady, New York, (1979).
6. M.J. BIBBY and J. GORDON PARR, JISI, 202, 100, (1964).
7. E.A. WILSON, S.M. VICKERS, C. QUIXALL and A. BRADSHAW, in "Phase Transformations", Proc. Conf., Inst. Met., York, (1979).
8. E.A. WILSON, Scripta Met. 4, 309, (1970).
9. G.D. BODA and D.J. MACK, Met. Trans., 1, 1455, (1970).
10. J.D. BOLTON and E.R. PETTY, Metal Sci. J., 5, 166, (1971).
11. J.V. BEE and R.W.K. HONEYCOMBE, Met. Trans. A., 9A, 587, (1978).
12. R.A. RICKS, P.R. HOWELL and R.W.K. HONEYCOMBE, Met. Trans. A., 10A, 1049, (1979).
13. R.A. RICKS, J. Mat. Sci., 16, 3006, (1981).
14. R.H. GOODENOW and R.F. HEHEMANN, Trans. TMS-AIME, 233, 1777, (1965).
15. R.W.K. HONEYCOMBE, Metal Sci., 14, 201, (1980).
16. C.A. DUBE, H.I. AARONSON, R.F. MEHL, Rev. Met., 55 201, (1958).
17. H.I. AARONSON in "Decomposition of Austenite by Diffusional Processes", (Eds. V.F. Zackay and H.I. Aaronson), Interscience, New York, (1962).
18. R.W.K. HONEYCOMBE, Met. Trans. A., 7A, 915, (1976).
19. H.I. AARONSON in "Phase Transformations", Proc. Conf., Inst. Met., York, (1979).
20. C.S. SMITH, Trans. ASM, 45, 533, (1953).
21. D.V. EDMONDS in "Phase Transformations", Proc. Conf., Inst. Met., York, (1979).
22. R.W. HECKEL and H.W. PAXTON, Trans. ASM, 53, 539, (1961).
23. R.D. TOWNSEND and J.S. KIRKALDY, Trans. ASM, 61, 605, (1968).

24. E.P. SIMONEN, H.I. AARONSON and R. TRIVEDI, Met. Trans. 4, 1239, (1973).

25. J.M. RIGSBEE and H.I. AARONSON, Acta Met., 27, 351, (1979).

26. K.R. KINSMAN, E. EICHEN and H.I. AARONSON, Met. Trans. A, 6A, 303, (1975).

27. H.C.H. CARPENTER and J.M. ROBERTSON, JISI, 123, 345, (1931).

28. H. HANNEMANN and A. SCHRADER, Atlas Metallographicus, 1, 19, (1933).

29. M. HILLERT in "Decomposition of Austenite by Diffusional Processes", (Eds. V.F. Zackay and H.I. Aaronson), Interscience, New York, (1962).

30. M.P. PULS and J.S. KIRKALDY, Met. Trans., 3, 2777, (1972).

31. R.F. MEHL and W.C. HAGEL, Progr. in Metal Phys., 6, 74, (1956).

32. C. ZENER, Trans. AIME, 167, 550, (1946).

33. R.A. GRANGE, Trans. ASM, 35, 879, (1947).

34. C.S. SMITH, Trans. ASM, 45, 533, (1953).

35. S. MODIN, quoted by R.W.K. HONEYCOMBE in "Steels: Microstructure and Properties", P40, Edward Arnold (Publishers) Ltd., London, (1981).

36. R.J. DIPPENAAR and R.W.K. HONEYCOMBE, Proc. Roy. Soc., 333, 455, (1973).

37. E.S. DAVENPORT and E.C. BAIN, Trans. AIME, 90, 117, (1930).

38. L.J. HABRAKEN and M. ECONOMOPOULOS, in "Transformation and Hardenability in Steels", Proc. Conf., Climax Moly. Co., Ann Arbor, (1967).

39. Y. OHMORI, H. OHTANI and T. KUNITAKE, Trans. ISIJ, 11, 250, (1971).

40. D.A. PORTER and K.E. EASTERLING in "Phase Transformations in Metals and Alloys", Von Nostrand Reinhold Co. Ltd., (1981).

41. R.W.K. HONEYCOMBE in "Steels: Microstructure and Properties", Edward Arnold (Publishers) Ltd., London, (1981).

42. H.I. AARONSON, Inst. of Metals Monograph No. 33, (1968).

43. J.M. OBLAK and R.F. HEHEMANN, in "Transformation and Hardenability in Steels", Proc. Conf., Climax Moly. Co., Ann Arbor, (1967).

44. H.K.D.H. BHADESHIA and D.V. EDMONDS, Acta Met., 28, 1265, (1980).

45. F.B. PICKERING, in "Transformation and Hardenability in Steels", Proc. Conf., Climax Moly. Co., Ann Arbor, (1967).

46. R.F. HEHEMANN, K.R. KINSMAN and H.I. AARONSON, Metall. Trans., 3, 1077, (1970).

47. P. VASUDEVON, L.W. GRAHAM and H.J. AXON, JISI, 190, 386, (1958).

48. H.K.D.H. BHADESHIA, Acta Met., 29, 1117, (1981).

49. H.K.D.H. BHADESHIA, Acta Met., 28, 1103, (1980).

50. R.D. TOWNSEND, in "Phase Transformations", Proc. Conf., Inst. Met., York, (1979).

51. P.M. KELLY and J. NUTTING, JISI, 197, 199, (1961).

52. P.M. KELLY and J. NUTTING, Proc. Roy. Soc.(A), 259, 45 (1960).

53. J.M. CHILTON, C.J. BARTON and G.R. SPEICH, JISI, 208, 184, (1970).

54. E. LEVINE and D.C. HILL, Met. Trans. A, 8A, 1453, (1977).

55. C.L. CHOI and D.C. HILL, Weld, J. Res. Supp. 57, 232-s, (1978).

56. P.L. HARRISON, Mechanical Engineering Dept., University of Southampton Report ME79/24,(1979).

57. M.N. WATSON, Ph.D. Thesis, Southampton University, (1980).

58. D.J. ABSON and R.E. DOLBY, Welding Institute Research Bulletin, 19, 202, (1978).

59. S.S. TULIANI, Ph.D. Thesis, Southampton University, (1973).

60. D.J. ABSON, R.E. DOLBY and P.H.M. HART in "Trends in Steels and Consumables for Welding ", Proc. Conf., Welding Inst. London, (1978).

61. G.S. BARRITTE, R.A. RICKS and P.R. HOWELL in "Quantitative Microanalysis with High Spatial Resolution", Proc. Conf., The Metals Society, London, (in press).

62. Y. ITO and M. NAKANISHI, Sumi Search, 15, 42, (1976).

63. T.H. NORTH, H.B. BELL, A. KOUKABI and I. CRAIG, Weld, J.Res. Supp. 58, 343-s, (1979).

64. P.R. KIRKWOOD, in written discussion in "Trends in Steels and Consumables for Welding", Proc. Conf., Weld. Inst., London, (1978).

65. J. BOSANSKY, D.A. PORTER, H. ASTROM and K.E. EASTERLING, Scand. J. Met., 6, 125, (1977).

66. A.H. COTTRELL, "An Introduction to Metallurgy", Edward Arnold (Publishers) Ltd., London,(1967).

67. ASTM Standards, "Dilatometric Analysis of Metallic Materials", E80, (1976).

68. M. ATKINS, "Atlas of Continuous Cooling Transformation Diagrams for Engineering Steels", British Steel Corporation, Sheffield, (1977).

69. W. STEVEN and G. MAYER, JISI, 174, 33, (1953).

70 "Transformation Characteristics of Direct Hardening Nickel Steels", 3rd Ed., Mon Nickel Co., Birmingham, (1958).

71. "Alloy Steels", Samuel Fox and Co. Ltd., Sheffield, (1961).

72. A.S. KENNEFORD, V.E. RANCE, and S. TURNER, JISI, 205, 665, (1967).

73. R.G. BAKER, B.W.R.A.Report B2/32/62 (1962).

74. P.J. ALBERRY and W.K.C. JONES, Metals Tech. 4, 360, (1977).

75. P.L. HARRISON, M.N. WATSON and R.A. FARRAR, Weld. Metal Fab.,49, 161, (1981).

76. G.S. BARRITE and D.V. EDMONDS, in "Advances in the Physical Metallurgy of Steels", Proc. Conf., The Metals Society, London, (in press).

77. "Atlas of Isothermal Transformation Diagrams", United States Steel Company, Pittsburgh, Pennsylvania, (1951).

78. "Supplement to the Atlas of Isothermal Transformation Diagrams", United States Steel Company, Pittsburgh, Pennsylvania, (1953).

79. "Atlas of Isothermal Transformation and Cooling Transformation Diagrams", American Society for Metals, Metals Park, Ohio, (1977).

80. W.W. CIAS, "Phase Transformation Kinetics and Hardenability of Medium-Carbon Alloy Steels", Climax Molybdenum Compamy, Greenwich, Connecticut, (1972).

81. W.W. CIAS, "Phase Transformation Kinetics of Selected Wrought Constructional Steels", Climax Molybdenum Company, Greenwich, Connecticut, (1977).

82. J.M. GRAY, In "Physical Metallurgy and Technology of Niobium Containing Microalloyed Steel", CBMM-CCPIT, Symp., Peking, (1979).

83. L.S. POPE and J.D. GROZIER, Met. Prog. 100, 75, (1971).

84. Y.E. SMITH and C.A. SIEBART, Met. Trans., 2, 1711, (1971).

85. G. DELBART, A. CONSTANT and A. CLERC, "Courbes de Transformation des Aciers de Fabrication Francaise", L'Institut de Recherches de la Siderurgie, Saint Germain-en-Laye, (1956).

86. B. SERIN, Y. DESALOS, P. MAITREPIERRE and J. ROFES-VERNIS, Mém. Sci. Rev. Mét., 75, 355, (1978).

87. F. WEVER, A. ROSE, W. PETER, W. STRASSBURG and L. RADEMACHER, "Atlas zur Wärmebehandlung der Stähle", Verlag Stahleisen mbH. Düsseldorf, (1961).

88. A. ROSE and H. HOUGARDY, "Atlas zur Wärmebehandlung der Stähle", Vol. 2., Verlag Stahleisen mbH., Düsseldorf, (1972).

89. W.E. LAUPRECH, et. al., Stahl und Eisen, 93, 1041, (1973).

90. H.J. PEETZ, Dissertation, TU Branschweig, (1979).

91. M. ECONOMOPOULOS, N. LAMBERT and L. HABRAKEN, "Diagrammes de Transformation des Aciers fabriqués dans le Benelux", Centre National de Recherches Métallurgiques, Brussels (1967).

92. A.A. POPOV and L.E. POPOVA, "Isothermal and Thermokinetic Diagrams of the Breakdown of Supercooled Austenite", Metalurgiya, Moscow, (1965).

93. M. SHORSHOROV et. al., Met. Sci. Heat Treat., 15. 598. (1973).

94. V. KRAUS, "Atlas Kiagramu pro Zuslecht'ovani Konstruckenich Oceli", Statni Nakladatelstvia Technicke Literatory, Prague, (1964).

95. M. INAGAKI and H. SEKIGUCHI, Trans. Nat. Res. Int. Met. 2, 40, (1960).

96. H. NAKAJIMA and T. ARAKI, Trans. Nat.Res. Inst. Met. 10, 75, (1968).

97. T. KUNITAKE and H. OHTANI, Sumi, Met., 20, 135, (1968).

98. A. BROWNRIGG and R. BOELEN, Private Communication (1981).

99. N. CHRISTENSEN and T. SIMONSEN, Scand. J. Met., 10, 147, (1981).

100. A. CONSTANT, ATB Met., 8, 59, (1968).

101. A.G. GLOVER, J.T. McGRATH, M.J. TINKLER and G.C. WEATHERLY, Weld J.Res. Supp. 56, 267, (1977).

102. D.V. DORLING, P.E.L.B. RODRIGUES and J.H. ROGERSON in "Trends in Steels and Consumables for Welding", Proc. Conf., Weld. Inst., London, (1978).

103. K.W. ANDREWS, JISI, 184, 414, (1956).

104. F. WEVER, Arch. Eisenhüttenwesen, 2, 739, (1928). Mitt K.W.I. Eisenforsch, 13, 193, (1931). Ergebnisse der Technischen Röntgenkunde, 2, 240, (1931).

105. C. ZENER, Trans. Amer. Inst. Min. Met. Eng., 167, 513, (1946).

106. J.S. KIRKALDY, B.A. THOMSON and E.A. BAGANIS in "Hardenability Concepts with Applications to Steel", Proc. Symp. Met. Soc. AIME, Chichago, (1977).

107. R.A. GRANGE, Met. Trans. 4, 2231, (1973).

108. G.T. ELDIS and W.C. HAGEL in "Hardenability Concepts with Applications to Steel", Proc. Symp. Met. Soc. AIME, Chicago, (1977).

109. P. MAYNIER, J. DOLLET and P. BASTIEN, Rev. Met., 67, 343, (1970).

110. G.T. ELDIS in "Hardenability Concepts with Applications to Steel", Proc. Symp. Met. Soc. AIME, Chicago, (1977).

111. T. KUNITAKE and H. OHTANI, Sumi, Search, 2, 18, (1969).

112. L. RONN. Thesis for Degree of Metallurgical Engineer. The Royal Institute of Technology, Stockholm, (1963).

113. K.E. DORSCHU and R.D. STOUT, Weld. J.Res. Supp., 40, 97, (1961).

114. G. DEN OUDEN, J.G. VERHAGEN, G.W. TICHELAAR, Weld. J. Res. Supp., 54, 87, (1975).

115. G.M. EVANS, IIW Doc. No.II-A-432-77, (1977): Weld. J. Res. Supp., 59, 67-s, (1980).

116. S.S. TULIANI in "Welding Research related to Power Plants", Proc. Conf., CEGB, Marchwood, (1972).

117. S.S. TULIANI and R.A. FARRAR, Weld Metal Fab., 43, 553, (1975).

118. G. ALQUIST et. al., in "Welding Research related to Power Plant", Proc. Conf., CEGB, Marchwood, (1972).

119. Y. YOSHINO and R.D. STOUT, Weld. J.Res. Supp., 58, 59-s,(1979).

120. J.G. GARLAND and P.R. KIRKWOOD, BSC-Report PROD/832/1/76/C.

121. J.G. GARLAND and P.R. KIRKWOOD, BSC-Report PROD/499/1/74/C.

122. J.M. SAWHILL Jr., Climax Moly. Rep. No. L176-115, (1973).

123. R.J.JESSEMAN, in "Microalloying 75", Proc. Conf., (1975).

124. R.E. DOLBY, Metal Construction, 13, 699, (1981).

125. D.J. ABSON and G.M. EVANS, IIW DOC. II-A-530-81, (1981).

126. D.J. ABSON and R.E. DOLBY, IIW DOC. IXJ-29-80, (1980).

127. P.R. KIRKWOOD in "Low Carbon Structural Steels for the Eighties", Proc. Conf., Inst. Met., Plymouth, (1977).

128. R. FREEMAN, IIW DOC. No. XII-B-234-78, (1978).

129. R.C. COCHRANE and P.R. KIRKWOOD, in "Trends in Steels and Consumables for Welding", Proc. Conf., Weld. Inst., London, (1978).

130. R.A. FARRAR and M.N. WATSON, Metal Const., 11, 285, (1979).

131. P. PAYSON and C.H. SAVAGE, Trans. ASM, 33, 261, (1944).

132. L.A. CARAPELLA, Met. Prog., 46, 108, (1944).

133. E.S. ROWLAND and S.R. LYLE, Trans. ASM, 37, 27, (1946).

134. A.E. NEHRENBERG, Trans. AIME, 167, 494, (1946).

135. E.C. ROLLASON, in "Metallurgy for Engineers", Edward Arnold (Publishers) Ltd., (1977).

136. LORD KELVIN, Phil. Mag., 24, 503, (1887).

137. O.O. MILLER, Trans. ASM, 43, 260, (1951).

138. P.A. BECK et. al., AIME Tech. Pub., 14, 2280, (1947).

139. P.A. BECK et. al., ibid. 15, 2326 (1948).

140. P.J. ALBERRY, B. CHEW and W.K.C. JONES, Metals Tech. 4, 317, (1977).

141. C. ZENER, Private Communication to C.S. Smith. Trans. AIME., 175, 15, (1949).

142. P. HELLMAN and M. HILLERT, Scand. J. Metal, 4, 211, (1975).

143. M. FERRANTE and R.A. FARRAR, J. Mat. Sci. (in press).

144. T. GLADMAN, Proc. Roy. Sco. A294, 298, (1966).

145. D.A. JONES and J.W. MITCHELL, Phil. Mag., 3, 1, (1958).

146. J.M. ARROWSMITH, Ph.D. Thesis, Cambridge University, (1960).

147. P. COTTERILL and P.R. MOULD, in "Recrystallization and Grain Growth in Metals", Surrey University Press, London, (1976).

148. F.P. GLASSER, Am. J.Sci., 256, 405, (1958).

149. R.A. RICKS, G.S. BARRITTE and P.R. HOWELL, Unpublished work.

150. D.J. WALKER and R.W.K. HONEYCOMBE, Metal Sci., 12, 445, (1978).

151. P.D. SOUTHWICK and R.W.K. HONEYCOMBE, Metal Sci., 14, 253, (1980).

152. J.W. CAHN, Acta Met., 5, 169, (1957).

153. D. McLEAN, in "Grain Boundaries in Metals", Oxford University Press, London, (1957).

154. DUNN and LIONETTI, J. Metals, 1, 125, (1949).

155. C.J. GILLHAM, Private Communication, (1979).

156. W.J.M. SALTER, "A Manual of Quantitative Electron Probe Microanalysis", Structural Publications Ltd., London, (1970).

157. M. ECONOMOPOULOS, Métaux (Corrosion Ind.) 461, 1, (1964).

158. K.J. IRVINE, F.B. PICKERING and T. GLADMAN, JISI, 205, 161, (1967).

159. J.E. HILLIARD, Met. Prog., 85, 99, (1964).

160. E.E. UNDERWOOD, in "Metals Handbook", 8, 37, (1973). A.S.M. Metals Park, Ohio 44073.

161. M. FERRANTE, Unpublished work.

162. T.F. RUSSEL, JISI, 139, 147, (1939).

163. W. STEVEN and A.G. HAYNES, JISI, 183, 349. (1956).

164. L. VAN NASSAU and H. DE HULLU, IIW DOC., No. II-A-475-79, (1979).

165. R. GAILLARD, S. DEBIEZ and M. DADIAN, IIW DOC., No. II-A-464-79, (1979).

166. R.B. LAZOR and H.W. KERR, in "Pipeline and Energy Plant Piping: Design and Technology," Proc. Conf., Weld. Inst. of Canada, Calgary, (1980).

167. M.N. WATSON, P.L. HARRISON and R.A. FARRAR, Weld. Metal Fab., 49, 101, (1981).

168. K.W. ANDREWS, JISI, 203, 721, (1965).

169. J.H. SWISHER and E.T. TURKDOGAN, Trans. Met. Soc. AIME, 239, 427, (1967).

170. R.C. SHARMA and G.R. PURDY, Met.Trans., 4, 2303, (1973).

171. R.A. FARRAR, L.G. TAYLOR and E.M. HARRISON, Metals Tech. 6, 380, (1979).

172. Metals Handbook, A.S.M. Metals Park, Ohio 44073.

173. T.G. NILAN, in "Transformation and Hardenability in Steels", Proc. Conf., Climax Moly. Co., Ann Arbor, (1967).

APPENDIX

LIMITATIONS AND ERRORS ASSOCIATED WITH CCT DIAGRAM DETERMINATIONS

Dilatometry

Dilatometry is a very accurate method of monitoring $\gamma \rightarrow \alpha$ transformation temperatures provided the temperature of the dilatometer specimens remain uniform. According to Eldis [1] the error associated with the location of the start of transformation (T_s) should not be greater than ±5°C if the cooling rate remains low. This error is primarily due to the accuracy of specimen temperature measurement, but is also dependent to some extent on the dilatometer sensitivity.

In the current investigation the errors associated with T_s temperature measurements at slow cooling rates are estimated as follows.

Temperature Measurement	Thermocouple error	±1°C
	Error due to welding thermocouple to specimen(measured experimentally)	±2°C
	Cold junction correction error	±2°C
	Total:	±5°C
	Error in locating T_s	±5°C
	Maximum total error	±10°C

The error associated with location of the finish of transformation (T_F) is generally large, due to the curvature of the dilatation versus temperature line as shown in Figure A1. This curvature arises from the variation of expansion coefficient with temperature and alloy content. In addition some combinations of alloying and cooling rate further exaggerate this curvature problem by producing small pools of enriched austenite in the latter stages of the $\gamma \rightarrow \alpha$ reaction which may transform to pearlite, bainite or martensite over a very wide temperature range. Location of the precise T_F temperature in such cases is extremely difficult. The magnitude of the error involved in locating T_F has been suggested by Eldis to be as high as ±35°C.

In the current investigation the errors associated with T_F measurements at slow cooling rates are considered to be as follows:-

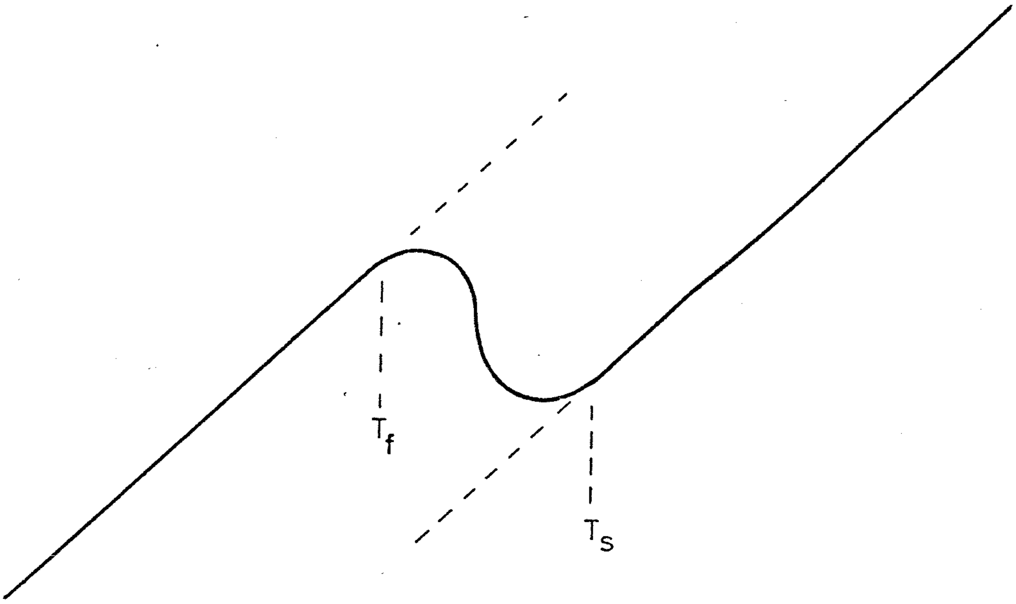

Idealised curve

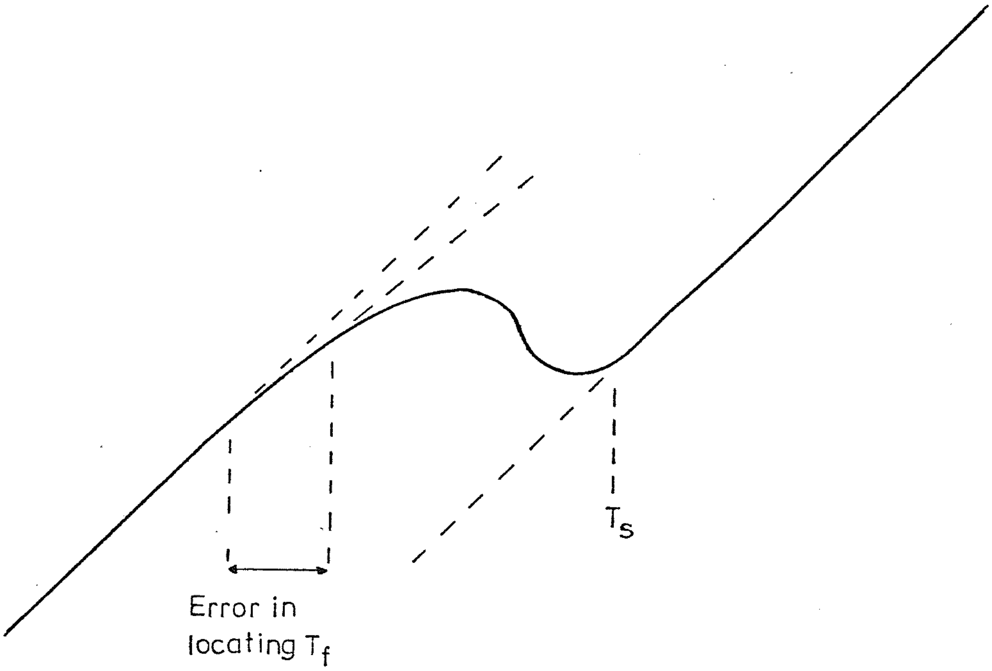

Severe case of curvature due to alloy system

Figure A1 Error in determining the finish of transformation (T_f).

Temperature Measurement	Thermocouple errors (As for T_s)	±5°C
	Error in locating T_F	±35°C
	<u>Maximum total error</u>	<u>±40°C</u>

In the event of microstructures containing a small volume fraction of enriched austenite (most weld metals investigated) the measured T_F is assumed to apply to the bulk transformation rather than the T_F of the microphases.

Temperature gradients occurring within the dilatometer specimen are also a major source of experimental error in high speed dilatometry. For example, during rapid cooling the dilatometer senses the $\gamma \rightarrow \alpha$ T_s as it starts to occur in the coolest part of the specimen. Unless the thermocouple position happens to correspond with this coolest position, the recorded value of T_s will be too high. The temperature gradients expected to occur in the Linseis (solid) and Theta (hollow) dilatometer specimens during rapid cooling are shown in Figure A2.

The magnitude of these dilatometer specimen temperature gradients has been measured experimentally during continuous cooling and the results are shown in Figure A3. From Figure A3(a) it can be seen that the recommended Linseis thermocouple arrangement will give an indicated T_s temperature some 10°C to 15°C too high in the 600°C to 800°C temperature range at a cooling rate of 50°C/sec. Similarly, the recommended Theta thermocouple arrangement also overreads T_s during rapid cooling. Figure A3(b) indicates the magnitude of the Theta specimen temperature gradients at various cooling rates, and it can be seen that the error in estimating T_s from the normal thermocouple arrangement can be as large as 200°C to 300°C at the fastest quench rates ($\sim$400°C/sec). To overcome this problem all the dilatometric results obtained with the Theta dilatometer at cooling rates >90°C/sec utilised a twin thermocouple arrangement as shown in Figure A3(b). This method provided a more satisfactory method of locating T_s and T_F. However, in view of the magnitude of the specimen temperature gradients it is believed that the T_s may be in error by as much as ±25°C when using this method.

Temperature gradients in rapidly cooled Linseis dilatometer specimens.

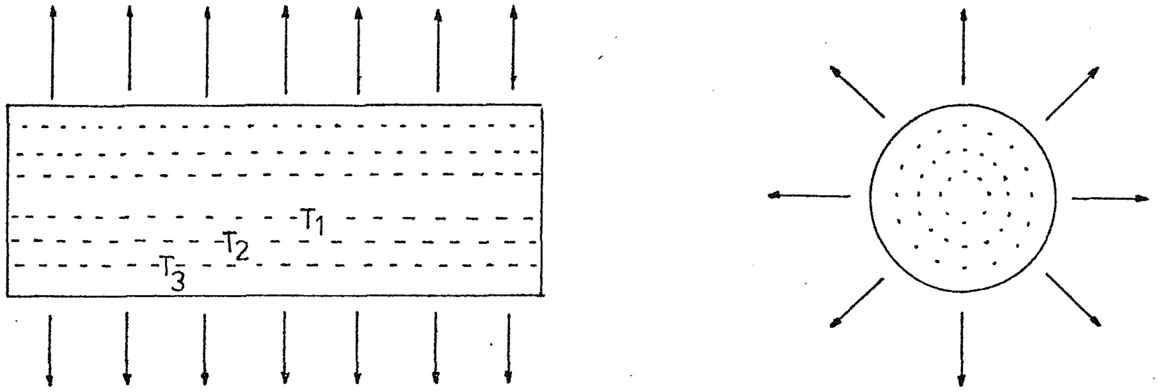

$T_1 > T_2 > T_3$

Temperature gradients in rapidly cooled Theta dilatometer specimens.

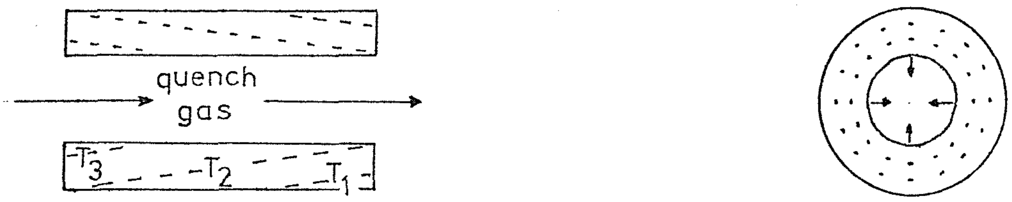

$T_1 > T_2 > T_3$

Figure A2 Temperature gradients in rapidly cooled dilatometer specimens (schematic).

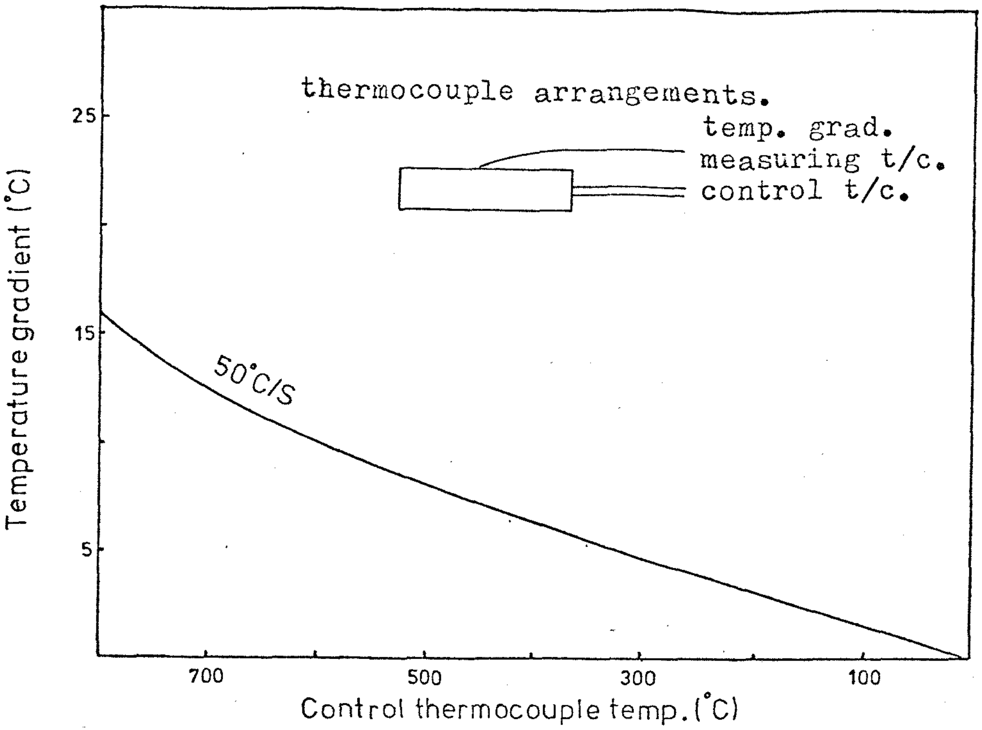

Figure A3(a) Temperature gradients occuring in a rapidly cooled Linseis dilatometer specimen.

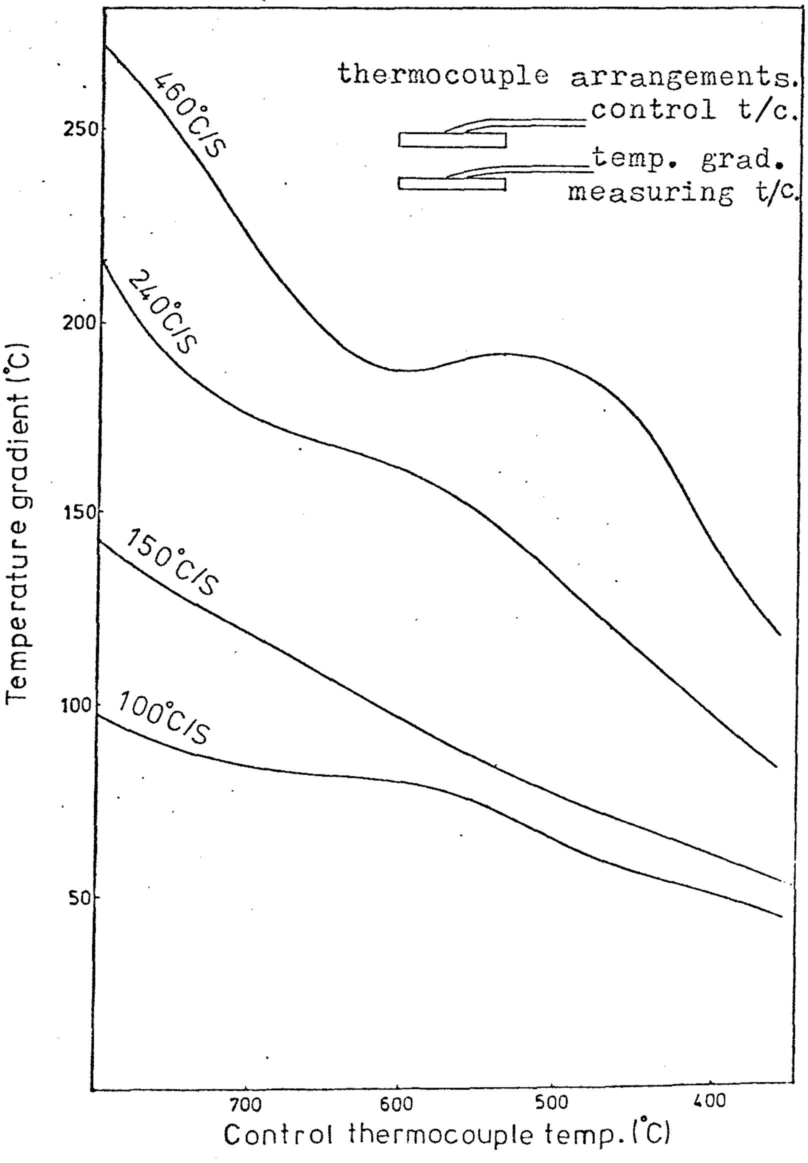

Figure A3(b) Temperature gradients occuring in a rapidly cooled Theta dilatometer specimen.

The maximum total error in locating T_s at fast cooling rates is therefore as follows:-

Temperature Measurement error	$\pm 5^{\circ}$C
Error in locating T_s	$\pm 5^{\circ}$C
Error due to temperature gradients	$\pm 25^{\circ}$C
Maximum total error	$\pm 35^{\circ}$C

Similarly the error associated with location of the finish of transformation (T_F) at fast cooling rates is estimated as follows:-

Temperature measurement	$\pm 5^{\circ}$C
Error in locating T_F	$\pm 35^{\circ}$C
Error due to temperature gradients	$\pm 25^{\circ}$C
Maximum total error	$\pm 65^{\circ}$C

The errors associated with the dilatometric technique used for CCT diagram determinations in the present work may be summarised as follows.

(1) At slow cooling rates (<10-20°C/sec i.e. the natural cooling rate of the specimens) the maximum error is that inherent in the dilatometric technique, i.e. $T_s \pm 10^{\circ}$C $T_F \pm 40^{\circ}$C

(2) At cooling rates between $\sim 20^{\circ}$C/sec and 90°C/sec temperature gradients in both types of specimen lead to an over-reading of T_s, ($+15^{\circ}$C for a Linseis specimen at 50°C/sec). However the T_F's should be reasonably accurate due to the thermocouple arrangements, i.e. $T_F \pm 40^{\circ}$C (as above).

(3) At very fast cooling rates twin thermocouples were used to reduce errors. In this case the magnitude of the error is estimated at $T_s \pm 35^{\circ}$C, $T_F \pm 65^{\circ}$C.

It should be appreciated that the above discussion relates to maximum errors and that in practice the majority of errors will be considerably smaller than those quoted. Unfortunately the nature of the dilatometric results precluded the possibility of making a statistical assessment of errors.

Dilatometer calibration

Calibration of each of the dilatometers was checked by constructing the CCT diagram for pure iron. Pure iron is a suitable material for this type of calibration as the $\gamma \rightarrow \alpha$ transformation temperature remains constant at $910^{o}C$ at slow cooling rates. Figure A4 shows the resylts of Bibby and Parr [2], Gilbert and Owen [3] and the results obtained from the Linseis and Theta dilatometers in the current investigation. It can be seen that all results lie reasonably close to the expected CCT curve for pure iron and thus give reasonable confidence to the results obtained for weld metal transformation temperatures in the current work.

Thermal Analysis

The various methods of thermal analysis used to determine phase transformations are detailed in ASTM standards No.E-14, "Recommended Practice for Thermal Analysis of Metals and Alloys".[4] The methods discussed include the time-temperature method, inverse rate method, direct rate method, differential method and the derived differential method. Few CCT diagrams have been derived totally by thermal analysis as the techniques are generally considered inferior to dilatometry in their ability to produce quantitative data. Russell [5] comprehensively reviewed the qualitative and quantitative interpretation of thermal curves and drew attention to a number of fallacies in the interpretation of thermal curves. For example a common pitfall in the interpreation of inverse rate curves is the belief that the rate of evolution of heat is proportional to the distance of the inverse-rate curve from the datum line. Russell showed that a "peak" on an inverse-rate curve may be due to either an abrupt increase in specific heat or an evolution of heat at a constant temperature. In the written correspondence following Russell's paper, Handford [6] made several suggestions regarding the use of thermal analysis techniques including the following:

(a) "That a time-temperature curve was generally preferable to any derived curves, on the grounds of easier and sometimes more full interpretation".

(b) "That, except for rough work on cases known to be very simple, it was a bad waste of time and dissipation of energy to take any derived curve in an uncontrolled furnace giving the usual asymptotic time-temperature relationship".

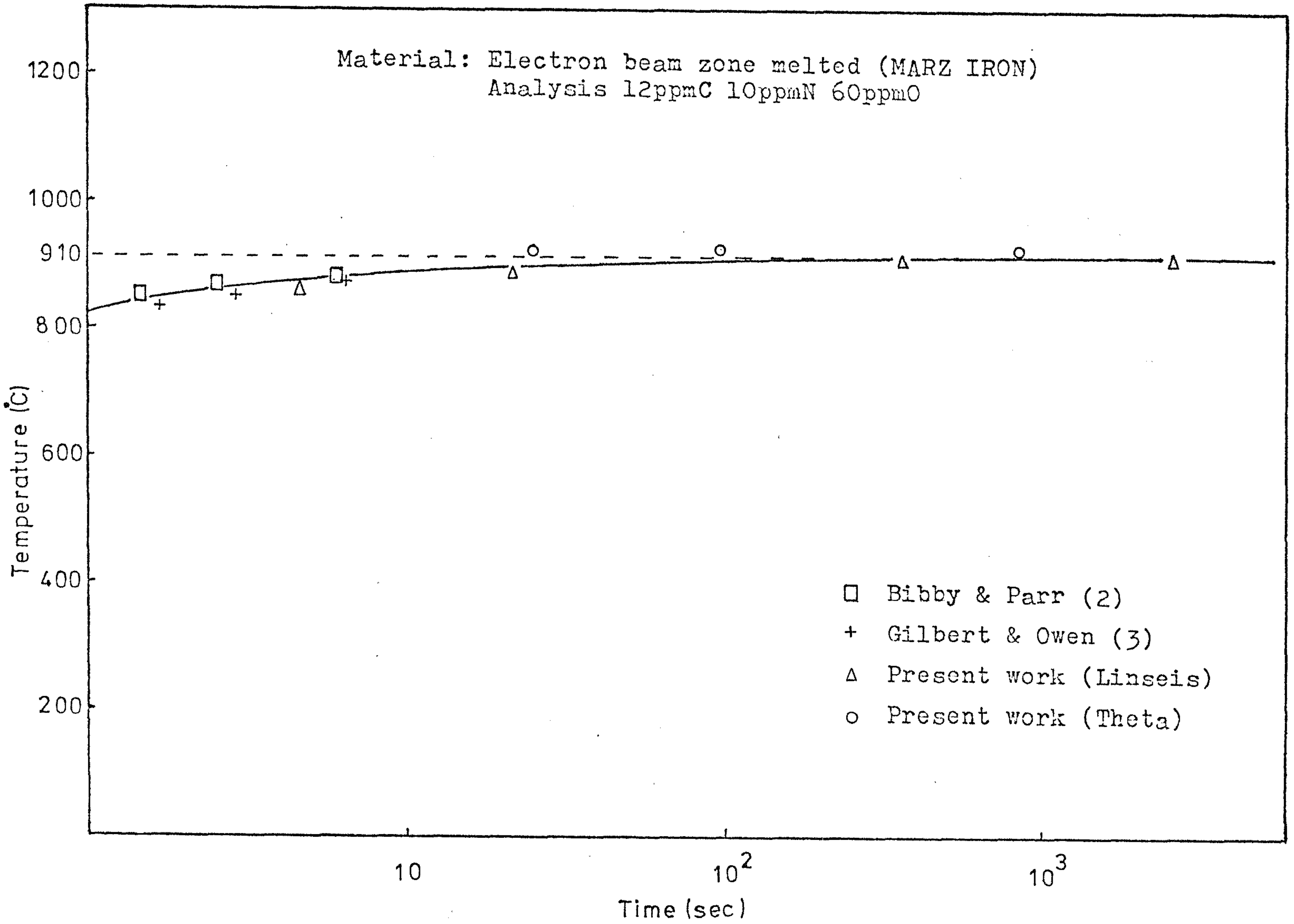

Figure A4 CCT diagram for pure iron.

The above points are particularly relevant to the measurement of phase transformations during welding, where the time-temperature relationship is clearly asymptotic.

A further major pitfall in applying thermal analysis techniques directly to welding, are problems associated with temperature gradients within the welded joint. It is clear that a steep temperature gradient exists between the weld bead and parent plate shortly after welding. This temperature gradient ensures that the $\gamma \rightarrow \alpha$ transformation will always start some distance from the weld centre line and travel inwards towards the centre line. It may therefore be expected that a thermocouple positioned on the weld bead centre line will detect the $\gamma \rightarrow \alpha$ transformation occurring some distance away from the thermocouple, and thus give a false and unpredictable result.

This hypothesis was checked experimentally by attaching a thermocouple to the austenitic end of an composite austenite/ferrite dilatometer specimen as shown in Figure A5. Although the thermocouple position was some 4mm distant from the ferritic material a discontinuity was observed in the cooling curve corresponding to the $\gamma \rightarrow \alpha$ transformation of the ferritic material. This result clearly shows that thermocouples may sense phase transformations occurring at some considerable distance from their point of contact with the specimen.

In the current work no attempt has been made to analyse transformation data obtained from real weld cooling curves. However a limited amount of thermal analysis was carried out on small rapidly cooled thin disc specimens. Following the previous suggestions of Handford, simple time-temperature curves were used rather than derivative curves and T_s positions were estimated directly. In view of the lack of accurate reference cooling curves for specimens not undergoing transformation, the estimated maximum error associated with these T_s measurements is thought to be about $\pm 25^{\circ}C$. It should also be appreciated that thermal analysis techniques are often insensitive in detecting split transformations such as ferrite/martensite or bainite/martensite especially if a large proportion of martensite is being formed [7]. In such cases only the martensite reaction will be detected even though a few percent transformation may be occurring prior to M_s.

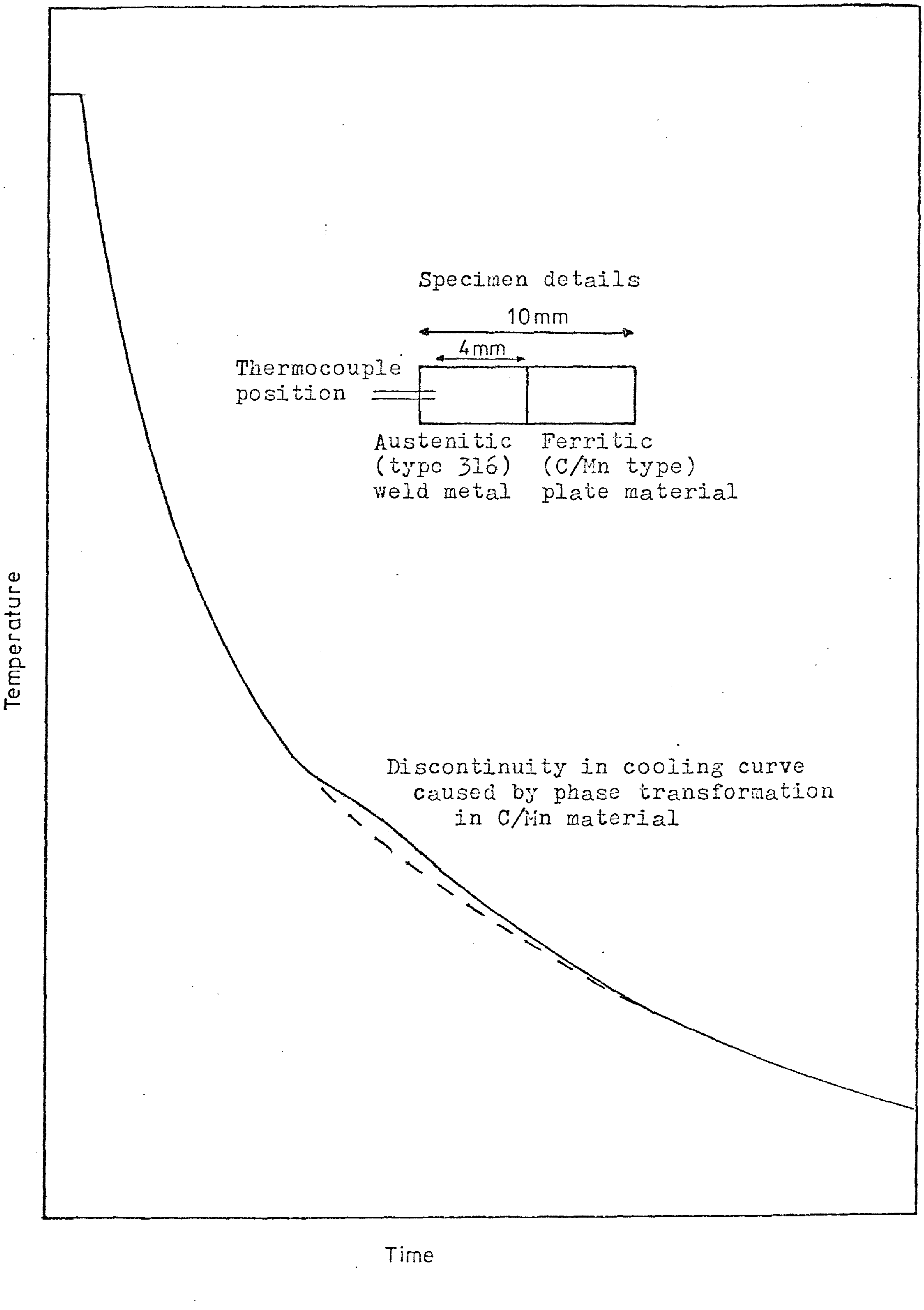

Figure A5 Cooling curve for composite austenitic / ferritic dilatometer specimen.

Quantitative Metallography

The internal division of transformation regimes within the weld metal CCT diagrams depends to a large extent on quantitative metallography. It is therefore of interest to consider the errors inherent in this type of analysis.

Pacey and Kerr [8] carried out quantitative studies on HSLA steel weld metals similar to those studied in the current work. Their investigation used very similar quantitative metallography techniques to those of the present investigation (i.e.∿1000 point counts at magnifications between x 350 and x800). Four different microstructural types were counted for: Proeutectoid ferrite (PF), Acicular ferrite (AF), Lath structures (LS) and "Others", i.e. blocky carbides and M-A complexes. Each weld was examined on three sections in order to assess the magnitude of the point counting errors. Table A1 shows the results of this investigation and gives a good indication of the range of errors to be expected in the current work. It can be seen that the maximum point counting error occurs when the counted phase fraction constitutes about 50% volume fraction. The magnitude of this maximum error is generally of the order of 10 volume %. This result is in good agreement with the maximum point counting errors previously quoted for the present work [9]. The effect of varying the point counting magnification between x350 and x800 was found to be within ±2 volume % and therefore constitutes very little error.

Microstructural phase	Range of volume %	Range of error (Volume %)
PF	1.5 - 20	0.4 - 4.7
AF	35 - 55	4.1 - 8.2
LS	30 - 46	3.8 - 11.3
Other	6 - 8	0.3 - 1.6

Table A1 Summary of errors in the quantitative microstructural analysis of weld metals after Pacey and Kerr (8).

REFERENCES

1. G.T. ELDIS in "Hardenability Concepts with Applications to Steel", Proc. Symp. Met.Soc. AIME, Chicago, (1977).

2. M.J. BIBBY and J. GORDON PARR, JISI, 202, 100, (1964).

3. A. GILBERT and W.S. OWEN, Acta Met., 10, 45, (1962).

4. ASTM Standards "Recommended Practice for Thermal Analysis of Metals and Alloys", Pt.31, 120, (1966).

5. T.F. RUSSELL, JISI, 139, 147, (1939).

6. C. HANDFORD, ibid. in correspondence.

7. R. H. PHILLIPS, Brit., Weld. J., 15, 547, (1968).

8. A.J. PACEY and H.W. KERR in "Weldments: Physical Metallurgy and Failure Phenomena", Proc. Conf., G.E.C. Schenectady, (1978).

9. P.L. HARRISON, Report No. ME79/24, Southampton University, (1979).

FIGURE AND TABLE INDEX

FIGURE NO: PAGE

FIGURE AND TABLE INDEX (Cont...)

FIGURE AND TABLE INDEX (cont:)

FIGURE AND TABLE CONTENTS (Cont...)

FIGURE AND TABLE CONTENTS (cont.....)

FIGURE NO. PAGE

FIGURE AND TABLE CONTENTS (Cont...)

FIGURE AND TABLE CONTENTS (Cont....)

FIGURE AND TABLE CONTENTS (Cont...)

FIGURE AND TABLE CONTENTS (Cont....)